Error and Uncertainty in Estimates of Reynolds Stress Using an ADCP in an Energetic Ocean State

by

Mark Rapo

Submitted to the Department of Mechanical Engineering
in partial fulfillment of the requirements for the degree of

Master of Science in Oceanographic Engineering

at the

MASSACHUSETTS INSTITUTE OF TECHNOLOGY

and the

WOODS HOLE OCEANOGRAPHIC INSTITUTION

Feb 2006

© Mark Rapo, MMVI. All rights reserved.

Author . . . .
Joint Program in Oceanography/Applied Ocean Science and Engineering
Massachusetts Institute of Technology
Woods Hole Oceanographic Institution
December, 2005

Certified by . . . .
James Preisig
Associate Scientist
Woods Hole Oceanographic Institution
Thesis Supervisor

Accepted by . . . .
Prof. Henrik Schmidt
Chairman, Joint Committee for Applied Ocean Science and Engineering
Massachusetts Institute of Technology

Error and Uncertainty in Estimates of Reynolds Stress Using an ADCP in an Energetic Ocean State

by

Mark Rapo

Abstract

The challenge of estimating the Reynolds stress in an energetic ocean environment derives from the turbulence process overlapping in frequency, or in wavenumber, with the wave process. It was surmised that they would not overlap in the combined wavenumber-frequency spectrum, due to each process having a different dispersion relationship. The turbulence process is thought to obey a linear dispersion relationship, as the turbulent flow is advected with the mean current (Taylor's frozen turbulence approximation). However, the Acoustic Doppler Current Profiler (ADCP) looks at radial wavenumbers and frequencies, and finds overlap. Another approach is to exploit the physical differences of each process, namely that the wave induced velocities are correlated over much larger distances than the turbulence induced velocities. This method was explored for current meters by Shaw and Trowbridge. Upon adapting the method for the ADCP, it is found that the resulting Reynolds stress estimates are of the correct order of magnitude, but somewhat noisy. The work of this thesis is to uncover the source of that noise, and to quantify the performance limits of estimating the Reynolds Stress when using ADCP measurements that are contaminated with strong wave-induced velocities. To that end, the space-time correlations of the error, turbulence, and wave processes are developed and then utilized to find the extent to which the environmental and internal processing parameters contribute to this error. It is found that the wave-induced velocities, even when filtered, introduce error variances which are of similar magnitude to that of the Reynolds stresses.

Acknowledgments

There are a number of people who I would like to thank for helping me along in a project such as this. First and foremost, it has been a pleasure to have worked with my advisor, Jim Preisig. He has taught me to proceed from first principles, to be thorough in application, and to question my results. He has provided a steadiness for me as I have grown from relying on his guidance to seeing my own way forward. It has been a journey fraught with many sidesteps, which were kept in check by the joyful forward steps. I am grateful to have had such a good mentor.

Secondly, I would like to thank my new advisors, Mark Grosenbaugh and Houshou Jiang, for allowing me the extra time needed to wrap up the thesis. The final preparations always seemed to take longer than expected, and they were fair and understanding in setting deadlines.

I am also thankful for the many friends I've made along the way, who have provided me with many joyful occasions. I think of playing tennis with Alex, ping pong with Jin-Shan, taking classes with Wen Yu, enjoying evening celebrations with Ioannis and Dee, and scuba diving, hanging out, and telling jokes with Brendan. I am so fortunate to have had great roommates, Biswajit, Goncalo, Asher, Song, and Morgan, who have made my place of living both enjoyable and a safe haven for being productive. I am thankful to Biswajit and Weichang, my office mate, for lending an ear as I worked through various challenges in my work.

I am grateful for Daniel Vine, who provided any needed technical assistance on a moments notice, and who has believed in me from day one. His help was significant, and I am glad to say he has been a friend to me for many years now.

I am thankful for Min Garabedian, who has provided me with moral support

and challenged me to think through the choices I have been making. He has been a support and a longtime friend. He has helped to carry the emotional burden of this thesis, and can rejoice in it's completion.

I am thankful for my family, who have been a listening ear and source of encouragement. They have seen me absorbed with my work, as it was always on my mind whenever we were together. I am grateful that they were understanding, and allowed me to partake in fellowship as I was able to. I think especially of my cross-country trip with my brother Bradley, where I had the computer running non-stop, even as we shared in all kinds of wonderful experiences.

I am thankful for Shannon, my sweetie, who has shared in the ups and downs of this process, and who has supported me throughout. She has experienced the losses and the successes firsthand, and deserves to share in the joy and celebration of its completion. It has been a learning process for us both, and we have tackled it together, and that has been wonderful. We have grown closer, and we look forward to many more adventures. And to all of her friends, who have supported and encouraged her, and who have prayed for me, I say thank you.

Finally, I reserve my greatest gratitude to God, who never ceases to surprise me, and fills me with great joy. At this turn, and the next, He proceeds me, and my journey is blessed.

Contents

Chapter 1

Introduction

Many theories which attempt to model various processes in the ocean rely on the accurate measurement of the Reynolds Stress. However, these measurements become suspect when energetic surface waves are present. Previously, Shaw and Trowbridge [19] utilized a method of filtering out the effects of the waves by exploiting the physics the problem, namely the assumption that the wave induced water velocities are coherent over much larger spatial scales than turbulent induced velocities. Their work used multiple current meters, vertically spaced off the ocean bottom. However, it would be desirable to obtain an entire column profile of measurements. This thesis examines the possibility of using radial velocity measurements from an Acoustic Doppler Current Profiler (ADCP) to estimate the Reynolds Stress.

The main thrust of this work is to develop and then analyze the performance of signal processing algorithms which filter out wave influences in the radial velocity measurements made by the ADCP. Performance will be evaluated by comparing results using real ocean data to results using statistical models of the data. In preparation for future work (beyond this thesis), steps to simulate the entire process are developed, so that there is access to data from the turbulent process and the wave process independently, which is not the case in the real ocean environment.

The theoretic groundwork of this thesis can roughly be divided into two major themes: the development and analysis of signal processing algorithms, and the numerical simulation of the turbulent and wave processes in space and time.

Simulation System
for Turbulent Velocity
Measurements with ADCPs

```
┌─────────────────┐         ┌─────────────────┐
│ ADCP & Signal   │         │ Signal          │
│ Transmission    │         │ Processing      │
└─────────────────┘         └─────────────────┘
        │                            ┊
        ▼                   ┌ ─ ─ ─ ─ ─ ─ ─ ─ ─ ┐
┌─────────────────┐           ┌───────────────┐
│ Scattering Model│         │ │ Velocity      │ │
│ With Doppler Shift│          │ Estimation    │
└─────────────────┘         │ └───────────────┘ │
        │                     ┌───────────────┐
        ▼                   │ │ Turbulent Signal│ │
┌─────────────────┐           │ Extraction    │
│ Turbulent and   │         │ └───────────────┘ │
│ Surface Wave    │          ─ ─ ─ ─ ─ ─ ─ ─ ─ ─
│ Velocity Fields │                   │
└─────────────────┘                   ▼
        │                   ┌─────────────────┐
        ▼                   │ Validation      │
┌─────────────────┐         └─────────────────┘
│ ADCP Received Signal │
└─────────────────┘
```
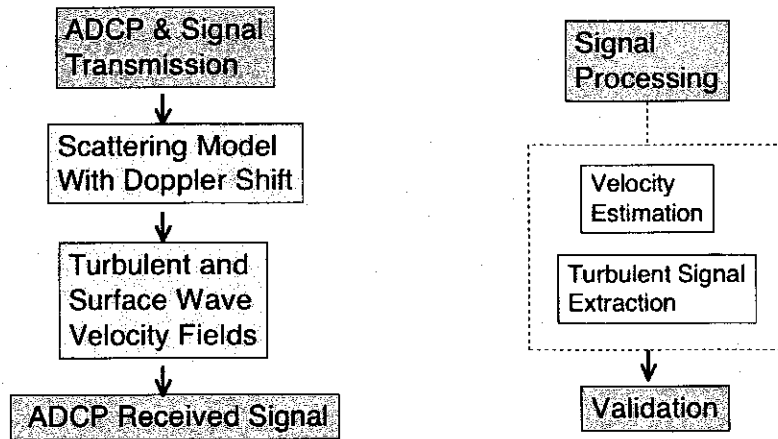
Figure 1-1: The two main themes of this thesis: modeling the ocean processes, and developing algorithms to which utilize them.

The introduction goes into more detail about the Reynolds stress, the problem of energetic surface waves, and general methods that have been used to address the problem. Chapter 2 formulates the estimates of Reynolds stress when waves have not been filtered out, and determines the variance of these estimates. Chapter 3 adapts the filter methods for the ADCP. Chapter 4 gives background specifics on how ADCP's work, and explains what limitations they might introduce in measuring the Reynolds stress. Chapters 5-7 present the theoretic work needed to determine the space-time correlations for the turbulence induced velocities. In addition, chapter 5 presents a method for simulating a turbulent flow. Chapter 8 develops the space-time correlations for wave induced velocities, and presents a method for simulating the surface wave field. Chapter 9 performs a wavenumber-frequency analysis of the combined processes in an attempt to understand how they combine in the radial direction. Chapter 10 presents the predicted error of the estimates of Reynolds stress when using the optimal linear filter, and how model parameters affect the error. Chapter 11 presents the full ocean-ADCP simulator. Finally, the conclusion will summarize the findings of this thesis.
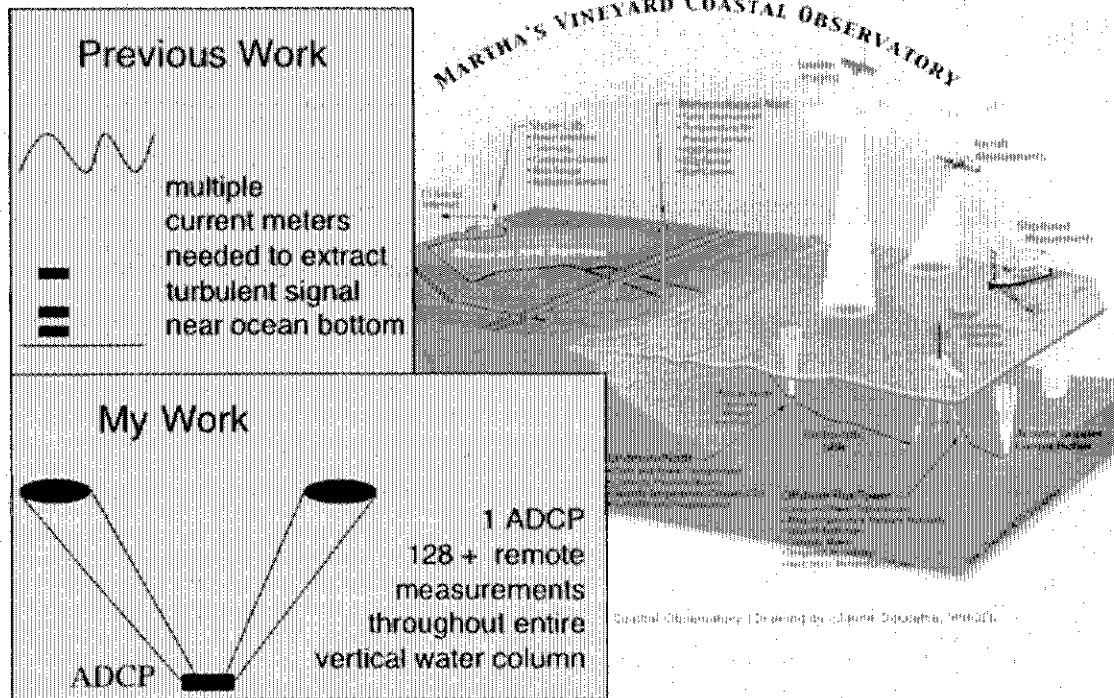
Figure 1-2: ADCP's have the ability to make measurements at many ranges. ADCP's are an integral part of ocean observing platforms. (3D Graphic by Jayne Doucette,WHOI)

1.1   Notation Conventions

ADCP Notation

v	Instantaneous (and actual) radial velocities
V	Measured radial velocities from slightly misaligned sensor
$V_{B1..B4}$	B1..B4 denote ADCP beams 1 to 4
ϕ	ADCP beam tilt angle (from vertical)
c	Speed of sound in water
$s(t)$	ADCP transmit signal
$q(t)$	ADCP received signal (including noise)
$Q(f)$	Fourier Transform of received signal

Waves and Turbulence Notation

$\vec{x}, \vec{r} = (x, y, z)$	Location vectors (from an origin) will be denoted by an arrow
$\vec{x}_{a..z}$	Subscripts denote different points in space or time
$\mathbf{t} = [t_1, t_2, ..t_N]$	Boldface denotes a series of points or velocities in space or time
$u_i, i = 1, 2, 3$	Instantaneous velocities in the x,y, and z directions
$\overline{u}$	Ensemble averages will be denoted by an overbar
$< u >$	Time average will be denoted by triangle brackets
u'	Turbulent quantities will be denoted by a prime
$\tilde{u}$	Wave quantities will be denoted by a tilde
U	Velocity as measured by a slightly misaligned sensor
A	Wave amplitude
h	Height to surface of water (from ocean floor)
λ	Wavelength
$\vec{k} = (k_x, k_y, k_z)$	Wavenumber vector
$k = |\vec{k}| = 2\pi/\lambda$	Magnitude of wavenumber vector
$r = |\vec{r}|$	Magnitude of separation vector (distance)
T	The period of a wave
f	Frequency (Hz)
$\omega = 2\pi f$	Angular frequency (radians)
θ	Direction of propagating waves
Θ	Random starting phase of progating wave
R_{ij}	Correlation tensor
S_{ij}	Power spectral density tensor (Fourier transform of R_{ij})
Φ_{ij}	Turbulent power spectral density tensor
Λ	Pierson-Moscowitz wave height power spectral density

Estimation Notation

X,Y   Random variables

x,y   Sample values of the random variables

E[X]   Expectation of a random variable

$\hat{x}$ Estimated quantities will be denoted by a hat

w   White Gaussian noise

h[n]   Filter weights

h   Boldface and lowercase denotes a vector

H   Boldface and capital denotes a matrix

1.2   Motivation

Turbulence is a very common phenomenon. Most people have encountered turbulence when flying on a plane, or watching smoke rise out of the chimey of an industrial plant, or being tumbled under water when large ocean waves break near shore. In the ocean, these unpredictable swirlings and tumblings occur near the sea floor as currents move past (such as due to the tides), and near the surface where breaking waves and changing winds lead to stirring and mixing motions. These motions are quite important in transporting momentum, heat, sediment, and other passive scalars. For scientists who study weather and climate, it is quite relevant to know how the ocean is removing and releasing heat. For geologists who study the effects of erosion, or for biologists who need to know how far larva will be carried when released into the water, the effects of turbulence near the ocean floor need to be known. Environmentalists worry about the impact of chemical spills, and they need to know what areas will be affected and to what degree. These are just a few examples which illustrate the importance of understanding turbulence.

The exact mechanisims which govern the transition from laminar flow to turbulent flow are not well understood. In the most general sense, turbulence arises when inertial forces overcome viscous forces. Small disturbances, which would normally be

damped out, become amplified. Reynolds number expresses this relationship. [28]

$$
\begin{aligned}
\text{inertial forces} \quad &\sim \text{mass x acceleration} \quad \sim (\rho L^3)(U^2/L) \\
\text{viscous forces} \quad &\sim \text{shear stress x area} \quad \sim (\mu \partial u/\partial y)(L^2) \sim (\mu U/L)(L^2) \\
R_e \quad = \frac{\text{inertial forces}}{\text{viscous forces}} \quad &\sim \frac{(\rho U^2 L^2)}{\mu U L} \sim \frac{\rho U L}{\mu}
\end{aligned}
\tag{1.1}
$$

Here, ρ is the density of water, μ is the viscosity of water, U is the velocity of the water, and L is the length scale of the flow. Depending on boundary conditions and overall flow conditions, turbulence can be begin at Reynolds numbers as low as 200.

Predicting the exact flow of a turbulent fluid is impossible at this time, so one method of studying turbulence is to look at time averaged quantities. The Reynolds-Averaged Navier-Stokes equation (since Reynolds is considered the first person to have taken this approach [2]), is

$$
\frac{\partial \overline{u_i}}{\partial t} + \overline{u}_j \frac{\partial \overline{u_i}}{\partial x_j} = \frac{1}{\rho} \frac{\partial}{\partial x_j} \left[\overline{\sigma_{ij}} - \rho \overline{u_i' u_j'} \right].
\tag{1.2}
$$

The pressure term is part of the stress tensor,σ_{ij}. The last term, $-\rho \overline{u_i' u_j'}$, is called the Reynolds stress, and is of great interest. It can be thought of as a transport term, where momentum is carried along at the rate of the second velocity. Many theories rely on this number, and having accurate empirical measurements is of utmost importance.

Laboratory methods of measuring turbulence include hot-wire anemometry (HWA), hot-film anemometry, and laser Doppler velocimetry (LDV), while deployable ocean instruments include Acoustic Doppler Velocimeters (ADV), Modular Acoustic Velocity Sensors (MAVS), Vector Averaging Current Meters (VACM), and Vector Mesasuring Current Meters (VMCM). These instruments are able to resolve the vector motions of the fluid at a given point in space. Other deployable ocean instruments, such as Acoustic Doppler Current Profilers (ADCP), send out beams of sound which enable sampling of the current at many locations. However, ADCP's must rely on statistical averaging in order to resolve the vector motions of the current, and this can be problematic if the statistics of the flow are changing in time.

18
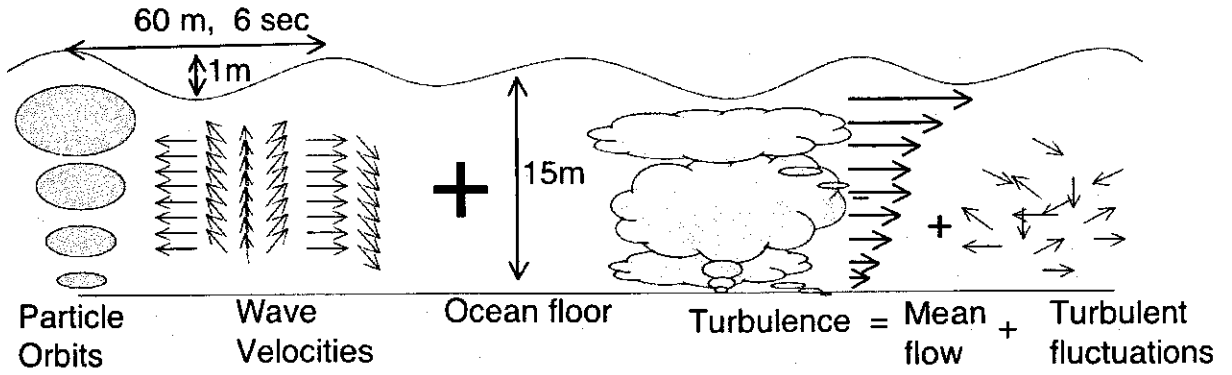
Figure 1-3: Wave motions are orders of magnitude larger than turbulent motions.

1.3 The Problem

In the presence of surface waves, a measured velocity component can be represented as the sum of its mean component, a fluctuating turbulent component, and a wave component.

$$u_i = \overline{u_i} + u_i' + \tilde{u}_i \tag{1.3}$$

Near the bottom boundary layer of the ocean, it can be assumed that the process responsible for creating the turbulence is independent of the process creating the surface waves. When two processes are independent, the cross correlation between turbulent fluctuations and wave induced velocities is zero, $\overline{u'\tilde{u}} = 0$. The cross-covariance of the two measured velocity components will consist of a turbulent term and a wave induced term.

$$
\begin{aligned}
\text{cov}(u_i, u_j) &= \overline{(u_i - \overline{u_i})(u_j - \overline{u_j})} \\
&= \overline{(u_i' + \tilde{u}_i)(u_j' + \tilde{u}_j)} \\
&= \overline{u_i'u_j'} + \overline{u_i'\tilde{u}_j} + \overline{\tilde{u}_iu_j'} + \overline{\tilde{u}_i\tilde{u}_j} \\
&= \overline{u_i'u_j'} + \overline{\tilde{u}_i\tilde{u}_j}
\end{aligned}
\tag{1.4}
$$

For typical ocean bottom measurements in a coastal region, the turbulent term, $\overline{u_i'u_j'}$, is on the order of $10^{-4}m^2s^{-2}$. The wave correlation term, $\overline{\tilde{u}_i\tilde{u}_j}$, is on the order $10^{-1}m^2s^{-2}$. [25] Normally, only the vertical transport of horizontal momentum is of interest (ie. where i=1,2 and j=3). For that case, the horizontal wave velocities are out of phase with vertical wave velocities, and the cross-covariance wave term is zero.

However, when there is uncertainty between the axes of the instrument and the principle wave axes, the measured radial velocities have wave and turbulent components which are correlated. A transformation of coordinates will reveal how any uncertianty in aligment leads to cross contamination of the horizontal and vertical velocities.

$$
\begin{bmatrix} U_1 \\ U_3 \end{bmatrix} = \begin{bmatrix} \cos\beta & \sin\beta \\ -\sin\beta & \cos\beta \end{bmatrix} \begin{bmatrix} u_1 \\ u_3 \end{bmatrix} \tag{1.5}
$$

U_1 and U_3 are the horizontal and vertical velocities as recorded by the slightly misaligned instrument, u_1 and u_3 are horizontal and vertical velocities in their true directions, and β is the unknown misalignment. With the sensor misaligment very small, $\cos\beta$ is about 1, and $\sin\beta$ is approximately β. A bias term appears when taking the cross correlation of the horizontal and vertical velocities.

$$
\begin{aligned}
\overline{U_1 U_3} &= \overline{(u_1 + \beta u_3)(-\beta u_1 + u_3)} \\
&= \overline{u_1 u_3} + \beta(\overline{u_3^2} - \overline{u_1^2}) - \beta^2 \overline{u_1 u_3} \\
&= \beta(\overline{u_3^2} - \overline{u_1^2})
\end{aligned} \tag{1.6}
$$

$\overline{u_1^2}$ and $\overline{u_3^2}$ are not zero, and for $\overline{\tilde{u}_1 \tilde{u}_3}$, to be 10% of $\overline{u_1' u_3'}$, β needs to be on the order of 10^{-4}. This is hardly practical, and so there needs to be a method of removing (or reducing) the wave velocities from the measurements.

1.4 Previous Solutions

1.4.1 Differencing strategies

Trowbridge [25] utilized the well known physics of the problem to separate the wave and turbulent components of velocity. In general, waves are coherent over much larger spatial scales than turbulence. Averaging the difference in velocities obtained from two sensors placed further apart than turbulence correlation scales, but less than wave correlation scales, the wave bias should disappear. Letting ΔU_1 and ΔU_3 be the horizontal and vertical velocity difference between the two sensors, the cross-covariance of velocity differences provides a good estimate of the $\overline{u_1' u_3'}$ term.

$$
\begin{aligned}
(1/2)\ \mathrm{cov}(\Delta U_1, \Delta U_3)\ &= \overline{(\Delta U_1 - \overline{\Delta U_1})(\Delta U_3 - \overline{\Delta U_3})} \\
&= \overline{(\Delta U_1' + \Delta \tilde{U}_1)(\Delta U_3' + \Delta \tilde{U}_3)} \\
&= \overline{\Delta U_1' \Delta U_3'} + \overline{\Delta \tilde{U}_1 \Delta \tilde{U}_3} \\
&\approx \overline{u_1' u_3'}
\end{aligned}
\tag{1.7}
$$

As will be seen, $\overline{\Delta U_1' \Delta U_3'} \approx 2\overline{u_1' u_3'}$, and the $\overline{\Delta \tilde{U}_1 \Delta \tilde{U}_3}$ term is approximately zero under the above assumptions.

For the turbulent term, small sensor misalignment has neglible impact on the fluctuating turbulent correlation terms (since $\beta(\overline{u_3'^2} - \overline{u_1'^2}) << \overline{u_1' u_3'}$), and can be negelected.

$$
\begin{aligned}
\overline{U_1 U_3}\ &= \overline{u_1' u_3'} + \beta(\overline{u_3'^2} - \overline{u_1'^2}) \\
&\approx \overline{u_1' u_3'}
\end{aligned}
\tag{1.8}
$$

Remembering that the turbulent velocities between sensors are uncorrelated, the turbulent cross-covariance of velocity difference is seen to be the sum of the turbulent correlations from each sensor.

$$
\begin{aligned}
\overline{\Delta u_1' \Delta u_3'}\ &= \overline{(u_1'(\vec{x_b}) - u_1'(\vec{x_a}))(u_3'(\vec{x_b}) - u_3'(\vec{x_a}))} \\
&= \overline{u_1'(\vec{x_b})u_3'(\vec{x_b})} - \overline{u_1'(\vec{x_b})u_3'(\vec{x_a})} - \overline{u_1'(\vec{x_a})u_3'(\vec{x_b})} + \overline{u_1'(\vec{x_a})u_3'(\vec{x_a})} \\
&= \overline{u_1'(\vec{x_b})u_3'(\vec{x_b})} + \overline{u_1'(\vec{x_a})u_3'(\vec{x_a})} \\
&\approx 2\overline{u_1' u_3'} \quad (\text{for } \overline{u_1'(\vec{x_b})u_3'(\vec{x_b})} \approx \overline{u_1'(\vec{x_a})u_3'(\vec{x_a})} \text{ at the same depth})
\end{aligned}
\tag{1.9}
$$

As already noted, small sensor misalignment does have impact on the wave correlation terms, since they are of significant magnitude. However, the cross-covariance of wave velocity difference is close to zero, even with sensor misalignment.

$$
\begin{aligned}
\overline{\Delta \tilde{U}_1 \Delta \tilde{U}_3} \quad &= \overline{(\tilde{U}_1(\vec{x_b}) - \tilde{U}_1(\vec{x_a}))(\tilde{U}_3(\vec{x_b}) - \tilde{U}_3(\vec{x_a}))} \\
&= \overline{\tilde{U}_1(\vec{x_b})\tilde{U}_3(\vec{x_b})} - \overline{\tilde{U}_1(\vec{x_b})\tilde{U}_3(\vec{x_a})} - \overline{\tilde{U}_1(\vec{x_a})\tilde{U}_3(\vec{x_b})} + \overline{\tilde{U}_1(\vec{x_a})\tilde{U}_3(\vec{x_a})} \\
&= \beta_b(\overline{\tilde{u_3}^2(\vec{x_b})} - \overline{\tilde{u_1}^2(\vec{x_b})}) + (\beta_b\overline{\tilde{u}_1(\vec{x_b})\tilde{u}_1(\vec{x_a})} - \beta_a\overline{\tilde{u}_3(\vec{x_b})\tilde{u}_3(\vec{x_a})}) \\
&\quad + (\beta_a\overline{\tilde{u}_1(\vec{x_a})\tilde{u}_1(\vec{x_b})} - \beta_b\overline{\tilde{u}_3(\vec{x_a})\tilde{u}_3(\vec{x_b})}) + \beta_a(\overline{\tilde{u_3}^2(\vec{x_a})} - \overline{\tilde{u_1}^2(\vec{x_a})}) \\
&= \beta_b(-\overline{\tilde{u_1}^2(\vec{x_b})} + \overline{\tilde{u}_1(\vec{x_a})\tilde{u}_1(\vec{x_b})}) + \beta_b(\overline{\tilde{u_3}^2(\vec{x_b})} - \overline{\tilde{u}_3(\vec{x_b})\tilde{u}_3(\vec{x_a})}) \\
&\quad + \beta_a(-\overline{\tilde{u_1}^2(\vec{x_a})} + \overline{\tilde{u}_1(\vec{x_b})\tilde{u}_1(\vec{x_a})}) + \beta_a(\overline{\tilde{u_3}^2(\vec{x_a})} - \overline{\tilde{u}_3(\vec{x_a})\tilde{u}_3(\vec{x_b})}) \\
&\approx 0 \quad (\text{when } \overline{\tilde{u_1}^2(\vec{x_b})} \approx \overline{\tilde{u}_1(\vec{x_a})\tilde{u}_1(\vec{x_b})}, \text{ etc.})
\end{aligned}
$$

$$(1.10)$$

With typical surface wavelengths of about 50 meters, and with the sensors spaced within a few meters (at roughly the same depth), the assumption that the individual components of the wave induced velocities are approximately equal at the two sensor locations is satisfactory. The final result is that $\frac{1}{2}$ cov($\Delta U_1, \Delta U_3$) is just an average of the vertical transport of horizontal momentum between the two sensor locations.
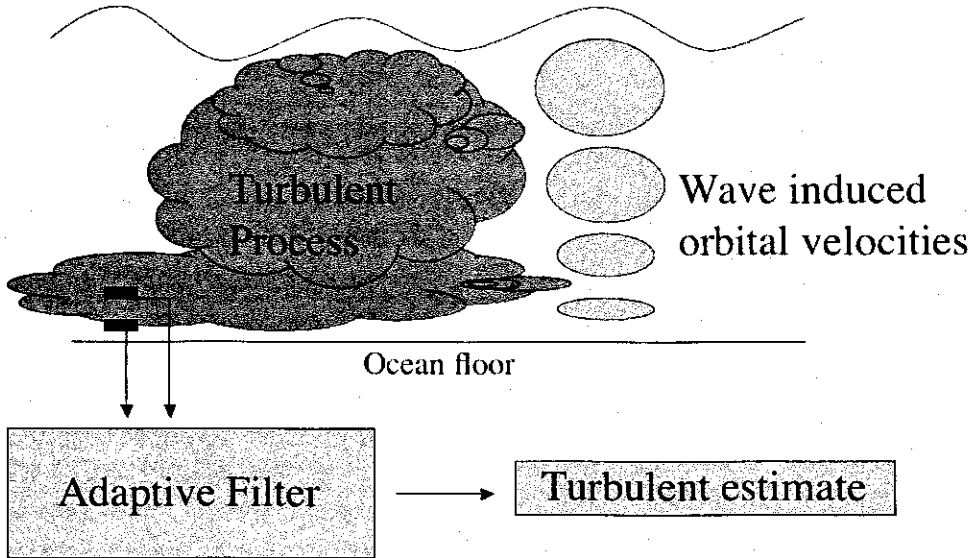
Figure 1-4: Main assumption: wave velocities are coherent over a much larger spatial scale than turbulent velocities.

1.4.2 Differencing strategies with filtering

Shaw and Trowbridge [19] then took a different approach in reducing the wave bias. Instead of assuming that the wave induced velocities at the two sensors are basically equal, it is enough to assume they are coherent. Then it is possible to use the velocity at one sensor to make an estimate of the coherent parts of the velocity at the other sensor.

$$U[\vec{x_b}, \text{n}] \longrightarrow \boxed{\quad \text{h[n]} \quad} \longrightarrow \hat{U}[\vec{x_a}, \text{n}]$$

$$\hat{U}[\vec{x_a}, \text{n}] = \sum_k \text{h[n-k]} U[\vec{x_b}, \text{k}] \tag{1.11}$$

The filter weights are those which make the best linear fit of the velocities at the second sensor (contained the data matrix $\mathbf{D}$), to the velocities at the first sensor (represented by the data vector $\mathbf{u}$). The standard least squares solution [20] to $\mathbf{Dh} = \mathbf{u}$, is $\mathbf{h} = (\mathbf{D}^T\mathbf{D})^{-1}\mathbf{D}^T\mathbf{u}$. Each column of the matrix $\mathbf{D}$ is a data series of length M, and each successive column is advanced one time step, until there are as many columns as there filter weights desired. The vector $\mathbf{u}$ has the same time steps as the middle

column in **D**. Taking the cross-covariance of the difference term (between estimated and actual horizontal velocity) with the vertical velocity term at one sensor gives the desired estimate.

$$
\begin{aligned}
\text{cov}(\Delta U_1, U_3) &= \overline{((U_1 - \hat{U}_1) - \overline{(U_1 - \hat{U}_1)})(U_3 - \overline{U_3})} \\
&= \overline{((U_1' + \tilde{U}_1) - (\hat{U}_1' + \hat{\tilde{U}}_1))(U_3' + \tilde{U}_3)} \\
&= \overline{(U_1' - \hat{U}_1')(U_3' + \tilde{U}_3)} \\
&= \overline{U_1' U_3'} + \overline{U_1' \tilde{U}_3} - \overline{\hat{U}_1' U_3'} - \overline{\hat{U}_1' \tilde{U}_3} \\
&= \overline{U_1' U_3'} \approx \overline{u_1' u_3'}
\end{aligned}
\tag{1.12}
$$

In the second line, the coherent parts, $\tilde{U}_1$ and $\hat{\tilde{U}}_1$, cancel out. In the fourth line, turbulent fluctuations are independent of the wave induced velocities, and cancel out. In addition, there is no way of estimating the turbulent fluctuation of one sensor, $\hat{U}_1'$, from another sensor since the sensors are out of the turbulent correlation range. That means that the estimate of the turbulent component is essentially random, and uncorrelated with either the actual turbulent fluctuation or the wave induced velocity. Therefore, the only term left is the desired term, $\overline{U_1' U_3'} \approx \overline{u_1' u_3'}$.

It is worth noting that this estimate effectively removes the wave influences, and is basically robust to small sensor misalignment. In addition, both $\text{cov}(\Delta U_1, U_3)$ and $\text{cov}(U_1, \Delta U_3)$ should give the same result, and this provides a way of error checking the validity of assumptions made using this method. This method also allows for a broader spatial arrangement of the sensors, including vertical separations, with the only requirement that the wave components remain coherent between the two sensors. Finally, an estimate can be made at each sensor independently, so averaging over the sensors is not required.

Chapter 2

Uncertainty in Estimates of Reynolds Stress Using an ADCP in an Energetic Ocean State

One of the advantages of an ADCP is that it is able to provide a profile of radial velocity measurements, which are then transformed into a profile of Reynolds stress estimates. In section 2.1, the basic method for forming estimates of Reynolds stress using radial velocity measurements from the ADCP is presented. The measurements are unfiltered, and in section 2.2 the effect of beam tilt on the estimates is considered. Finally, in section 2.3, a method for calculating the variance of the estimates directly from the data is presented using the work of Williams and Simpson [26]. The conclusion is that the ADCP can provide approximate estimates of the Reynolds stess when there is minimal beam tilt, or when the wave-induced velocities are not energetic.

2.1   Calculating Reynolds Stress using ADCP measurements

One of the advantages of an ADCP is that it is able to provide a profile of velocity measurements, whereas many other measuring instruments provide vector measure-
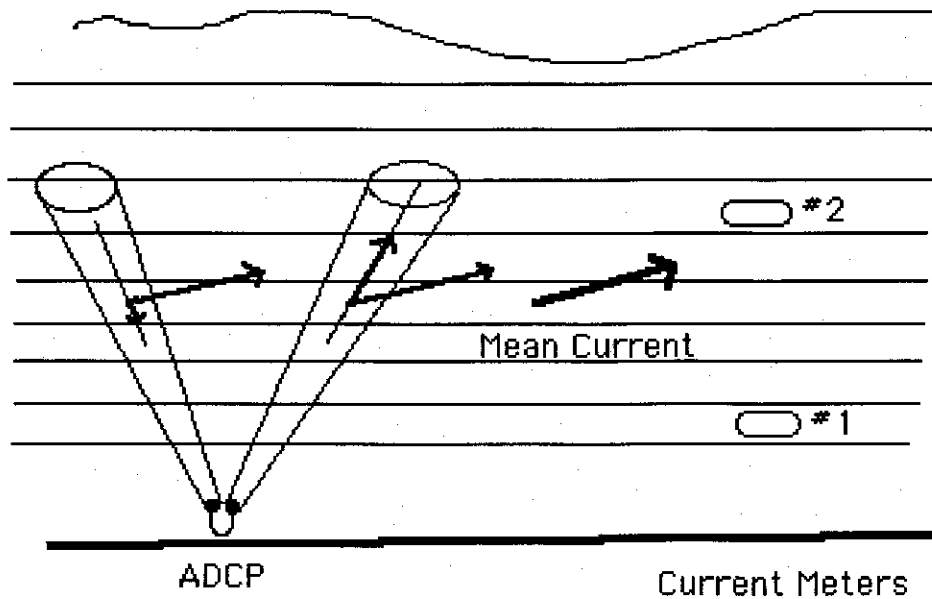
Figure 2-1: One ADCP remotely measures radial velocities at many locations, whereas current meters need to be physically present at each location.

ments of the velocity at individual locations. It also has the advantage leaving the flow being measured undisturbed, since it only sends out beams of sound (see figure 2-1).

One of the disadvantages of the ADCP is that it only makes measurements of velocity in the direction of each beam. Whereas many of the single point instruments are able to give a velocity vector measurement, the ADCP must rely on the stationarity of the statistics in the ocean medium in order to give mean velocity vector components.

The sound beams of the ADCP are at an angle ϕ from the vertical. As each sound beam travels through the water, it scatters off small organisms that float passively, and returns to the ADCP transducer. After some internal processing, the result is a profile of radial velocities, V, for each beam. Assuming that the mean velocity vector is the same at any given vertical level, then the geometry of the beams allow for the

Beams are angled 20° - 30° from the vertical.
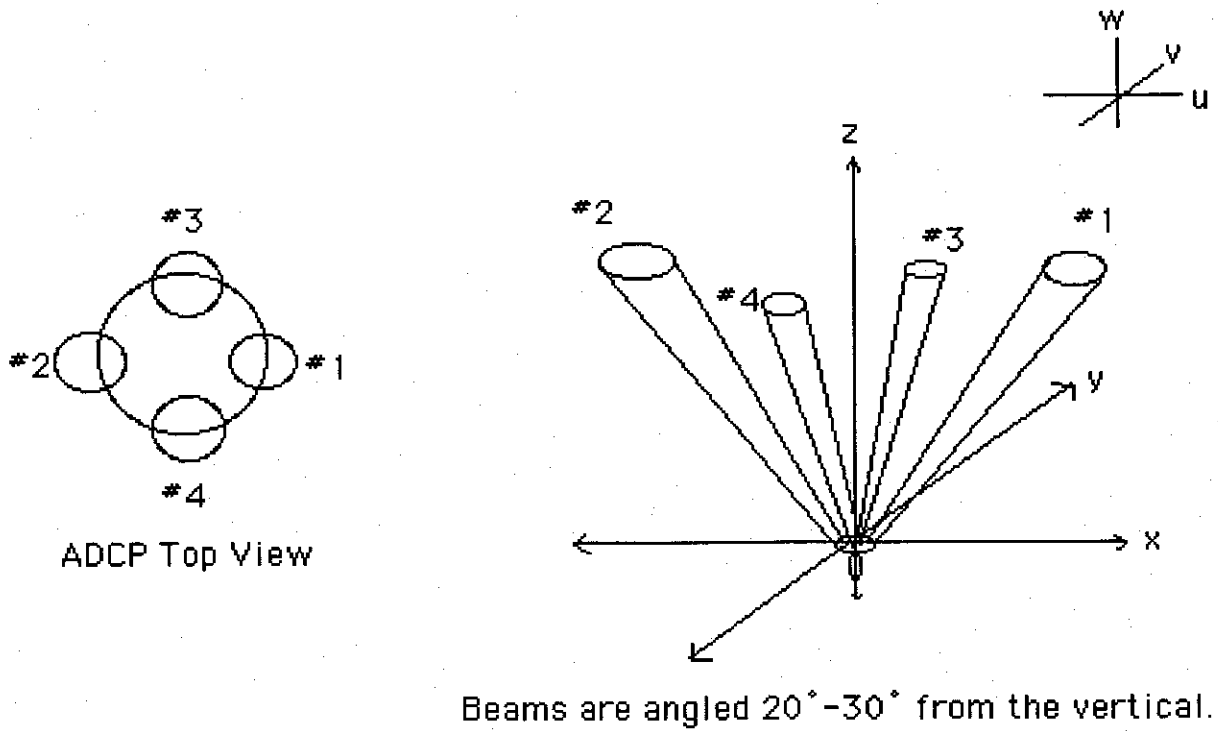
Figure 2-2: The top view and side view geometries of the ADCP.

mean current to be calculated. (See figure 2-2 for the geometry and numbers.)

$$\overline{U_1} = \frac{\overline{V_{B2}} - \overline{V_{B1}}}{2\sin\phi}, \qquad \overline{U_2} = \frac{\overline{V_{B4}} - \overline{V_{B3}}}{2\sin\phi}, \qquad \overline{U_3} = \sum_{i=1}^{4} \frac{\overline{V_{Bi}}}{4\cos\phi} \qquad (2.1)$$

The radial velocity is a combination of its component velocities. As a convention, ADCPs record radial velocities toward the transducers as positive, and away from the transducers as negative. From the previous beam geometry, the radial turbulent velocities at similar radial distances on two separate beams are given as follows:

$$
\begin{aligned}
V_{B1}(\vec{x}_a, t) &= -U_1(\vec{x}_a, t)\sin\phi - U_3(\vec{x}_a, t)\cos\phi \\
V_{B2}(\vec{x}_b, t) &= U_1(\vec{x}_b, t)\sin\phi - U_3(\vec{x}_b, t)\cos\phi
\end{aligned} \qquad (2.2)
$$

The radial variances for points at similar radial distances on at beam tilt, ϕ, are as

27

follows:

$$\overline{(V_{B1}(\vec{x}_a, t))^2} = \overline{(U_1(\vec{x}_a, t))^2}\sin^2\phi + \overline{(U_3(\vec{x}_a, t))^2}\cos^2\phi + 2\overline{(U_1(\vec{x}_a, t)U_3(\vec{x}_a, t))}\sin\phi\cos\phi$$

$$\overline{(V_{B2}(\vec{x}_b, t))^2} = \overline{(U_1(\vec{x}_a, t))^2}\sin^2\phi + \overline{(U_3(\vec{x}_b, t))^2}\cos^2\phi - 2\overline{(U_1(\vec{x}_b, t)U_3(\vec{x}_b, t))}\sin\phi\cos\phi$$

$$(2.3)$$

In order to finish the calculations and estimate the Reynolds Stress at a particular vertical location, it is necessary that the Reynolds Stress be the same at similar vertical locations. This requirement of spatial homogeniety is reasonable since it is very unlikely that there is some disruption of the flow in the relatively short span between beams.

$$\overline{U_1(\vec{x}_a, t)U_3(\vec{x}_a, t)} = \overline{U_1(\vec{x}_b, t)U_3(\vec{x}_b, t)}, \qquad \overline{U_1(\vec{x}_a, t)^2} = \overline{U_1(\vec{x}_b, t)^2} \qquad (2.4)$$

Using the assumptions of spatial homogeneity and stationarity of statistics,

$$\begin{aligned}
\overline{(V_{B1}(\vec{x}_a, t))^2} - \overline{(V_{B2}(\vec{x}_b, t))^2} &= 4\overline{U_1 U_3}\sin\phi\cos\phi \\
[\overline{(V_{B1}(\vec{x}_a, t))^2} - \overline{(V_{B2}(\vec{x}_b, t))^2}]/(4\sin\phi\cos\phi) &= \overline{U_1 U_3}
\end{aligned} \qquad (2.5)$$

Since each measurement of radial velocity can be decomposed into mean, turbulent, wave, and error component,

$$V_{Bi}(\vec{x}, t) = \overline{V}_{Bi}(\vec{x}) + V'_{Bi}(\vec{x}, t) + \tilde{V}_{Bi}(\vec{x}, t) + V^e_{Bi}(\vec{x}, t), \qquad (2.6)$$

$-\rho\overline{U_1 U_3}$ will not give the desired Reynolds stress, $-\rho\overline{u'_i u'_j}$. However, subtracting the two radial variances will lead to an $-\rho\overline{u_i u_j}$ estimate which is close to the one desired.

$$\widehat{\overline{u'_1 u'_3}} \approx [\text{var}(V_{B1}(\vec{x}_a, t)) - \text{var}(V_{B2}(\vec{x}_b, t))]/(4\sin\phi\cos\phi) \qquad (2.7)$$

where

$$\begin{aligned}
\text{var}(V_{Bi}(\vec{x}, t)) &= \overline{(V_{Bi}(\vec{x}, t)) - \overline{V_{Bi}(\vec{x}, t))^2})} \\
&= \overline{(V'_{B1}(\vec{x}, t) + \tilde{V}_{B1}(\vec{x}, t) + V^e_{B1}(\vec{x}, t))^2} \qquad (2.8) \\
&= \overline{(V'_{B1}(\vec{x}, t))^2} + \overline{(\tilde{V}_{B1}(\vec{x}, t))^2} + \overline{(V^e_{B1}(\vec{x}, t))^2}
\end{aligned}$$

The final equality results from assuming that the cross-covariance terms are zero, based on the assumption that the wave, turbulent, and error processes are independent from each other. These assumptions will be true to the extent that the processes are not coupled.

The error terms, $V_{Bi}^e(\vec{x}, t)$, from individual ADCP measurements of the radial velocity, are very likely random. The error is based on the measurement of the phase of the return signal, which is subject to irregular fluctuations due to individual scatter orientations and distances, in addition to any other noise factors that interfere. This would indicate that the error associated with each radial velocity measurement is independent of every other measurement in space and time. Although this does not rule out correlation with the wave and turbulent processes, it is unlikely that it is significant.

For the wave and turbulent processes, there could be some coupling near the surface, where crashing waves will introduce their own turbulence. However, after a few meters, the processes that create turbulence, such as the tidal flow, are independent of the wave processes. Any real coupling is beyond the extent of this thesis, and is worthy of future research.

Revisiting $\overline{U_i' U_j'}$, the error terms $\overline{(V_{Bi}^e(\vec{x}, t))^2}$ are independent of direction, and should cancel out upon subtraction. Therefore

$$
\begin{aligned}
\overline{\hat{u}_1' u_3'} &\approx \overline{U_1' U_3'} + \overline{\tilde{U}_1 \tilde{U}_3} \\
&\approx \overline{U_1' U_3'} \\
&\approx \overline{u_1' u_3'}
\end{aligned} \tag{2.9}
$$

The second equality is approximately true when uncertainty in beam tilt is minimal, so that $\overline{\tilde{U}_1 \tilde{U}_3} \approx \overline{\tilde{u}_1 \tilde{u}_3} \approx 0$. Therefore, the Reynolds stress estimate is $-\rho \overline{\hat{u}_i' u_j'}$. The next section examines the effect that beam tilt has on the estimates.

2.2 ADCP Tilt and Beam Alignment Uncertainty

There are two factors which lead to cross contamination of component velocities. The first is the tilt of the ADCP resting on the ocean bottom, and the second is the additional individual tilt of each beam. It is very difficult to get the beams to point in the true direction, so at factory installation their installed tilts are measured and recorded for subsequent post processing. In addition, the ADCP has sensors which detect the overall tilt.

First it will be instructive to see how the general tilt of the ADCP affects the measured radial velocities, and then if necessary, to examine the affect of each beam individually.

Knowing the tilt of the ADCP (to within some given resolution) is very useful for finding the true mean velocity components of the current, $\overline{U_1}, \overline{U_2}$, and $\overline{U_3}$. Since the velocity components are a linear combination of the radial velocities (see equation 2.1), corrections can be applied at any point in the process using a standard rotation matrix.

$$
\begin{bmatrix} \overline{u_1} \\ \overline{u_2} \\ \overline{u3} \end{bmatrix} = \begin{bmatrix} 1 & -\gamma & \beta \\ \gamma & 1 & -\psi \\ -\beta & \psi & 1 \end{bmatrix} \begin{bmatrix} \overline{U_1} \\ \overline{U_2} \\ \overline{U_3} \end{bmatrix}
\tag{2.10}
$$

where ψ, β and γ are small counter-clockwise rotations about the x, y, and z axes respectively.

Unfortunately, this is not the case for the Reynolds stress estimates. Although it is possible to calculate u_i on a per measurment basis using the known tilts of the ADCP and each beam, forming the estimate $\overline{u_i u_j}$ will not give the Reynolds stress. These measurements are constructed by using radial velocities on opposing beams, and are therefore the cross correlation measurements made at large lag (the span of the beams).

There is also no hope of performing post corrections. Since the Reynolds stress is a nonlinear term, any tilt in a beam leads to contamination of the three main directions, u_i^2, and all of their cross products, $u_i u_j$. Therefore each radial velocity is a

combination of 6 terms, and there are only four beams with which to solve for these unknowns.

The value in knowing the beam tilt is that it provides a measure of the uncertianty in the Reynolds stress estimate. To begin with, the inverse of the rotation matrix (which is just its transpose for small γ, β, ψ) can be utilized to show how the true velocity components appear in the tilted ADCP.

$$
\begin{aligned}
U_1 &= u_1 + \gamma u_2 - \beta u_3 \\
U_2 &= -\gamma u_1 + u_2 + \psi u_3 \\
U_3 &= \beta u_1 - \psi u_2 + u_3.
\end{aligned} \tag{2.11}
$$

Generally, ψ, β, and γ are on the order of a few degrees, 3*pi/180 $\approx$ 1/20. A safe estimate would be 1/10. Keeping the first order ψ, β, and γ terms (since their products cause a reduction of 1/100), the Reynolds Stress estimates are given by

$$
\begin{aligned}
\overline{U_1 U_3} &= \overline{(u_1 + \gamma u_2 - \beta u_3)(\beta u_1 - \psi u_2 + u_3)} \\
&= \overline{u_1 u_3} + \beta(\overline{u_1^2} - \overline{u_3^2}) + \gamma \overline{u_2 u_3} - \psi \overline{u_1 u_2} \\
&\approx \overline{u_1' u_3'} + \beta(\overline{\tilde{u}_1^2} - \overline{\tilde{u}_3^2}) \\
\overline{U_2 U_3} &= \overline{(-\gamma u_1 + u_2 + \psi u_3)(\beta u_1 - \psi u_2 + u_3)} \\
&= \overline{u_2 u_3} + \psi(\overline{u_3^2} - \overline{u_2^2}) - \gamma \overline{u_1 u_3} + \beta \overline{u_1 u_2} \\
&\approx \overline{u_2' u_3'} + \psi(\overline{\tilde{u}_3^2} - \overline{\tilde{u}_2^2})
\end{aligned} \tag{2.12}
$$

The final equality follows from the fact that $\overline{\tilde{u}_i \tilde{u}_j} = 0$ ($i \neq j$), and $\overline{\tilde{u}_i^2} >> \overline{u_i'^2}$. To determine the magnitude of the error terms, $(\overline{u_i^2} - \overline{u_j^2})$ ($i \neq j$), the approximation $\overline{U_i^2} \approx \overline{\tilde{u}_i^2}$ can be used since the principal wave component dominates all other terms, including any terms that result from beam tilt. Using data from the Martha's Vineyard Coastal Observatory, $(\overline{u_1^2}, \overline{u_2^2}) >> \overline{\tilde{u}_3^2}$ (about 5-15 times greater), so that $\overline{u_i^2} - \overline{u_3^2} \approx \overline{u_i^2}$ ($i = 1, 2$). From the ocean floor to a depth of about 8 meters above, some typical $\overline{u_1^2}, \overline{u_2^2}$ values are 0.005-0.020 $(m/s)^2$. From 8 meters until the surface, there is a quick increase in the $\overline{u_1^2}, \overline{u_2^2}$ values, with a range from about 0.1-0.6 $(m/s)^2$. The ADCP used in the Martha's Vineyard Coastal Observatory has one axes tilted

31

at 0.5 degrees, and another at 6 degrees. The error in the Reynolds stress estimate due to each of the beam tilts, respectively, ranges from $\approx (0.05, 0.5)Nm^{-2}$ near the ocean floor to $\approx (0.2, 2)Nm^{-2}$ near the 8 meter range, to $\approx (4, 50)Nm^{-2}$ near the ocean surface. Figure 2-3 shows a typical mean velocity profile and the corresponding profile of Reynolds stress estimates. In the high shear region, between 10 and 12 meters above the ocean floor, the error in the $-\rho\overline{uw}$ estimates is between 0.5-3.5 N m^{-2} and the error in the $-\rho\overline{vw}$ estimates is between 6-40 N m^{-2}. This means that the $-\rho\overline{uw}$ estimate of Reynolds stress can be trusted, whereas the $-\rho\overline{vw}$ estimate of Reynolds stress cannot be trusted.
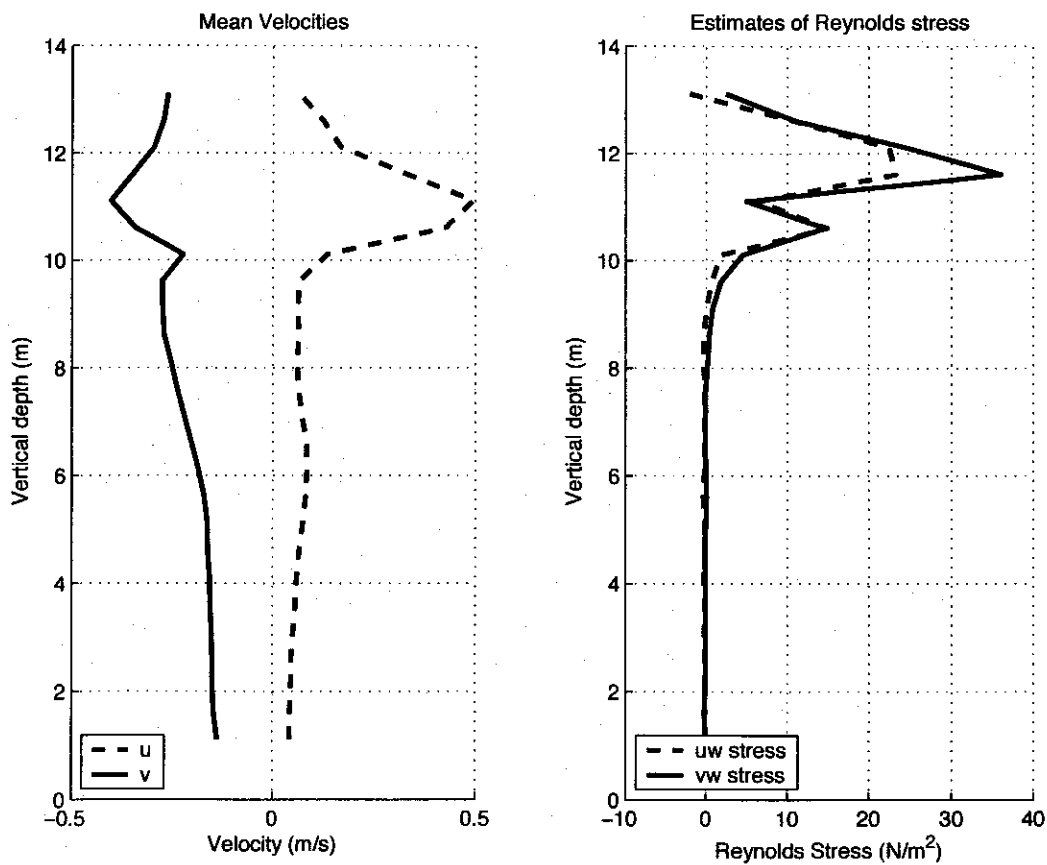
Figure 2-3: The first graph shows the mean velocity profile above the ADCP at Martha's Vineyard Coastal Observatory, on yearday 153, 2005, at 10pm. The second graph shows the corresponding Reynolds stress estimates. The uw axis tips up at about 0.5 degrees, and the vw axis dips down at about 6 degrees.

Figure 3.3 shows Reynolds stress estimates from the same velocity profile as figure 3.3, in the range of 1 to 10 meters. The error in the $-\rho\overline{uw}$ estimates is between 0.05-0.13 N m^{-2} and the error in the $-\rho\overline{vw}$ estimates is between 0.6-2.5 N m^{-2}. Again, this indicates that the $-\rho\overline{uw}$ estimate of Reynolds stress can be trusted, whereas the $-\rho\overline{vw}$ estimate of Reynolds stress cannot be trusted.

In addition to introducing an error term in the estimates of Reynolds stress, the radial wave-induced velocities lead to larger variances of the estimate. Section 2.3 will discuss the uncertainty of the estimates.
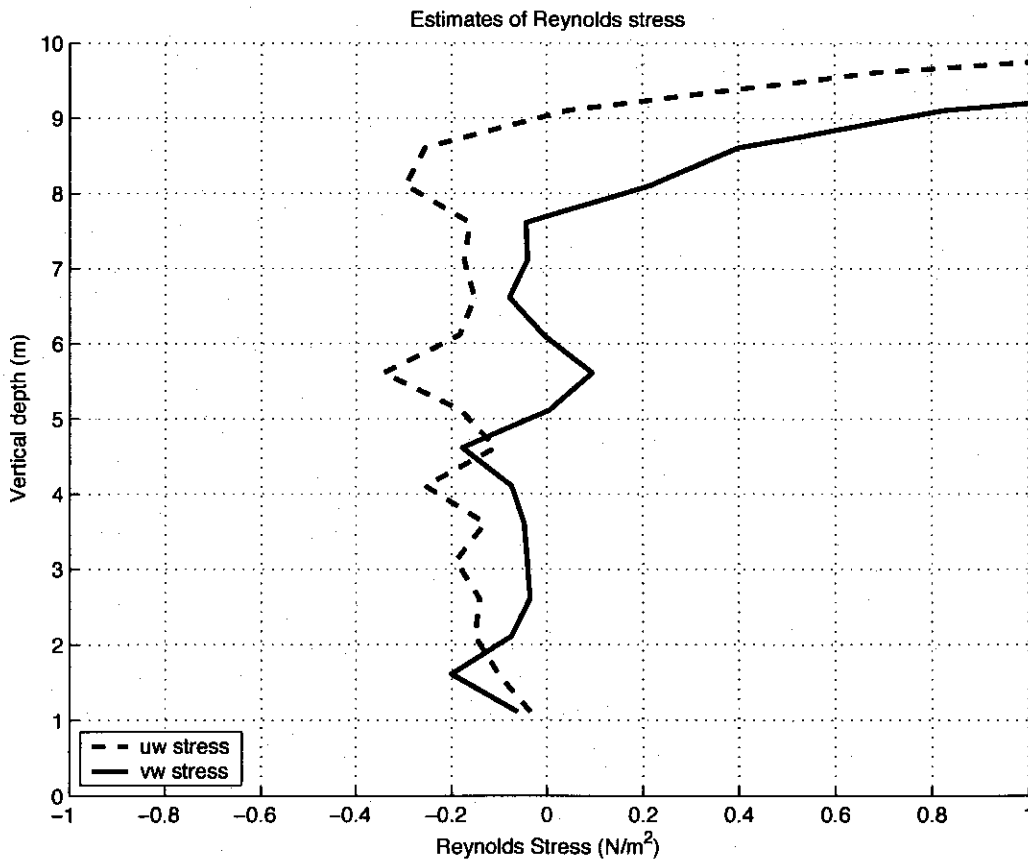
Figure 2-4: A zoomed in view of the Reynolds stress estimates in the range from 1 to 10 meters above the ocean floor. The ADCP data used is from the Martha's Vineyard Coastal Observatory, on yearday 153, 2005, at 10pm. The uw axis dips at about 0.5 degrees, and the vw axis dips at about 6 degrees.

2.3 Variance of the estimates of Reynolds stress

In addition to the errors introduced from a tilted ADCP, there is also error due to the variance of the data itself. The uncertainty in the estimate of Reynolds stress is given as $-\rho\sigma_R$, where

$$
\begin{aligned}
\sigma_R^2 &= \text{var}(-\hat{\overline{u_i' u_j'}}) \\
&= \frac{1}{16\sin^2\phi\cos^2\phi}\text{var}(\overline{(V_{B2}(\vec{x}_b,t)^2} - \overline{(V_{B1}(\vec{x}_a,t)^2}) \\
&= \frac{1}{16\sin^2\phi\cos^2\phi}\text{var}\left[\frac{1}{M}\sum_{m=1}^{M}V_{B2}(\vec{x}_b,m)^2 - \frac{1}{M}\sum_{m=1}^{M}V_{B1}(\vec{x}_b,m)^2\right]
\end{aligned}
\tag{2.13}
$$

and $V_{Bi}(\vec{x},m)$ is the radial velocity with the mean removed, with m indexing individual samples in time. Williams and Simpson [26] then expand this to give

$$
\begin{aligned}
\sigma_R^2 &= \frac{1}{16M^2\sin^2\phi\cos^2\phi}\{\textstyle\sum_{i=1}^{2}\sum_{m=1}^{M}\text{var}[(V_{Bi}(\vec{x},m)^2] \\
&\quad +2\textstyle\sum_{i=1}^{2}\sum_{m=1}^{M-1}\sum_{n=m+1}^{M}\text{cov}[(V_{Bi}(\vec{x},m)^2,(V_{Bi}(\vec{x},n)^2] \\
&\quad -2\textstyle\sum_{m=1}^{M}\sum_{n=1}^{M}\text{cov}[(V_{B1}(\vec{x},m)^2,(V_{B2}(\vec{x},n)^2]\}
\end{aligned}
\tag{2.14}
$$

The last term in equation 2.14 is significantly less in magnitude than the first two terms. The second term represents the correlation of squared fluctuations at one point on a beam between successive measurements, and can be simplified as

$$
\sum_{m=1}^{M-1}\sum_{n=m+1}^{M}\text{cov}[(V_{Bi}(\vec{x},m)^2,(V_{Bi}(\vec{x},n)^2] \approx M\sum_{n=2}^{K}\text{cov}[(V_{Bi}(\vec{x},1)^2,(V_{Bi}(\vec{x},n)^2].
\tag{2.15}
$$

Using the condition of stationarity, so that $\sum_{m=1}^{M}\text{var}[(V_{Bi}(\vec{x},m)^2] = M\text{var}[\overline{(V_{Bi}(\vec{x},t)^2}]$, a correction term, γ_R can be defined as

$$
\gamma_R = 1 + 2\frac{\sum_{n=2}^{K}\text{cov}[(V_{Bi}(\vec{x},1)^2,(V_{Bi}(\vec{x},n)^2]}{\text{var}[\overline{(V_{Bi}(\vec{x},t)^2}]},
\tag{2.16}
$$

so that the uncertainty can be written as

$$
\sigma_R^2 = \frac{\gamma_R\{\text{var}[\overline{(V_{B1}(\vec{x},t)^2}] + \text{var}[\overline{(V_{Bi}(\vec{x},n)^2}]\}}{16M\sin^2\phi\cos^2\phi}.
\tag{2.17}
$$

If the distribution of the fluctuations, $V_{Bi}(\vec{x}, t)$, is Gaussian, then the fourth moment is equal to 3 times the second moment ($\mu_4 = 3\mu_2$), making

$$\text{var}[\overline{(V_{Bi}(\vec{x}, t)^2}] = 2(\overline{(V_{Bi}(\vec{x}, t)^2})^2. \tag{2.18}$$

Finally, using the fact that $\sin\phi\cos\phi = 2\sin 2\phi$, the uncertainty in the estimate of Reynolds stress is $-\rho\sigma_R$, where

$$\sigma_R^2 = \frac{\gamma_R\{(\overline{(V_{B1}(\vec{x}, t)^2})^2 + (\overline{(V_{B2}(\vec{x}, t)^2})^2\}}{2M\sin^2 2\phi}. \tag{2.19}$$

This is the very practical result put forth by Williams and Simpson. Returning to the data taken from the ADCP at the Martha's Vineyard Coastal Observatory, the correction factor is found to vary from about $\gamma_R \approx 1$ near the extremes of the beam, to around $\gamma_R \approx 3.5$ near the middle of the beams. In addition, the distribution for this particular data set is found to be close to Gaussian, with $\mu_4/\mu_2^2 \approx 3.10 - 3.15$ (a perfect Gaussian distrubtion has $\mu_4/\mu_2^2 = 3$). Other data sets have distributions even closer to being Gaussian. Figure 2-5 shows the profile of Reynolds stress estimates with the uncertainty as given by the data and using equation 2.19.

Looking at the plots, it appears that precise measurements of the Reynolds stress is not possible when wave-induced velocities are present. The overall conclusion for both the error and the uncertainty in the estimates of Reynolds stress using an ADCP is that approximate estimates are possible when the beam tilt is minimal and the wave-induced velocities are minimal. As the wave-induced velocities increase in amplitude, or as the beam tilt increases, the estimates become far less reliable. For more precise estimates, the wave-induced velocities must be removed. The next chapter will explore this possiblitity.
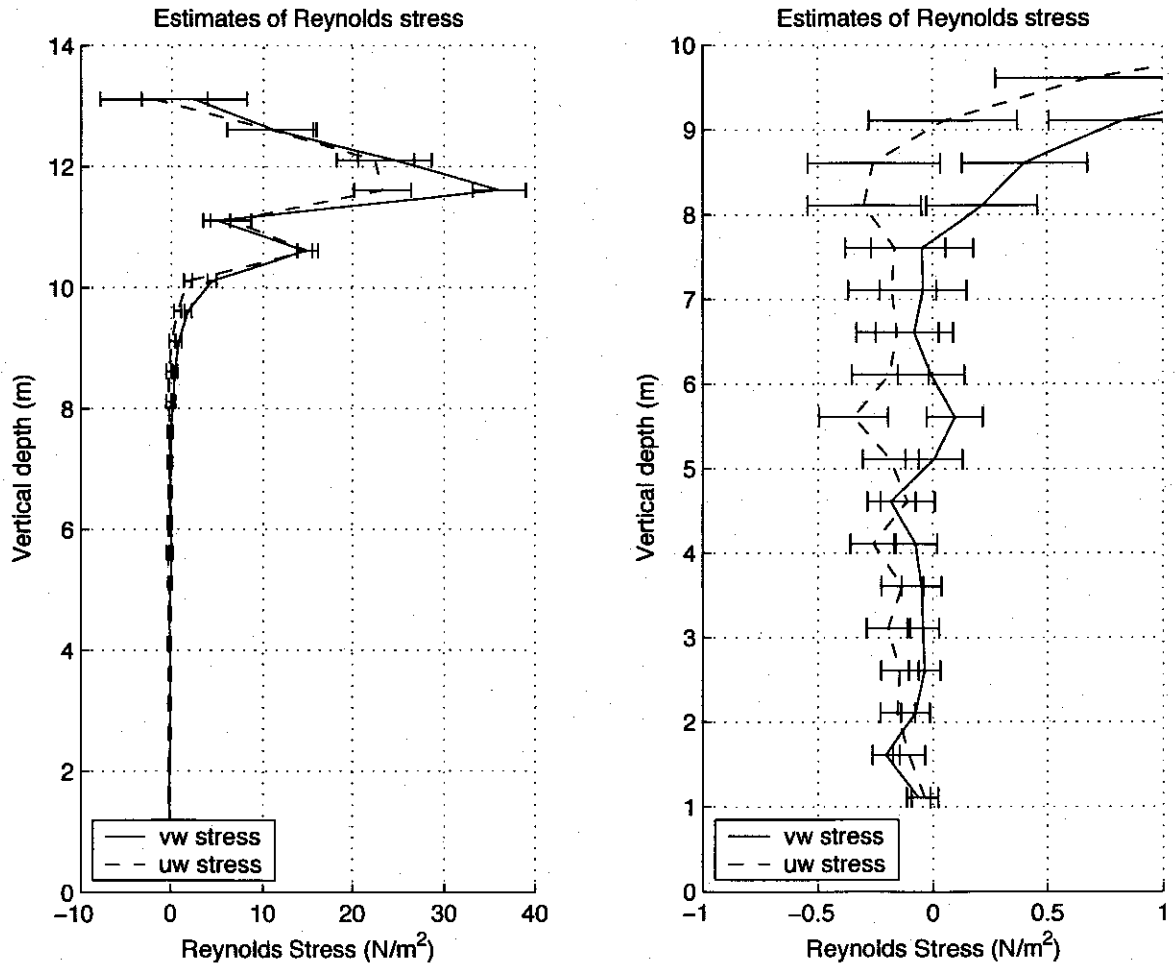
Figure 2-5: The first graph shows the profile of Reynolds stress estimates above an ADCP at the Martha's Vineyard Coastal Observatory, with data taken on yearday 153, 2005, at 10pm. The second graph shows the same profile, but in the range from 1 to 10 meters above the ocean floor. The error bars give the uncertainty in the estimates due to the variance in the data itself.

Chapter 3

Error and Uncertainty in Estimates of Reynolds Stress Using Spatially and Temporally Filtered Data from an ADCP in an Energetic Ocean State

In this chapter, the technique used by Shaw and Trowbridge is adapted for use with an Acoustic Doppler Current Profiler (ADCP). The important step is to come up with estimates of the turbulent radial velocities. This is done by making estimates of the coherent wave-induced velocities first, and then subtracting them from the actual radial velocities to arrive at incoherent estimates. Linear least squares estimation will be used, and in section 3.1, basic estimation theory is presented to show explicity that linear least squares estimation is formulated by making the error in the estimate orthogonal to the data used to form the estimate. The estimate is of the coherent wave-induced radial velocities between various locations along the beams, and the incoherent part, or error, contains the turbulence induced velocities. Section 3.2 forms the estimate of the variance of the radial turbulent velocities, $\overline{V'_{Bi}(\vec{x}, t)\hat{V'_{Bi}}(\vec{x}, t)}$, and

section 3.3 applies the technique to ADCP data from the Martha's Vineyard Coastal Observatory. In section, 3.4, the temporal paramaters of the filter are determined, and two estimates of the variance of the radial turbulent velocities are compared. In addition, the variance of the estimates of Reynolds stress is calculated directly from the filtered data. Finally, in section 3.5 the usefulness of developing first and second order statistical models in order to help predict estimate error is discussed.

3.1 Basic Estimation Theory

The Shaw and Trowbridge technique exploits the physics of the situation, namely that wave-induced velocities remain coherent over larger distances than turbulence-induced velocities. Basic estimation theory is presented to develop the mechanics of how the coherent portions between locations can be estimated, and then removed. When full statistical information is available, the optimal estimators are nonlinear. When only first and second order statistics are available, the linear least squares estimator is optimal. Section 3.1.5 looks specifically at which first and second order statistics are necessary to form the estimates of the radial turbulent velocities.

3.1.1 Estimation of a random variable

There are a number of different ways to estimate a random variable (X) based on information gathered from another random variable (Y) or a series of random variables $(\mathbf{y} = [Y_1 \ Y_2 \ ... \ Y_N]^T)$. [23] In general there is a cost assosicated with making the estimation, and the goal is to minimize the expected value of the cost.

$$\min \ E[C(X,\hat{X})] \tag{3.1}$$

Often, this cost will only depend on the error between the estimator and the random variable.

$$X_\epsilon \equiv X - \hat{X}(\mathbf{y}) \tag{3.2}$$

38

With this type of cost, the estimator is calculated in such a way as to minimize either the mean-square error, X_ϵ^2, the absolute error, $|X_\epsilon|$, or the uniform cost, $C(X_\epsilon)=1$ for $|X_\epsilon| > \Delta/2$, and 0 otherwise.

The total risk is the sum over all the error,

$$\int_{-\infty}^{\infty} dx \int_{-\infty}^{\infty} C(x - \hat{X}(\mathbf{y})) f_{X,\mathbf{y}}(x, \mathbf{y}) d\mathbf{y}, \qquad (3.3)$$

where (x) is a value of (X) whose occurance is given by the joint probability density function $f_{X,\mathbf{y}}(x, \mathbf{y})$, each realization of data $(Y_1{=}y_1, Y_2{=}y_2,...,Y_n{=}y_n)$ leads to one estimate $\hat{X}(\mathbf{y})$, and the corresponding error is $(x - \hat{X}(\mathbf{y}))$.

When $C(x - \hat{X}(\mathbf{y}))$ is X_ϵ^2, the estimator that minimizes the mean-square error is the conditional mean.

$$\hat{X}(\mathbf{y}) = \int_{-\infty}^{\infty} x f_{X|\mathbf{y}}(x|\mathbf{y}) dx \qquad (3.4)$$

When $C(x - \hat{X}(\mathbf{y}))$ is $|X_\epsilon|$, the estimate that minimizes the absolute error is just the median of the a posteriori density, $f_{X|\mathbf{y}}(x, \mathbf{y})$.

$$\int_{-\infty}^{\hat{X}(\mathbf{y})} f_{X|\mathbf{y}}(x, \mathbf{y}) dx = \int_{\hat{X}(\mathbf{y})}^{\infty} f_{X|\mathbf{y}}(x, \mathbf{y}) dx \qquad (3.5)$$

When $C(x - \hat{X}(\mathbf{y}))$ is $C(X_\epsilon)=1$, the estimate that minimizes the uniform cost function is the maximum a posteriori estimate. It is commonly found by finding the maximum of the logarithm of the a posteriori probability, since the logarithm is just a monotone function.

$$\left. \frac{\partial \ln p_{X|\mathbf{y}}(x|\mathbf{y})}{\partial x} \right|_{x=\hat{x}(\mathbf{y})} = 0 \qquad (3.6)$$

In all three cases, the risk is $E[\hat{X}(\mathbf{y})]$, or the average of the conditional variance over all $\mathbf{y}$.

It is not always clear which type of error should be minimized, and sometimes the determination is whatever type of error is most tractable in solving. In the case of estimating turbulence, the mean-square error will be minimized since it has the effect of reducing larger errors.

3.1.2 Estimation of a Random Vector

This theory naturally extends to multiple random variable estimation. The error is now an error vector,

$$\mathbf{x}_\epsilon(\mathbf{y}) = \begin{bmatrix} \hat{X}_1(\mathbf{y}) - X_1 \\ \hat{X}_2(\mathbf{y}) - X_2 \\ \vdots \\ \hat{X}_k(\mathbf{y}) - X_k \end{bmatrix}, \tag{3.7}$$

and the cost function is just a sum of the squares of the errors. Since each term of the cost function is positive, each can be minimized individually,

$$\hat{X}_i(\mathbf{y}) = \int_{-\infty}^{\infty} x_i f_{\mathbf{x}|\mathbf{y}}(\mathbf{x}|\mathbf{y}) d\mathbf{x}. \tag{3.8}$$

3.1.3 Linear Least Squares Estimation

When there is full statistical information of the processes involved, using the conditional mean as the estimate provides a lower bound on the mean-square error. However, when there is only partial statistical information, in particular, first and second order statistics, then the linear least squares estimate provides the reachable lower bound. [27]

In the scalar case, (and assuming that the random variable being estimated is zero mean, or that the mean has been removed), the linear estimator is $\hat{X}_i(\mathbf{y}) = \mathbf{h}^T \mathbf{y}$, where $\mathbf{h}$ is a vector of weights. To determine $\mathbf{h}$, a system of equations must be solved, where for each equation the error is made orthogonal to the data of each Y_i.

$$\int_{-\infty}^{\infty} \int_{-\infty}^{\infty} (x_i - \hat{X}_i(\mathbf{y})) y_i f_{X_i, \mathbf{y}}(x_i, \mathbf{y}) dx_i d\mathbf{y} = 0. \tag{3.9}$$

In vector notation, and using E for expectation, the equation becomes

$$E[(X_i - \hat{X}_i(\mathbf{y}))\mathbf{y}^T] = 0 \tag{3.10}$$

Replacing $\mathbf{h}^T \mathbf{y}$ for $\hat{X}_i(\mathbf{y})$, and pulling $\mathbf{h}^T$ outside of the expectation (since it is non-

random), the equation becomes

$$E[X_i \mathbf{y}^T] - E[\mathbf{h}^T \mathbf{y}\mathbf{y}^T] = 0. \tag{3.11}$$

The weighting vector is then

$$\mathbf{h}^T = E[X_i \mathbf{y}^T](E[\mathbf{y}\mathbf{y}^T])^{-1}, \tag{3.12}$$

and the linear least squares estimator is

$$\hat{X}_i(\mathbf{y}) = E[X_i \mathbf{y}^T](E[\mathbf{y}\mathbf{y}^T])^{-1}\mathbf{y}. \tag{3.13}$$

Extending this to the estimation of multiple random variables, the linear estimate is $\hat{\mathbf{x}}(\mathbf{y}) = \mathbf{H}^T\mathbf{y}$, where $\mathbf{H}$ is a matrix of weights given by

$$\mathbf{H}^T = E[\mathbf{x}\mathbf{y}^T](E[\mathbf{y}\mathbf{y}^T])^{-1}, \tag{3.14}$$

and the linear least squares estimate is

$$\hat{\mathbf{x}}(\mathbf{y}) = E[\mathbf{x}\mathbf{y}^T](E[\mathbf{y}\mathbf{y}^T])^{-1}\mathbf{y}. \tag{3.15}$$

These equations are also known as the Normal Equations. First order statistical information is required initially to remove the mean components. Joint second-moment statistical information is required in order to make the estimate.

3.1.4 Predicted Error Variances

The predicted error covariances can be calculated as follows:

$$
\begin{aligned}
\text{Predicted Error} \quad &= \mathrm{E}[(\hat{\mathbf{x}}(\mathbf{y}) - \mathbf{x})(\hat{\mathbf{x}}(\mathbf{y}) - \mathbf{x})^T] \\
&= \mathrm{E}[(\hat{\mathbf{x}}(\mathbf{y}) - \mathbf{x})(\hat{\mathbf{x}}(\mathbf{y}))^T] + \mathrm{E}[(\hat{\mathbf{x}}(\mathbf{y}) - \mathbf{x})(-\mathbf{x})^T] \\
&= \mathrm{E}[(\hat{\mathbf{x}}(\mathbf{y}) - \mathbf{x})(-\mathbf{x})^T] \\
&= \mathrm{E}[\mathbf{x}\mathbf{x}^T] - \mathrm{E}[\hat{\mathbf{x}}(\mathbf{y})\mathbf{x}^T] \\
&= \mathrm{E}[\mathbf{x}\mathbf{x}^T] - \mathrm{E}[\mathbf{x}\mathbf{y}^T](\mathrm{E}[\mathbf{y}\mathbf{y}^T])^{-1}\mathrm{E}[\mathbf{y}\mathbf{x}^T].
\end{aligned}
\tag{3.16}
$$

In the second line, the error is orthongal to the data (or any linear estimate based on the data), and so the first expression is zero. The individual error variances lie on the diagonal, and the covariances lie on the off-diagonals.

3.1.5 Estimation To Remove Coherent Wave Components

The ADCP measures radial velocities, which can be decomposed into mean, turbulent, wave, and error components.

$$
\begin{aligned}
\mathbf{y} &= \overline{\mathbf{y}} + \mathbf{y}' + \widetilde{\mathbf{y}} + \mathbf{y}^e \\
\mathbf{X} &= \overline{\mathbf{X}} + \mathbf{X}' + \widetilde{\mathbf{X}} + \mathbf{X}^e
\end{aligned}
\tag{3.17}
$$

The coherent estimate $\hat{\mathbf{X}}(\mathbf{y}) = \mathrm{E}[\mathbf{X}\mathbf{y}^T](\mathrm{E}[\mathbf{y}\mathbf{y}^T])^{-1}\mathbf{y}$ can be examined componentwise.

$$
\begin{aligned}
\mathrm{E}[\mathbf{X}\mathbf{y}^T] \quad &= \mathrm{E}[(\mathbf{X}' + \widetilde{\mathbf{X}} + \mathbf{X}^e)(\mathbf{y}' + \widetilde{\mathbf{y}} + \mathbf{y}^e)^T] \\
&= \mathrm{E}[X'\mathbf{y}'^T] + \mathrm{E}[\widetilde{X}\widetilde{\mathbf{y}}^T] \\
\mathrm{E}[\mathbf{y}\mathbf{y}^T] \quad &= \mathrm{E}[(\mathbf{y}' + \widetilde{\mathbf{y}} + \mathbf{y}^e)(\mathbf{y}' + \widetilde{\mathbf{y}} + \mathbf{y}^e)^T] \\
&= \mathrm{E}[\mathbf{y}'\mathbf{y}'^T] + \mathrm{E}[\widetilde{\mathbf{y}}\widetilde{\mathbf{y}}^T] + \mathrm{E}[\mathbf{y}^e\mathbf{y}^{eT}]
\end{aligned}
\tag{3.18}
$$

As discussed in section 2.1, the cross-correlation terms are zero based on the assumption that the wave, turbulent, and error processes are truly independent from each other, and the error is only correlated with itself.

The incoherent estimate, which contains the desired turbulent term, is obtained by

subtracting the coherent estimate, $\hat{X}(\mathbf{y})$, from the actual velocities being estimated,

$$\hat{X}'(\mathbf{y}) = X - \hat{X}(\mathbf{y}). \tag{3.19}$$

The next section will look explicity at what terms contribute to the error in the estimate of the variance of the radial turbulent velocities.

3.2   Forming the estimate of the variance of the radial turbulent velocities, $\overline{V'_{Bi}(\vec{x},t)\hat{V}'_{Bi}(\vec{x},t)}$

To arrive at any statistics using the data, ergodicity must be invoked so that the average in time is equal to the ensemble average. Letting $\mathbf{v}_x$ be the radial velocity time series at one location (with the mean removed),

$$\mathbf{v}_x = [V_{B1}(\vec{x}_a, t_1) \cdots V_{B1}(\vec{x}_a, t_N)]^T \tag{3.20}$$

the variance is calculated as

$$\text{var}(\mathbf{v}_x) = \frac{1}{N}\mathbf{v}_x^T \mathbf{v}_x = \overline{V_{B1}(\vec{x}_a, t)V_{B1}(\vec{x}_a, t)}. \tag{3.21}$$

To achieve a different statistic (nonzero radial or time lag), $\mathbf{v}_x$ is combined with a different radial velocity times series. For example, let

$$\mathbf{v}_y = [V_{B1}(\vec{x}_b, t_1) \cdots V_{B1}(\vec{x}_b, t_N)]^T, \tag{3.22}$$

then the estimate with a spatial lag of $\vec{r} = \vec{b} - \vec{a}$ is given by

$$\text{cov}(\mathbf{v}_x, \mathbf{v}_y) = \frac{1}{N}\mathbf{v}_x^T \mathbf{v}_y = \overline{V_{B1}(\vec{x}_a, t)V_{B1}(\vec{x}_b, t)}. \tag{3.23}$$

When forming a statistic involving a nonzero time lag, both series must be shortened by the amount equal to the lag.

$$
\begin{aligned}
\mathbf{v}_x &= [V_{B1}(\vec{x}_a, t_1) \cdots V_{B1}(\vec{x}_a, t_{N-\tau})]^T \\
\mathbf{v}_y &= [V_{B1}(\vec{x}_a, t_{\tau+1}) \cdots V_{B1}(\vec{x}_a, t_N)]^T
\end{aligned}
\tag{3.24}
$$

To use formulate a space-time linear filter, let $\mathbf{V_y}$ be a matrix of radial velocity time series,

$$
\mathbf{V}_y^T =
\begin{bmatrix}
V_{B1}(\vec{x}_b, t_1) \cdots V_{B1}(\vec{x}_b, t_{N-\tau}) \\
V_{B1}(\vec{x}_b, t_2) \cdots V_{B1}(\vec{x}_b, t_{N-\tau+1}) \\
\vdots \\
V_{B1}(\vec{x}_b, t_{\tau+1}) \cdots V_{B1}(\vec{x}_b, t_N) \\
\vdots \\
V_{B1}(\vec{x}_f, t_{\tau+1}) \cdots V_{B1}(\vec{x}_f, t_N) \\
\vdots \\
V_{B4}(\vec{x}_z, t_{\tau+1}) \cdots V_{B4}(\vec{x}_z, t_N)
\end{bmatrix}.
\tag{3.25}
$$

The linear least squares estimate of the coherent components of of $\mathbf{v_x}$ is

$$
\hat{\mathbf{v}}_x = \mathbf{V_y}(\mathbf{V}_y^T \mathbf{V_y})^{-1} \mathbf{V}_y^T \mathbf{v}_x,
\tag{3.26}
$$

where

$$
\frac{1}{N}\mathbf{V}_y^T\mathbf{V_y} =
\begin{bmatrix}
\overline{V_{B1}(\vec{x}_b, t)\hat{V}_{B1}(\vec{x}_b, t)} & \cdots & \overline{V_{B1}(\vec{x}_b, t)\hat{V}_{B4}(\vec{x}_z, t+\tau)} \\
\overline{V_{B1}(\vec{x}_b, t+\hat{t}s)V_{B1}(\vec{x}_b, t)} & \cdots & \\
\vdots & \cdots & \\
\overline{V_{B1}(\vec{x}_b, t+\hat{\tau})V_{B1}(\vec{x}_b, t)} & \cdots & \\
\vdots & \cdots & \vdots \\
\overline{V_{B1}(\vec{x}_f, t+\hat{\tau})V_{B1}(\vec{x}_b, t)} & \cdots & \\
\vdots & \cdots & \\
\overline{V_{B4}(\vec{x}_z, t+\hat{\tau})V_{B1}(\vec{x}_b, t)} & \cdots & \overline{V_{B4}(\vec{x}_z, t)\hat{V}_{B4}(\vec{x}_z, t)}
\end{bmatrix},
\tag{3.27}
$$

and

$$\frac{1}{N}\mathbf{V_y^T v_x} = [\overline{V_{B1}(\vec{x}_b, t)\hat{V}_{B1}(\vec{x}_a, t)} \cdots \overline{V_{B4}(\vec{x}_z, t+\tau)\hat{V}_{B1}(\vec{x}_a, t)}]^T, \qquad (3.28)$$

The incoherent estimate is

$$\Delta \mathbf{v_x} = \hat{\mathbf{v}}'_x = \mathbf{v}_x - \hat{\mathbf{v}}_x. \qquad (3.29)$$

Finally, the estimate for the variance of the radial turbulent velocities at one location on a beam is $\text{cov}(\mathbf{v_x}, \Delta\mathbf{v_x})$, (or equivalently $\text{cov}(\Delta\mathbf{v_x}, \Delta\mathbf{v_x})$ when the beam tilt is minimal)

$$
\begin{aligned}
\overline{V'_{B1}(\vec{x}_a, t)\hat{V}'_{B1}(\vec{x}_a, t)} &= \text{cov}(\mathbf{v_x}, \Delta\mathbf{v_x}) \\
&= \tfrac{1}{N}\mathbf{v_x}^T \Delta\mathbf{v_x} \\
&= \tfrac{1}{N}\mathbf{v_x}^T(\mathbf{v_x} - \hat{\mathbf{v}_x}) \\
&= \tfrac{1}{N}[\mathbf{v_x}^T\mathbf{v_x} - \mathbf{v_x}^T\hat{\mathbf{v}_x}] \\
&= \tfrac{1}{N}[\mathbf{v_x}^T\mathbf{v_x} - \mathbf{v_x}^T\mathbf{V_y}(\mathbf{V_y^T V_y})^{-1}\mathbf{V_y^T v}_x],
\end{aligned}
\qquad (3.30)
$$

where

$$
\begin{aligned}
\mathbf{v_x}^T\mathbf{v_x} &= (\mathbf{v'_x} + \tilde{\mathbf{v}}_x + \mathbf{v_x^e})^T(\mathbf{v'_x} + \tilde{\mathbf{v}}_x + \mathbf{v_x^e}) \\
&= \mathbf{v'_x}^T\mathbf{v'_x} + \tilde{\mathbf{v}}_x^T\tilde{\mathbf{v}}_x + \mathbf{v_x^e}^T\mathbf{v_x^e}
\end{aligned}
\qquad (3.31)
$$

and similarly

$$\mathbf{v_x}^T\mathbf{V_y}(\mathbf{V_y^T V_y})^{-1}\mathbf{V_y^T v}_x = (\mathbf{v'_x}^T\mathbf{V'_y} + \tilde{\mathbf{v}}_x^T\tilde{\mathbf{V}}_y)(\mathbf{V'_y}^T\mathbf{V'_y} + \tilde{\mathbf{V}}_y^T\tilde{\mathbf{V}}_y + \mathbf{V_y^e}^T\mathbf{V_y^e})^{-1}(\mathbf{V'_y}^T\mathbf{v'_x} + \tilde{\mathbf{V}}_y^T\tilde{\mathbf{v}}_x).$$
$$(3.32)$$

As a reminder, all covariances between turbulence and waves, turbulence and error, and waves and error are zero. In addition, the error will be shown to be only correlated with itself (for the most part), so that $\frac{1}{N}\mathbf{v_x^e}^T\mathbf{V_y^e} = 0$ as well.

The error in the estimate for one location on the beam is

$$
\begin{aligned}
e_{B1}(\vec{x}_a, \vec{x}_a, \tau = 0) &= \overline{V'_{B1}(\vec{x}_a, t)\hat{V}'_{B1}(\vec{x}_a, t)} - \overline{V'_{B1}(\vec{x}_a, t)V'_{B1}(\vec{x}_a, t)} \\
&= \tfrac{1}{N}\mathbf{v_x}^T\Delta\mathbf{v_x} - \tfrac{1}{N}\mathbf{v'_x}^T\mathbf{v'_x} \\
&= \tfrac{1}{N}[\tilde{\mathbf{v}}_x^T\tilde{\mathbf{v}}_x + \mathbf{v_x^e}^T\mathbf{v_x^e} - \mathbf{v_x}^T\mathbf{V_y}(\mathbf{V_y^T V_y})^{-1}\mathbf{V_y^T v}_x].
\end{aligned}
\qquad (3.33)
$$

45

Estimates of the covariances of the radial turbulent velocities at spatial and temporal lags have the error variance term removed. Lag estimates are formed by including a velocity time series with spatial and temporal lag, $\mathbf{v}_{xb} = [V_{B1}(\vec{x}_b, t_{\tau+1}) \cdots V_{B1}(\vec{x}_b, t_N)]^T$, in the covariance estimate.

$$
\begin{aligned}
\overline{V'_{B1}(\vec{x}_b, t+\tau)\hat{V}'_{B1}(\vec{x}_a, t)} \quad &= \text{cov}(\mathbf{v}_{xb}, \Delta\mathbf{v_x}) \\
&= \tfrac{1}{N}\mathbf{v_{xb}}^T \Delta\mathbf{v_x} \\
&= \tfrac{1}{N}\mathbf{v_{xb}}^T(\mathbf{v_x} - \hat{\mathbf{v}}_x) \\
&= \tfrac{1}{N}[\mathbf{v_{xb}}^T\mathbf{v_x} - \mathbf{v_{xb}}^T\hat{\mathbf{v}}_x] \\
&= \tfrac{1}{N}[\mathbf{v_{xb}}^T\mathbf{v_x} - \mathbf{v_{xb}}^T\mathbf{V_y}(\mathbf{V_y^T V_y})^{-1}\mathbf{V_y^T v_x}],
\end{aligned}
\tag{3.34}
$$

where

$$
\begin{aligned}
\mathbf{v_{xb}}^T\mathbf{v_x} \quad &= (\mathbf{v'_{xb}} + \tilde{\mathbf{v}}_{xb} + \mathbf{v_{xb}^e})^T(\mathbf{v'_x} + \tilde{\mathbf{v}}_x + \mathbf{v_x^e}) \\
&= \mathbf{v'_{xb}}^T\mathbf{v'_x} + \tilde{\mathbf{v}}_{xb}^T\tilde{\mathbf{v}}_x
\end{aligned}
\tag{3.35}
$$

and similarly

$$
\mathbf{v_{xb}}^T\mathbf{V_y}(\mathbf{V_y^T V_y})^{-1}\mathbf{V_y^T v_x} = (\mathbf{v'_{xb}}^T\mathbf{V'_y} + \tilde{\mathbf{v}}_{xb}^T\tilde{\mathbf{V}}_y)(\mathbf{V'_y}^T\mathbf{V'_y} + \tilde{\mathbf{V}}_y^T\tilde{\mathbf{V}}_y + \mathbf{V_y^e}^T\mathbf{V_y^e})^{-1}(\mathbf{V'_y}^T\mathbf{v'_x} + \tilde{\mathbf{V}}_y^T\tilde{\mathbf{v}}_x).
\tag{3.36}
$$

The next section examines the results of using linear least squares estimation on data from an ADCP at the Martha's Vineyard Coastal Observatory.

3.3 Use of linear least squares estimation in determining estimates of Reynolds stress using ADCP data from the Martha's Vineyard Coastal Observatory

In the previous section, the error in the estimate of the variance of the radial turbulent velocities was shown to consist of a measurement error term, $(1/N)\mathbf{v_x^e}^T\mathbf{v_x^e}$, and whatever portion of the wave-induced component which did not cancel out, $\overline{\Delta \tilde{V}}^e = (1/N)[\tilde{\mathbf{v}}_\mathbf{x}^T \tilde{\mathbf{v}}_\mathbf{x} - \mathbf{v_x}^T \hat{\mathbf{v}}_\mathbf{x}]$. Secondly, for estimates at spatial and temporal lag, the error covariance term is zero.

The first graph of figure 3-1 shows the estimate of the variance of radial turbulent velocities at height of $5.6m$ along beam 1 for spatial lags of $r = 0m$, $0.5m$, and $-0.5m$.
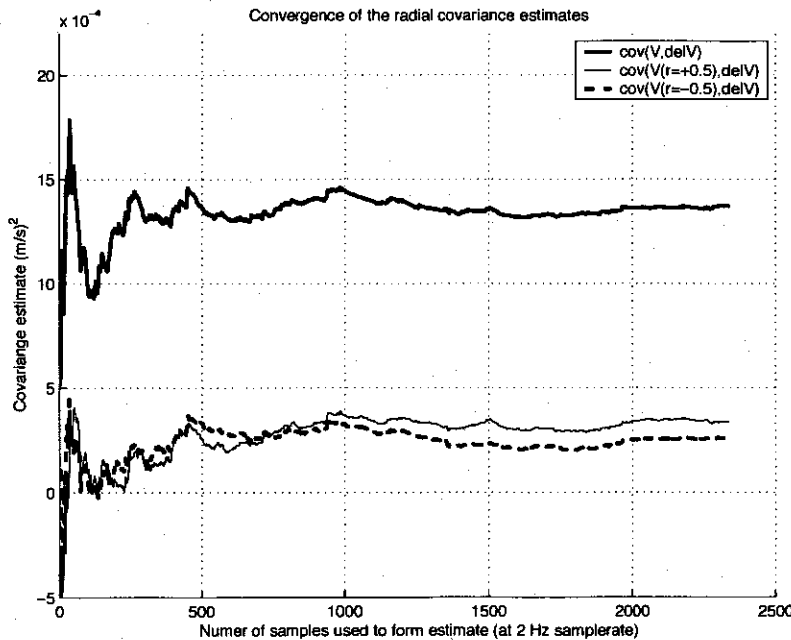

Figure 3-1: The convergence of the radial cross covariance estimates, cov($V_{B1}(z + r = 5.6m + r, t), \Delta V_{B1}(z = 5.6m, t))$, for spatial lags of $r = 0m, +0.5m$, and $-0.5m$. The $r = 0m$ lag estimate includes the error variance term, whereas the $r = \pm 0.5m$ lag cross covariance estimates are free of the error covariance terms.

The $r = 0$ lag estimate converges at about $15 \cdot 10^{-4}(m/s)^2$, whereas the expected variance of the process is about $4 \cdot 10^{-4}(m/s)^2$. The estimates at nonzero spatial lags, $r = \pm 0.5$, take advantage of the fact that the measurement error, V^e, is likely only correlated with itself at approximately zero time and spatial lags. Therefore, if the difference measurement ΔV is instead multiplied with the time series of the next nearest location (spatial lag), or with a delayed time series of the same location (time lag), or both, then the error variance term should disappear in the cross covariance estimate.

Figure 3-1 shows that the $r = \pm 0.5m$ lag cross covariance estimates converge to about $3.4 \cdot 10^{-4}(m/s)^2$, and $3 \cdot 10^{-4}(m/s)^2$, indicating that the error covariance terms have been removed. In addition, decay due to spatial separation is also present, since their values are less than the zero lag value of $4 \cdot 10^{-4}(m/s)^2$. The two lag estimates are close in value, but not equal. This is to be expected, for in shear currents different vertical locations have different variances. When the lag estimates converge to the same value (as seen in other data sets), it indicates that this particular portion of the water column is likely to be homogeneous and isotropic.

The cross covariance estimates at any lag other than zero will not give us the radial turbulent variance needed to eventually form the Reynolds stress estimate. However, they may be quite useful in providing an indirect means of arriving at the desired zero lag estimate. Both the spatial lag and temporal lag curves must converge to the same point, as seen in figure 3-2. Using appropriate resolution (spatial and temporal lags which are larger than the decay rate of the error process, but small enough to reveal the structure of turbulent decay in proximately of the zero lag estimate), the desired radial turublent variance can be extrapolated. In the case that the appropriate resolution is not obtainable or available, as is the case for the data obtained from the Martha's Vineyard Coastal Observatory, then modeling is required in order to do a curve fit. This will be explored in subsequent chapters, but the estimate obtained in this manner is only as good as how well the model actually matches what is physically occuring in the ocean.

Figure 3-3 presents the full space-time radial cross covariance estimates, and will
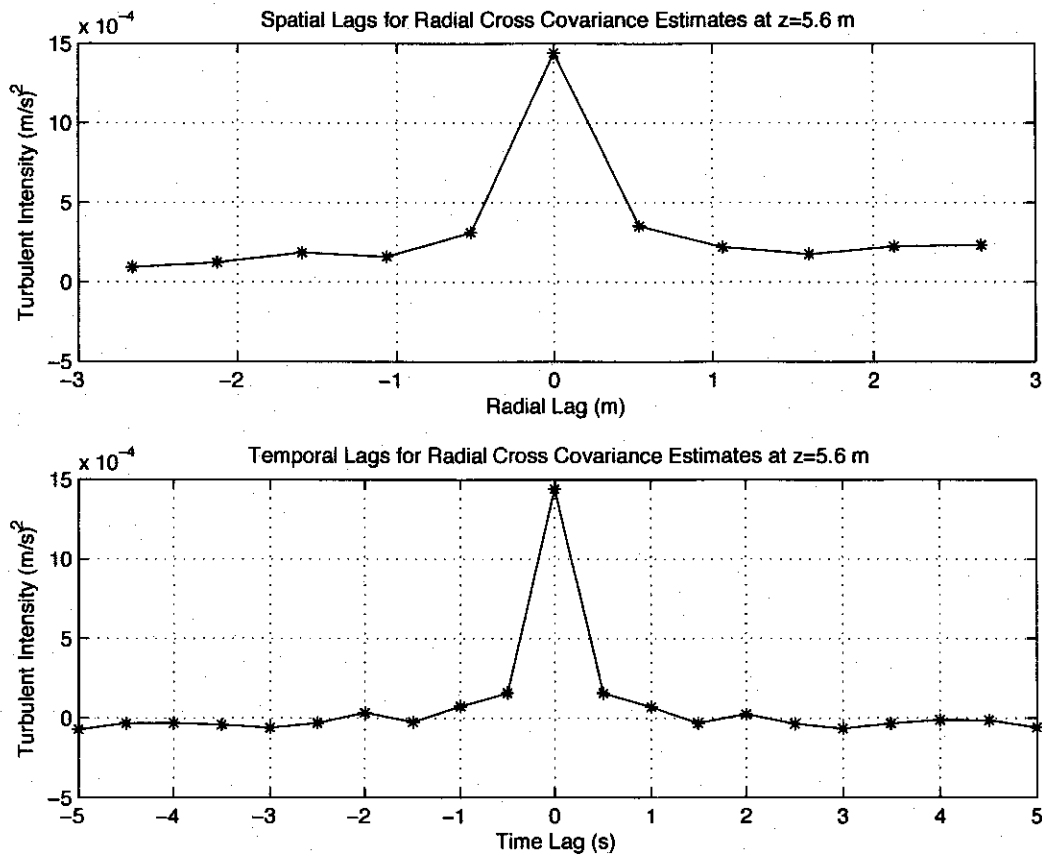
Figure 3-2: Radial cross covariance estimates at spatial and temporal lags. The zero tag values include the error variance term, whereas the non-zero lags are free of the error variance term. By proper extrapolation, the error free radial turbulent variance term can be estimated.

be of significant help in the modeling process.

If the statistics of the ADCP measurement error variance are beam independent, stationary and ergodic, then a sufficient number of data points used in forming the estimate should lead to convergence of the estimate (which is what seems to be the case from the results presented in figure 3-1). The Reynolds stress estimate is formed by subtracting the two radial cross covariance estimates, and due to stationarity of the process and covergence in the estimates, the error variance terms in each beam should be equal, and should cancel out. However, the wave error terms should still
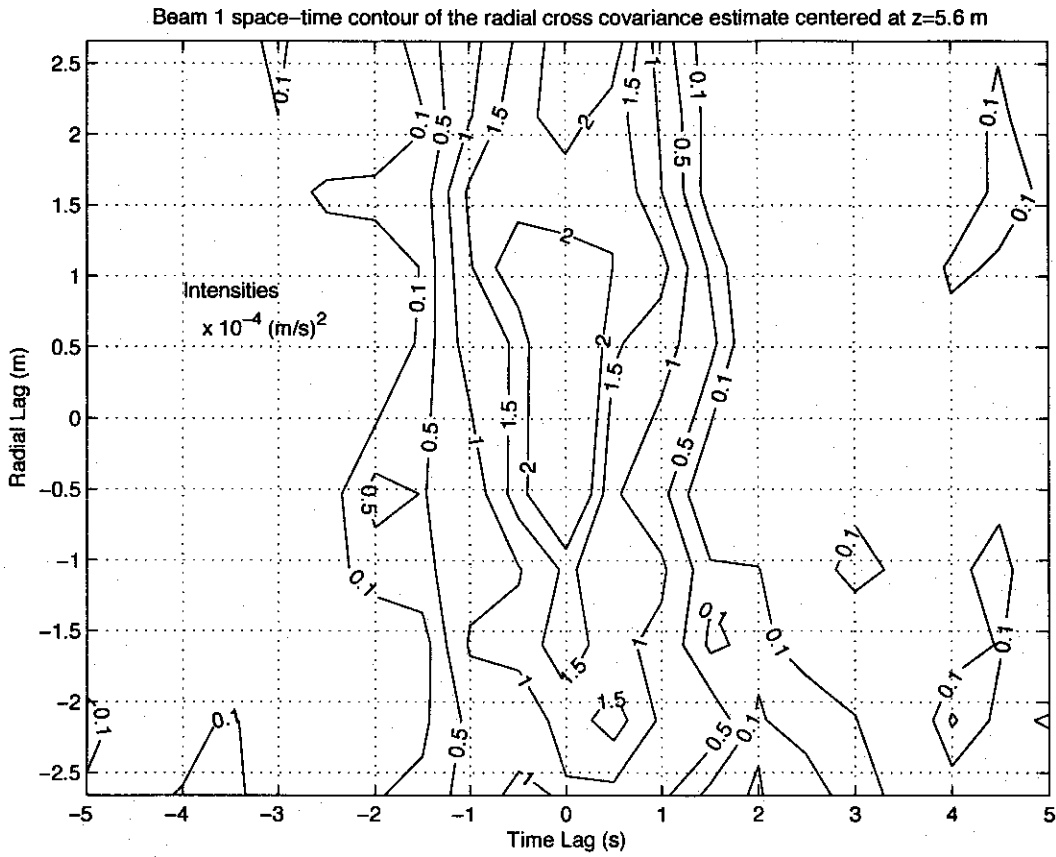
Figure 3-3: The combined space-time radial cross covariance estimates for z=5.6 m location on beam 1 of the ADCP. This will aid in the modeling process.

be present, as is seen in the last set of terms of equation 3.37.

$$
\begin{aligned}
\widehat{\overline{u_1' u_3'}} &= [\text{cov}(V_{B1}'(\vec{x}_a, t), \Delta V_{B1}'(\vec{x}_a, t)) - \text{cov}(V_{B2}'(\vec{x}_b, t), \Delta V_{B2}'(\vec{x}_b, t))]/(4 \sin \phi \cos \phi) \\
&= \tfrac{1}{N}[(\mathbf{v_{x1}}^T \mathbf{v_{x1}} - \mathbf{v_{x1}}^T \hat{\mathbf{v}_{x1}}) - (\mathbf{v_{x2}}^T \mathbf{v_{x2}} - \mathbf{v_{x2}}^T \hat{\mathbf{v}_{x2}})]/(4 \sin \phi \cos \phi) \\
&= \tfrac{1}{N}[(\mathbf{v_{x1}'}^T \mathbf{v_{x1}'} + \tilde{\mathbf{v}}_{x1}^T \tilde{\mathbf{v}}_{x1} + \mathbf{v_{x1}^e}^T \mathbf{v_{x1}^e} - \mathbf{v_{x1}}^T \hat{\mathbf{v}_{x1}}) - \\
&\qquad (\mathbf{v_{x2}'}^T \mathbf{v_{x2}'} + \tilde{\mathbf{v}}_{x2}^T \tilde{\mathbf{v}}_{x2} + \mathbf{v_{x2}^e}^T \mathbf{v_{x2}^e} - \mathbf{v_{x2}}^T \hat{\mathbf{v}_{x2}})]/(4 \sin \phi \cos \phi) \\
&= \tfrac{1}{N}[\mathbf{v_{x1}'}^T \mathbf{v_{x1}'} - \mathbf{v_{x2}'}^T \mathbf{v_{x2}'}]/(4 \sin \phi \cos \phi) + \\
&\qquad \tfrac{1}{N}[(\tilde{\mathbf{v}}_{x1}^T \tilde{\mathbf{v}}_{x1} - \mathbf{v_{x1}}^T \hat{\mathbf{v}_{x1}}) - (\tilde{\mathbf{v}}_{x2}^T \tilde{\mathbf{v}}_{x2} - \mathbf{v_{x2}}^T \hat{\mathbf{v}_{x2}})]/(4 \sin \phi \cos \phi)
\end{aligned}
$$

(3.37)

Figure 3-4 shows a few Reynolds stress profiles for data taken from a 1200 kHz ADCP located in about 12 meters of water. This 12 meter node from the Martha's Vineyard Coastal Observatory is set to ping at 2 Hz, and is set to obtain radial velocity estimates at about 50 cm intervals. Comparing these results to that of figure (where
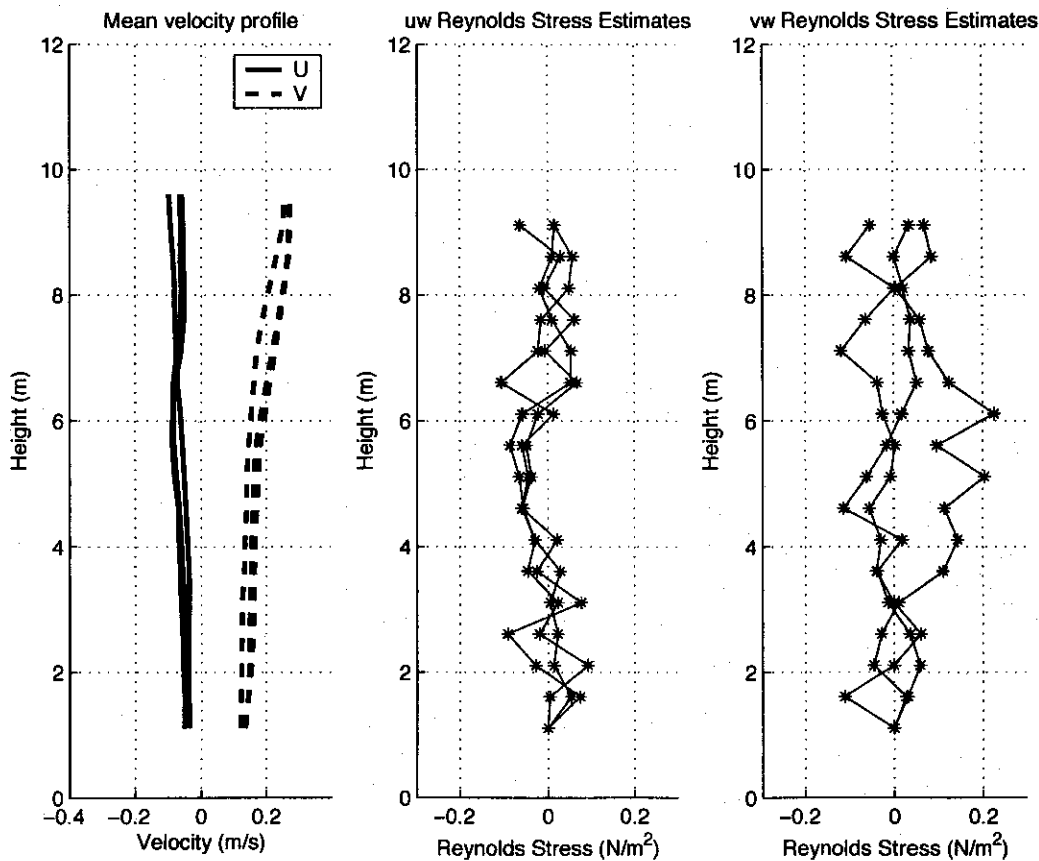
Figure 3-4: Current profiles from MVCO ADCP data of yearday 153, 2005, at 9:20, 9:40, 10:00 p.m. The day and start time was randomly chosen, but the subsequent data sets were chosen close enough in time that their mean current profiles would hopefully be similar.

no filtering has occured), it appears that the Reynold stress estimates are reduced in magnitude, but have similar profiles and similar noise characteristics. As previously explored for estimates obtained without filtering, there is bias and variance due to the wave-induced velocities and due to the beam tilt. In these new filtered estimates, the large wave influences have been effectively removed, but it appears that the wave error terms introduced (see last terms of equation 3.37) are of equal magnitude to that of the Reynolds stress. Chapter 10 will examine what affects the wave error terms in more detail. The next section will examine choosing the appropriate time intervals of the data series used in the linear least squares estimation.

3.4 Determining the temporal parameters of the estimation algorithm

Of immediate importance is determining the length of the time series used in the linear least squares estimation. This should not be much of an issue for the turbulence process, since it should be stationary over a long period of time (10-20 minutes). However, waves have periods on the order of seconds, and the linear least squares estimation should adapt to changing conditions.

For the linear least squares filter to work properly, the length of the data series (number of rows) should be about 3 times the length of the temporal and spatial depth (number of columns).
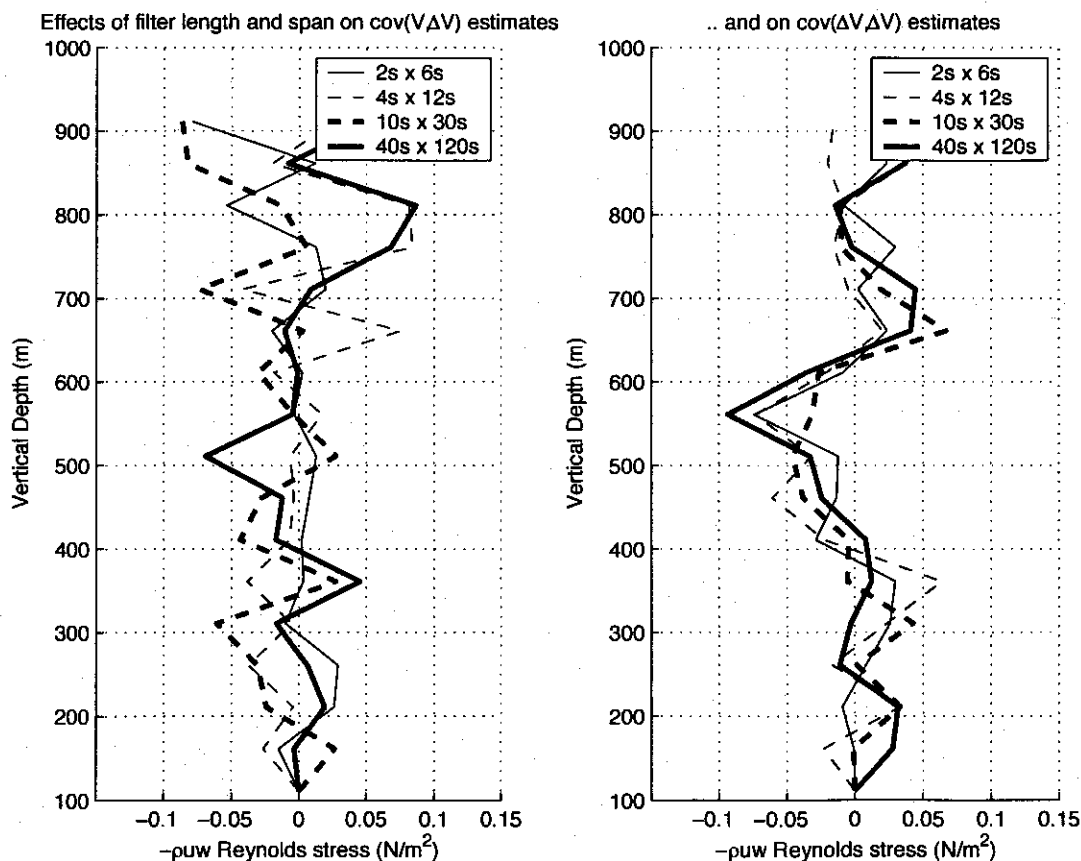
Figure 3-5: The first graph shows the results of varying the temporal filter size when using the $\text{cov}(\mathbf{v_x}, \Delta\mathbf{v_x})$ estimates of the variance of the radial turbulent fluctuations. The second graph shows the effects of using the same temporal filter dimensions with the $\text{cov}(\Delta\mathbf{v_x}, \Delta\mathbf{v_x})$ estimates.

Figure 3-5 shows the results of varying the temporal dimensions of the filter when using either the $\mathrm{cov}(\mathbf{v_x}, \Delta\mathbf{v_x})$ estimates or the $\mathrm{cov}(\Delta\mathbf{v_x}, \Delta\mathbf{v_x})$ estimates of the variance of the radial turbulent fluctuations. It appears that the $\mathrm{cov}(\mathbf{v_x}, \Delta\mathbf{v_x})$ estimates are much more sensitive to changes in filter dimensions, and that error dominates the estimates. This can be concluded because when the filter dimensions are close in size, the estimates should be fairly overlapping. That is the case for the $\mathrm{cov}(\Delta\mathbf{v_x}, \Delta\mathbf{v_x})$ estimates, which are much more robust to changes in the filter dimensions.

However, as figure 3-6 shows, both types of estimates converge in the limit of large filter dimensions (as the theory would predict).
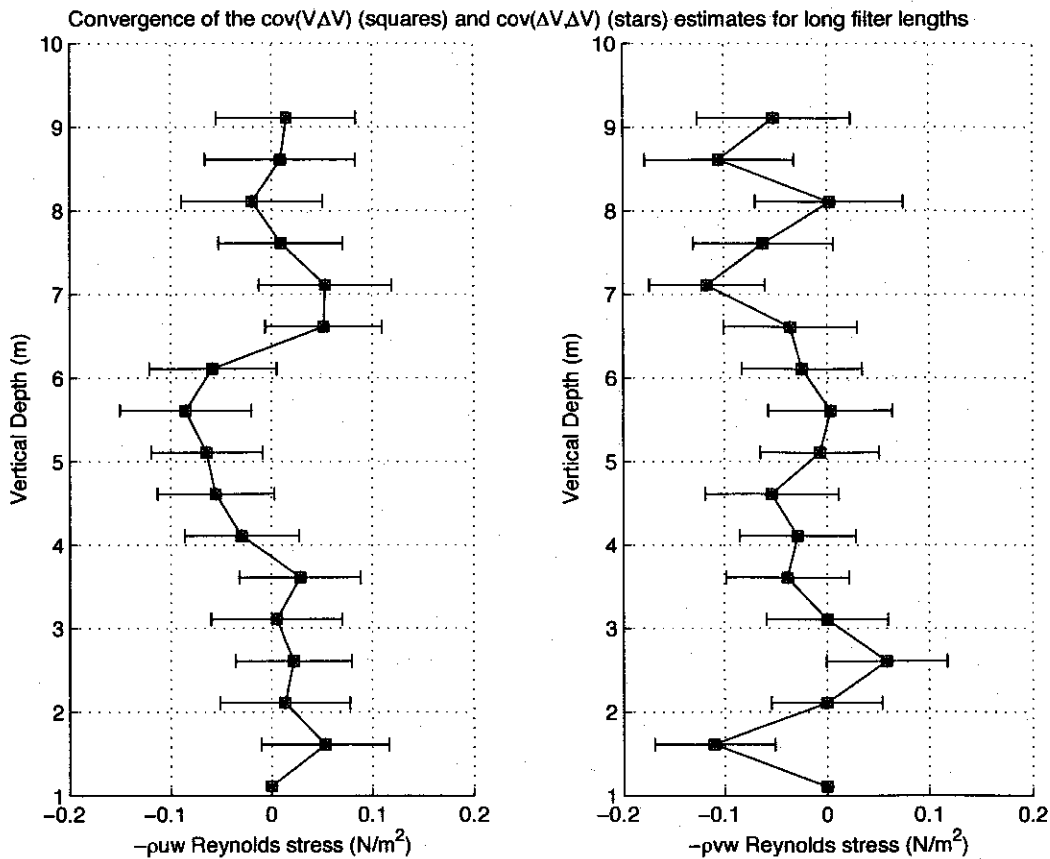
Figure 3-6: These plots show that in the limit of long filter lengths, there is convergence of both the $\mathrm{cov}(\mathbf{v_x}, \Delta\mathbf{v_x})$ and $\mathrm{cov}(\Delta\mathbf{v_x}, \Delta\mathbf{v_x})$ estimates of the variance of the radial turbulent fluctuations. Error bars are included to show the uncertainty in the Reynold stress estimates.

The uncertainty in the estimates was calculated using the method presented in section 2.3, and the error bars of the standard deviation were included. Even with wave influences removed from the estimates, the error is still of the same order of magnitude as the estimates. The next section explores how the error can better be predicted, and what steps might be able to be taken to reduce the error and uncertainty further.

3.5 Predicting the error in the estimate of the Reynolds stress

In the previous sections, actual data was used to form the estimates of the Reynolds stress and to estimate the uncertainty in these estimates. However, when the wave-induced velocities cannot be fully removed, the error and the variance of the estimate of Reynolds stress are both affected. Without full knowledge of the ocean state, it is difficult to know what data to use in order to perform optimal coherent estimates of wave-induced velocities while minimizing correlation of the turbulence-induced velocities.

It will be possible to gain some reasonable insights into how to select the appropriate data for estimating other data by introducing various statistical models. For example, using general sea state models, wave induced velocities and their correlations can be calculated. Likewise, various models for turbulent fluctuations and their correlations can be used, such as assuming the turbulence is homogeneous and isotropic, advected by a mean current, or assuming that the turbulence is non-homogeneous and non-isotropic being advected in a shear current. Exploring how the error in the ADCP measurements is introduced will help to determine if the error variance terms will indeed cancel out, or if they are even significant.

Optimal linear estimation requires knowledge of only second order statistics. From the second graph of figure 3-5, it appears that it will be possible to use long filter lengths in the estimation process. That means models which use second order statis-

tics should approximate actual results fairly well.

Using the models, it will be possible to determine directly the effect that beam tilt has on the error of the estimate. In addition, they can be used to help determine whether the reduction in magnitude of the filtered estimates of Reynolds stress accurately predicts the true values, since the wave-induced velocities have been removed, or if there is additional reduction due to the algorithm used.

Therefore, the rest of this thesis will be the development and modeling of the space-time correlations of each of these processes. In addition, simulating the process will allow for the optimal estimation algorithms to be tested.

Chapter 4

ADCP Measurement Error and Theory

Determining the ADCP measurement error is perhaps the most significant aspect of this thesis (and perhaps the most involved). The reason for this is that the error is in part determined by the choices made by the user, in part by the algorithms used to estimate the velocity, and in part by the ocean environment itself.

This chapter will address a number of critical issues:

- User defined goals (spatial and temporal resolution for example)
- The use of the Doppler shift to obtain velocity measurements
- Methods for estimating the Doppler shift
- Signal transmission and it's effect on spatial and temporal resolution
- Limited space-time characterizations of the error variance

There are two main results of this chapter. The first is that the error variance is asymptotically unbiased. Therefore, its effect on the random fluctions seen in the Reynolds stress estimates can be mitigated by chosing a long enough averaging period.

The second is that the error in each radial velocity estimate can be approximated as independent and uncorrelated with all other measurement errors as long as spatial and temporal resolution is not finer than the decorrelation limits of the error process.

4.1 Chapter Overview

The chapter will begin with the basics of how an ADCP works, introduce measurement goals, and provide a derivation of the fundamental equation used to determine radial velocities. Then each aspect of the ADCP will be examined in greater detail in order to find potential problems in meeting the stated goals. This examination will be divided into three main areas: estimating the mean Doppler shift and the error variance; understanding the effects of signal transmission; and finding the limits of spatial and temporal resolution based on user defined goals, signal transmission, and the resulting error process.

First, methods used to estimate the mean Doppler shift and the variance of the ocean process will be presented. This includes the basic equations of signal transmission and reception, followed by theoretical derivations for the spectral and covariance approaches. Practical methods for calculating the Doppler shift and velocity estimates are explained, and a theoretical lower bound on the variance is given.

Second, the effects of pulse transmission are explored. The ADCP is named according to the method of transmission used. The Narrowband ADCP transmits a single pulse, and waits for the return signal before transmitting its next pulse. This leads to a velocity resolution $\leftrightarrow$ spatial resolution trade-off. The Pulse-to-Pulse Coherent ADCP transmits short pulses and measures the phase change between pings. This leads to a maximum range $\leftrightarrow$ maximum velocity trade-off. Finally, the Broadband ADCP transmits it's second pulse before receiving back it's first, and introduces pulse coding to solve transmission energy issues.

It is only the Broadband ADCP which is found to meet most of the stated measurement goals. Therefore, the final section of this chapter will explore the trade-offs of minimizing error variance while meeting the stated goals. The effect of user choices will be used to formulate the space-time correlations of the error variance.

4.2 Why Choose an ADCP?

The goal of this thesis is to examine the possibility of obtaining an entire vertical profile of Reynolds stress estimates. Whereas many measuring instruments provide vector measurements of the velocity at individual points, the Acoustic Doppler Current Profiler (ADCP) is able to provide a profile of measurements. It also has the advantage of leaving the flow being measured undisturbed, since it only sends out beams of sound.
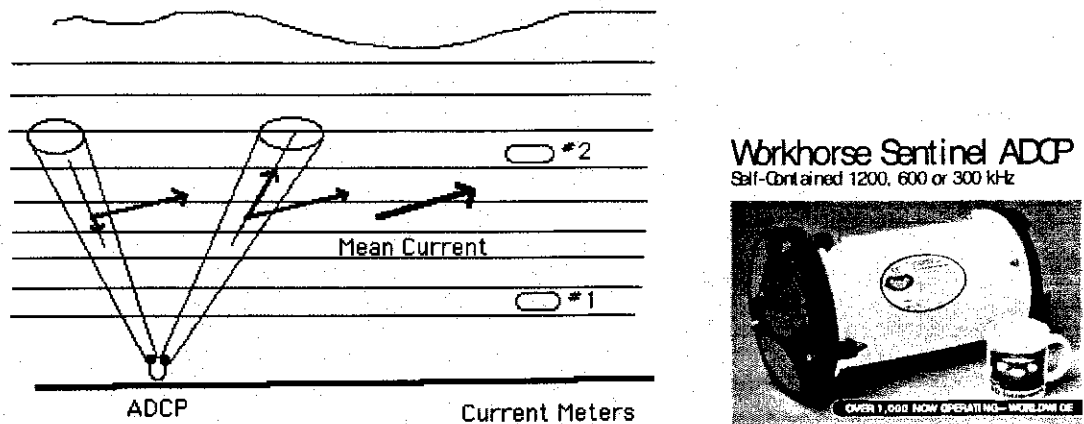
The Workhorse Sentinal ADCP from RD Instruments is able to remotely measure radial velocities at many ranges. The picture is used with permission from RDI. [8]

4.2.1 Basic Configuration and Operation

RD Instruments has a primer for the broadband ADCP which provides an excellent introduction into the workings of an ADCP. [9] The ADCP has four ceramic transducers arranged in a Janus configuration (beams lie along perpendular bisecting planes). Each transducer, tilted between 20-30 degrees from the vertical, emits a directed sound beam. As the sound travels through the water, it encounters small organisms which are assumed to be floating passively with the water. Though most of the sound is transmitted, some of the scattered sound is directed back towards the transducer. The return signal is Doppler shifted in frequency due to the motion of the scatterers. The return signal is time-gated and averaged, and the result is a

59
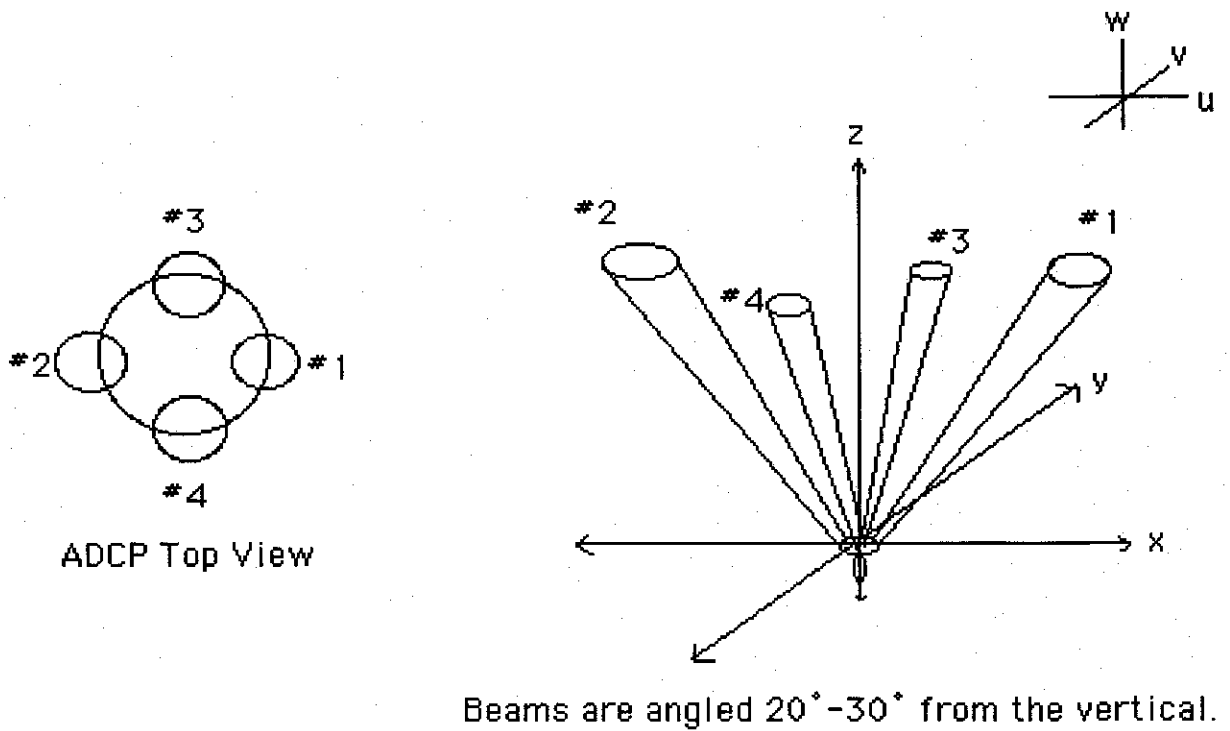
Figure 4-1: The top view and side view geometries of the ADCP.

profile of radial velocities at specific points along each beam.

If the flow was perfectly uniform and unchanging, then beams in opposing directions could be used to transform instantaneous radial velocities, v_{Bi}, into instantaneous u_1, u_3 velocities in the x and z directions, or u_2, u_3 in the y and z directions. The two independent calculations of u_3 provide a way to error check. Since the error for any individual ping is generally quite large, a number of pings must be averaged. When the statistics are stationary, or unchanging in time, then averaging will indeed reduce the error, and the mean u_1, u_2, and u_3 velocity components can be calculated.

$$\overline{u_1} = \frac{\overline{v_{B2}} - \overline{v_{B1}}}{2\sin\phi}, \qquad \overline{u_2} = \frac{\overline{v_{B4}} - \overline{v_{B3}}}{2\sin\phi}, \qquad \overline{u_3} = \sum_{i=1}^{4} \frac{\overline{v_{Bi}}}{4\cos\phi} \qquad (4.1)$$

4.3 Measurement Goals

REQUIREMENTS	HOR./VER.	RADIAL
Spatial Resolution	10 cm	11 cm
Temporal Resolution	0.1 s	0.1 s
Max. Vertical Range	15 m	16 m
Instantaneous Velocity Resolution	n/a	n/a
$\overline{u_1' u_3'}$ Resolution	10 % of true	see below
Max. Horizontal Velocity	2 m/s	1.6 m/s
Max. Vertical Velocity	1 m/s	
Max. Averaging Period	20 min	20 min

Listed in the table above are the user defined goals (first column), the desired resolutions and environmental constraints (second column), and the corresponding radial requirements that the ADCP will need to meet (column three). The geometry of the ADCP will largely determine the resulting radial measurement goals.

A typical nearshore deployment will have an ADCP in about 15 meters of water, with max current speeds of about 1 m/s, and max wave velocities of about 1 m/s. The spatial and temporal resolutions were chosen small enough to resolve the higher wavenumbers and frequencies of turbulence, and to aid in the accurate modeling of the turbulent space-time correlations. The averaging time needs to be as long as possible for estimations to converge to their steady values and to reduce error variances, but short enough that the statistics remain stationary. Typically, the averaging time is about 20 minutes.

Instantaneous velocity resolution in the horizontal and vertical directions is not obtainable from the ADCP, as previously discussed, because the ADCP needs to average a number of pings in order to resolve radial velocities into their respective $\overline{U_1}, \overline{U_2}$, and $\overline{U_3}$ velocities.
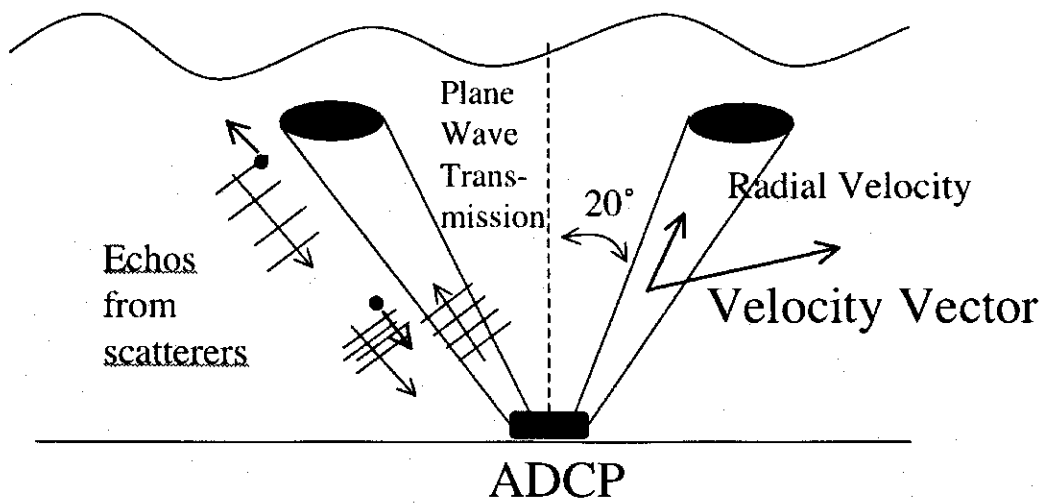
Figure 4-2: Only the radial component of the scatterer's velocity is measured.

Except for averaging period and velocity resolution, all other radial requirements were calculated based on the beam geometry, assuming a 20 degree tilt from the vertical. Averaging time is independent of beam geometry, so those numbers are the same in both columns.

Beam geometry will have an effect on spatial resolution, because the combination of the natural beam spreading and the tilt of the beam creates radial slices that are not exactly horizontal. The vertical spatial resolution is the difference between the top corner of the ensonified volume to the opposite bottom corner, projected onto the vertical axis. This will become more pronounced the further the radial distance. For instance, for a typical 2 degree beam spread for a Broadband ADCP, with beams tilted at 20 degrees, and with the radial bin size set to 10.6 cm, the vertical spacing deviates from the desired 10 cm spacings. (Values in the table are in meters.)

bin center	top corner	bot corner	difference
13.00	13.14	12.86	0.28
9.00	9.11	8.88	0.23
5.00	5.09	4.91	0.18
1.00	1.06	0.93	0.13

In addition, adjacent bin centers will have some common overlap of ensonified volume. If the beams are tilted more than 20 degrees, these vertical spacings will only increase, even when the radial slices remain thin (10.6 cm thickness for example).

The most important criteria, the $\overline{u_1' u_3'}$ resolution necessary to obtain an accurate Reynolds stress estimate, $-\rho \overline{u_1' u_3'}$, will depend on the radial variance.

To determine the error variance resolution, the formula for $\overline{U_1' U_3'}$ (see equation 3.37) can be rewritten as,

$$\overline{u_1' u_3'} + \Delta \overline{u_1' u_3'} = \overline{U_1' U_3'} = \frac{\overline{V_{B1}'}^2 - \overline{V_{B2}'}^2 + \Delta \overline{V^e V^e}}{4 \sin \phi \cos \phi}. \tag{4.2}$$

With $\overline{\Delta u_1' u_3'}$ required to be 10 % of $\overline{u_1' u_3'} \approx 1 (cm/s)^2$, the radial velocity error variance difference for the two beams is $(4 \sin 20 \cos 20)(0.1)(1) \approx 0.13 \ (cm/s)^2$. This requires that the bias in the radial error variance for each beam be $\approx 0.07 \ (cm/s)^2$. This will be a challenge to overcome.

The next section will introduce how it is the ADCP is able to measure radial velocities. The fundamental principle in using sound propagation to measure velocity is that any changes in motion by the source or receiver result in a time dialation, or comparably, a shift in frequency, of the received signal. The Doppler shift in frequency is linearly related to the velocity of the scatterer. The next few sections look at this fundamental relationship, and later sections show how to make estimates of the Doppler shift based on the received signal.

4.4   Using the Doppler Shift to Determine Velocity

When small marine organisms carried by the water move towards or away from the sound source, the frequency they encounter will be increased or decreased respectively. This occurs because the time it takes for one wavelength of the sound source to pass the scatterers is either decreased or increased respectively. This change in frequency due to motion is called the Doppler shift, and it is similar to what one hears when a whistling train passes by. Only the motion in line with the direction of sound propagation is measured, and is given by

$$v_{Bi} = \left(\frac{1}{2} \frac{c}{f} \right) \hat{f_d}, \tag{4.3}$$

63

where v_{Bi} is the velocity of the scatterer in the direction opposite of sound propagation, c is the speed of sound in water, f is the transmit frequency, and $\hat{f}_d$ is the Doppler shift frequency. The factor of $(1/2)$ is the result of the scatterer acting as both receiver and source, basically due to the scatterer's motion being accounted for twice. This is more easily seen by looking at the overall change in frequency that occurs from source, f, to receiver, f', and back to source again, f'':

$$f'' \approx \left(1 + \frac{2v_{Bi}}{c}\right) f, \tag{4.4}$$

for $v_{Bi} << c$. The next few sections track the changes in frequency from source, to receiver, and back to source again.

4.4.1 Stationary Source and Moving Receiver

If the period, T, is the time for one wavelength to pass a stationary point, then T - ΔT is the time for one wavelength to pass the moving scatterers. (Note: ΔT is positive when the relative motion of the source and receiver is towards one another.) Frequency for the source, f, and for the scatterers, f', can be written:

$$f = \frac{1}{T}, \qquad f' = \frac{1}{T - \Delta T}. \tag{4.5}$$

As the scatterers drift with the current, v is their component of velocity that is in the direction of the sound propagation. The distance they move while one wavelength of sound passes them is

$$d = vt \quad \longrightarrow \quad \Delta d = (T - \Delta T)v. \tag{4.6}$$

where again, v and d are positive when the relative motion of the source and receiver are towards one another. The ΔT it takes for the propagating sound source wavelength to pass the drifting scatterers depends on how far they have moved, Δd. The

64

speed of sound, c, can be considered approximately constant for illustration purposes.

$$c = d/t \quad \longrightarrow \quad \Delta t = \frac{\Delta d}{c} \quad \longrightarrow \quad \Delta T = \frac{(T - \Delta T)v}{c} \tag{4.7}$$

Solving for ΔT in terms of T:

$$c\Delta T = vT - v\Delta T \quad \longrightarrow \quad c\Delta T + v\Delta T = vT \quad \longrightarrow \quad \Delta T = \frac{vT}{c + v} \tag{4.8}$$

Plugging ΔT into f', and solving f' in terms of f (with $T=1/f$):

$$f' = \frac{1}{T - \Delta T} = \frac{1}{T + \frac{vT}{c+v}} = \frac{1}{\frac{1}{f} - \frac{v}{(c+v)f}} = \frac{(c+v)f}{c+v-v} = \left(\frac{c+v}{c}\right)f \tag{4.9}$$

There is also an effect on the Doppler shift due to the motion of the source, which will be considered next.

4.4.2 Moving Source and Stationary Receiver

A moving source emits a wavelength that is either lengthened or shortened when the source is moving away from or in the direction of sound propagation. The time dilation or contraction, $\Delta T'$, is related to the distance moved by the source while emitting the sound for one period, T.

$$\Delta T' = \frac{\Delta d'}{c} = \frac{v'T'}{c} \tag{4.10}$$

The frequency that the stationary receiver hears, f'', written in terms of the emitted frequency, f', is

$$f'' = \frac{1}{T' - \frac{v'T'}{c}} = \frac{1}{\frac{1}{f'} - \frac{v'}{f'c}} = \left(\frac{c}{c - v'}\right)f' \tag{4.11}$$

4.4.3 Scatterers as both Moving Reciever and Moving Source

As discussed, the scatterers experience sound at frequency f' while moving either away from or towards the source of sound at frequency f. However, the echo they

65

reflect back towards the sound source makes them a moving source. The original source now becomes the stationary receiver, and the return echo is frequency f''. Plugging f' into f'', and noting v'=v:

$$f' = \left(\frac{c+v}{c}\right) f, \quad \text{and} \quad f'' = \left(\frac{c}{c-v'}\right) f'$$

$$f'' = \left(\frac{c}{c-v'}\right)\left(\frac{c+v}{c}\right) f = \left(\frac{c+v}{c-v}\right) f \tag{4.12}$$

4.4.4 Doppler Shift frequency of received echo off scatterers

The Doppler shifted frequency is just the difference between the original frequency of the source, f, and the received echo freqency, f''.

$$f_d = f'' - f \tag{4.13}$$

$$f_d = \left(\frac{c+v}{c-v}\right) f - f = \left(\frac{c+v}{c-v} - \frac{c-v}{c-v}\right) f = \left(\frac{2v}{c-v}\right) f \tag{4.14}$$

Finally, since c $\gg$ v in the water,

$$\boxed{f_d = \left(\frac{2v}{c}\right) f.} \tag{4.15}$$

This indicates that a moving scatterer causes a double shift in frequency. If the scatterers are moving away from the source ($v < 0$), then there is an overall decrease in the received freqency. If the scatterers are moving toward the source ($v > 0$), then there is an overall increase in the received frequency. The key to estimating the radial velocity is to estimate the Doppler shift, and the next few sections will examine methods for obtaining this estimate.

4.5 Methods for Estimating the Doppler Shift

The Doppler shift frequency can be estimated in either the frequency domain or the time domain, and both methods will be explored. The estimate of the Doppler shift frequency using frequency domain information is unbiased, but requires that the full spectrum of the return signal be calculated. The estimate of the Doppler shift frequency using time domain information is biased, but needs only pairs of points to make the estimate and therefore saves on calculation time. [13]

The next few sections will provide basic equations for the transmitted and received signal, and explain how both the spectral method (frequency domain) and covariance method (time domain) can be used to make an estimate of the Doppler Shift.

4.5.1 Basic Representations of the Transmitted and Received Signal

The transmitted signal $s_{tx}(t)$ can be represented as the real part of a complex signal, with carrier frequency, f, amplitude, A, and pulse duration τ_p.

$$s_{tx}(t) = Re\{Ae^{-j2\pi ft}p(t)\}, \quad p(t) = \begin{cases} 1, & 0 < t \leq \tau_p \\ 0, & t > \tau_p \end{cases} \tag{4.16}$$

Since the transmitted signal has a pulse of duration τ_p, at any instant of time, the front of the pulse will be at a farther distance from the ADCP than the back of the pulse. When the front of the transmitted pulse encounters a scatterer and begins its return trip, it can be joined by the tail end of the pulse which happens to hit a different scatterer just as the front of the return pulse passes by. In this manner, the signal that returns to the ADCP is actually a superposition of a range of scatterer echos. The maximum range covered is then half of the pulse duration times the speed of sound in water, $c\tau_p$. In addition to covering a radial range, there is slight beam spreading. This means that a volume of scatterers is ensonified.
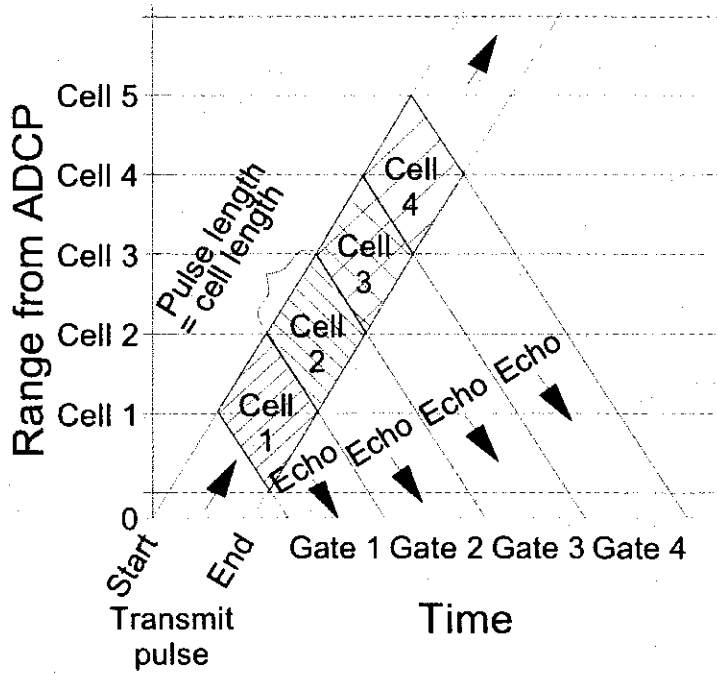
Figure 4-3: The return signal at any time instant is a superposition of a small range of scatterer echos. The graphic is used with permission from RDI. [9]

Letting R_c be the centroid of the volume of scatterers ensonified, and δr_n be the differential change in distance in the direction of sound propagation to reach a particular scatterer, the location of a particular scatterer relative to the ADCP is

$$r_n = R_c + \delta r_n. \tag{4.17}$$

Since actual scattering off any ocean organism is quite complicated (depending on composition, shape, orientation, etc.), it is reasonable to treat really small organisms as point scatterers with a random amplitude.

$$a_n = |A_n| e^{j\phi_n} \tag{4.18}$$

The amplitude term, A_n, includes the attenuation of the plane wave transmission signal of amplitude A as it travels to reach the scatterer, and the spherical spreading loss of a point scatterer on the return trip. The return signal for an individual scatter is

$$s_n(r_n, t) = a_n e^{j2\pi((2r_n/c)-t)f_n''}, \tag{4.19}$$

68

where c is the speed of sound in water and f_n'' is the adjusted frequency due to the moving scatterer acting as both receiver and source (see 4.12). Representing the velocity of each scatter as some small deviation from the mean velocity of ensonified scatterers, the individual adjusted frequency of a scatterer can be represented as

$$f_n'' = f'' + \delta f_n''. \tag{4.20}$$

When accounting for the volume V of ensonified scatterers, the return signal at one instant of time is

$$\begin{aligned}
s_{ret}(t) &= \sum_{n \in V} a_n e^{j2\pi((2r_n/c)-t)f_n''} \\
&= \sum_{n \in V} a_n e^{j2\pi((2r_n/c)-t)(f''+\delta f_n'')} \\
&= \sum_{n \in V} a_n e^{j2\pi[((2R_c/c)+(2\delta r_n/c)-t)f''+((2r_n/c)-t)\delta f_n'']} \\
&= e^{-j2\pi f''t} e^{j2\pi(2R_c/c)f''} \sum_{n \in V} a_n e^{j2\pi[(2\delta r_n/c)f''+((2r_n/c)-t)\delta f_n''-\delta f_n''t]} \\
&= e^{-j2\pi f''t} e^{j2\pi(2R_c/c)f''} G(t) e^{j\alpha(t)}
\end{aligned} \tag{4.21}$$

The $G(t)e^{\alpha(t)}$ term is the polar form of a complex Gaussian random variable. This Gaussian nature of the distribution can be understood in light of the Central Limit Theorem, which says that the sum of many independent, identically distributed random variables has an overall probability distribution which is Normal.

The return signal is then mixed to baseband by multiplying it by the carrier signal, $e^{j2\pi ft}$, and low pass filtering. Mathematically, this is equivalent to multiplying by $e^{j2\pi ft}$.

$$\begin{aligned}
s_{bb}(t) &= s_{ret}(t) e^{j2\pi ft} \\
&= e^{-j2\pi f''t} e^{j2\pi(2R_c/c)f''} G(t) e^{j\alpha(t)} e^{j2\pi ft} \\
&= e^{j2\pi(f-f'')t} e^{j2\pi(2R_c/c)f''} G(t) e^{j\alpha(t)} \\
&= e^{j2\pi f_d t} e^{j2\pi(2R_c/c)f''} G(t) e^{j\alpha(t)}
\end{aligned} \tag{4.22}$$

where f_d is the Doppler shift frequency. This equation is very similar to one proposed by Theriault, [22]

$$s_{ret}(t) = s_{tx}(t) G_{cpx}(t) e^{j2\pi f_d t} \tag{4.23}$$

69

where s_{tx} is the transmitted signal and G_{cpx} is the complex Gaussian variable ($=$ $G(t)e^{j\alpha(t)}$). Combining the rapidly fluctuating phase terms,

$$e^{j\phi(t)} = e^{j2\pi(2R_c/c)f''+j\alpha(t)}, \qquad (4.24)$$

the received signal mixed to baseband can be written as

$$s_{bb}(t) = G(t)e^{j2\pi f_d t + j\phi(t)}. \qquad (4.25)$$

The $\phi(t)$ term leads to phase jitter. It is a highly fluctuating term, and is the result of all of the small scale motions within the ensonified volume. Small scale turbulence and beam divergence cause these motions. Beam divergence (spreading) captures the changes in internal wave-induced velocities and surface wave-induced velocities throughout the ensonified volume.

4.5.2 The Spectral Approach

Aysmptotically unbiased estimates of the mean and variance exist, but the disadvantage is that the time series needs to be of considerable length for the estimates to be unbiased, and the entire spectrum must be calculated first in order to make the estimates.

Assuming that there is an additional noise component, $n(t)$, due to background sounds in the environment and due to random fluctuations introduced by the equipment itself, the total received signal, $q(t)$, is

$$q(t) = s_{bb}(t) + n(t). \qquad (4.26)$$

Since $q(t)$ has probabilistic components ($G(t)$, $n(t)$), it is a random process. Defining $q_n(t)$ as an independent sample of $q(t)$, an estimate of the sample spectrum is [13]

$$\hat{Q}_n(f) = \frac{1}{2T}\left|\int_{-T}^{T} q_n(t)e^{-j2\pi ft}\,dt\right|^2, \qquad (4.27)$$

where T is much less than the time interval indexed by n. Taking an average of a number of independent spectral estimates, $\hat{Q}_n(f)$, the overall estimate of the true spectrum, $Q(f)$, is

$$\hat{Q}(f) = \frac{1}{N} \sum_{n=1}^{N} \hat{Q}_n(f).$$ (4.28)

The mean value of the spectrum is found by normalizing a weighted average of the estimate spectrum. When the random noise, $n(t)$, is small compared to the received signal, this estimate is the needed Doppler shift frequency, and the radial velocity of the scatterers can be calculated.

$$\hat{f}_d = \frac{\int_{-\infty}^{\infty} f \hat{Q}(f) \, df}{\int_{-\infty}^{\infty} \hat{Q}(f) \, df}$$ (4.29)

The variance of the estimated spectrum is just the normalized second moment minus the mean squared.

$$\hat{\sigma}_d^2 = \frac{\int_{-\infty}^{\infty} f^2 \hat{Q}(f) \, df}{\int_{-\infty}^{\infty} \hat{Q}(f) \, df} - \hat{f}_d^2$$ (4.30)

The variance captures the effects of the phase jitter, providing insight into the strength of the small scale (and unresolvable) turbulence and the changing wave field.

Miller and Rochwarger [11] went further and assumed that signal power spectral density, the noise power spectral density, and pulse duration functions were all Gassian-shaped functions. Their work was not for ADCP's in particular, but for a broad class of applications. They found that the estimate of the mean of the signal spectrum was unbiased, and that the variance of that estimate fit the following curve:

$$\text{var}(\hat{f}_d) = \frac{\sigma_d}{2N\tau_p} \left(1 + \frac{1.6}{SNR} + \frac{3}{SNR^2}\right) + O(N^{-2})$$ (4.31)

where SNR is the signal to noise ratio. They also found that the estimate of the variance was biased, and found the following curves fit the mean and variance of the estimate of the standard deviation:

$$\text{mean}(\hat{\sigma}_d) = \sigma_d - \frac{3}{32N\tau_p} \left(1 + \frac{5.8}{SNR} + \frac{38}{SNR^2}\right) + O(N^{-2})$$ (4.32)

71

$$\text{var}(\hat{\sigma}_d) = \frac{3\sigma_d}{16N\tau_p}\left(1 + \frac{1.9}{SNR} + \frac{23}{SNR^2}\right) + O(N^{-2}) \tag{4.33}$$

4.5.3   The Covariance Approach

The autocovariance function is related to the power spectral density of a wide sense stationary process through its inverse Fourier transform. It is possible to use the autocovariance to obtain the first and second moments of the spectrum. This means that estimating the entire spectrum is not needed, and a great savings in calculations occurs.

The disadvantage of this method is that the mean and variance of the estimated spectrum are biased due to the fact that the slope of the autocovariance function at a lag of $h = 0$ is approximated. [13]

The Fourier transform relationships for the autocorrelation and power spectral density are given as follows:

$$\begin{aligned} S_{qq}(f) &= \int_{-\infty}^{\infty} R_{qq}(\beta)e^{-j2\pi f\beta}\,d\beta, \\ R_{qq}(\beta) &= \int_{-\infty}^{\infty} S_{qq}(f)e^{j2\pi f\beta}\,df. \end{aligned} \tag{4.34}$$

Differentiating the second expression will aid in the derivation of the mean and variance of the power spectral densities.

$$\begin{aligned} \dot{R}_{qq}(\beta) &= (j2\pi)\int_{-\infty}^{\infty} fS_{qq}(f)e^{j2\pi f\beta}\,d\beta \\ \ddot{R}_{qq}(\beta) &= (j2\pi)^2\int_{-\infty}^{\infty} f^2 S_{qq}(f)e^{j2\pi f\beta}\,d\beta \end{aligned} \tag{4.35}$$

The mean and variance of the Doppler shift frequency spectrum can now be obtained using only time domain functions, evaluated at lag $\beta = 0$.

First Moment (Mean):	$\mu(S_{qq}(f)) = \dfrac{\int_{-\infty}^{\infty} f S_{qq}(f)\, df}{\int_{-\infty}^{\infty} S_{qq}(f)\, df} = \dfrac{\dot{R}_{qq}(0)}{(j2\pi) R_{qq}(0)}$ (4.36)
Second Moment:	$\dfrac{\int_{-\infty}^{\infty} f^2 S_{qq}(f)\, df}{\int_{-\infty}^{\infty} S_{qq}(f)\, df} = \dfrac{\ddot{R}_{qq}(0)}{(j2\pi)^2 R_{qq}(0)}$ (4.37)
Variance = 2nd Moment - (Mean)^2:	$\sigma^2(S_{qq}(f)) = \dfrac{\ddot{R}_{qq}(0)}{(j2\pi)^2 R_{qq}(0)} - \left(\dfrac{\dot{R}_{qq}(0)}{(j2\pi) R_{qq}(0)} \right)^2$ (4.38)

This is the approach put forward by Miller and Rochwarger. [12] They go further to show how $\dot{R}_{qq}(0)$ and $\ddot{R}_{qq}(0)$ can be solved in terms of $R_{qq}(\beta)$ and $R_{qq}(0)$. With magnitude $A(\beta)$, phase $2\pi\phi(\beta)$, and where * denotes the complex conjugate, the one ping estimate of $R_{qqn}(\beta)$ in polar form is

$$\hat{R}_{qqn}(\beta) = \frac{1}{2T - |\beta|} \int_{-T + \frac{1}{2}|\beta| - \frac{1}{2}\beta}^{T - \frac{1}{2}|\beta| - \frac{1}{2}\beta} q_n(t + \beta) q_n^*(t)\, dt \qquad (4.39)$$

$$\text{Polar Form} \longrightarrow \hat{R}_{qqn}(\beta) = A(\beta) e^{j2\pi\phi(\beta)} \qquad (4.40)$$

Taking the first derivative of $\hat{R}_{qqn}(\beta)$:

$$\dot{\hat{R}}_{qqn}(0) = \frac{d(A(\beta))}{d\beta} \bigg|_{\beta=0} e^{j2\pi\phi(0)} + (j2\pi) \frac{d\phi(\beta)}{d\beta} \bigg|_{\beta=0} A(0) e^{j2\pi\phi(0)} \qquad (4.41)$$

Because the autocorrelation function is an even function, both the phase and the slope of the magnitude evaluated at $\beta = 0$ are zero. That will remove the first term. Then dividing through by $(j2\pi)A(0)e^{j2\pi\phi(0)}$ leaves $\dot{\phi}(0)$.

For small β:

$$\dot{\phi}(0) = \frac{d\phi(\beta)}{d\beta} \bigg|_{\beta=0} \approx \frac{\phi(\beta) - \phi(0)}{\beta} = \frac{\phi(\beta) - 0}{\beta} = \frac{\phi(\beta)}{\beta} \qquad (4.42)$$

$$\text{Phase} = 2\pi\phi(\beta) = \arctan \frac{\text{Im}\{\hat{R}_{qqn}(\beta)\}}{\text{Re}\{\hat{R}_{qqn}(\beta)\}} \longrightarrow \phi(\beta) = \frac{1}{2\pi} \arctan \frac{\text{Im}\{\hat{R}_{qqn}(\beta)\}}{\text{Re}\{\hat{R}_{qqn}(\beta)\}} \qquad (4.43)$$

$$\mu(S_{qqn}(f)) = \dot{\phi}(0) \approx \frac{\phi(\beta)}{\beta} = \frac{1}{2\pi\beta} \arctan \frac{\text{Im}\{\hat{R}_{qqn}(\beta)\}}{\text{Re}\{\hat{R}_{qqn}(\beta)\}} \qquad (4.44)$$

Remembering that $s_{bb}(t)$, the desired signal, is really the received signal with the noise removed,

$$s_{bb}(t) = q(t) - n(t), \qquad (4.45)$$

and by linearity of the autocorrelation operation,

$$\hat{R}_{ssn}(\beta) = \hat{R}_{qqn}(\beta) - \hat{R}_{NNn}(\beta), \qquad (4.46)$$

then the Doppler shift frequency can be found from the time domain information of the received signal and knowledge of the noise background.

$$\boxed{\hat{f}_d = \mu(\hat{S}_{ssn}(f)) \approx \frac{1}{2\pi\beta} \arctan \frac{\text{Im}\{\hat{R}_{qqn}(\beta) - \hat{R}_{NNn}(\beta)\}}{\text{Re}\{\hat{R}_{qqn}(\beta) - \hat{R}_{NNn}(\beta)\}}} \qquad (4.47)$$

The ideal time lag, β, depends on the shape of the spectral density function in question. Miller and Rochwarger [12] found that for a signal with a Gaussian spectral density distribution corrupted by noise with Guassian wide-band distribuion, the ideal lag β should be long enough that the noise becomes uncorrelated. If that lag is not obtainable, then it should be as long as possible, such as the length of the transmitted signal, τ_p. Hansen [7] found that for oceanic reverberation without a corrupting noise signal, the ideal time lage β should actually be as short as possible, in this case the sampling frequency, $1/f_s$. This is because the volume of water compared at two different times is at two different ranges, and by keeping the lag as small as possible, the information used to calculate the velocity (echos from scatterers) is basically the same.

Applying the same process to find the variance of the process:

$$\ddot{R}_{qqn}(\beta) = \ddot{A}(\beta)e^{j2\pi\phi(\beta)} + 2\dot{A}(\beta)e^{j2\pi\phi(\beta)}(j2\pi)\dot{\phi}(\beta)$$
$$+ A(\beta)e^{j2\pi\phi(\beta)}(j2\pi)^2\dot{\phi}(\beta)\dot{\phi}(\beta) + A(\beta)e^{j2\pi\phi(\beta)}(j2\pi)\ddot{\phi}(\beta) \tag{4.48}$$

Evaluating this expression at $\beta = 0$ removes the second term (as previously argued for $\dot{A}(0)$). Assuming that the phase $2\pi\phi(\beta)$ is approximately linear, then the first derivitive (just previously solved) is a constant, and the second derivitive would be zero. That removes the fourth term. Then dividing through by $(j2\pi)^2 R_{qqn}(\beta)$ evaluated at $\beta = 0$, which is just $(j2\pi)^2 A(0)e^{j2\pi\phi(0)}$, leaves only two terms:

$$\text{The second moment} = \frac{\ddot{R}_{qq}(0)}{(j2\pi)^2 R_{qq}(0)} = \frac{\ddot{A}(0)}{(j2\pi)^2 A(0)} + (\dot{\phi}(0))^2 \tag{4.49}$$

The second term is just the mean squared, so the variance then becomes:

$$\sigma^2(S_{qqn}(f)) = \frac{\ddot{A}(0)}{(j2\pi)^2 A(0)} = -\frac{1}{4\pi^2}\frac{\ddot{A}(0)}{A(0)} \tag{4.50}$$

For small β, a second difference can be calulated as follows:

$$\ddot{A}(0) \approx \frac{A(\beta) - 2A(0) + A(-\beta)}{\beta^2} \tag{4.51}$$

Since correlation functions are even, $A(\beta) = A(-\beta)$. Dividing by $A(0)$ the equation becomes:

$$\frac{\ddot{A}(0)}{A(0)} \approx \frac{2A(\beta) - 2A(0)}{\beta^2 A(0)} = \frac{-2}{\beta^2}\left[\frac{A(0) - A(\beta)}{A(0)}\right] \tag{4.52}$$

Remembering that $A(\beta) = |R_{ssn}(\beta)|$, the variance becomes:

$$\sigma^2(S_{ssn}(f)) \approx \frac{1}{2\pi^2\beta^2}\left[1 - \frac{A(\beta)}{A(0)}\right] = \frac{1}{2\pi^2\beta^2}\left[1 - \frac{|R_{ssn}(\beta)|}{R_{ssn}(0)}\right] \tag{4.53}$$

$$\boxed{\hat{\sigma}^2(\hat{S}_{ssn}(f)) \approx \frac{1}{2\pi^2\beta^2}\left[1 - \frac{|R_{qqn}(\beta) - R_{NNn}(\beta)|}{R_{qqn}(0) - R_{NNn}(0)}\right]} \tag{4.54}$$

Miller and Rochwarger [12] found that the estimates of the mean and variance were biased due to estimating the slope of the phase at small lag. They give the following equations for the mean and variance of the Doppler shift estimate:

$$\text{mean}(\hat{f}_d) = \frac{\phi_s(\beta)}{\beta} - \frac{A^2(\beta)\sin 4\pi[\phi(\beta) - \phi_s(\beta)]}{4N\pi\beta A_s^2(\beta)} + O(N^{-2}) \qquad (4.55)$$

$$\text{var}(\hat{f}_d) = \frac{A^2(0) - A^2(\beta)\cos 4\pi[\phi(\beta) - \phi_s(\beta)]}{8N\pi^2\beta^2 A_s^2(\beta)} + O(N^{-2}) \qquad (4.56)$$

where ϕ_s and A_s are the phase and amplitude of the autocovariance of the return signal, s_{bb}. Even if there was no noise, so that $\phi_s(\beta) = \phi(\beta)$, the mean of the Doppler estimate would only be unbiased if the Doppler shift spectrum was symmetric so that $\phi_s(\beta)$ would be a liner function.

The error variance can be reduced by averaging, and by increasing the lag, β. However, increasing the lag will be shown to affect spatial resolution.

4.5.4 Calculating the Doppler Shift and Velocity Estimates

An estimate of the covariance at small lag is needed in order to make an estimate of the Doppler shift, and there are various ways of obtaining it. This section will present practical ways to obtain the estimates of the covariance using different averaging strategies.

In calculating the covariance, both time averaging within a pulse (or ping) and ensemble averaging (between pings) can be employed. Both types of averaging are interchangeable when a process is ergodic, as is assumed to be the case with the ocean environment (over proper time intervals). For a given lag, β, the covariance within a ping can be calculated using time averaging. Alternately, picking the same point in time after the start of each ping, and the same second point at an added time of β, the covariance for those two points in time can be calculated using ensemble averaging. Once either time averaging or ensemble averaging has been employed, the other method may be employed for further averaging.

The velocity is calculated using an estimate of the Doppler shift, which in turn

depends on the estimate of the covariance. Therefore, the order in which time averaging, ensemble averaging, and velocity calculations are done can lead to slightly different estimates of the velocity. Hansen [7] presents three iterations of this process for calculating the covariance and velocity.

The following notation will be used with the next few equations:

$\hat{R}_i$ = the estimate of the covariance from the ith ping

tm = the time that places the echo response at the center of the chosen bin

β = the time lag

L = the bin size

k = index that spans the length of one bin

f_s = sampling frequency

q_i = the received signal from the ith ping

$\hat{V}_N$ = the velocity estimate after averaging over N pings

N = number of pings to average over

c = speed of sound in water

$\hat{f}_{di}$ = estimate of the Doppler shift frequency from the ith ping

f = the transmit frequency

In one method, the covariance is calculated by averaging within a bin, then computing the Doppler estimate, and finally averaging over pings.

$$
\begin{aligned}
\hat{R}_i(tm + \beta, tm) &= \tfrac{1}{L+1} \sum_{k=-\frac{L}{2}}^{\frac{L}{2}} q_i(tm + \tfrac{k}{f_s} + \beta) q *_i \left(tm + \tfrac{k}{f_s}\right) \\
\hat{V}_N(tm) &= \sum_{i=1}^{N} \tfrac{c\hat{f}_{di}(tm)}{2f}
\end{aligned}
\tag{4.57}
$$

Using another method, the Doppler estimate is calculated after averaging both within a bin and over pings, and then the velocity estimate is computed.

$$
\begin{aligned}
\hat{R}_i(tm + \beta, tm) &= \tfrac{1}{L+1} \sum_{k=-\frac{L}{2}}^{\frac{L}{2}} \left[\tfrac{1}{N} \sum_{i=1}^{N} q_i(tm + \tfrac{k}{f_s} + \beta) q *_i \left(tm + \tfrac{k}{f_s}\right) \right] \\
\hat{V}_N(tm) &= \tfrac{c\hat{f}_{di}(tm)}{2f}
\end{aligned}
\tag{4.58}
$$

Cell 3

Cell 2

Cell 1

Center of
depth cell

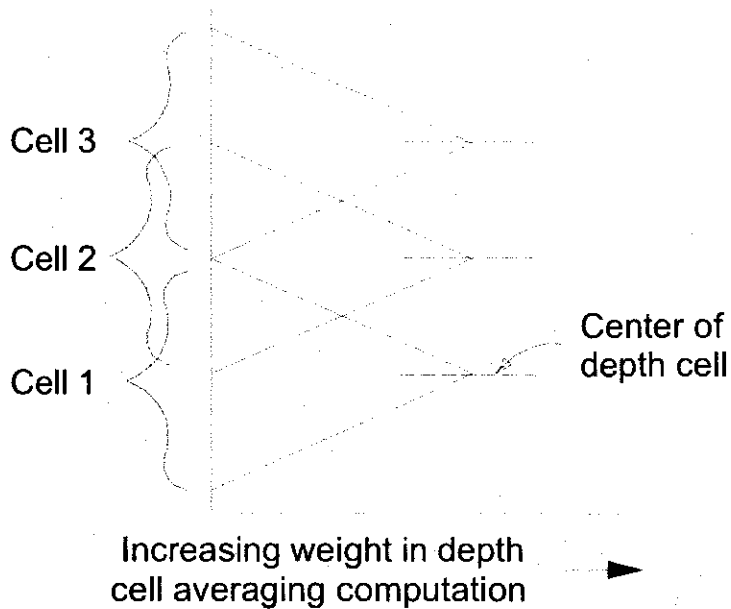Increasing weight in depth
cell averaging computation ▶

Figure 4-4: Time averaging leads to a triangle weighting function. The graphic is used with permission from RDI. [9]

In the final method, the covariance is calculated after averaging over pings, then the Doppler estimate is computed, and then averaged within a bin to form the velocity estimate.

$$
\begin{aligned}
\hat{R}_i(tm + \beta, tm) &= \frac{1}{N} \sum_{i=1}^{N} q_i(tm + \beta) q *_i (tm) \\
\hat{V}_N(tm) &= \frac{1}{L+1} \sum_{k=-\frac{L}{2}}^{\frac{L}{2}} \frac{c\hat{f}_{di}(tm+\frac{k}{f_s})}{2f}
\end{aligned}
\tag{4.59}
$$

By averaging over a portion of the received signal, echos from a certain range get a larger weighting than echos from nearby ranges. This center location defines the center of a range bin. The size of the bin itself depends on the averaging time, which is typically equal to the pulse duration, τ_p. When the segments of the signal that are being averaged are sequential in time, a portion of each time averaged signal overlaps in range with the two adjacent segments. The bin length is then $L = (1/2)c\tau_p$. Since velocity is determined by the covariance function, a small overlap in space will contribute to the correlation of velocity estimates between range bins.

4.5.5 Lower Bound on the Variance of the Doppler Shift Estimate

Theriaut [22] uses a common estimation theory tool to estimate the lowest possible value of the variance of the Doppler shift estimate. The Cramer-Rao Lower bound can be used for any unbiased estimation algorithm, and is calculated from the Fisher Information Matrix. Theriault found the variance proportional to $1/\tau_p^2$, and therefore the velocity resolution (or standard deviation) proportional to $1/\tau_p$. This makes sense, for longer pulse durations allow for reduction of noise through averaging. However, there is a trade-off between reducing the velocity variance with longer pulse durations, and losing range resolution due to larger volumes of ensonified water. It will be shown in section 4.7, that the range resolution– velocity resolution product is approximately constant for a given system, and so a trade-off will exist. Equivalently, the time–bandwidth product of a system is fixed, so decreasing one increases the other, leading to losses in resolution.

4.6 ADCP Pulse Transmission

The same ADCP can be designed to transmit signals in a number of different ways (see figure 4-5), and each method has strengths and weaknesses based on its intended purpose. Some important factors to consider are the range, spatial resolution, maximum water velocities, and velocity resolution. The ADCP is named based on its chosen style of pulse transmission. In the next half of this chapter, each type of ADCP will be examined to see the broadband ADCP will work and the Incoherent and Pulse-Coherent ADCP's will fail to meet the stated measurement goals.

ADCP Pulse Transmission
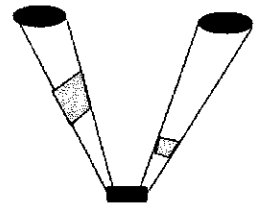
Pulse Duration	- Spatial Resolution
Pulse Separation	- Max Range
Frequency, Coding	- Energy/Range
*Time Lag	- Velocity Res. / Max Velocity

Narrowband (Incoherent)   20 ms   0.1 - 0.4 s   300 kHz

Pulse-to-Pulse Coherent   20 ms   20 ms   600 kHz   10 μs

Broadband (Coded Pulses)   20 ms   0.04 - 0.4 s   600 kHz   10 μs
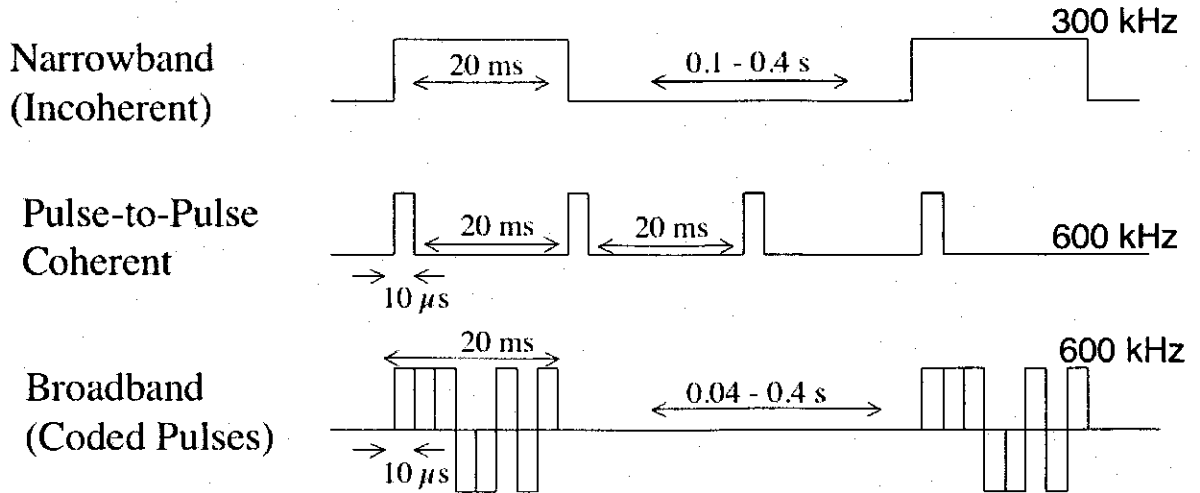
Figure 4-5: Operation modes of an ADCP are based on signal transmission.

4.7 The Incoherent ADCP

The Incoherent ADCP sends out a sound pulse of duration τ_p from four transducers arranged in a Janus configuration. The transducers are usually slanted about 20-30 degrees from the vertical, and the sound emmited is in the form of a narrow beam. As the sound travels through the water, scatterers reflect it back to the transducers, which then become receivers. As scatterers are pretty much uniformly distributed, there is an almost instant continuous receiving of echoed sound. Before recording the received signal, there needs to be a gap in time after the transmitted pulse leaves to allow the instrument to stop ringing (from high intensity sound immediately reflected right around the transducer). Before the next ping of sound can be sent, the first ping needs to reach the surface and have returned. The pings are incoherent from one to the next, and hence its name.
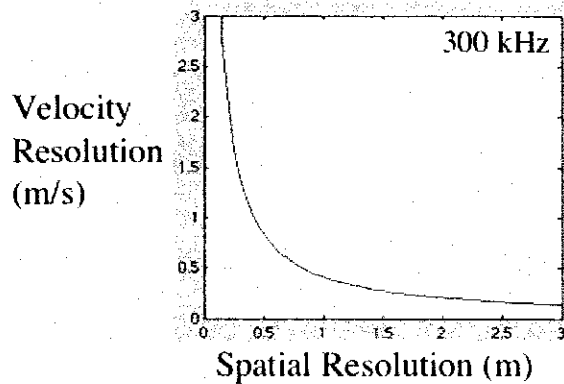
⌐⌐_⌐⌐ Narrowband ADCP Problem:

Velocity Resolution ⟷ Spatial Resolution Trade-Off

$$\Delta v \sim \left(\frac{c}{2f_i}\right)\frac{1}{2\pi \text{ß}} \qquad\qquad \Delta r = \frac{1}{2}ct_p$$

lag time (ß)
≤ pulse duration (t$_p$)

(Δv is the std. dev. of estimate, Δr is the range of contributing echos per estimate)

Velocity Resolution (m/s) — 300 kHz — Spatial Resolution (m)

Conclusion: NB ADCP can't meet set criteria of 0.2 cm/s velocity std. dev. __AND__ 11 cm spatial res.

Figure 4-6: The NBADCP can't resolve both range and velocity at the same time.

As discussed earlier, the longer the transmit pulse, the more accurate the spectral resolution. However, this leads to a trade off in spatial resolution. Averaging over τ_p covers a distance of $c\tau_p$, which is defined as twice the bin size. Individual velocities within this range are lost to the mean velocity in that range.

The standard deviation of the velocity is proportional to the standard deviation of the Doppler shift frequency. Using the terminology previously described:

$$\hat{v} = \left(\frac{c}{2f}\right)\hat{f}_d \qquad \longrightarrow \qquad \sigma_v = \left(\frac{c}{2f}\right)\sigma_{f_d} \qquad\qquad (4.60)$$

The Doppler shift variance lower bound, coupled with the bin size range, imposes the Range-Resolution ⟷ Velocity Error trade off, or equivalently, the Time-Bandwidth trade-off. Figure 4-8 includes a plot illustrating that trade-off.

$$\text{Range Resolution} \qquad \longleftrightarrow \qquad \text{Variance Lower bound} \qquad (4.61)$$

$$L = \frac{1}{2}c\tau_p \qquad \longleftrightarrow \qquad \sigma_{f_d}^2 \sim \frac{1}{\tau_p^2} \qquad (4.62)$$

$$L = \frac{1}{2}c\tau_p \quad \longrightarrow \quad L \sim \frac{1}{2}c\left(\frac{1}{\sigma_{f_d}}\right) \quad \longrightarrow \quad L \sim \frac{1}{2}c\left(\frac{c}{2f\sigma_v}\right) \qquad (4.63)$$

$$\boxed{L\sigma_v \sim \frac{c^2}{4f}} \qquad (4.64)$$

Brumley et. al. [4] report a commonly used constant of proportionality as follows:

$$L\sigma_v = \left(\frac{1.4}{8\pi}\right)\frac{c^2}{f} \qquad (4.65)$$

Pinkel and Smith [18] present a functional form of Theriault's [22] lower bound on the velocity variance estimate that has a dependency on the number of pings.

$$\sigma_v = \left(\frac{c}{2f}\right)\sigma_{f_d} \quad \longrightarrow \quad \sigma_v \sim \left(\frac{c}{2f}\right)\left(\frac{1}{\tau_p}\right) \quad \longrightarrow \quad \tau_p\sigma_v \sim \left(\frac{c}{2f}\right) \qquad (4.66)$$

$$\sqrt{N}\tau_p\sigma_v = \frac{c}{4\pi f} \qquad (4.67)$$

Averaging over a large number of pings has the advantage of lowering the velocity variance, but decreasing temporal resolution. The following tables illustrate the trade-offs. (Ping rate is 2 Hz)

Temporal Resolution Problem

N Pings	Experiment Duration
1	0.5 sec
100	50 sec
1000	8 min 20 sec
10,000	1 hr 23 min 20 sec

Range Resolution Problem

Pulse Duration	Bin Length (L)
0.2 ms	15 cm
2 ms	1.5 m
10 ms	7.5 m
20 ms	15 m

The velocity variance problem is illustrated in these tables of standard deviation of velocity. N is number of pings, and L is bin length.

f = 300 kHz, $\sigma_v(cm/s)$

N \ L	15cm	1.5m	7.5m	15m
1	279	28	6	2.8
100	28	2.8	0.56	0.28
1000	9	0.88	0.18	0.09
10,000	2.8	0.28	0.06	0.03

f = 1200 kHz, $\sigma_v(cm/s)$

| N \ L	15cm	1.5m	7.5m	15m
1	70	7	1.4	0.7
100	7	0.7	0.14	0.07
1000	2.2	0.2	0.04	0.02
10,000	0.7	0.07	0.01	0.01

It is clear from the tables that increasing frequency improves the velocity variance. However, in the ocean, the intensity of sound decreases with range and frequency because of spherical spreading and absorption. The transmission loss due to absorption (α) and range (r_{max}) is usually limited to 10 decibels.

$$\alpha r_{max} = 10dB \tag{4.68}$$

Very high frequency can severly limit the effective range of the NBADCP. For a 300 kHz frequency, $\alpha \approx 0.07$, giving an effective two-way range of about 140 meters. For a 1200 kHz frequency, $\alpha \approx 0.5$, giving an effective two-way range of about 20 meters. [9]
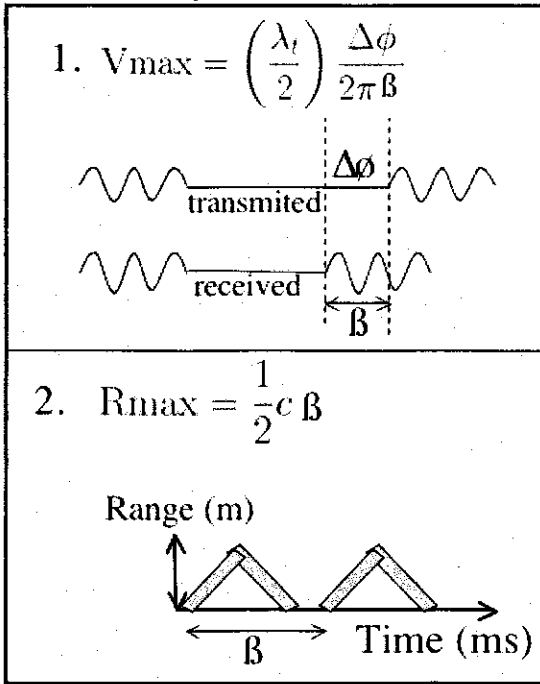
In conlcusion, the velocity resolution–range resolution trade off is a significant limitation for this type of signal transmission and processing. It takes averaging over a great number of pings to improve the velocity resolution while keeping a reasonable range resolution, but then the sacrifice is temporal resolution. Finally, trying to increase the frequency to improve resolution limits the ultimate range of sound transmission. A different method is needed to meet the stated goals, and the next operating mode of the ADCP to is the pulse-to-pulse coherent mode.
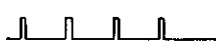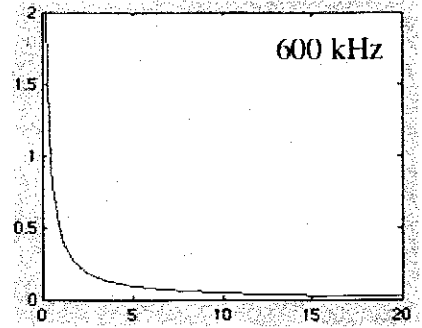
Maximum Velocity ⟷ Maximum Range Trade-Off

Extending lag time (ß) limits:

1. $V\text{max} = \left(\dfrac{\lambda_t}{2}\right)\dfrac{\Delta\phi}{2\pi\beta}$

transmited

$\Delta\phi$

received

ß

2. $R\text{max} = \dfrac{1}{2}c\,\beta$

Range (m)

ß Time (ms)

600 kHz

Vmax (m/s)

Rmax (m)

Conclusion:

PPC ADCP can't meet the requirements of Vmax =1.6m/s __AND__ Range =16 m

Figure 4-7: The PPC ADCP can't handle high velocities and long range at the same time, causing those particular goals to be missed.

4.8   Pulse-to-Pulse Coherent ADCP's

An alternative to measuring the Doppler shift frequency from one ping over the range of one bin is to measure the shift between two pings at the exact same location. The phase change from one pulse to the next is linearly related to the velocity of the scatterer.

$$v = \frac{c\phi(\phi)}{4\pi f\beta}, \qquad \phi(\phi) \in [-\pi, \pi] \tag{4.69}$$

To see how this arises, examine the covariance of those two points.

$$
\begin{aligned}
E[s_{ret}(R_{c1},t)s^*_{ret}(R_{c2},t)] &= E[e^{j2\pi((2R_{c1}/c)-t)f''}G(R_{c1},t)e^{j\alpha(R_{c1},t)} \\
&\quad\text{x}\quad e^{-j2\pi((2R_{c2}/c)-t)f''}G(R_{c2},t)e^{-j\alpha(R_{c2},t)}] \tag{4.70} \\
&= E[G(R_{c1},t)G(R_{c2},t)]E[e^{j\Delta\alpha}]e^{j2\pi f''(2\Delta R/c)}
\end{aligned}
$$

Considering the highly fluctuating portion of the phase, $\Delta\alpha$, to be a zero mean Gaussian random variable, then

$$E[e^{j\Delta\alpha}] = e^{-\frac{1}{2}E[(\Delta\alpha)^2]} = e^{-\frac{1}{2}\mathrm{var}(\Delta\alpha)}. \tag{4.71}$$

The change in location of the centroid, ΔR, is due to the average motion of the scatterers, and can be written

$$\Delta R = v\beta, \tag{4.72}$$

where v is the average velocity of the scatterers and β is the time between pings. The covariance between pings is

$$E[s_{ret}(R_{c1}, t)s_{ret}^*(R_{c2}, t)] = (Ae^{-\frac{1}{2}\mathrm{var}(\Delta\alpha)})e^{j2\pi f''(2v\beta/c)} \tag{4.73}$$

Setting the phase change, $\phi(\beta)$, equal to the phase of the covariance, noting that $f \approx f''$ in the denominator, and solving for v, equation 4.69 is obtained.

The spatial resolution is vastly improved since the covariance will be independent of range. The time lag β is forced to be the ping rate. This leads to the problem of aliasing. Before there was a continuous range to choose β to assure propper resolution, but in this case it is possible for the velocity of the scatterers to be faster than the pulse rate is able to resolve. To avoid aliasing, $|\phi(\beta)| \leq \pi$.

Remembering that $\beta = 1/f_s$ (sampling frequency):

$$v \leq \frac{c\pi}{4\pi f\beta} \qquad \longrightarrow \qquad v \leq \frac{cf_s}{4f} \qquad \longrightarrow \qquad \frac{4fv}{c} \leq f_s \tag{4.74}$$

Plugging in the Doppler shift frequency relationship:

$$f_s \geq \frac{4f\left(\frac{f_d c}{2f}\right)}{c} \qquad \longrightarrow \qquad \boxed{f_s \geq 2f_d} \tag{4.75}$$

This is the Nyquist sampling rate. Rearranging slightly:

$$\beta \leq \frac{c}{4fv}, \qquad \beta v_{max} \leq \frac{c}{4f} \tag{4.76}$$

The following table looks at sampling frequencies needed to measure some potential current (scatterer) velocities. High transmit frequencies have short wavelengths, and therefore need very fast sampling rates.

v_{max}	f_s(min.) for f = 150kHz	f_s(min.) for f = 300kHz	f_s(min.) for f = 600kHz
10 cm/s	40 Hz	80 Hz	160 Hz
50 cm/s	200 Hz	400 Hz	800 Hz
1 m/s	400 Hz	800 Hz	1600 Hz
2 m/s	800 Hz	1600 Hz	3200 Hz
5 m/s	2000 Hz	4000 Hz	8000 Hz

The second major limitation is the range dependency on f_s. One pulse must go out and return before the second pulse is emmited, so the range is limited.

$$r_{max} = \frac{1}{2}c\beta \qquad \longrightarrow \qquad \frac{2r_{max}}{c} = (\beta) \qquad \longrightarrow \qquad \frac{2r_{max}}{c} \leq \frac{c}{4fv_{max}} \qquad (4.77)$$

$$\boxed{r_{max}v_{max} \leq \frac{c^2}{8f}} \qquad (4.78)$$

The following table illustrates this Range $\longleftrightarrow$ Velocity trade-off (and figure 4-7 illustrates it graphically).

v_{max}	r_{max} for f = 150kHz	r_{max} for f = 300kHz	r_{max} for f = 600kHz
10 cm/s	18.75m	9.38m	4.69m
50 cm/s	3.75m	1.88m	0.93m
1 m/s	1.87m	0.93m	0.47m
2 m/s	0.94m	0.47m	0.24m
5 m/s	0.38m	0.19m	0.09m

Brumley et al. [4] relate Zrnic's (1977) finding of the standard deviation of the velocity estimate:

$$\sigma_v = \left(\frac{c}{2f}\right)\sigma_{f_d} = \frac{cB}{f\sqrt[4]{\pi}\sqrt{N\beta B}} \qquad (4.79)$$

Here B is the Doppler bandwidth, determined solely by the ocean enviroment and scatterer effects, not the pulse length τ_p. $N\beta$ is called the observation time, and $1/(2\pi B)$ is called the decorrelation time. The above equation is true for large Signal to Noise ratios and decorrelation time $> \beta$. Therefore, the decorrelation time sets a limit to how large β can be, which in turn limits the ultimate range of the transmission. However, it is clear that increased observation time is possible, leading to greatly reduced velocity variances.

In conclusion, the PPC ADCP offers greatly improved spatial resolution because pulses can be kept short, since estimates are not formed within a pulse but between coherent pulses. The lag time is increased, reducing the velocity variance, so the overall time-bandwidth product is decreased. Measuring phase changes between coherent pings is has the drawback of sampling the process in time, and to avoid aliasing of velocity measurements, the Nyquist rate must be met. Therefore maximum velocity measurements determine how short the ping interval must be, but this can severely limit the range of the beam (since ping to ping interference must be avoided). Again, the PPC ADCP faults on some of the stated goals, and so the final option is to consider the Broadband ADCP.

Range now independent of ß.
Instead, depends on freq. & energy issues.

Range (m)

Lag time (ß):
velocity res., max velocity

Short pulse duration (t_p):
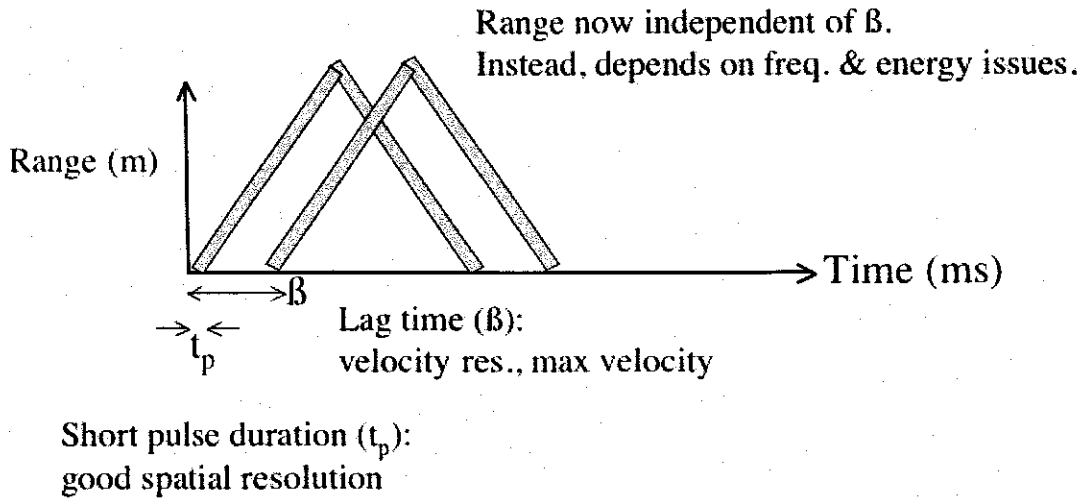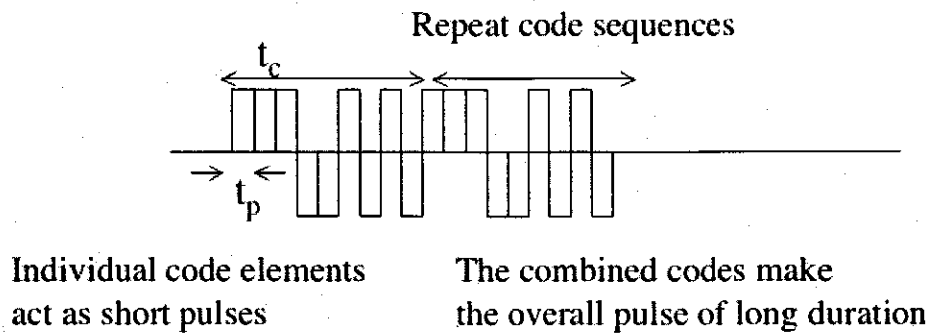good spatial resolution

Time (ms)

Figure 4-8: The Broadband ADCP sends two overlapping pulses.

4.9 Broadband Acoustic Doppler Current Profilers

To gain the range while avoiding aliasing, the BBADCP's send two pulses within a very short time of each other. Since β is small (or f_s is large), aliasing does not occur. The two pulses travel any desired range (within acceptable transmission losses), and the spatial resolution is extremely accurate because the same location is compared at each pulse (see figure 4-8). The drawback is that the received signal is a combination of both pulses, and the phase still needs to be recovered. This is solved by taking the autocovariance of the received signal. Since the two transmitted pulses are identical but separated by a time lag, then looking at the autocovariance at that time lag should reveal any phase change. The phase change at β is linearly proportional to the scatterer's velocity.

Pulse Coding - to handle energy issues

Repeat code sequences

Individual code elements
act as short pulses

The combined codes make
the overall pulse of long duration

Barker Codes are designed to have autocorrelation side-lobes at set time lags and to be zero elsewhere.
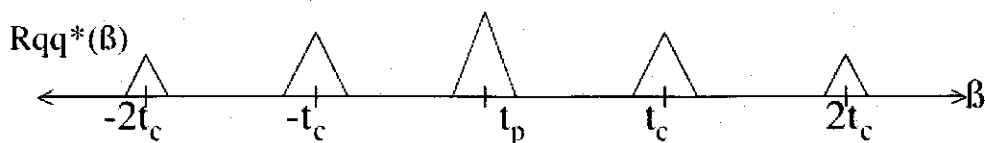

Figure 4-9: Phase coding can reduce the variance of the velocity estimate.

Brumely et al. [4] relate how BBADCP's are peak power limited do to cavitation and shock. If the pulse length is too short, the intensity will not be large enough to provide information over the desired range. This is solved by using Bi-Phase coding. It is as if many independent pulses are joined together to create one long pulse. The combined pulse length is increased enough in order to acheive sufficient transmission energy, yet the bandwidth is almost as wide as that produced by one of the independent pulses.

Phase Coding

Pinkel and Smith [18], and Trevorrow and Farmer [24], worked on coding the transmitted signal in a manner which could reduce the variance of the velocity estimates upon decoding. The Barker Codes are designed to minimize the covariance, except at desired time lags (see figure 11-2). This is accomplished by selecting special sequences of 1's and 0's, or 1's and -1's, and then repeating the sequence until the code duration is equal to the pulse length. These sequences change the phase on the transmit signal.

89

To construct the complete coded pulse, the basic signal (see equation 4.16) is multiplied by a series of subcodes, z_m. The pulse duration of that individual subcode, τ_c, is shortened to reach the desired bandwidth. Letting b_m represent the complex return signal for one subcode, $s_{ret}(R_c, t)$ (equation 4.21), at a particular instant of time, t, the complete pulse will be a sum of these subcoded pulses.

$$s_{coded}(t) = \sum_{m=1}^{N_c N_r} z_m b_m, \tag{4.80}$$

where N_c is the number of subcode elements in a combined sequence, and N_r is the number of times the sequence is repeated. The total transmission time is then $\tau_c N_c N_r$. The return coded signal at some time later, $t + n\xi$, has an additional phase shift based on the extra travel time,

$$s_{coded}(t + n\xi) = e^{j2\pi f'' n\xi} \sum_{m=1}^{N_c N_r} z_m b_{m+n}. \tag{4.81}$$

The autocovariance of the return coded signal is

$$s_{coded}^*(t) s_{coded}(t + n\xi) = e^{j2\pi f'' n\xi} \sum_{l=1}^{N_c N_r} \sum_{m=1}^{N_c N_r} z_l^* z_m b_l^* b_{m+n} \tag{4.82}$$

When the return signals are spatially homogeneous (due to an even distribution of scatterers and their similar types of scatterering returns), the average intensity of the return signal is fairly uniform, $b = <|b_m|>$. The expected value of the autocovariance is basically zero at any lag other than $n\tau_c N_c$,

$$\begin{aligned} <s_{coded}^*(t) s_{coded}(t + n\xi)> \quad &= b e^{j2\pi f'' n\xi} \sum_{m=1}^{N_c N_r} z_m^* z_{m+n} \\ &\approx \begin{cases} b\tau_c(N_c - n)e^{j2\pi f'' n\tau_c N_c} &, \xi = \tau_c N_c \\ 0 &, \text{otherwise} \end{cases} \end{aligned} \tag{4.83}$$

Equations (4.80),(4.81),(4.82),and (4.83) are equations (3a),(3b),(4) and (5) from Pinkel and Smith [18], with notation changed for this thesis. The variance for a single estimate is larger than the signal itself, but the variance can be significantly

reduced by range averaging. This occurs because the error in nearby estimates are uncorrelated due to the coding, and averaging over a range (up to that specified by the transmission length) gives N_c independent estimates. They give the following equation for the variance on the velocity estimate: [18]

$$\sigma_v^2 = \left(\frac{c}{4\pi f}\right)^2 \frac{1}{N_c T_{ovl} T_{avg}} \left(1 + \frac{T_{avg}}{2T_{ovl}}\right), \qquad (4.84)$$

where $T_{ovl} = (N_r - 1)\tau_c N_c$ is the portion of the range that overlaps in the covariance function, and T_{avg} is the time length of averaging, generally up to the duration of the transmitted pulse, $\tau_c N_c N_r$.

Brumley et al [4] present the standard deviation of the velocity estimate in a form which explicity shows how various parameters may be adjusted to reach the desired velocity resolution.

$$\sigma_v = \frac{\sigma_\phi v_{max}}{\pi\sqrt{MN}}, \qquad (4.85)$$

where ≈ 1.5 is a constant which accounts for nonideal aspects of the code and signal processing, M is the number of code elements incorporated in the averaging, N is the number of pings, σ_ϕ is the standard deviation of the phase estimate, and where v_{max} is set to avoid the unambiguous velocity,

$$v_{max} = \frac{1}{4}\left(\frac{\lambda}{T_o}\right). \qquad (4.86)$$

λ is the wavelength of the transmitted signal ($\lambda = c/f$), and T_o is the pulse separation lag, generally equal to $\tau_c N_c$. RD Instruments [10] give the variance of the phase estimate as

$$\sigma_\phi^2 = \frac{1}{2}\left(\frac{1}{R^2} - 1\right), \qquad (4.87)$$

where R is the correlation at lag T_o.

The larger the number of code elements, the greater the velocity resolution, but the smaller the maximum velocity it can measure. Averaging over a number of pings improves velocity resolution, but decreases temporal resolution.

91

4.10   Error variance management

For the pulse coherent ADCP and for the broadband ADCP, the Doppler bandwidth is no longer dependent on the pulse duration, as was the case for the narrowband ADCP. Instead, it is determined by a number of physical processes in the ocean environment, and causes the transmit wavelength - Doppler Bandwidth (λB) product to stay within a small range of values. [4]

One source of noise results from the accelerations of the fluid. The estimate of the Doppler shift is approximated as a linear function, and deviations from this will be noise.

Brumley et al. [4] say that the two most dominant sources of noise are the turbulent velocity fluctuations and the effects of beam divergence. In general, λB is proportional to the larger of either the rms turbulent velocity fluctuations or the cross-beam velocity component multiplied by the beam width in radians. For a current of 2 m/s, and a beam spread of 2 degrees (0.035 rad), that would lead to $\lambda B \approx 7$ cm/s, whereas the turbulent velocity fluctuations are about 2 cm/s. For a broadband ADCP, transmitting at 1200 kHz carrier frequency, that would indicate that $B = (\lambda B)/(c/f) = 0.067 * 1200000/1500 \approx 54$ Hz, and the decorrelation time $1/(2\pi B) \approx 3.0$ ms. Slower cross beam velocities will increase the decorrelation time, setting the lower bound on error independence. For cross beam velocities of only 10 cm/s (typical velocities seen closer to the ocean floor), the decorrelation time will be 20 times larger, ≈ 60 ms. This is still under the desired 10 Hz sampling frequency, and indicates that the error variance for typical flows will be independent in time.

Another source of noise is from the change of scatterers in the volume of water being measured. Scatterers near the boundaries of the fluid volume move out and new ones move in, adding to the phase jitter. Physically, in order to make an accurate estimate of the velocity, the scatters need to be present at both measuring times.

To determine the lower bound on spatial resolution, it is necessary to find the spatial decorrelation length. Since the broadband transmission signal consists of a series of repeated codes, each of which is a sequence of subcodes, their respective

ensonified volumes of water are grouped accordingly. The codes are designed to suppress the covariance of the return signal at any time lag other than a multiple of the duration of one complete sequence. This allows range averaging to provide a series of independent estimates of the covariance.

The covariance estimate, even at the proper time lag, is still affected by noise. In addition to the physical sources of noise just mentioned, there is the added noise of unwanted volumes of water. This occurs because comparing the signal to itself at a time lag will automatically cause certain volumes of water to fall out of the overlapped region. This is essentially the same problem as scatterers moving out of the volume, and new ones moving in, except now it is entire volumes of water that change during the comparrison. It is these volumes of water which will be correlated with the error of other estimates.

Pinkel and Smith [18] provide a relationship for the correlated part of the sampling error in one estimate of the covariance.

$$e_i(\beta = \tau_c N_c) = \frac{1}{2}(< \hat{R}_i(0) > -(< \hat{R}_i(\beta) > -(< \hat{R}_i(-\beta) >) \qquad (4.88)$$

where $\hat{R}_i(\beta)$ is the estimate of the covariance (see equations 4.57, 4.58, 4.59). This is what leads to the variance in the phase estimate. They do not provide a relationship for correlating the error between estimates. Therefore, it will be useful to appeal to the physical situation for guidance.

As shown in figure 4-4, range averaging leads to the center volumes of water being weighted more heavily than volumes near the end of the bin range. The error contribution from these edge volumes have a limited effect on the total error in the covariance estimate.

To be safe in setting the upper bound of the error correlation length, it will be assumed that there is perfect correlation of the error in volumes that overlap from one covariance estimate to the next. However, they should be weighted in proportion to each of their contributions to the total error of their respective estimates. Then

one potential relationship for error correlation is

$$
\begin{aligned}
R_{e_1 e_2}(r) &= \frac{\text{overlap area (of triangular weight function)}}{\text{non-overlap area (of triangular weight function)}} \\
&= \frac{\frac{1}{2}(c\tau_p - r)\left(\frac{(c\tau_p - r)}{c\tau_p}\right)}{\frac{1}{2}(c\tau_p)(1)} \\
&= \left(1 - \frac{r}{c\tau_p}\right)^2
\end{aligned}
\tag{4.89}
$$

where r is the spatial lag, c is the speed of sound in water, and τ_p is the duration of the transmitted pulse. This is valid for $r \le c\tau_p$, and $R_{e_1 e_2}(r) = 0$ for $r > c\tau_p$. If the volumes of water used to formulate each covariance estimate are completely different, there can be no error correlation. Therefore, for $r > c\tau_p$ the resulting error variances are independent.

The working model of the space-time correlations for the error variance will be

$$
R_{ij}(\vec{r}, \tau) = \begin{cases}
0, & r > c\tau_p, \ \tau > (2\pi B)^{-1} \\
\left(1 - \frac{r}{c\tau_p}\right)^2 \delta_{ij} & r \le c\tau_p, \ \tau > (2\pi B)^{-1} \\
\text{undetermined} & r \le c\tau_p, \ 0 < \tau \le (2\pi B)^{-1} \\
\delta_{ij} & r = 0, \ \tau = 0
\end{cases}
\tag{4.90}
$$

where $r = |\vec{r}|$, and the δ_{ij} is the chronecker delta function, which is appropriate for error which is isotropic in nature.

Now it is possible to recast the formulas for error variance in terms of the user chosen parameters of frequency, f, and bin length, Δr. It will be assumed that the ADCP will then maximize the other parameters, such as the number of code elements, M, the unambiguous velocity, v_{max}, and the wavelength-bandwidth product.

The decorrelation time $(2\pi B)^{-1} \gg \beta$ can be used to set an upper limit on β.

$$
\beta_{max} = \frac{1}{10(2\pi B)}
\tag{4.91}
$$

The unambiguous velocity becomes

$$
\begin{aligned}
v_{max} &= \tfrac{1}{4}\left(\frac{\lambda}{\beta_{max}}\right) \\
&= \tfrac{1}{4}(\lambda)(10)(2\pi B).
\end{aligned}
\tag{4.92}
$$

The bin length can be used to maximize the number of code elements,

$$
M = \frac{\Delta r}{c\tau_c},
\tag{4.93}
$$

where RDI sets $\tau_c = 4/f$ for their ADCPs. M will be a bit generous, but it can be compensated for by setting the phase variance a bit high. With correlation R=0.5 at lag β_{max}, the $\sigma_\phi^2 = 1.5$.

Combining the above, the single ping standard deviation is

$$
\sigma_v = (10)\frac{(1.5)^{3/2}(\lambda B)\sqrt{c}}{\sqrt{\Delta r f}}.
\tag{4.94}
$$

The standard deviation of the error varinace can be reduced through averaging in time in proportion to $N^{-1/2}$. Therefore, using the estimates in figure 4-10, when the the $\lambda B \approx 6 \ cm/s$, the standard deviation is 12 cm/s, and the error variance at the 10cm bin interval can be reduced to 0.07 $(cm/s)^2$ after 2400 pings (20 minutes at 2 Hz). However, as figure 4-10 also shows, an increased λB product (due to a more energetic ocean environment) leads to an increase in the standard deviation, and so for $\lambda B > 6 \ cm/s$, a greater number of samples are needed to reduce it to acceptable levels. Sampling at 10 Hz, a 20 minute period would allow for 12000 samples, causing the error variance for the $\lambda B = 12 \ cm/s$ to be reduced to 0.05 $(cm/s)^2$. Again, the stated goals should be acheived.
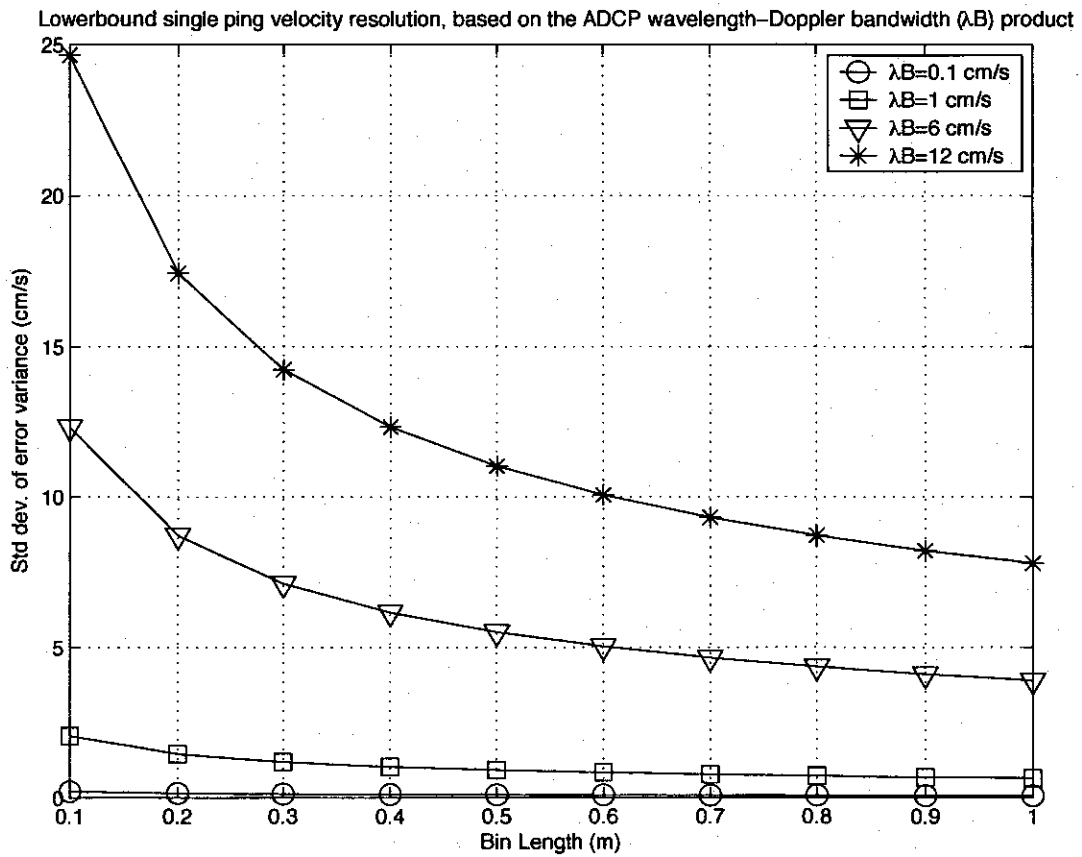
Figure 4-10: The single ping standard deviation based on the user choices of bin length, the ocean evironment wavelength-Doppler bandwidth product λB, and assuming a transmit frequency of 1200 kHz.

Chapter 5

Simulating a Spatially Homogeneous, Isotropic, Turbulent Field

Many applications require the simulation of an idealized environment in order to set preliminary bounds on the performance of the system of interest. Traditional numerical schemes which propagate the numerical solution of the governing equations of fluid can require large amounts of memory and processing time.

An alternative is to utilize the average quantities of the flow, meaning a statistical characterization of the flow is considered appropriate. In this case, methods in signal processing may be employed to take advantage of the statistical properties, and to generate flows which are governed by the statistics.

To reduce computational requirements, the flow will be simulated in two steps. The first step will be to freeze time and create a spatial turbulent field. This can be accomplished by passing white noise through a set of filters which are designed match the 2nd order statistics of the output to those of the turbulent process. The 3-D least squares filters can be designed using an analytic expression for the spectrum of homogenous, isotropic turbulence. The second step will be to simulate the time evolution of the flow. This will be explored in the next chapter, and will make use of Taylor's frozen turbulence hypothesis.

5.1 Chapter Overview

In the second section, the analytic expression for the turbulent spectrum will be derived from first principles. In the third section, basic theory for generating processes of particular statistics will be given. In addition, there will be discussion on sampling in space and wavenumber domain, the use of Cholesky decomposition for numerical stability, and the choice of least squares for the construction of a 3-D spatial filter. In the fourth section, results from a statistically generated flow will be presented, along with methods for verifying the statistics. Finally, the space-time correlations will be developed for turbulence induced velocities being advected by the mean current.

5.2 Analytic Expression for the Spectrum of Homogeneous, Isotropic Turbulence

The derivation of an analytic expression for the spectrum of homogeneous, isotropic, turbulence is borrowed from Batchelor [1], and is presented here in skeleton form for completeness.

5.2.1 Homogeneous, Isotropic, Turbulence

As a starting point, the fluid flow must be constrained a bit in order to make the problem of simulation tractable. The flow we will be considering is one in which the fluid is of infinite dimension, with density ρ, and viscosity μ. By requiring the flow to be homogeneous, the average properties of the flow are independent of location. This kind of flow does not really exist, although in some situations, such as a uniform stream passing through a mesh grid, the downstream motions can be approximately homogeneous. [1] Secondly, the flow will be isotropic, which means it is independent of the direction of the axes of reference.

98

5.2.2 Governing Equations

In an incompressible fluid, the conservation of mass leads to

$$\frac{\partial u_i}{\partial x_i} = 0 \qquad (5.1)$$

where repeated indices imply summation, and the velocity component u_i is the instantaneous velocity at time t and location $\vec{x}$. The mean component has been removed, and by definition, the mean of the fluctuations is also zero,

$$\overline{u_i'(\vec{x}, t)} = 0. \qquad (5.2)$$

The fluid flow also satisfies the Reynolds Averaged Navier Stokes equation

$$\frac{\partial \overline{u_i}}{\partial t} + \overline{u_j} \frac{\partial \overline{u_i}}{\partial x_j} = \frac{1}{\rho} \frac{\partial}{\partial x_j} \left[\overline{\sigma_{ij}} - \rho \overline{u_i' u_j'} \right]. \qquad (5.3)$$

Given an initial statistical state, the future state is governed by the above equations, and therefore its outcome is determined. However, in the complexity of coupled interactions, the final state will basically be independent of the intial conditions, but its statistics should still reflect the underlying probability laws of the system.

5.2.3 Velocity Correlations and the Spectrum Tensor

The main effect of a probability law is to give a relative likelihood of values that could be observed for the variables being measured. If the velocity at a point in space were measured many times over independent trials, the range and relative occurance of the values would match the probability density function for that point. This is true for every point in space-time, and every combination of points in space-time.

The mean (average) value for a single component of turbulent velocity in space-time, is given by

$$\overline{u_i(\vec{x}, t)} = \int \alpha f_{u_i}(\alpha) d\alpha, \qquad (5.4)$$

where $f_{u_i}(\alpha)$ is the probability density function for the ith component of velocity at

that single point in space and time, and where α is in the set of possible values that $u_i(\vec{x}, t)$ can take. For the vector $\mathbf{u}$, the mean is handled componentwise, so

$$\overline{\mathbf{u}} = [\,\overline{u_1(\vec{x}, t)} \quad \overline{u_2(\vec{x}, t)} \quad \overline{u_3(\vec{x}, t)}\,]. \tag{5.5}$$

The mean of a function of components at any space-time locations requires a joint probability density function, and is taken over all the possible combinations, $\alpha, ..., \beta$, that the individual components can take.

$$\overline{u_i(\vec{x}_1, t_1)...u_j(\vec{x}_N, t_N)} = \int \alpha...\beta \, f_{u_i...u_j}(\alpha, ..., \beta) \, d\alpha...d\beta \tag{5.6}$$

When the spatial field is homogeneous, the statistics depend only on the relative configuration (separation) between points, and are independent of absolute location. Letting $\vec{x}$ be any starting position, and $\vec{r} = \vec{x}_2 - \vec{x}_1$, and dropping the time dependence (assuming that both points are measured at the same time), then the correlation between these two points can be expressed as

$$\begin{aligned} E[u_i(\vec{x}_1), u_j(\vec{x}_2)] \quad &= \overline{u_i(\vec{x} + \vec{x}_1)u_j(\vec{x} + \vec{x}_2)} \\ &= \overline{u_i(\vec{x})u_j(\vec{x} + \vec{x}_2 - \vec{x}_1)} \\ &= \overline{u_i(\vec{x})u_j(\vec{x} + \vec{r})} \\ &= Rij(\vec{r}). \end{aligned} \tag{5.7}$$

The correlation of velocity fluctuations between two points in space is represented by the tensor $R(\vec{r})$, and its components are $R_{ij}(\vec{r})$.

$$\mathbf{R}(\vec{r}) = \begin{bmatrix} R_{11}(\vec{r}) & R_{12}(\vec{r}) & R_{13}(\vec{r}) \\ R_{21}(\vec{r}) & R_{22}(\vec{r}) & R_{23}(\vec{r}) \\ R_{31}(\vec{r}) & R_{32}(\vec{r}) & R_{33}(\vec{r}) \end{bmatrix} \tag{5.8}$$

Using Fourier transform relations, the components of the spectral tensor $\Phi(\vec{k})$ can be defined as

$$\Phi_{ij}(\vec{k}) = \frac{1}{(2\pi)^3} \int R_{ij}(\vec{r}) e^{-j\,\vec{k}\cdot\vec{r}} d\vec{r}, \tag{5.9}$$

100

where $\vec{k}$ is the wavenumber vector with components (k_1, k_2, k_3), and $d\vec{r} = dr_1 dr_2 dr_3$ is over the spatial directions. Batchelor uses the convention of assigning the $1/(2\pi)^3$ to the transform, rather than to its inverse transform. The inverse Fourier transform is defined as,

$$R_{ij}(\vec{r}) = \int \Phi_{ij}(\vec{k}) e^{j\vec{k}\cdot\vec{r}} d\vec{k}, \tag{5.10}$$

where $d\vec{k} = dk_1 dk_2 dk_3$. Also, the 'j' in the exponential is not indexing, but is defined as $\sqrt{-1}$.

5.2.4 Isotropic Constraints on the Spectrum Tensor

When considering an isotropic system, certain constraints are placed on any second order tensor. Since the correlation tensor (and its transform, the spectral tensor) are considered second order tensors, they too must conform to the general constraints. The resulting structure will provide a wealth of information about the nature and physical relationships of homogeneous, isotropic, turbulence, and will subsequently provide guidelines for what a simulated process should look like. The next set of steps will show the analytical formulation of the spectrum tensor, which will be used in the simulation process.

Batchelor shows that an isotropic second-order two-point tensor has the form

$$T_{ij}(\vec{k}) = A(\xi)k_i k_j + B(\xi)\delta_{ij}, \tag{5.11}$$

where k_i, k_j are the components of $\vec{k}$, $A(\xi)$ and $B(\xi)$ are scalar functions, and $\xi^2 = k_1^2 + k_2^2 + k_3^2$. Using $\partial u_j / \partial x_j = 0$, then

$$\frac{\partial R_{ij}(\vec{r})}{\partial r_j} \quad = \quad \overline{u_i(\vec{x})\frac{\partial u_j(\vec{x}+\vec{r})}{\partial x_j}} \quad = \quad 0, \tag{5.12}$$

which in spectral terms means that

$$0 = \frac{\partial \Phi_{ij}(\vec{k})}{\partial r_j} = k_j \Phi_{ij}(\vec{k}). \tag{5.13}$$

B can be solved in terms of A by applying this spectral relation to the constrained tensor form.

$$
\begin{aligned}
k_j \Phi_{ij}(\vec{k}) = k_j[A(\xi)k_i k_j + B(\xi)\delta_{ij}] &= 0 \\
k_i[A(\xi)k_i k_i + B(\xi)] &= 0 \\
k_i[A(\xi)\xi^2 + B(\xi)] &= 0 \\
B(\xi) &= -A(\xi)\xi^2
\end{aligned}
\tag{5.14}
$$

$A(\xi)$ is then defined in relation to a new function, $E(\xi)$, which is the total energy contributed from spheres of radii ξ and $\xi + d\xi$ in wavenumber space.

$$
\begin{aligned}
E(\xi) &= 4\pi\xi^2 \cdot \tfrac{1}{2}\Phi_{ii} \\
&= 4\pi\xi^2 \cdot \tfrac{1}{2}[A(\xi)k_i k_i + B(\xi)\delta_{ii}] \\
&= 4\pi\xi^2 \cdot \tfrac{1}{2}[A(\xi)\xi^2 + 3B(\xi)] \\
&= 4\pi\xi^2 \cdot \tfrac{1}{2}[-2A(\xi)\xi^2],
\end{aligned}
\tag{5.15}
$$

To see that $\Phi_{ii}(\vec{k})$ really is a valid measure of energy distributed among the wavenumbers, look at the autocorrelation at a lag of 0 meters:

$$
\int \Phi_{ii}(\vec{k})d\vec{k} \equiv R_{ii}(0) \equiv \overline{u_i(\vec{x})u_i(\vec{x})}.
\tag{5.16}
$$

Solving for $A(\xi)$ in terms of $E(\xi)$, and plugging back into the spectrum tensor equation gives the analytic spectral expression for homogeneous, isotropic turbulence.

$$
\begin{aligned}
\Phi_{ij}(\vec{k}) &= A(\xi)k_i k_j + B(\xi)\delta_{ij} \\
&= A(\xi)k_i k_j + A(\xi)\xi^2 \delta_{ij} \\
&= -A(\xi)(\xi^2 \delta_{ij} - k_i k_j)
\end{aligned}
$$

$$
\Phi_{ij}(\vec{k}) = \frac{E(\xi)}{4\pi\xi^4}(\xi^2 \delta_{ij} - k_i k_j)
\tag{5.17}
$$

Finallly, Tennekes and Lumley [21] have worked out an expression for $E(\xi)$:

$$
E(\xi) = \alpha\epsilon^{2/3}\xi^{-5/3}e^{-\frac{3}{2}\pi\beta\alpha^{1/2}(\xi l)^{-4/3}},
\tag{5.18}
$$

where $\alpha = 1.5$ is an empirically determined constant, $\beta = 0.3$ is a constant that assures $E(\xi)$ integrates to $\frac{1}{2}\overline{u_i u_i}$, l is the eddy size (3 meters can be considered reasonable), and $\epsilon = \mu^3/l$, where μ is the size of turbulent fluctuations (0.02 m/s can be considered reasonable).

5.3   Designing the Least Squares 3-D Spatial Filter

The basic way to create the spatial field will be to convolve a specially designed filter with a velocity field whose individual components are white Gaussian noise.

$$\mathbf{u}(\vec{x}) = \mathbf{h}(\vec{x}) * \mathbf{w}(\vec{x})$$

$$= \sum_{\vec{n}} \mathbf{h}(\vec{x} - \vec{n})\mathbf{w}(\vec{n})$$

$$= \sum_{\vec{n}=-\infty}^{\infty} \begin{bmatrix} h_{11}(\vec{x}-\vec{n}) & h_{12}(\vec{x}-\vec{n}) & h_{13}(\vec{x}-\vec{n}) \\ h_{21}(\vec{x}-\vec{n}) & h_{22}(\vec{x}-\vec{n}) & h_{23}(\vec{x}-\vec{n}) \\ h_{31}(\vec{x}-\vec{n}) & h_{32}(\vec{x}-\vec{n}) & h_{33}(\vec{x}-\vec{n}) \end{bmatrix} \begin{bmatrix} w_1(\vec{n}) \\ w_2(\vec{n}) \\ w_3(\vec{n}) \end{bmatrix} \qquad (5.19)$$

It is important to remember that $\vec{x}$ and $\vec{n}$ are vectors, so $\sum \vec{n}$ is $\sum n_1 \sum n_2 \sum n_3$. One of the important properties of an independent and identically distributed white Gaussian noise process is that it is only correlated with itself at zero lag, with variance σ^2.

$$\overline{w_i(\vec{x})w_j(\vec{y})} = \begin{cases} \sigma_{ij}^2, & \vec{x} = \vec{y} \ \& \ i = j \\ 0, & \vec{x} \neq \vec{y} \text{ or } i \neq j \end{cases} \qquad (5.20)$$

The correlation of the new process is then

$$\begin{aligned} \overline{\mathbf{u}(\vec{x})\mathbf{u}(\vec{y})^T} &= \overline{\sum_{\vec{n}} \mathbf{h}(\vec{x}-\vec{n})\mathbf{w}(\vec{n}) \sum_{\vec{m}} \mathbf{h}(\vec{y}-\vec{m})\mathbf{w}(\vec{m})^T} \\ &= \sum_{\vec{n}} \sum_{\vec{m}} \mathbf{h}(\vec{x}-\vec{n})\overline{\mathbf{w}(\vec{n})\mathbf{w}(\vec{m})^T}\mathbf{h}(\vec{y}-\vec{m})^T \\ &= \sigma^2 \sum_{\vec{n}} \sum_{\vec{m}} \mathbf{h}(\vec{x}-\vec{n})\mathbf{I}\delta(\vec{n}-\vec{m})\mathbf{h}(\vec{y}-\vec{m})^T \\ &= \sigma^2 \sum_{\vec{n}} \mathbf{h}(\vec{x}-\vec{n})\mathbf{h}(\vec{y}-\vec{n})^T \end{aligned} \qquad (5.21)$$

Putting this into a more familiar form,

$$\begin{aligned}\mathbf{R}(\vec{r}) &= \sigma^2 \sum_{\vec{n}} \mathbf{h}(-\vec{n})\mathbf{h}(\vec{r}-\vec{n})^T \\ &= \sigma^2 \mathbf{h}(-\vec{r}) * \mathbf{h}(\vec{r})^T.\end{aligned} \qquad (5.22)$$

Taking the Fourier transform componentwise leads to

$$\Phi(\vec{k}) = \sigma^2 \mathbf{H}(-\vec{k})\mathbf{H}(\vec{k})^T, \qquad (5.23)$$

which reveals what the filter needs to be. Since $\mathbf{u}(\vec{x})$ is real, $\mathbf{h}(\vec{x})$ and $\mathbf{w}(\vec{x})$ are real, and that means that for $\mathbf{H}(\vec{k})$ the real parts are even and the imaginary parts are odd. Looking more closely at $\Phi(\vec{k})$, it is clear that it is symmetric, real, and even. That means that $\mathbf{H}(\vec{k})$ must be real, and so

$$\Phi(\vec{k}) = \sigma^2 \mathbf{H}(\vec{k})\mathbf{H}(\vec{k})^T. \qquad (5.24)$$

This is a square root factorization at every $\vec{k}$. There are various methods for finding $\mathbf{H}(\vec{k})$, such as using an eigenvalue decomposition, or using the Cholesky decomposition. However, because $\Phi(\vec{k})$ must be sampled, it turns out that some methods are far more robust numerically.

5.3.1 Eigenvalue vs. Cholesky Decomposition

One possible way to find $\mathbf{H}(\vec{k})$ is through eigenvalue decomposition. This works because $\Phi(\vec{k})$ is symmetric, and can be diagonalized by unitary matrices.

$$\Phi(\vec{k}) = \mathbf{U}\mathbf{\Lambda}\mathbf{U}^T = \mathbf{U}(\mathbf{\Lambda})^{1/2}(\mathbf{U}(\mathbf{\Lambda})^{1/2})^T \qquad (5.25)$$

However, it turns out that this decomposition is numerically sensitive, and it is difficult to recover the orginal $\Phi(\vec{k})$ matrix if any kind of resampling occurs (such as when doing a tranform of the spatially convolved filters).

A more robust method is to carry out the Cholesky decomposition, [3] which factors a positive definite matrix into a lower triangular matrix and its transpose, $\mathbf{LL}^T$. However, $\Phi(\vec{k})$ is in general not positive definite, and so a zero pivot is often encountered. There are algorithms (such as the Incomplete Cholesky decomposition) which can handle the zero pivot. Once $\Phi(\vec{k})$ is factored into $\mathbf{L}(\vec{k})\mathbf{L}(\vec{k})^T$, the six individual spatial filters are found from doing a componentwise multidimensional inverse Fourier transform (IFTn) of $\mathbf{L}(\vec{k})$.

$$\mathbf{H}(\vec{r}) = \begin{bmatrix} \text{IFTn}\{L_{11}(\vec{k})\} & 0 & 0 \\ \text{IFTn}\{L_{21}(\vec{k})\} & \text{IFTn}\{L_{22}(\vec{k})\} & 0 \\ \text{IFTn}\{L_{31}(\vec{k})\} & \text{IFTn}\{L_{32}(\vec{k})\} & \text{IFTn}\{L_{33}(\vec{k})\} \end{bmatrix} \qquad (5.26)$$

5.3.2 Sampling rates in the spatial and wavenumber domains

There are important decisions to be made about the sampling rates in the spatial and wavenumber domains. To avoid the aliasing of high frequencies onto low frequencies, the sampling frequency must exceed the Nyquist rate.

$$\frac{2\pi}{\text{sampling interval}} \geq 2 \times \text{highest wavenumber (radians/meter)} \qquad (5.27)$$

Examining $\Phi(\vec{k})$, a conservative boundary for when it drops below 1% of its maximum value is $\xi > 4/\text{meter}$. Using the above formula, this corresponds to sampling in the spatial domain at a radial distance of 0.78 meters or less, which translates to sampling at less than 0.45 meters in each of the three cardinal directions. There is a dual expression for sampling in the wavenumber domain.

$$\frac{2\pi}{\text{sampling rate}} \geq 2 \times \text{longest correlation} \qquad (5.28)$$

A conservative choice for maximum correlation length in the radial direction is 10 meters, leading to a radial wavenumber sampling rate that is roughly 0.6/meter or less, and 0.35/meter or less in each of the cardinal wavenumber directions.

Memory and computational issues have to be considered as well. For example,

sampling in a 10 cm grid pattern in the spatial domain sets the limits of integration in the wavenumber domain from -31.4/meter to 31.4/meter in each of the cardinal wavenumber directions. Then sampling in the wavenumber domain in a 0.25/meter grid will give 252x252x252 points, which is 122 MB of memory (per filter, using 8 bits per point). Once sampling rates have been decided on, each of the six filters is found using the inverse multidimensional discrete Fourier transform: [5]

$$h_{ij}[r_1, r_2, r_3] = \frac{1}{N_1 N_2 N_3} \sum_{k1=0}^{N_1-1} \sum_{k2=0}^{N_2-1} \sum_{k3=0}^{N_3-1} L_{ij}[k_1, k_3, k_3] \cdot \exp\left(-\frac{j2\pi r_1 k_1}{N_1} - \frac{j2\pi r_2 k_2}{N_2} - \frac{j2\pi r_3 k_3}{N_3}\right)$$
$$(5.29)$$

where each filter L_{ij} is size N_1 x N_2 x N_3. It can be difficult for programs such as Matlab to handle transforms of this size. As an alternative, h_{ij} may be computed through three stages of single dimensional transforms. First, iterate through two dimensions (k_1, k_2) while doing a transform of the third dimension (k_3). Second, using the partially transformed matrix, iterate through two different dimensions (k_1, k_3) while tranforming a different dimension (k_2). Finally, take that matrix and iterate through (k_2, k_3) while tranforming the (k_1) dimension. This was method used in this thesis.

5.3.3 Scaling issues

It must be remembered that sampling in the spatial domain will cause a scaling of the true wavenumber spectrum by a factor of 1/(sample length). [14]

$$\Phi(\vec{k})_{\text{discrete}} = \frac{\Phi(\vec{k})_{\text{continuous}}}{\text{spatial sample length}} \qquad (5.30)$$

Secondly, it is important to remember the 2π convention that Batchelor uses in defining the Fourier transforms is the opposite of current convention. After doing the inverse multidimensional discrete Fourier transform, the quantity must be multiplied by $(2\pi)^3$.

There is one final scaling issue that is a result of sampling. The inverse Fourier transorm is defined from $-\infty$ to ∞, but sampling in the spatial domain reduces the

106

limits of integration in the wavenumber domain. With the limits of integration set from sampling a 10 cm grid, the results of the inverse Fourier transform must be multiplied by 1.03 in order to arrive at the proper variance of the process.

5.3.4   Least Squares Filter

A filter that is 252x252x252, though accurate, is quite large. It is desirable to reduce its size while minimizing the mean squared error in the wavenumber domain.

$$\text{minimize } \| \Phi_{ij}(\vec{k}) - \hat{\Phi}_{ij}(\vec{k}) \|_2^2 \quad = \quad \min \left[\sum_{\vec{r}} \left(h_{ij}(\vec{r}) - \hat{h}_{ij}(\vec{r}) \right) e^{-j2\pi\vec{k}\cdot\vec{r}/N} \right]^2 \quad (5.31)$$

Denoting the region $\vec{R}$ of the least squares filter, the equation becomes [5]

$$= \min \left[\sum_{\vec{r} \in \vec{R}} \left(h_{ij}(\vec{r}) - \hat{h}_{ij}(\vec{r}) \right) + \sum_{\vec{r} \notin \vec{R}} h_{ij}(\vec{r}) \right]^2 \quad (5.32)$$

The error is minimized by setting $\hat{h}_{ij}(\vec{r}) = h_{ij}(\vec{r})$, $\vec{r} \in \vec{R}$. Using the previously stated values for the constants and sampling rates, a block of the first 127x127x127 points centered around $\vec{r}=0$ accurately reproduces the desired spectrum. The following table compares the variance recovered by filters of a particular size to that of the true variance of the system. Each of the filters is created from what is considered to be the true filter, 255x255x255. It must be remembered that since sampling in the spatial domain has occured, wavenumbers have a finite limit, and this accounts for the maximum of 94.8 % of the true variance in each direction. Also, the L_{33} component has the greatest effect on performance because it is approximately an impulse in the wavenumber domain, causing it to be uniformly distributed in the spatial domain. Then, any reducing of filter size has immediate impact on L_{33}.

Least Squares filter size	% var(u_1)	% var(u_2)	% var(u_3)
31x31x31	88.7	82.6	43.7
63x63x63	92.7	88.9	63.6
127x127x127	93.5	91.8	81.5
189x189x189	94.1	93.5	89.4
255x255x255 (true)	94.8	94.8	94.8

$$(5.33)$$

5.3.5   Block Convolution

As stated previously, by convolving $\mathbf{h}(\vec{x})$ with the white Gaussian noise field $\mathbf{w}(\vec{x})$, the turbulent flow at one time instant is produced. With a filter of significant size, convolution is time consuming. It is recommended that this process be completed in the wavenumber domain, where the operation of convolution becomes multiplication. Then programs which excel at matrix multiplication can be used (such as Matlab). The follow will explain the common overlap-save method of block convolution.

The turbulent process may be created in blocks of computationally reasonable size. Before taking Fourier transforms of the filters and of the current block of white noise, the six filters must be zero padded to match the size of the block of white noise. Then multiplication is carried out at each $\vec{k}$.

$$
\begin{bmatrix} U_1(\vec{k}) \\ U_2(\vec{k}) \\ U_3(\vec{k}) \end{bmatrix} = \begin{bmatrix} H_{11}(\vec{k}) & 0 & 0 \\ H_{21}(\vec{k}) & H_{22}(\vec{k}) & 0 \\ H_{31}(\vec{k}) & H_{32}(\vec{k}) & H_{33}(\vec{k}) \end{bmatrix} \begin{bmatrix} W_1(\vec{k}) \\ W_2(\vec{k}) \\ W_3(\vec{k}) \end{bmatrix} \qquad (5.34)
$$

After taking inverse Fourier transforms of $\mathbf{U}$ componentwise, the convolution process is complete but the edge points which did not fully overlap with the filter must be discarded. By matching the filter size to the white noise block size, the trailing edge points are automatically discarded, so only the leading edge points are affected. Therefore, the kernal of good points would be the block represented by the matrix (127:end,127:end,127:end).

Seeing that the leading edge points are always discarded, these points in the next

block of white noise must overlap with the previous block. That way, though they are discarded in the second group of block convolution, they were the good points kept in the first group. The process continues until the whole turbulent flow has been generated.

5.4 Results

Figures are presented at the end of this chapter. There is good agreement between the ideal correlation functions and the correlations that result from using the 127x127x127 least squares filters, with the exception of the predicted decrease in magnitude in the R33 correlation.

To obtain the statistics of the generated data, ergodic theory can be invoked. Since regions of space are considered to be statistically similar, ergodic theory says that averaging over a large spatial volume will be equivalent to averaging at one point over many trials. The idea is that the values that are likely to be found at that one point over many realizations will likely be found at other locations throughout the region.

Using a 258x258x258 block of data, the correlations were found to be slightly less in magnitude than what the least square correlations predict. Extending the data block size to 516x516x516 lead to much better agreement in correlations.

5.5   Space-time correlations for turbulence induced velocities advected by the mean current

Batchelor gives the following spatial correlation tensor:

$$
\begin{aligned}
R'_{ij}(\vec{r}) &= E[u'_i(\vec{x})u'_j(\vec{x}+\vec{r})] \\
&= (u')^2 \left(\frac{f-g}{r^2} r_i r_j + g\delta_{ij} \right)
\end{aligned}
\tag{5.35}
$$

where $\vec{r}$ is the vector separation between the two points being compared,

$$
\vec{r} = r_1 \hat{\mathbf{i}} + r_2 \hat{\mathbf{j}} + r_3 \hat{\mathbf{k}} = \Delta x \hat{\mathbf{i}} + \Delta y \hat{\mathbf{j}} + \Delta z \hat{\mathbf{k}},
\tag{5.36}
$$

r is the magnitude of the displacement between the two points being compared,

$$
r = |\vec{r}| = \sqrt{(\Delta x)^2 + (\Delta y)^2 + (\Delta z)^2},
\tag{5.37}
$$

u is the root mean square of the velocity components,

$$
u^2 = \frac{1}{3}\overline{(u'_1)^2 + (u'_2)^2 + (u'_3)^2},
\tag{5.38}
$$

and f(r) and g(r) are the longitudinal and lateral velocity correlations,

$$
f(r) \approx e^{-\alpha|\vec{r}|}, \qquad g(r) = f + \frac{1}{2}r\frac{\partial f}{\partial r}.
\tag{5.39}
$$

Longitudinal correlations are of velocities which are parallel with the separation vector, $\vec{r}$, and lateral correlations are of velocities which are perpendicular to it.

The turbulent statistics have been solved for spatial correlations, but not for time correlations. However, using Taylor's Frozen Turbulence Hypothesis, it can be assumed that the turbulent field is advected along by the main current. One point in space will see the spatial correlations as time correlations. As a simple approximation,

the conversion between the time and space coordinates is

$$\tau = \frac{r}{v} \tag{5.40}$$

where τ is the time separation, r is the space separation, and v is the mean velocity of the current. If the mean current has some angle φ, then the conversion along the coordinate axes is

$$\Delta x_\tau = (v \cos \varphi)\tau, \qquad \Delta y_\tau = (v \sin \varphi)\tau. \tag{5.41}$$

Then r is modified as follows,

$$
\begin{aligned}
r_\tau = |\vec{r_\tau}| \quad &= \sqrt{(\Delta x + \Delta x_\tau)^2 + (\Delta y + \Delta y_\tau)^2 + (\Delta z + \Delta z_\tau)^2} \\
&= \sqrt{(\Delta x + v\tau \cos \varphi)^2 + (\Delta y + v\tau \sin \varphi)^2 + (\Delta z)^2}
\end{aligned} \tag{5.42}
$$

Finally, the space-time correlations for turbulence induced velocities advected by mean current with velocity v is given by

$$
\begin{aligned}
R'_{ij}(\vec{r}, \tau) \quad &= E[u'_i(\vec{x}, t)u'_j(\vec{x} + \vec{r}, t + \tau)] \\
&= E[u'_i(\vec{x})u'_j(\vec{x} + \vec{r_\tau})] \\
&= (u')^2 \left(-\frac{r_{\tau i} r_{\tau j}}{2 r_\tau} \frac{\partial f}{\partial r_\tau} + (f + \frac{r_\tau}{2} \frac{\partial f}{\partial r_\tau})\delta_{ij} \right).
\end{aligned} \tag{5.43}
$$

This will accurately predict correlations for the simulated flow when the flow is advected by the mean current.
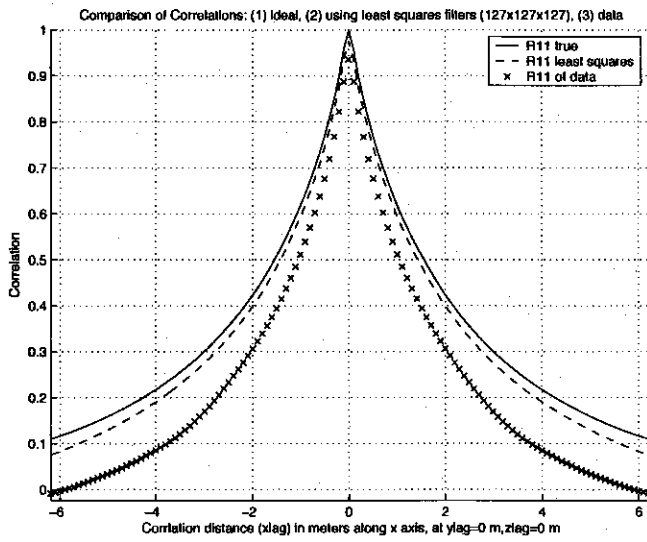
Figure 5-1: Correlation of R11 using a 258x258x258 data block
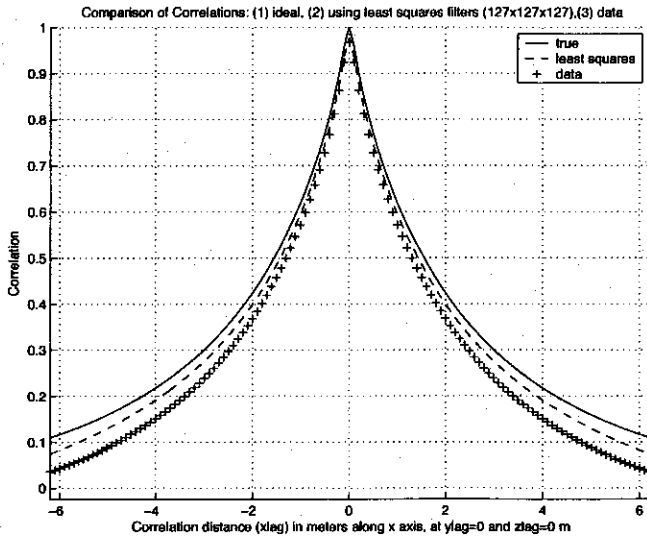
Figure 5-2: Correlation of R11 using a 516x516x516 data block
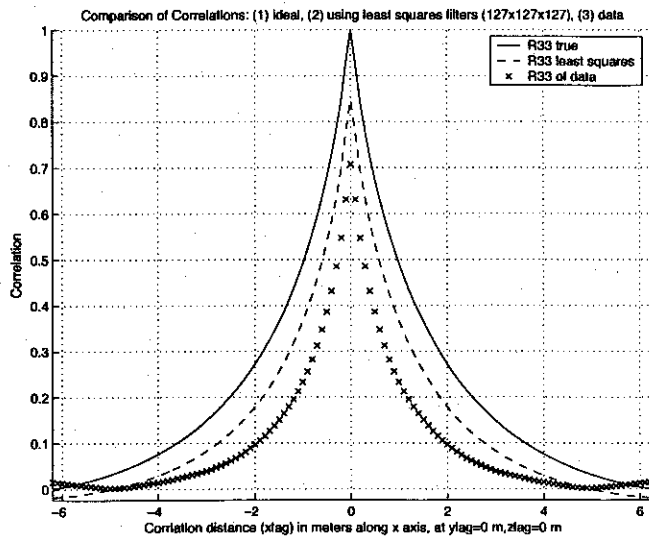
Figure 5-3: Correlation of R33 using a 258x258x258 data block
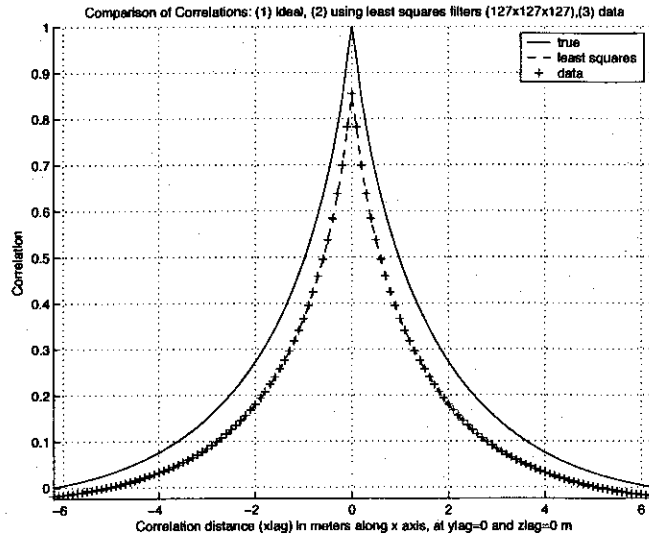
Figure 5-4: Correlation of R33 using a 516x516x516 data block

113
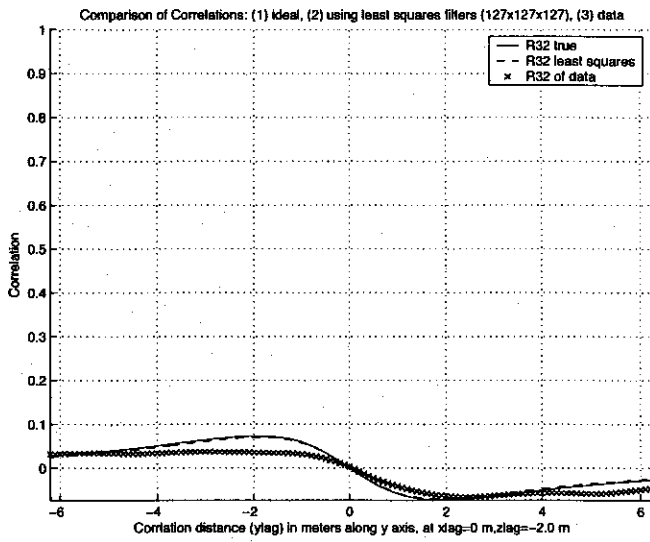
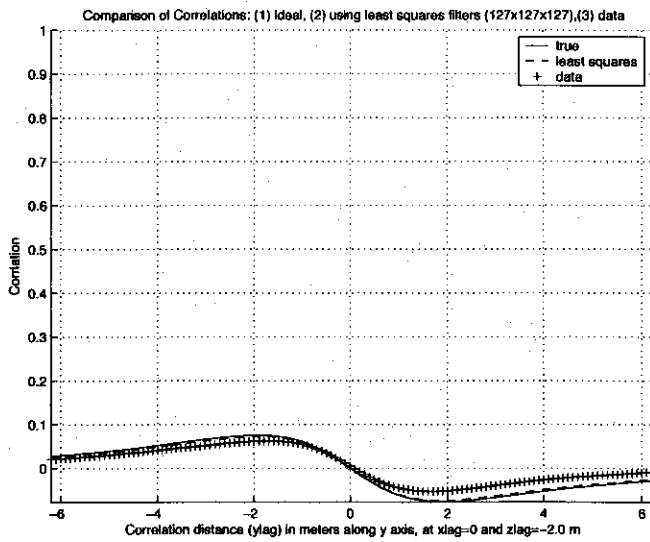Figure 5-5: Correlation of R32 using a 258x258x258 data block

Figure 5-6: Correlation of R32 using a 516x516x516 data block

114
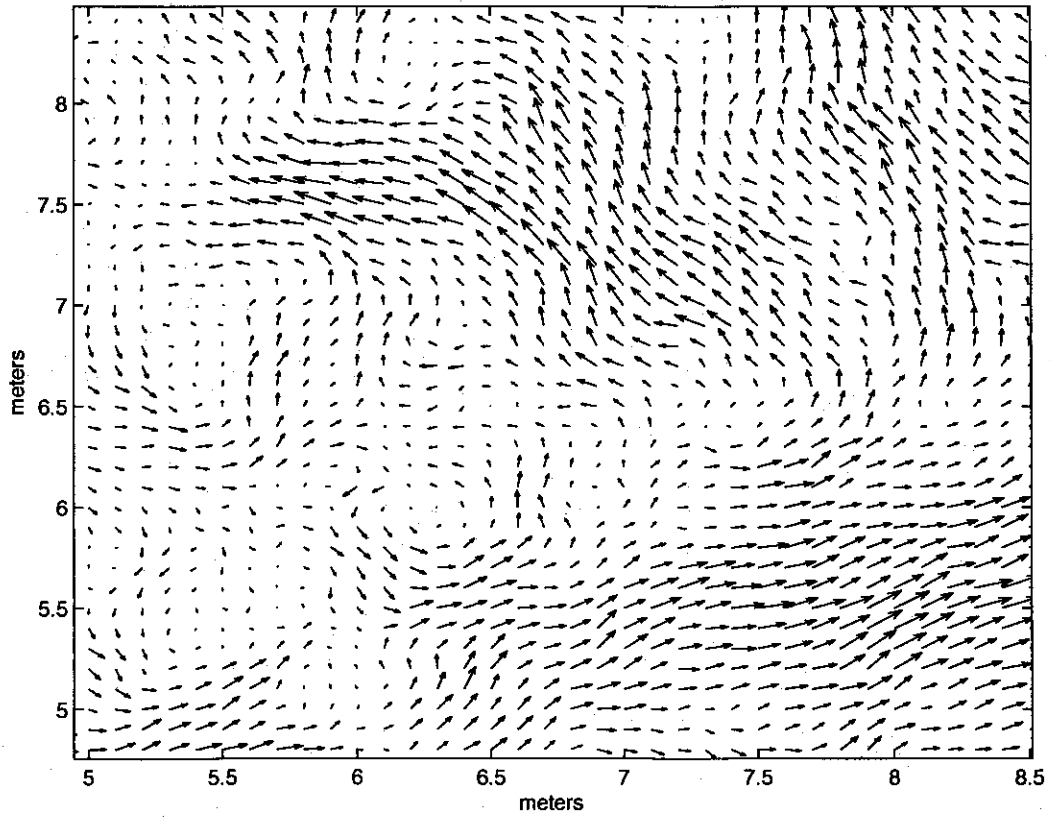
Figure 5-7: Snapshot of a 2-D vertical slice through turbulent flow. This were generated using a spatial sampling rate of 0.1 m, and using a least squares filter that is 127x127x127 points.
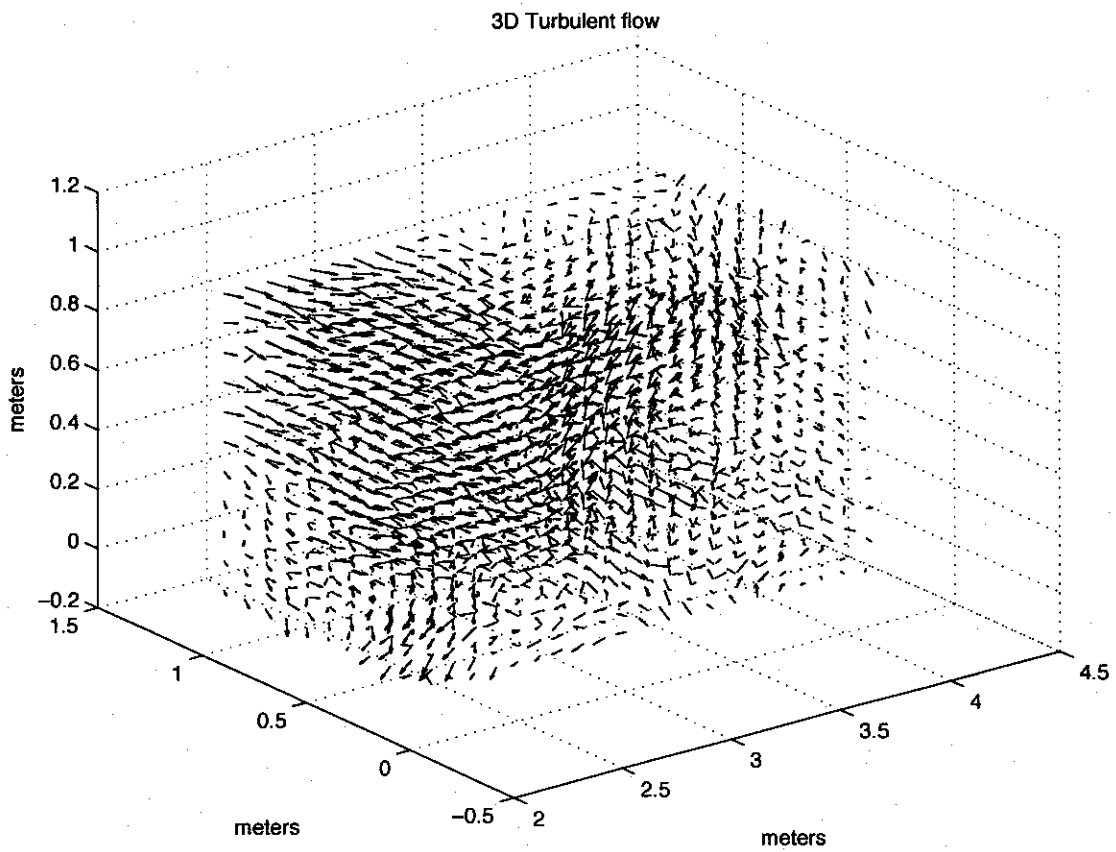
Figure 5-8: 3-D section of turbulent flow. This were generated using a spatial sampling rate of 0.1 m, and using a least squares filter that is 127x127x127 points.

Chapter 6

Simulating a Time-Evolving, Homogeneous, Isotropic Turbulent Flow

The previous chapter was concerned with simulating a statistically correct, spatially homogeneous, isotropic turbulent field. The basic idea was to design filters that matched the 2nd order statistics of the output to those of the turbulent process, and then convolve these filters with a white noise field. It would be possible to add the dimension of time to the filters, but that means that spatial fields that are already large in size (say 516x516x516= 1 gigabyte per component u,v,w) are multiplied by the number of time steps (say 20 min for an ocean process at 10 Hz = 12000). These computational demands will be to great, and potentially not necessary.

Adding the dimension of time to the simulation of the turbulent flow would more likely be necessary for studying the mechanisms of turbulence itself, rather than employing the statistics of turbulence. For studying the mechanisms of turbulence, it makes more sense to use the traditional schemes which seek the numerical solution of the governing Navier-Stokes equations. However, when only the statistics of turbulence are necessary, there may be other ways to simulate time evolving statistics.

Taylor's hypothesis, or Taylor's frozen turbulence approximation, says that a probe traversing the spatial field at high enough velocity U will see a spatial tur-

bulent field which has changed very little in that short period of time. The probe will have a time series of velocity fluctuations, which correspond to locations in space related by $x = Ut$. This approximation holds as long as probe speed U is much larger than the turbulent fluctuations, u. Analogously, the probe can remain still and the turbulent field advected by it at velocity U.

This would indicate that if $U >> u$, the frozen spatial field (as described in the previous chapter) would be sufficient for creating the type of statistics that the ADCP might observe in the ocean. However, U in the ocean may be on the order of 10-50 cm/s, and u on the order of 2 cm/s, so only at the high speeds is this approximation valid. Therefore, in general, some sort of time evolution of the statistics is still needed.

To approximate time evolution, one spatial direction $(+z)$ will be forfeited for a time direction by advecting the frozen spatial field in that direction. Looking at correlations in any direction other than the one chosen for time will appear as time evolution of the statistics.

6.1   Chapter Overview

In the second section, the Kovasznay-Corrsin conjecture will be explored as the basis for developing space-time correlations. [16] In the third section, the equations for the space-time correlations will be formulated. In the final section, the validity of substituting a spatial direction for time evolution will be evaluated using simulated data.

6.2   The Kovasznay-Corrsin conjecture

Phillips [16] presents the basic idea of the Kovasznay-Corrsin conjecture – that space-time correlations can be written as spatial correlations which have diminished in time. Kovasznay reasoned that any diminuation in correlation over time from its initial value at $\vec{r} = 0, \tau = 0$ is due to turbulent diffusion. With slight change of notation (to match

that of this thesis), Phillip's equation (2.1) is as follows:

$$< u_i u_j > R_{ij}(\vec{x}; \vec{r}, t) = \int < u_i(\vec{x}, t) u_j(\vec{x} + \vec{p}, t)\theta(\vec{x} + \vec{p} - \vec{r}, t + \tau) > d\vec{p}, \qquad (6.1)$$

where $\theta(\vec{q}, \tau)$ is a scalar function which relates how the spatial correlation will diminish in time. Corrsin reasoned that after a long enough time, the distribution of random displacements $\vec{r}$ from $\vec{x}$ must behave as a random walk process. In essence, local values of velocity will not have memory of their initial location. Phillip's equation (2.2) is as follows:

$$R_{ij}(\vec{x}; \vec{r}, t) = \int R_{ij}(\vec{x}; \vec{p}, 0)\overline{\theta}(\vec{p} - \vec{r}, t + \tau)d\vec{p}, \qquad (6.2)$$

where $\overline{\theta}(\vec{q}, \tau)$ is the probability that a fluid particle travels $\vec{q}$ in time τ. Allowing for advection by mean current $\mathbf{V} = (V_1, V_2, V_3)$, and assigning a Normal distribution for the diminuation in time, $\overline{\theta}$ is as follows (basically Phillip's equation (2.3)):

$$(2\pi)^{3/2}(< y_1^2 >< y_2^2 >< y_3^2 >)^{1/2}\overline{\theta}(\vec{p}-\vec{r}, \tau) = \exp\left[-\frac{1}{2}\left\{\frac{(r_j - p_j - V_j\tau)^2}{< y_j^2 >}\right\}\right], \quad j = 1, 2, 3$$
$$(6.3)$$

where $< y_i^2 >$ is the mean square displacement of a fluid particle in time τ, and where repeated indices indicates a summation. Given an equation for $R_{ij}(\vec{p}, 0)$, all that is required is to carry out the integrations.

6.3 Space-time correlations for homogeneous, isotropic turbulence advected by a uniform current

Batchelor [1] presents the spatial correlations as follows:

$$\begin{aligned} R'_{ij}(\vec{r}) &= E[u'_i(\vec{x})u'_j(\vec{x} + \vec{r})] \\ &= (u')^2\left(\frac{f(r)-g(r)}{r^2}r_i r_j + g(r)\delta_{ij}\right) \end{aligned} \qquad (6.4)$$

where f(r) and g(r) are the longitudinal and lateral velocity correlations, with

$$g(r) = f + \frac{1}{2}r\frac{\partial f}{\partial r},$$ (6.5)

where $\vec{r}$ is the vector separation between the two points being compared,

$$\vec{r} = r_1\hat{\mathbf{i}} + r_2\hat{\mathbf{j}} + r_3\hat{\mathbf{k}} = \Delta x\hat{\mathbf{i}} + \Delta y\hat{\mathbf{j}} + \Delta z\hat{\mathbf{k}},$$ (6.6)

r is the magnitude of the displacement between the two points being compared,

$$r = |\vec{r}| = \sqrt{(\Delta x)^2 + (\Delta y)^2 + (\Delta z)^2},$$ (6.7)

and u is the root mean square of the velocity components,

$$u^2 = \frac{1}{3}\overline{(u_1')^2 + (u_2')^2 + (u_3')^2},$$ (6.8)

To carry out integrations, an equation for $f(r)$ is required. Batchelor notes that in the region close to $r = 0$, $f(r)$ is not Gaussian, but becomes so for $r > r_o$, where $f(r_o) \approx 0.6$. This can be explained from the physics of the situation. Any one point is subject to a large number of eddies of various sizes being swept by, and according to the Central Limit Theorem, should have a distribution of velocities which is normal. However, two points in space are intimately related through the Navier-Stokes equations. In close proximity the velocities may be under the influence of one particular eddy, whereas at larger separations, there is more likely the change of being a part of different eddies, and that will introduce the appearance of randomness. [1] (sections 8.1,8.2).

In simulating the spatial turbulent field (in the previous chapter), the structure of $f(r)$ was imposed upon it by the analytical formulation of the spectrum tensor for homogeneous, isotropic turbulence, $\Phi_{ij}(\vec{k})$, which included an empirical energy function. In fact, based on the inverse Fourier Transform of $\Phi_{ij}(\vec{k})$ (as presented in

the previous chapter),

$$f(r) \approx e^{-\alpha |\vec{r}|}, \tag{6.9}$$

where α was found to be $\approx 1/(2.34)$. Figure 6-1 compares possible functions for f(r). The empirical model agrees closely with Batchelor's figure (7.8) [1], where it is plotted against r/M with $M \approx 2$ times the size of the energy containing eddies.
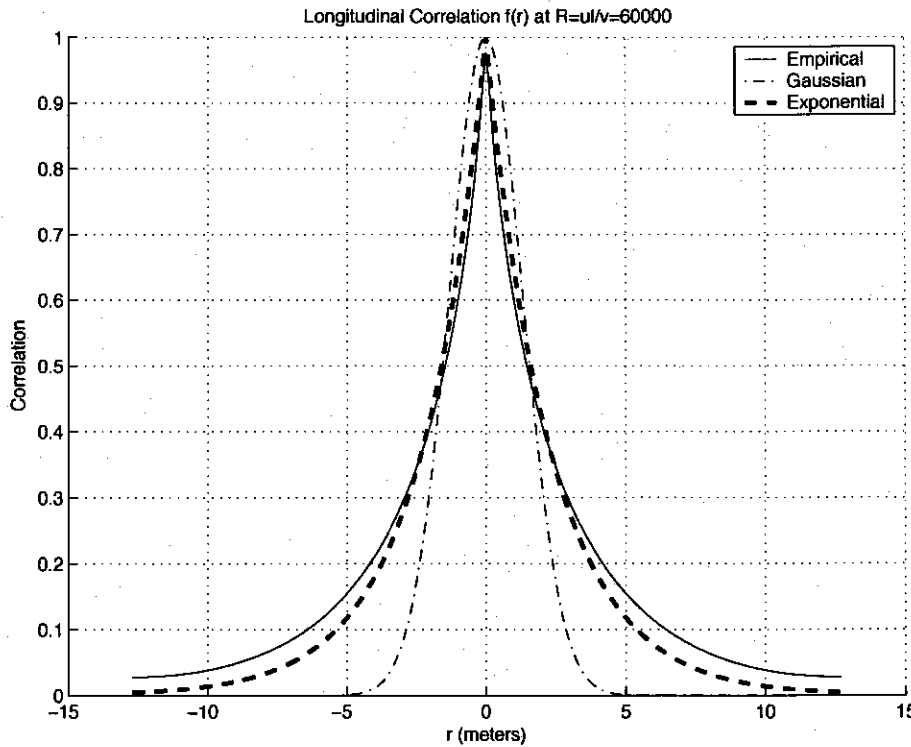

Figure 6-1: Empirical, Gaussian, and Exponential functions as possibilities for the longitudinal correlation function f(r). These functions were formed using energy containing eddies of l=3 meters, and turbulent fluctuations of u=2 cm/s.

However, for tractability in solving the space-time equations, it may be appropriate to approximate $f(r)$ as Gaussian, as has been done in previous studies with fairly successful results. [6] [16] Letting

$$f(r) \approx \exp\left[-\frac{1}{2}\left(\frac{|\vec{r}|}{L}\right)^2\right], \tag{6.10}$$

121

where L is a length scale to be determined, then

$$
\begin{aligned}
R_{ij}(\vec{p},0) &= (u')^2 \left(-\frac{p_i p_j}{2p}\frac{\partial f}{\partial p} + (f + \frac{p}{2}\frac{\partial f}{\partial p})\delta_{ij} \right) \\
&= (u')^2 \left(\frac{p_i p_j}{2L^2}e^{-\frac{1}{2}(p/L)^2} + (e^{-\frac{1}{2}(p/L)^2} - \frac{p^2}{2L^2}e^{-\frac{1}{2}(p/L)^2})\delta_{ij} \right)
\end{aligned}
\tag{6.11}
$$

First solving 6.2 for the case when $i \neq j$,

$$
\begin{aligned}
R_{ij}(\vec{r},\tau) &= (u')^2 \int\int\int \left(\frac{1}{(2\pi)^{3/2}(<y_1^2><y_2^2><y_3^2>)^{1/2}} \right)\left(\frac{p_i p_j}{2L^2} \right) \\
&\cdot\ e^{-\frac{1}{2}\frac{p_1 p_1}{L^2}}e^{-\frac{1}{2}\frac{p_2 p_2}{L^2}}e^{-\frac{1}{2}\frac{p_3 p_3}{L^2}} \\
&\cdot\ e^{-\frac{1}{2}\frac{(r_1-p_1-V_1\tau)^2}{<y_1^2>}}e^{-\frac{1}{2}\frac{(r_2-p_2-V_2\tau)^2}{<y_2^2>}}e^{-\frac{1}{2}\frac{(r_3-p_3-V_3\tau)^2}{<y_3^2>}}\ dp_1 dp_2 dp_3
\end{aligned}
\tag{6.12}
$$

This equation is separable, and integrating the j terms:

$$
\begin{aligned}
&\int p_j \exp\left\{ -\frac{1}{2}\frac{1}{L^2<y_j^2>}\left[p_j^2(<y_j^2>+L^2) - 2p_j(r_j-v_j\tau)L^2 + (r_j-v_j\tau)^2L^2 \right] \right\} dp_j \\
&= \int p_j \exp\left\{ -\frac{1}{2}\frac{<y_j^2>+L^2}{L^2<y_j^2>}\left[p_j^2 - 2p_j\frac{(r_j-v_j\tau)L^2}{<y_j^2>+L^2} + \frac{(r_j-v_j\tau)^2L^2}{<y_j^2>+L^2} \right] \right\} dp_j \\
&= \int p_j \exp\left\{ -\frac{1}{2}\frac{<y_j^2>+L^2}{L^2<y_j^2>}\left[\left(p_j - \frac{(r_j-v_j\tau)L^2}{<y_j^2>+L^2} \right)^2 - \left(\frac{(r_j-v_j\tau)L^2}{<y_j^2>+L^2} \right)^2 + \frac{(r_j-v_j\tau)^2L^2}{<y_j^2>+L^2} \right] \right\} dp_j \\
&= \left[\int p_j \exp\left\{ -\frac{1}{2}\frac{<y_j^2>+L^2}{L^2<y_j^2>}\left(p_j - \frac{(r_j-v_j\tau)L^2}{<y_j^2>+L^2} \right)^2 \right\} dp_j \right]\exp\left\{ \frac{(r_j-v_j\tau)^2L^2}{2<y_j^2>(<y_j^2>+L^2)} \right\}\exp\left\{ -\frac{(r_j-v_j\tau)^2}{2<y_j^2>} \right\} \\
&= \left[\sqrt{2\pi\frac{L^2<y_j^2>}{<y_j^2>+L^2}}\left(\frac{(r_j-v_j\tau)L^2}{<y_j^2>+L^2} \right) \right]\exp\left\{ \frac{(r_j-v_j\tau)^2L^2-(r_j-v_j\tau)^2(<y_j^2>+L^2)}{2<y_j^2>(<y_j^2>+L^2)} \right\} \\
&= \left[\sqrt{2\pi\frac{<y_j^2>}{1+\frac{<y_j^2>}{L^2}}}\left(\frac{(r_j-v_j\tau)}{1+\frac{<y_j^2>}{L^2}} \right) \right]\exp\left\{ -\frac{(r_j-v_j\tau)^2}{2L^2(1+\frac{<y_j^2>}{L^2})} \right\} \\
&= \frac{\sqrt{2\pi<y_j^2>}}{D_j}\left(L\frac{N_j}{D_j} \right)\exp\left\{ -\frac{1}{2}N_j^2 \right\}
\end{aligned}
\tag{6.13}
$$

where (in using the general form of Phillip's notation), [16]

$$
N_j = \frac{(r_j-v_j\tau)}{L\sqrt{1+\frac{<y_j^2>}{L^2}}}, \quad N_j^2 = \frac{(r_j-v_j\tau)^2}{L^2(1+\frac{<y_j^2>}{L^2})}, \quad D_j = \sqrt{1+\frac{<y_j^2>}{L^2}}.
\tag{6.14}
$$

The term in brackets was just the first moment of a Gaussian distribution, which is the mean. This will be the same for integration of the i terms, and the final terms which are neither i nor j are just the integration of a Gaussian distribution. Combining all

terms, the space-time correlation function for $i \neq j$ is given by

$$
\begin{aligned}
R_{ij}(\vec{r}, \tau) &= (u')^2 \big(\tfrac{1}{2L^2(2\pi)^{3/2}(<y_1^2><y_2^2><y_3^2>)^{1/2}} \big) \tfrac{\sqrt{2\pi<y_1^2>}}{D_1} \tfrac{\sqrt{2\pi<y_2^2>}}{D_2} \tfrac{\sqrt{2\pi<y_3^2>}}{D_3} \\
&\quad \cdot \big(L\tfrac{N_i}{D_i} \big) \big(L\tfrac{N_j}{D_j} \big) \exp\big\{ -\tfrac{1}{2}N_1^2 \big\} \exp\big\{ -\tfrac{1}{2}N_2^2 \big\} \exp\big\{ -\tfrac{1}{2}N_3^2 \big\} \qquad (6.15) \\
&= (u')^2 \tfrac{e^{-\frac{1}{2}N^2}}{D^3} \Big[\tfrac{N_i N_j}{2 D_i D_j} \Big]
\end{aligned}
$$

where

$$
N^2 = N_1^2 + N_2^2 + N_3^2, \quad D^3 = D_1 D_2 D_3. \qquad (6.16)
$$

When considering the case of $i = j$, the terms multiplied by the delta function now need to be included. However, looking back at 6.11, notice that the only real change is that instead of finding the first moment of a Gaussian function, now the second moment will be found (since $p^2 = p_1^2 + p_2^2 + p_3^2$). The second moment is the squared mean added to the variance:

$$
\begin{aligned}
\mu^2 + \sigma^2 &= \left(\frac{(r_j - v_j\tau)L^2}{<y_j^2>+L^2} \right)^2 + \frac{L^2<y_j^2>}{<y_j^2>+L^2} \\
&= \left(\frac{(r_j - v_j\tau)}{1 + \frac{<y_j^2>}{L^2}} \right)^2 + \frac{<y_j^2>}{1 + \frac{<y_j^2>}{L^2}} \\
&= \frac{L^2}{1 + \frac{<y_j^2>}{L^2}} \left[\frac{(r_j - v_j\tau)^2}{L^2 \left(1 + \frac{<y_j^2>}{L^2} \right)} + \frac{<y_j^2>}{L^2} \right] \qquad (6.17) \\
&= L^2 B_j
\end{aligned}
$$

where in keeping with Phillip's notation,

$$
B_j = \frac{1}{1 + \frac{<y_j^2>}{L^2}} \left[\frac{<y_j^2>}{L^2} + \frac{(r_j - v_j\tau)^2}{L^2 \left(1 + \frac{<y_j^2>}{L^2} \right)} \right]. \qquad (6.18)
$$

Adding the extra integrated terms terms which came from 6.11, the space-time correlation function for $i = j$ is given by

$$
\begin{aligned}
R_{i(i)}(\vec{r}, \tau) &= (u')^2 \frac{e^{-\frac{1}{2}N^2}}{D^3} \Big[\frac{B_i}{2} + 1 - \big(\frac{B_1}{2} + \frac{B_2}{2} + \frac{B_3}{2} \big) \Big] \\
&= (u')^2 \frac{e^{-\frac{1}{2}N^2}}{D^3} \Big[1 - \tfrac{1}{2}(B - B_i) \Big]
\end{aligned} \qquad (6.19)
$$

123

where $i(i)$ indicates no summation over indices, and in keeping with Phillip's notation

$$B = B_1 + B_2 + B_3. \tag{6.20}$$

Finally, combining both cases, $i \neq j$ and $i = j$, the result is

$$R_{ij}(\vec{r}, \tau) \quad = (u')^2 \frac{e^{-\frac{1}{2}N^2}}{D^3} \left[\frac{N_i N_j}{2D_i D_j} + \left(1 - \tfrac{1}{2}(B - B_i) - \frac{N_i N_j}{2D_i D_j}\right) \delta_{ij} \right] \tag{6.21}$$

Although the notation is Phillip's, these equations for R_{ij} do not exactly match his equations for homogeneous isotropic turbulence convected by a mean current. The reason is that these equations are the complete general equations, whereas his equations reflect the special case of $V = (V, 0, 0)$, and $= R_{ij}(x_1, 0, 0, \tau)$. In addition, these equations have the additional $(u')^2$ term in keeping with Batchelor's notation. [1]

6.4   Experimental Validation

Favre performed experiments on turbulence generated from an air flow passing through a mesh grid. From measurements, he verified that the turbulent field is advected with the mean velocity. He did this by measuring space-time correlations with points downstream. Peaks occured at optimum delay, when $T_i = X_i/V$, where X_i are the chosen points of correlation downstream, and V is the mean velocity of the air flow.

Using the ideas of Kovasnay and Corrsin, Favre formulated the longitudinal space-time correlation, [6]

$$R_{11}(r_1, 0, 0, \tau) = \int_{-\infty}^{\infty} f(p) e^{-\frac{(r_1 - p - v_1 \tau)^2}{2u^2 \tau^2}} \frac{dp}{\sqrt{2\pi u^2 \tau^2}} \int_0^{\infty} g(q) e^{-\frac{q^2}{2u^2 \tau^2}} \frac{q \, dq}{u^2 \tau^2}, \tag{6.22}$$

with $f(r)$ and $g(r)$ being determined empirically. Favre's computed results matched his experimental results for homogeneous, isotropic, turbulence. Figure 6-2 displays results similar in spirit to Favre's work. The time axis is normalized against Δ, which

is the correlation over space at optimum delay, t_{opt}:

$$\Delta = \int_0^\infty R_{11}(r_1, 0, 0, \tau)\frac{dr_1}{v_1}. \tag{6.23}$$

The two envelope curves are of the decay at optimal delay. Compared are the exponential curves (which are close approximations to Favre's empirical relations), and the Gaussian curves as just developed. Figure 6-2 illustrates that peak correlations of downstream locations occur at the optimal delay time. Using the Gaussian approximation for $f(r)$ results in higher correlation for shorter times, and lower correlation in the tails (as compared to results using an exponential $f(r)$). In addition, the Gaussian prediction for optimal delay required that the ratio $< y_i^2 > /L^2$ be three times larger than the equivalent ratio of the exponential approximation of $f(r)$.
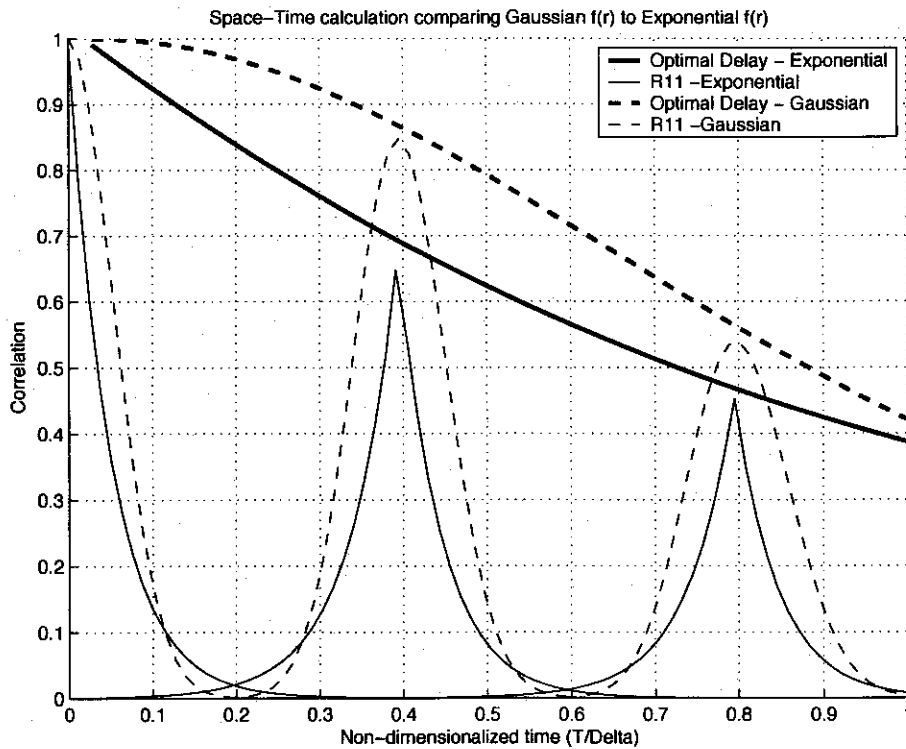

Figure 6-2: Results that are similar in spirit to Favre's figure 5 [6], where the space-time correlations for $R_{11}(r_1, 0, 0, \tau)$ are postdicted. τ is the independent variable for three selected r_1 locations.

6.5 Experimental Extension and Application

Favre's work validated using the diminuation in time of spatial correlations for the longitudinal case, R_{11}. The extension would be to use the full R_{ij} in the ocean setting. In order to do that, both correlation length, L, and the ratio of mean-square distance traveled to correlation length, $<y_i^2>/L^2$, need to be extracted from the data. ADCP data from the Martha's Vineyard Coastal Observatory will serve as a starting point. This data is sampled at 2 Hz and measured at 50 cm vertical spacings. This is less than the desired 10 Hz sampling rate and 10 cm vertical spacings, but will at least allow for rough approximations of the space-time correlations. Figure 6-3 shows the mean horizontal currents, the space-time countour centered at height of 5.6 m from the ocean bottom, and the mean radial spatial and temporal correlations over all beam 1 locations. What is missing from the plots is the radial velocity correlation,
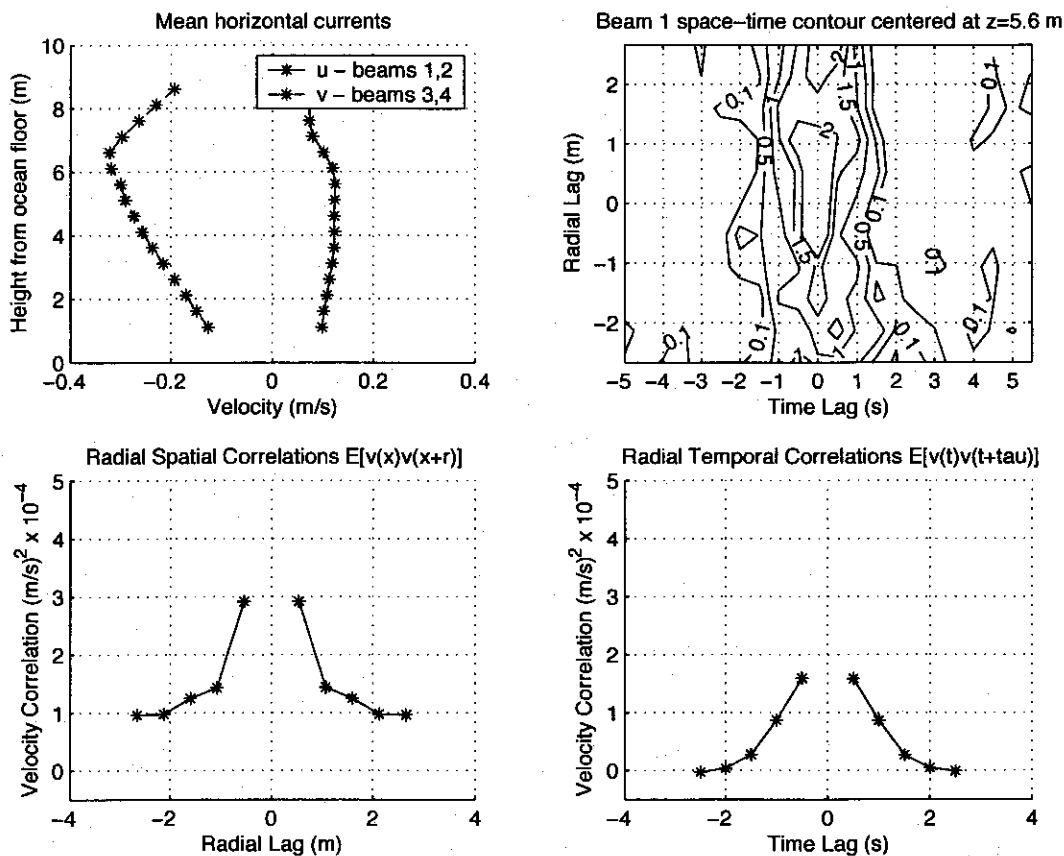

Figure 6-3: Various aspects of ADCP beam 1 data from the Martha's Vineyard Coastal Observatory, yearday 260, 2005, at 8:40 am

126

$E[v'(0,0),v'(0,0)]$. That correlation is central to obtaining the Reynolds stress, which is the goal of this thesis. One method of estimating that point is to do a fit with the theoretical models just presented. With low resolution data, this is a balancing act. The correlation length, L, is simultaneously varied along with $E[v'(0,0),v'(0,0)]$. Fortunately, there is only a small range of values that will lead to an approximate fit of given spatial correlations. Empirically, $E[v'(0,0),v'(0,0)] \approx 4.4x10^{-4}(cm/s)^2$, and $L \approx 1.5m$. Then, following Favre's lead that the diffusion is quadratic in time, the mean square distance for the random walk of small fluid elements moving with the mean flow is

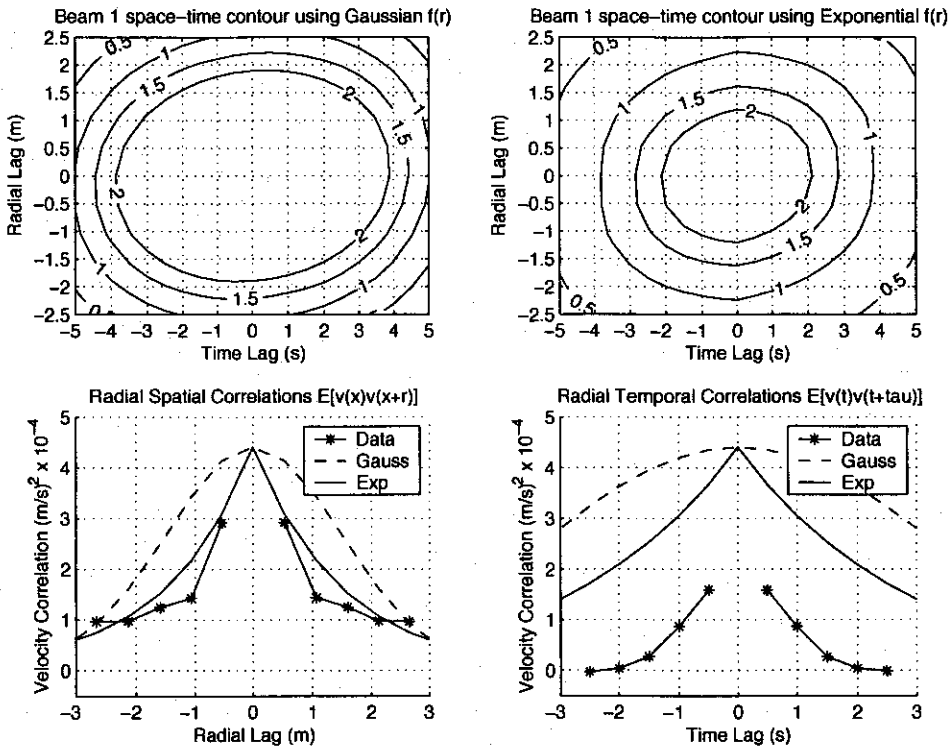$$< y_i^2 >= (4.4 \cdot 10^{-4}(m/s)^2)\tau^2. \tag{6.24}$$

Figure 6-4: Radial spatial, temporal, and space-time correlations for data at locations along beam 1 of the ADCP. The correlation length is determined by fitting an exponential function to the radial spatial correlation.

What we see in figure 6-4 is that this prediction is too slow. In Favre's work, the turbulence was advected with steady mean flow, and the fluid elements moved according to their fluctuations. In the ocean, interaction with the waves is clearly

affecting the diffusion rate. Secondly, the exponential function for $f(r)$ fits the data better for the spatial correlation, and the Gaussian approximation for $f(r)$ doesn't decay fast enough at the small lags. Finally, we see that the space-time correlations have some similar structure to that given by the data, but that this first approximation is a poor one.

The next step is to allow $< y_i^2 > /L^2$ to be determined empirically, indirectly leading to estimates of the mean square path of the fluid elements,

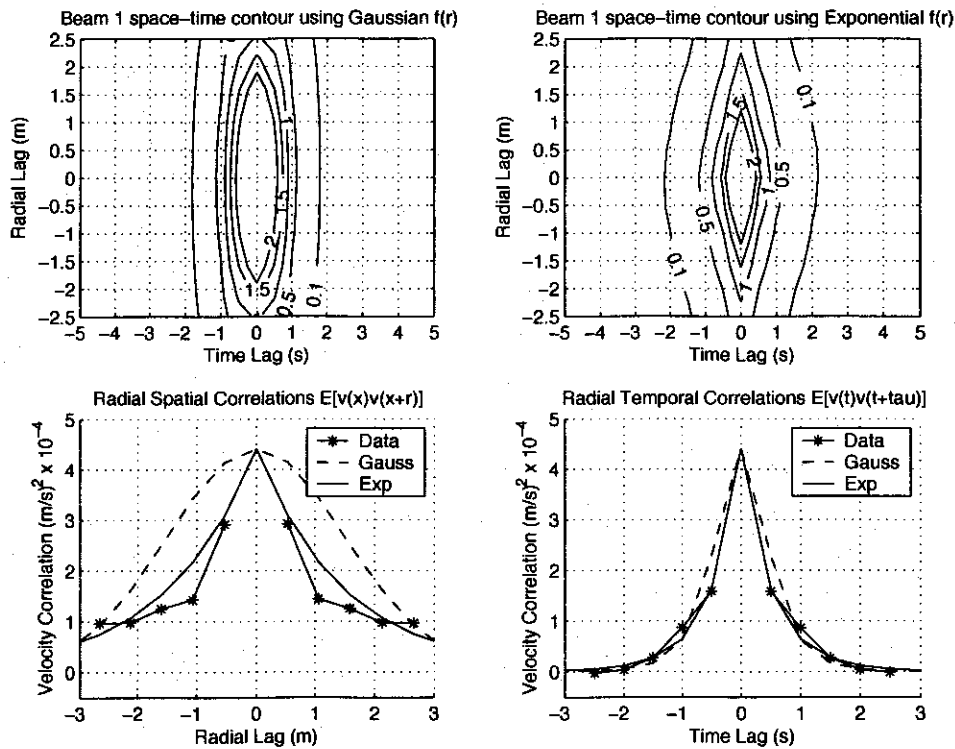$$< y_i^2 > \approx (1(m/s)^2)\tau^2. \qquad (6.25)$$

Figure 6-5: Radial spatial, temporal, and space-time correlations for data at locations along beam 1 of the ADCP. The temporal decay rate is found by adjusting $< y_i^2 > /L^2$ until the model matches the radial temporal correlations.

Looking at figure 6-5, the agreement between model and data is much improved. Now in addition to individual agreement with spatial and temporal correlations, the space-time correlations show remarkable similarities with the data. Though the exponential approximation for $f(r)$ more closely matches the spatial and temporal cor-

relations on the axes, the Gaussian approximation for $f(r)$ more closely matches the off-axes space-time correlations.

6.6 Simulated flow results

Chapter 3 presented techniques to simulate turbulent data for a spatially homogeneous, isotropic field that is not evolving in time. To illustrate the process of diffusion, consider a random walk of the fluid elements (which carry the velocity fluctuations). As time progresses, neighbors move further apart, and the overall effect on the correlation is towards homogeniety of fluctuations.
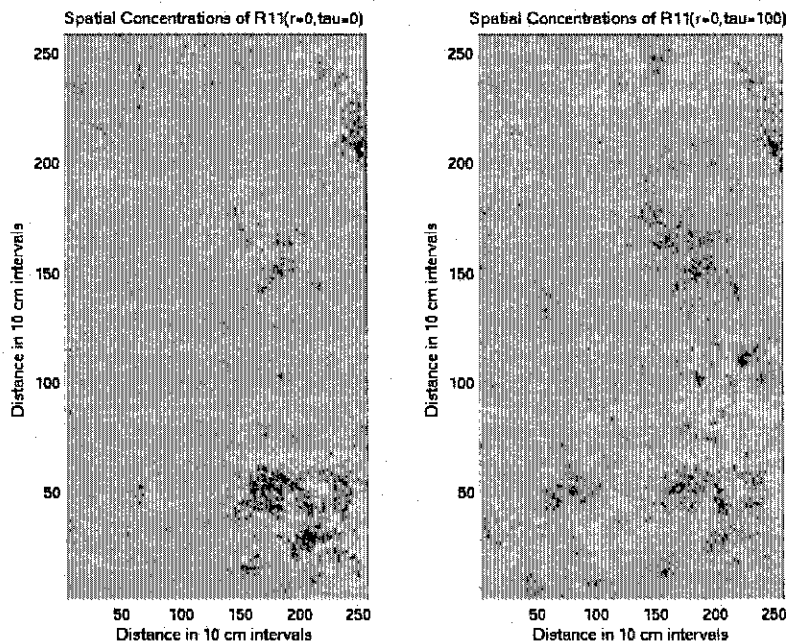

Figure 6-6: Diffusion illustrated by a random walk of fluid elements. Decorrelation occurs with time as the spatial field tends toward uniformity.

The random walk example works for temporal correlations, but not for simulating an evolving flow which is always in the present time ($\tau = 0$). In addition, evoking a random walk from time step to time step will destroy the homogeneous, isotropic nature of the spatial field at $\tau = 0$. Instead, it was postulated that one of the directions can be sacrificed in order to create the illusion of time evolution. Since the flow already will advect in the horizontal plane with the mean current, it is natural

to consider a vertical direction for time evolution. This can work for the situation where time series in small selected regions are needed (radial beam locations).

The main goal is that locations on the beams will arrive at correlations that are based on an evolving flow. This will fail if any beam locations receive the exact same data from some other beam locations. For example, looking at the distances between points on beam 1 and points on the opposite beam 2, figure 6-7 shows that only locations close to the ADCP will see the same data over a 15 second period of consideration.
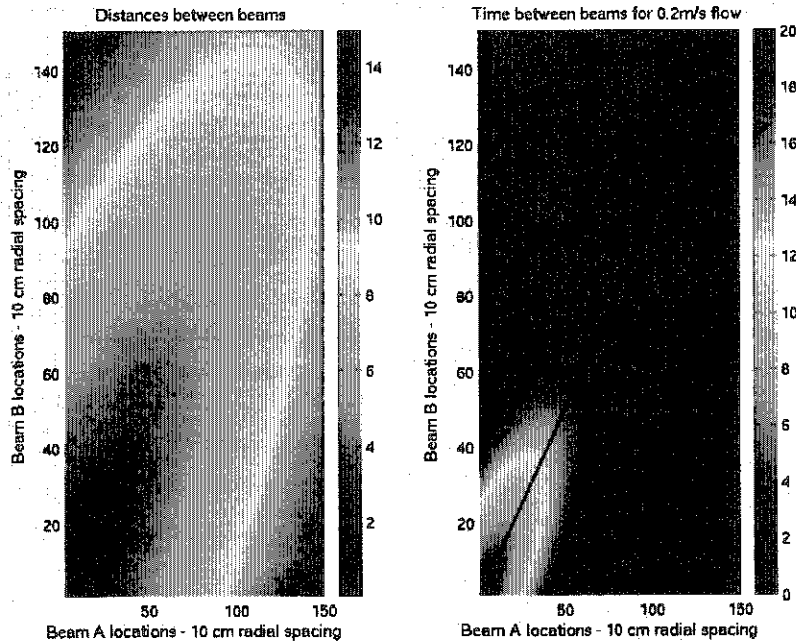

Figure 6-7: Distances between beam 1 locations and beam 2 locations, and the corresponding locations were data overlaps within 15 seconds of time for a flow moving at 0.2 m/s.

By moving the data in a vertical direction, the effective spatial distance is increased which causes decorrelation in the data. In addition, as the data is advected horizontally, control can be exercised to make sure that data does not overlap at other beam locations.

6.7 Boundary Issues

This chapter presented the derivations for the full space-time correlations for homogeneous, isotropic, turbulence. In the ocean setting, this approximation should work where the shear is not significant, and in fact, could help confirm whether the flow is homogeneous and isotropic in those regions. But what about near the boundaries, or in significant shear? Figure 6-8 shows the radial space-time correlations for the flow near the ocean bottom. Notice that the presence of the boundary significantly changes things. The next chapter presents a model for space-time correlations in non-homogeneous, non-isotropic shear flows.
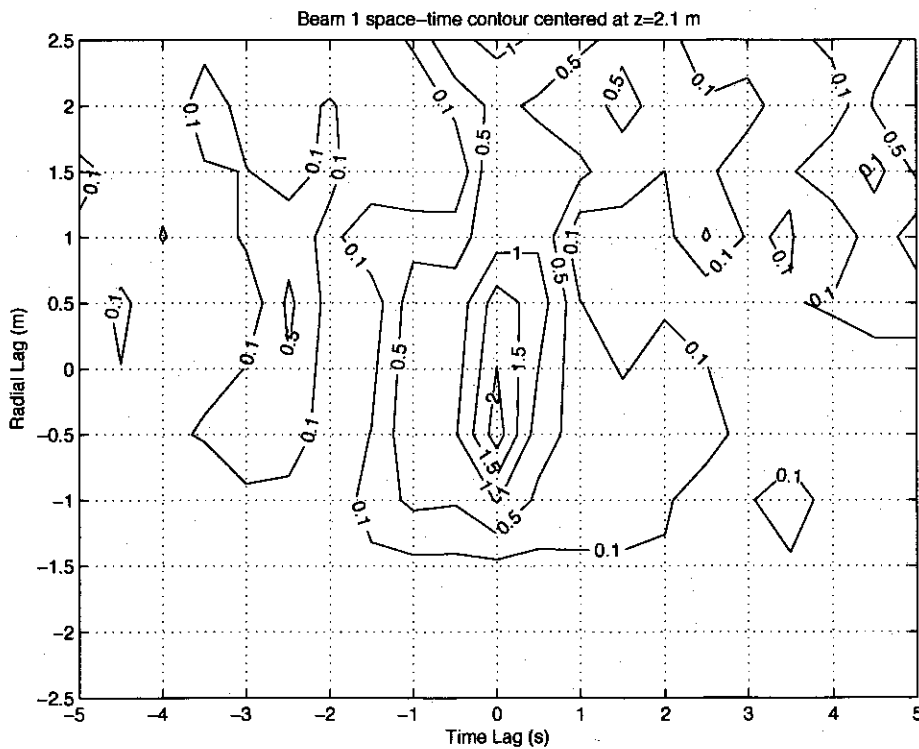

Figure 6-8: Space-time correlations for beam 1 ADCP data, from the Martha's Vineyard Coastal Observatory, yearday 260, 2005, at 8:40 am. The space-time correlations around the center point of 2.1m become distorted near the ocean bottom.

Chapter 7

Non-Homogeneous,Anisotropic
Turbulent Shear Flows

It was seen in the data that, although the model developed for the space-time correlations of homogeneous, isotropic turbulence will be useful in some regions of the flow, there are regions closer to the ocean bottom that are not istropic. Phillips presents a working model for space-time correlations in turbulent shear flows.[16] This model was developed for boundary layer flow, and to the extent that the wave process is truly independent from the turbulent process, the model should prove useful.

The foundational observation which Phillips will utilize is that in any horizontal plane of fixed depth, the space-time correlations are very similar to those for homogeneous, isotropic turbulence. By utilizing empirical data from boundary layers, the basic space-time correlations developed for homogeneous, isotropic turbulence can be modified for directionality. In particular, the $< y_i^2 > /L^2$ can be modeled according to shear flow data, and additional contraints can be imposed on the more general equations which will lead to the non-homogeneous, anisotropic model.

7.1   Chapter Overview

In the section 7.2, basic theory of the flow near a boundary layer is presented, along with the introduction of some dimensional scaling factors. In section 7.3, Phillips

133

method will be presented. In addition, predictions using the complete space-time cross-correlation equation will be compared with data from Favre [6].

7.2   Basic Boundary Layer Structure

The basic theory for boundary layer flows has been well established, and what is presented here is from [2].

A turbulent boundary layer flow consists of a small viscous layer influenced by viscosity, a large intermediate region where similarity models are used to predict velocities, and the outer region where the turbulence blends in with the free-stream flow. The viscous layer is further divided into a very thin viscous sublayer and a buffer layer. The buffer layer is the transition from the thin vicscous layer to the intermediate layer, and is where much of the turbulence is generated.

Near the edge of the free stream region, the boundary fluctuates between turbulent regions and laminar regions, which are changing in time. This is called intermittancy, and is found to occur between $0.5 \leq z/\delta \leq 1.3$. Therefore, any measure of the boundary layer thickness must be a statistical one. One possible measure of the thickness, $\delta(x)$, is to assign it the distance from the boundary when the mean flow is 99 % of the free stream flow. Another common definition is that of displacement thickness,

$$\delta^*(x) = \int_0^\infty \left(1 - \frac{\overline{u}(x,z)}{u_\infty}\right) dz \qquad (7.1)$$

which transforms the mass flux deficit into an equivalent thickness of the free stream layer. In the near coastal zone of ocean, the boundary layer thickness could vary well be the whole layer itself.

Boundary layer varaibles are often scaled by terms which are characteristic of the flow in that region. This leads to flows of very disparate sizes having similar behaviour when scaled by these terms.

The friction velocity is defined as

$$U_\tau = \left(\frac{\tau_w}{\rho}\right)^{1/2},$$
(7.2)

where ρ is the density and τ_w is the shear stress at the wall,

$$\tau_w = \mu \frac{\partial u}{\partial z}(0).$$
(7.3)

Distances are scaled by a corresponding length scale, ν/U_τ, so that wall units are represented as

$$z^+ = \frac{U_\tau z}{\nu}.$$
(7.4)

Finally, the Reynolds number for boundary layer flows is given as

$$R_\tau = \frac{U_\tau \delta}{\nu}.$$
(7.5)

The mean flow near the boundary depends on z, τ_w, ν, and ρ. These parameters combine to form the friction velocity, U_τ, and the length scale, ν/U_τ. Therefore $\overline{u}/U_\tau = f(z^+)$. The velocity at the boundary is zero (by the no slip condition), and very close to the boundary (up to $z^+ \approx 5$), the mean velocity is found to vary linearly.

$$\overline{u}^+(z^+) = z^+$$
(7.6)

This is called the Law of the Wall.

In the intermediate region, von Karman developed a Log Law, which has recently been challenged by some who think a Power Law is more appropriate.

The Log Law is developed from matching the buffer region to the intermediate region. In the buffer region, the main stress is no longer due to viscous effects, but is now dominated by the Reynolds stress, and so the parameters of interest are z, τ_w, and ρ. Instead of using $\overline{u}$ (which has the no slip boundary constraints), $d\overline{u}/dz$ is used, leading to $d\overline{u}/dz \sim U_\tau/z$ Introducing the von Karman constant, κ, and integrating,

135

gives

$$\overline{u}(z^+) = \frac{1}{\kappa} \ln z^+ + C \tag{7.7}$$

The Power Law is currently based on an empirical fit to the data (although theoretical work is begin developed to justify it).

$$\overline{u}(z^+) = \beta(z^+)^\alpha \tag{7.8}$$

β and α are found to be Reynolds number dependent.

In the outer region, the mean flow depends on U_τ, z, and δ. This leads to the Velocity Defect Law:

$$\frac{u_\infty - u(z)}{U_\tau} = f(\xi). \tag{7.9}$$

This law deviates from the Log Law in the region $0.1 \leq \xi \leq 1$, though modifications such as Cole's law of the wake remedy that. It is also possible to fit a second power law to this region. Perhaps the simplist empirical relationship was developed by Hana, which says

$$f(\xi) = 9.6(1 - \xi^2). \tag{7.10}$$

In addition to characterizing the mean flow, it is possible to formulate the structure of the mean square turbulent fluctuations in an ideal shear flow (without wave effects). Phillips [15, 17] has worked out the asymptotic expressions for the turbulent intensities at high Reynolds number for the wall, intermediate, and outer regions.

From the wall region into the intermediate region, the approximate solutions are

$$\frac{\overline{u}}{U_\tau} = \chi(z^+) = \frac{1}{2} \int_0^{z^+} \frac{1 + e^{-[(1/8)\kappa^2\lambda]^3}}{[1 + (1/8)(\kappa\lambda)^3]^{1/3}} d\lambda + O\left(\frac{U_\tau}{u_\infty}\right) \tag{7.11}$$

$$\frac{\overline{uw}}{U_\tau} = \phi(z^+) = \frac{d\chi}{dz^+} - 1 \tag{7.12}$$

$$\frac{\overline{w^2}}{U_\tau} = \theta(z^+) = \frac{\kappa^2}{2} \int_0^{z^+} \frac{[(\kappa/2)\lambda]^3(e^{-[(\kappa/4)^2\lambda]^3} - \kappa^2/3)}{[1 + [(\kappa/2)\lambda]^3]^{4/3}} d\lambda + O\left(\frac{U_\tau}{u_\infty}\right) \tag{7.13}$$

136

$$\frac{\overline{u^2}}{U_\tau} = \beta(z^+) = \frac{1}{4} \int_0^{z^+} \frac{\lambda[e^{-[(\kappa/4)\lambda]^3} - (8/7)\kappa^3 e^{-[(\kappa/4)^2\lambda]^3}\kappa^3/4]}{[1 + [(\kappa/4)\lambda]^3]^{2/3}} d\lambda + \theta(z^+) + O\left(\frac{U_\tau}{u_\infty}\right)$$

(7.14)

$$\frac{\overline{v^2}}{U_\tau} = \zeta(z^+) = \frac{\kappa^2}{4} \int_0^{z^+} \frac{\lambda[(1+\kappa)e^{-[(1/8)\kappa^2\lambda]^3} - \kappa]}{[1 + [(\kappa/2)\lambda]^3]^{2/3}} d\lambda + \kappa\theta(z^+) + O\left(\frac{U_\tau}{u_\infty}\right)$$

(7.15)

These are Phillips' equations (32-36) [15], with notation changed to be consistent with this thesis, and the results are plotted in figure 7-1. κ is von Karman's constant, 0.41. At high z^+, the asymptotic expressions are given by

$$(\beta_\infty, \theta_\infty, \zeta_\infty) = (5.789, 1.128, 4.248) - (\kappa, \kappa^3/3, \kappa/\sqrt{2}) \ln z^+.$$
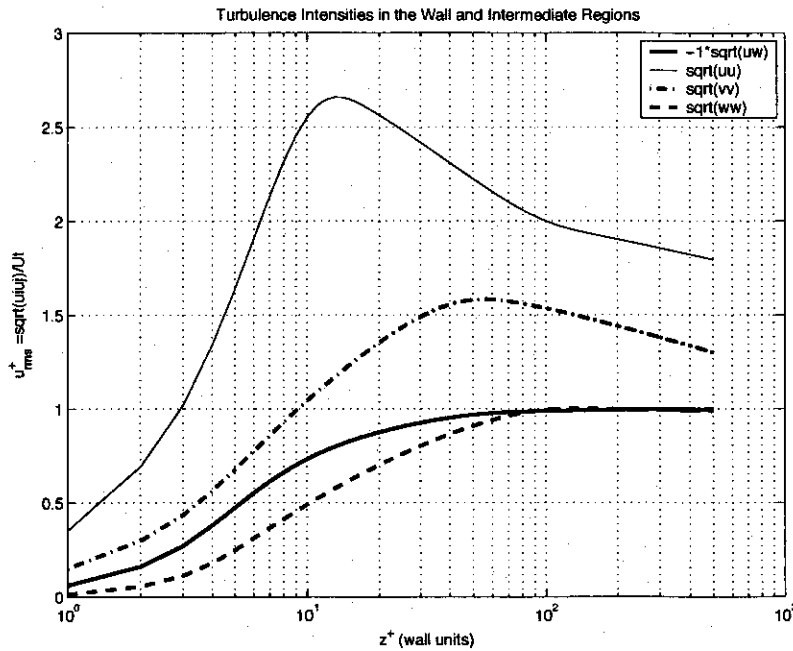
(7.16)

Figure 7-1: Turbulent intensities in the wall and intermediate regions.

From the intermediate region through the outer region, Phillips joins the asymptotic expressions developed for the wall and intermediate region to a velocity defect law in the outer region. [17] He develops a turbulence law of the wake in the spirit of Cole's law of the wake. Figure 7-2 shows the turbulence intensities throughout the entire boundary layer for $Re_\delta \approx 17000$.
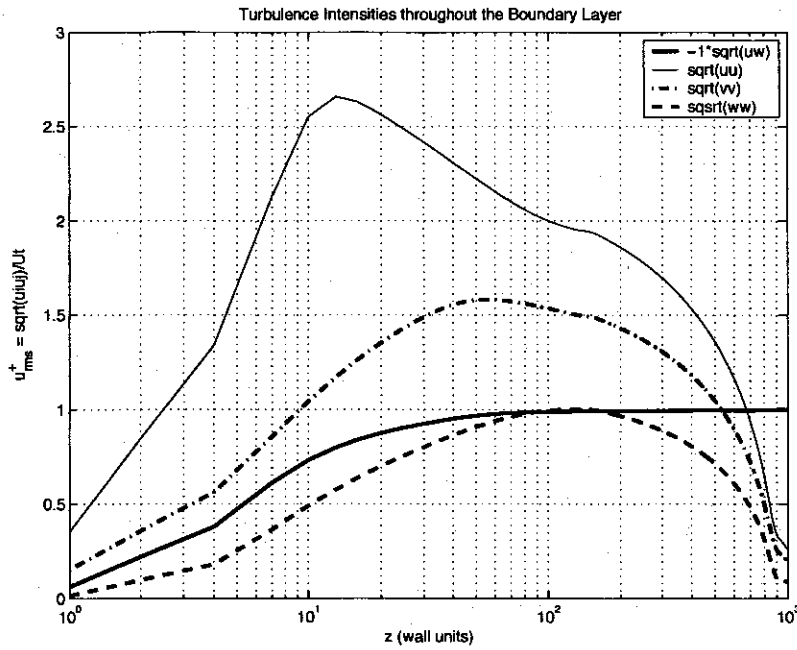
Figure 7-2: Turbulent intensities throughout the entire boundary layer at $Re_\delta \approx$ 17000.

7.3 Phillip's Model for $Rij(\vec{r}, \tau)$

Phillips' overall methodology is to begin with the longitudinal, $f(r)$, and lateral, $g(r)$, correlations at optimal delay, and to introduce componentwise modifications consistent with shear flow data. The first modification is to introduce directionality into the correlation length.

$$L \longrightarrow L_i, \qquad \frac{<y_i^2>}{L^2} \longrightarrow \frac{<y_i^2>}{L_i^2} \tag{7.17}$$

Then the longitudinal correlation, $R_{11}(r_1, 0, 0, \tau)$, and lateral correlations, $R_{22}(r_1, 0, 0, \tau)$, $R_{33}(r_1, 0, 0, \tau)$, in the mean flow $\vec{v} = (v_1, 0, 0)$ are given by (Phillips equation 2.12),

$$R_{ii}(\vec{r}, \tau) = \frac{e^{-N^2/2}}{D^3}[1 - \frac{1}{2}\Delta_{ii}B] \tag{7.18}$$

where $i = 1, 2, 3$, repeated indices do not indicate summation, and $\Delta_{ii} = \delta_{i2} + \delta i3$. Phillips then defines L_i as that optimal distance $r_1 = v_1\tau$ where the correlation is 1/2. Figure 7-3 presents the longitudinal and lateral correlations at optimal delay.
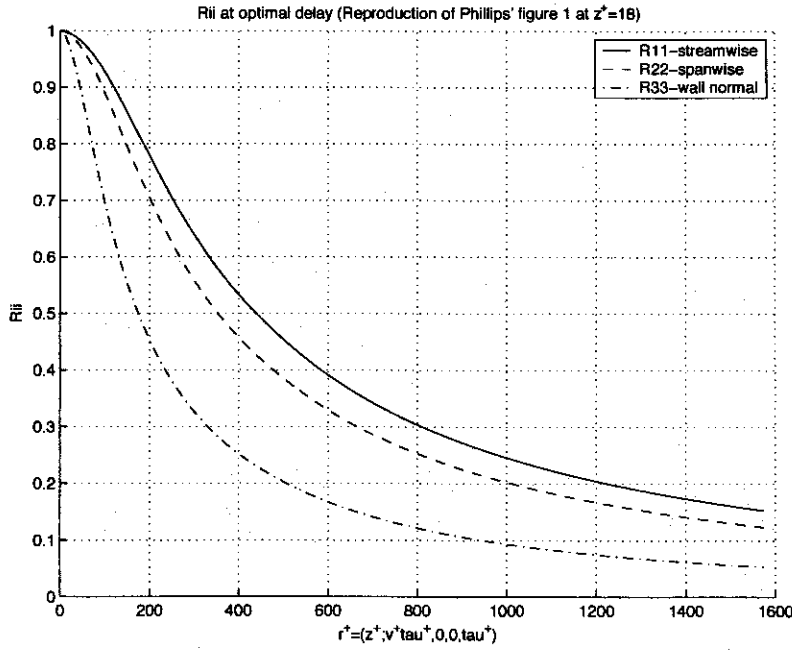
138

Figure 7-3: Correlations at optimal delay (Reproduction of Phillips figure 1)

When they are plotted against the nondimensional variable, η, (Phillips equation 3.1)

$$\eta = \frac{(r_1)_i}{L_i} = \frac{v\tau_i}{L_i},\qquad(7.19)$$

the plots collapse to a single line. Since at optimal delay (at a given height, z^+), $R_{ii}(z^+; v_1^+ \tau^+, 0, 0, \tau^+) = 1/D^3$ collapse to a single line, a new correlation function at optimal delay is proposed by Phillips: (equation 3.4)

$$R(\eta) = (1 + F(\eta))^{-3/2}.\qquad(7.20)$$

Phillips finds a good fit to the data given by (equation 3.2)

$$F(\eta) = \frac{\eta^2}{(1 + A\eta^n)^{1/n}},\qquad(7.21)$$

139

where $A = \gamma^n - 1$, $\gamma \approx 1.7024$ to insure that the correlations are $1/2$ at $\eta = 1$, and $n = 2$. The relationship is independent of height, and is given by

$$\frac{< y_i^2 >}{L_i^2} = \frac{(v_1\tau)^2/L_i^2}{(1 + A(v_1\tau/L_i)^n)^{1/n}}. \tag{7.22}$$

In the absence of a convection velocity, the mean square path is just due to the diffusion of the fluctuating turbulent velocities, $< y_i^2 >=< u_i^2(z) > \tau^2$. Therefore, Phillips replaces v_1 with $v+ < u_i^2 >$, where v close to the boundary layer will be determined by the basic boundary layer theory.

$$\frac{< y_i^2 >}{L_i^2} = \frac{(v+ < u_i^2 >^{1/2})^2\tau^2}{L_i^2 \left[1 + A\left(\frac{(v+<u_i^2>^{1/2})\tau}{L_i}\right)^n\right]^{1/n}}. \tag{7.23}$$

In addition, it is known that for short times that $< y_i^2 > /L_i^2$ varies quadratically in τ, but that for longer times it varies linearly. The time which governs this transition is called the Lagrangian time scale, T_i. Introducing these changes, the final form is (Phillips equation 3.3)

$$\frac{< y_i^2 >}{L_i^2} = \frac{(v+ < u_i^2 >^{1/2})^2\tau^2}{L_i^2 \left[1 + \left(\frac{\tau}{T_i}\right)^n\right]^{1/n}} \tag{7.24}$$

Comparing the two equations, an equation for the Lagrangian time scale is given as (Phillips equation 3.6)

$$T_i(z) = \frac{vL_i}{\gamma(v^2+ < u_i^2 >)}. \tag{7.25}$$

At this point, Phillips develops an empirical expression for T_i, normalized by it's free stream value for broader application. (Phillips equation 3.7)

$$\frac{T_i}{T_{i_\infty}} = \left(\frac{v}{u_\infty}\right)^m + \alpha_i\frac{z}{z_\infty}\exp\left[-\left(\frac{z - z_o}{\beta z_\infty}\right)^2\right] \tag{7.26}$$

where $\alpha_i = (8.5, 9.9, 2.0)$, $z/z_\infty \approx 0.4$, $\beta \approx 0.1$, and m=5/2. All that is needed is information about $< u_i^2 >$ and v. Phillips uses the theoretical values for $< u_i^2 >$ developed in the preceding section, and constructs an empirical expression for the

convection velocity, v.(Phillips equation 3.8)

$$v^+ = 0.55\overline{u}_\infty^+ \frac{d\overline{u}/dz}{(d\overline{u}/dz)(0)} + \frac{z^+}{z_\infty^+}\left(\frac{z_\infty^+ + z_1^+}{z^+ + z_1^+}\right) \qquad (7.27)$$

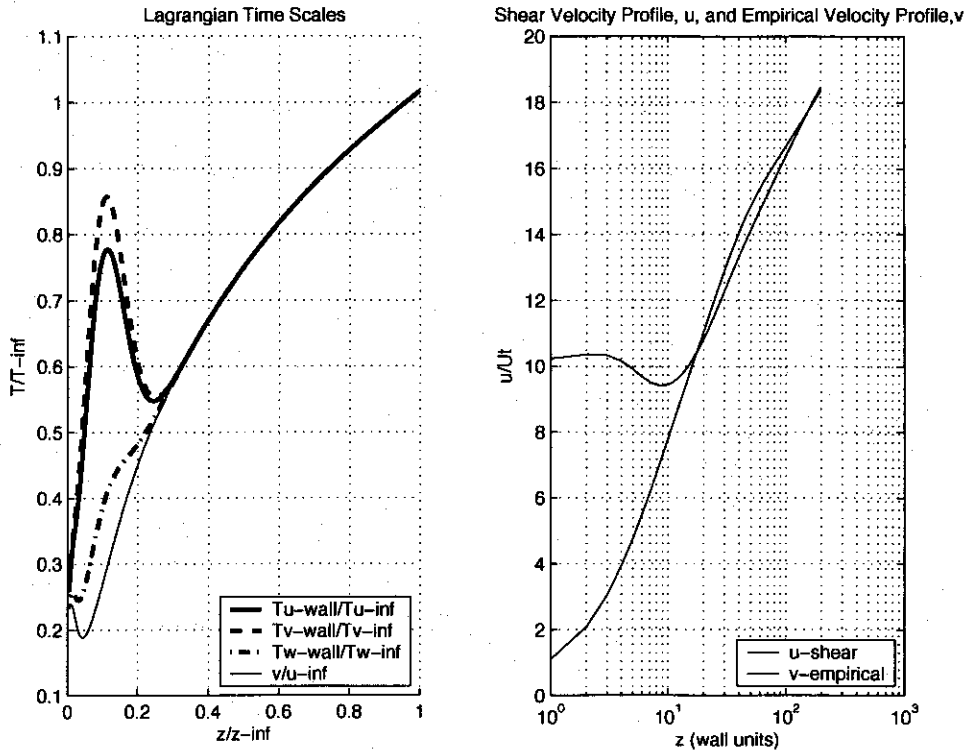Figure 7-4 presents Phillips' results.

Figure 7-4: Plots of the empirically developed T_i/T_{i_∞} and v.

These equations provide all that is needed to determine R_{ij} at optimal delay. To determine how R_{ij} will behave at non-optimal delay, Phillips again turns to the data and modifies N_j and B_j to incorporate the additional vertical dependencies.

$$(N_i^*)^2 = 2h_i^2 N^2, \quad B_i^* = 2h_i^2 B, \quad h_i = \alpha_i\left(9\frac{z}{z_\infty} + 1.5\right) \qquad (7.28)$$

with $\alpha_i = (1, 1.8, 1.8)$. The final modification for B_j is to change $< y_i^2 >$ to $< u_i^2 >$ in the term that represents changes reletive to the convected component. Otherwise

141

that term is dominated by the mean velocity, v.

$$B_j = \frac{1}{1 + \frac{<y_j^2>}{L^2}} \left[\frac{<u_j^2>}{L^2} + \frac{(r_j - v_j\tau)^2}{L^2 \left(1 + \frac{<y_j^2>}{L^2}\right)} \right]. \qquad (7.29)$$

The final equation for the cross-correlations in a shear flow is (Phillips equation 5.1)

$$R_{ij}(\vec{r}, \tau) = \frac{e^{-N_i^* N_j^*/2}}{(D_i D_j)^{3/2}} [1 - \frac{1}{4}(\Delta_{ii} + \Delta_{jj})(B_i^* B_j^*)^{1/2}] \qquad (7.30)$$

Phillips compared $R_{31}(r_1, 0, r3, \tau)$ with Favre's data at $z/\delta = 0.135$, and found that it predicted the results quite well.
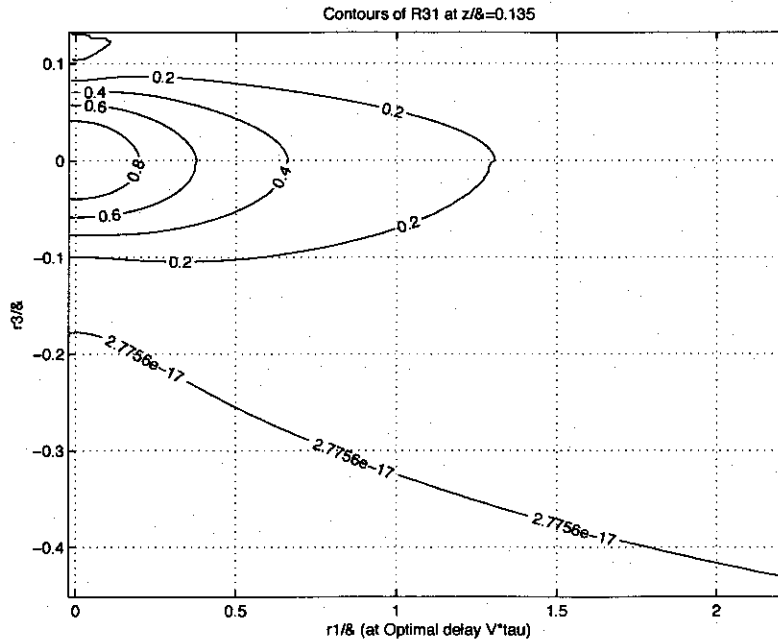

Figure 7-5: Phillips' $R_{31}(r_1, 0, r3, \tau)$ as a prediction of Favre's data at $z/\delta = 0.135$.

When comparing $R_{11}(r_1, 0, r3, \tau)$ with Favre's data at $z/\delta = 0.03, 0.135, 0.77$, the form is essentially correct but exhibiting faster decay. This decay rates will not be an issue when being used with ocean data because they will be determined empirically.
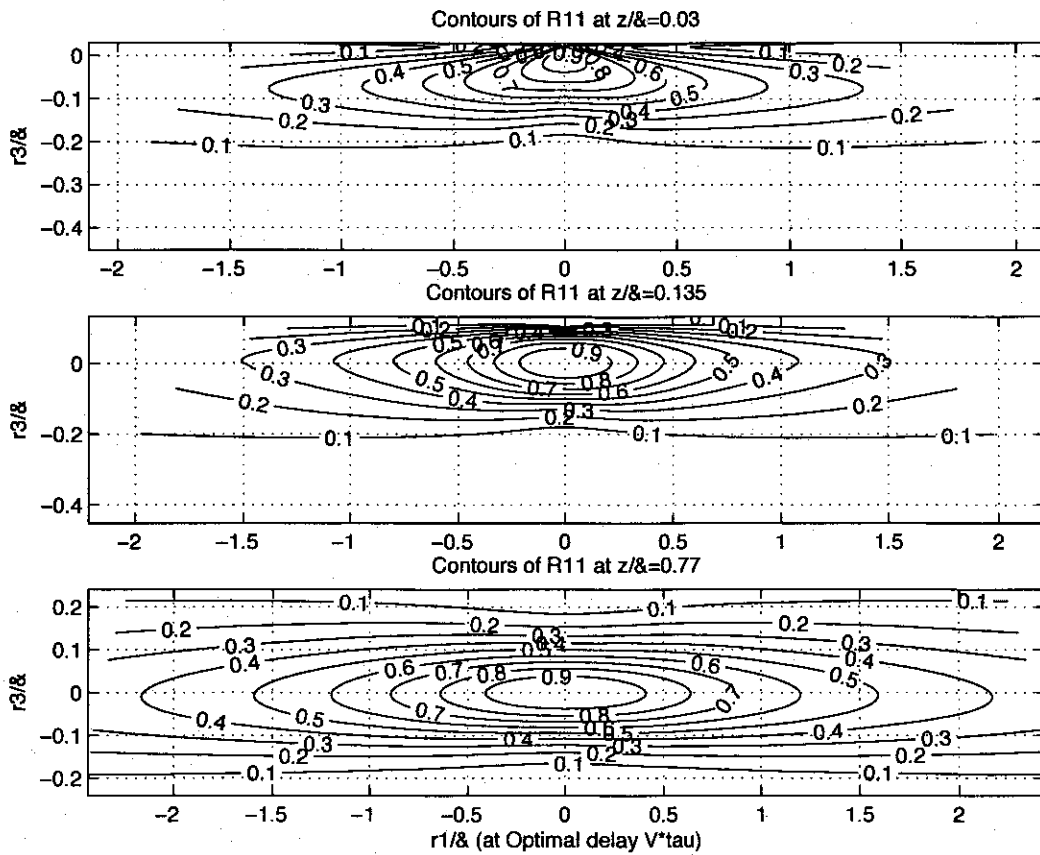
Figure 7-6: Phillips' $R_{11}(r_1, 0, r3, \tau)$ as a prediction of Favre's data at $z/\delta = 0.03, 0.135, 0.77$.

Chapter 8

Space-time correlations for Wave Induced Velocities

This chapter will develop the space-time correlations for the wave induced velocities. It will begin with monochromatic waves, and build in complexity as needed. This will include formulations for a random sea state, a multi-directional sea state, and multi-events. Not all of this is necessary, but it makes the model more adaptable.

8.1   Monochromatic Waves

As a starting point, the surface waves will originate from one direction, θ, be of one wavelenth, λ, and have random phase, Θ. Horizontal wave velocities at a given point, $\vec{\mathbf{x}}$, along beam 1, are given by

$$\tilde{u}_1(\vec{\mathbf{x}}) = A\omega(\cos\theta)\frac{\cosh(kz)}{\sinh(kh)}\cos(k\cos\theta x + k\sin\theta y - \omega t + \Theta), \qquad (8.1)$$

$$\tilde{u}_2(\vec{\mathbf{x}}) = A\omega(\sin\theta)\frac{\cosh(kz)}{\sinh(kh)}\cos(k\cos\theta x + k\sin\theta y - \omega t + \Theta), \qquad (8.2)$$

where A is the amplitude of the wave, ω is the frequency, $k = 2\pi/\lambda$ is the wavenumber, z is the height above the ocean floor, and h is the depth of the water. The dispersion

relationship is given by

$$\omega^2 = gk \tanh(kh), \tag{8.3}$$

where g is the accleration of gravity $(9.81 ms^{-2})$. The vertical wave velocities at the same point along beam 1 are given by

$$\tilde{u}_3(\vec{\mathbf{x}}) = A\omega \frac{\sinh(kz)}{\sinh(kh)} \cos(k\cos\theta x + k\sin\theta y - \omega t + \Theta), \tag{8.4}$$

The space-time wave correlations for two points along beam 1 are then,

$$
\begin{aligned}
\widetilde{R}_{11}(\vec{x}_a, t_a, \vec{x}_b, t_b) &= E[\tilde{u}_1(\vec{x}_a, t_a)\tilde{u}_1(\vec{x}_b, t_b)] \\
&= A^2\omega^2(\cos^2\theta)\frac{\cosh(kz_a)\cosh(kz_b)}{\sinh^2(kh)} E[\cos(k\cos\theta x_a + k\sin\theta y_a - \omega t_a + \Theta) \\
&\qquad\qquad \cdot \cos(k\cos\theta x_b + k\sin\theta y_b - \omega t_b + \Theta)] \\
&= A^2\omega^2(\cos^2\theta)\frac{\cosh(kz_a)\cosh(kz_b)}{\sinh^2(kh)} \left(\tfrac{1}{2}\cos(k\cos\theta(x_b - x_a) + \omega(t_b - t_a))\right)
\end{aligned} \tag{8.5}
$$

$$
\begin{aligned}
\widetilde{R}_{13}(\vec{x}_a, t_a, \vec{x}_b, t_b) &= E[\tilde{u}_1(\vec{x}_a, t_a)\tilde{u}_3(\vec{x}_b, t_b)] \\
&= A^2\omega^2(\cos\theta)\frac{\cosh(kz_a)\sinh(kz_b)}{\sinh^2(kh)} E[\cos(k\cos\theta x_a + k\sin\theta y_a - \omega t_a + \Theta) \\
&\qquad\qquad \cdot \sin(k\cos\theta x_b + k\sin\theta y_b - \omega t_b + \Theta)] \\
&= A^2\omega^2(\cos\theta)\frac{\cosh(kz_a)\sinh(kz_b)}{\sinh^2(kh)} \left(\tfrac{1}{2}\sin(k\cos\theta(x_b - x_a) + \omega(t_b - t_a))\right)
\end{aligned} \tag{8.6}
$$

$$
\begin{aligned}
\widetilde{R}_{31}(\vec{x}_a, t_a, \vec{x}_b, t_a) &= E[\tilde{u}_3(\vec{x}_a, t_a)\tilde{u}_1(\vec{x}_b, t_b)] \\
&= A^2\omega^2(\cos\theta)\frac{\sinh(kz_a)\cosh(kz_b)}{\sinh^2(kh)} E[\sin(k\cos\theta x_a + k\sin\theta y_a - \omega t_a + \Theta) \\
&\qquad\qquad \cdot \cos(k\cos\theta x_b + k\sin\theta y_b - \omega t_b + \Theta)] \\
&= - A^2\omega^2(\cos\theta)\frac{\sinh(kz_a)\cosh(kz_b)}{\sinh^2(kh)} \left(\tfrac{1}{2}\sin(k\cos\theta(x_b - x_a) + \omega(t_b - t_a))\right)
\end{aligned} \tag{8.7}
$$

$$
\begin{aligned}
\widetilde{R}_{33}(\vec{x}_a, t_a, \vec{x}_b, t_a) &= E[\tilde{u}_3(\vec{x}_a, t_a)\tilde{u}_3(\vec{x}_b, t_b)] \\
&= A^2\omega^2\frac{\sinh(kz_a)\sinh(kz_b)}{\sinh^2(kh)} E[\sin(k\cos\theta x_a + k\sin\theta y_a - \omega t_a + \Theta) \\
&\qquad\qquad \cdot \sin(k\cos\theta x_b + k\sin\theta y_b - \omega t_b + \Theta)] \\
&= A^2\omega^2\frac{\sinh(kz_a)\sinh(kz_b)}{\sinh^2(kh)} \left(\tfrac{1}{2}\cos(k\cos\theta(x_b - x_a) + \omega(t_b - t_a))\right)
\end{aligned} \tag{8.8}
$$

The final line of equation equation was obtained by evaluating the expectation. This was done using standard trigonometric identities such as $\cos A\cos B = \frac{1}{2}((\cos(A+$

146

$B) + \cos(A - B))$. The $\cos(A + B)$ term has a random phase of 2Θ, which integrates to zero (since Θ has a uniform probability distribution). In the $\cos(A - B)$ term, the Δy terms disappear along beam 1 (just as the x terms would disappear along beam 2).

Generalizing then,

$$\tilde{R}_{ij}(\vec{x}_a, t_a, \vec{x}_b, t_a) = \frac{A^2 \omega^2}{\sinh^2(kh)} D_i(\theta) D_j(\theta) F_i(kz_a) F_j(kz_b) G_{ij}(\vec{k} \cdot \Delta \vec{x} + \omega \tau) \qquad (8.9)$$

where

$$
\begin{aligned}
D_i(\cdot) &= \{\cos(\cdot), \sin(\cdot), 1\}, \ i = \{1, 2, 3\} \\
F_i(\cdot) &= \{\cosh(\cdot), \sinh(\cdot)\}, \ i = \{(1,2), 3\} \\
G_{ij}(\cdot) &= \begin{cases} (1/2)\cos(\cdot) & \text{i=j and i,j=(1,2),(2,1)} \\ (1/2)\sin(\cdot) & \text{i=1,2, j=3} \\ (-1/2)\sin(\cdot) & \text{i=3, j=1,2} \end{cases} \\
\vec{k} &= (k\cos\theta, k\sin\theta) \\
\Delta\vec{x} &= (\Delta x, \Delta y) \\
\tau &= \Delta t
\end{aligned}
\qquad (8.10)
$$

8.2   Random Sea State

To create a random sea surface state, various canonical spectrums may be used depending on which best reflects the region where work is being done. The Pierson-Moskowitz Spectrum represents a fully devloped sea state, and will suffice for the purpose of this thesis work.

The construction of a random sea state is straight forward. The amplitude at each frequency is just the square root of the spectrum at each frequency multiplied by the sampling interval. In addition, random phases are assigned.

$$\text{P-M Spectrum} = \Lambda(\omega_o) = \frac{\alpha g^2}{\omega_o^5} e^{-\beta(\frac{\omega_s}{\omega_o})^4} \qquad (8.11)$$

where α, β, and ω_s are constants determined by wind speed and other factors, and g
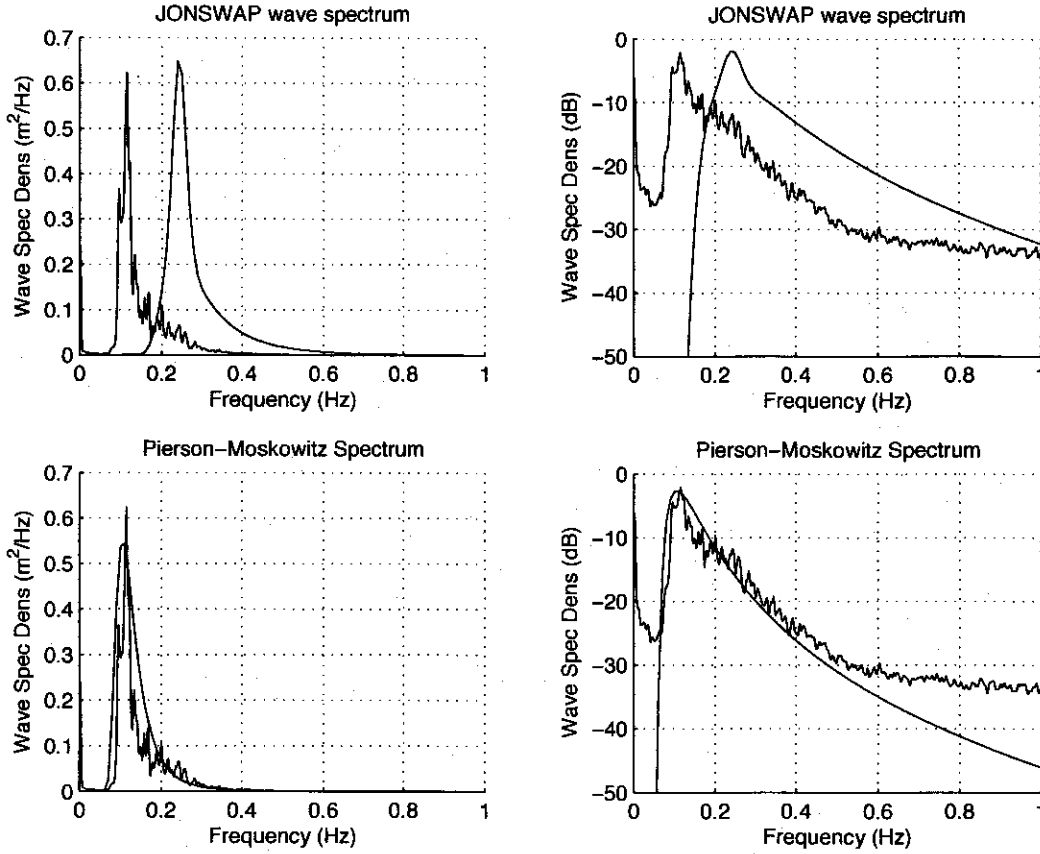
Figure 8-1: The Jonswap and Pierson-Moskowitz spectrums compared against the wave spectral density of data taken from the Martha's Vineyard Coastal Observatory array setup. The Jonswap spectrum is unable to match the data at low frequencies, whereas the Pierson-Moskowitz spectrum is unable to accurate represent the higher frequencies.

is gravity.

$$\text{Amp} = A_m = \sqrt{\frac{1}{\sqrt{2\pi}}\Lambda(\omega_m)dw} \tag{8.12}$$

where $dw = 2\pi df$, and $1/\sqrt{2\pi}$ is a normalizing factor that arises for discrete sampling of the spectrum.

$$
\begin{aligned}
\tilde{u}_1(\vec{\mathbf{x}}) &= \sum_m A_m \omega_m (\cos\theta)\frac{\cosh(k_m z)}{\sinh(k_m h)}\cos(k_m \cos\theta x + k_m \sin\theta y - \omega_m t + \Theta_m) \\
\tilde{u}_2(\vec{\mathbf{x}}) &= \sum_m A_m \omega_m (\sin\theta)\frac{\cosh(k_m z)}{\sinh(k_m h)}\cos(k_m \cos\theta x + k_m \sin\theta y - \omega_m t + \Theta_m) \quad (8.13) \\
\tilde{u}_3(\vec{\mathbf{x}}) &= \sum_m A_m \omega_m \frac{\sinh(k_m z)}{\sinh(k_m h)}\cos(k_m \cos\theta x + k_m \sin\theta y - \omega_m t + \Theta_m)
\end{aligned}
$$

When looking to find the wave correlations, it is important to remember that
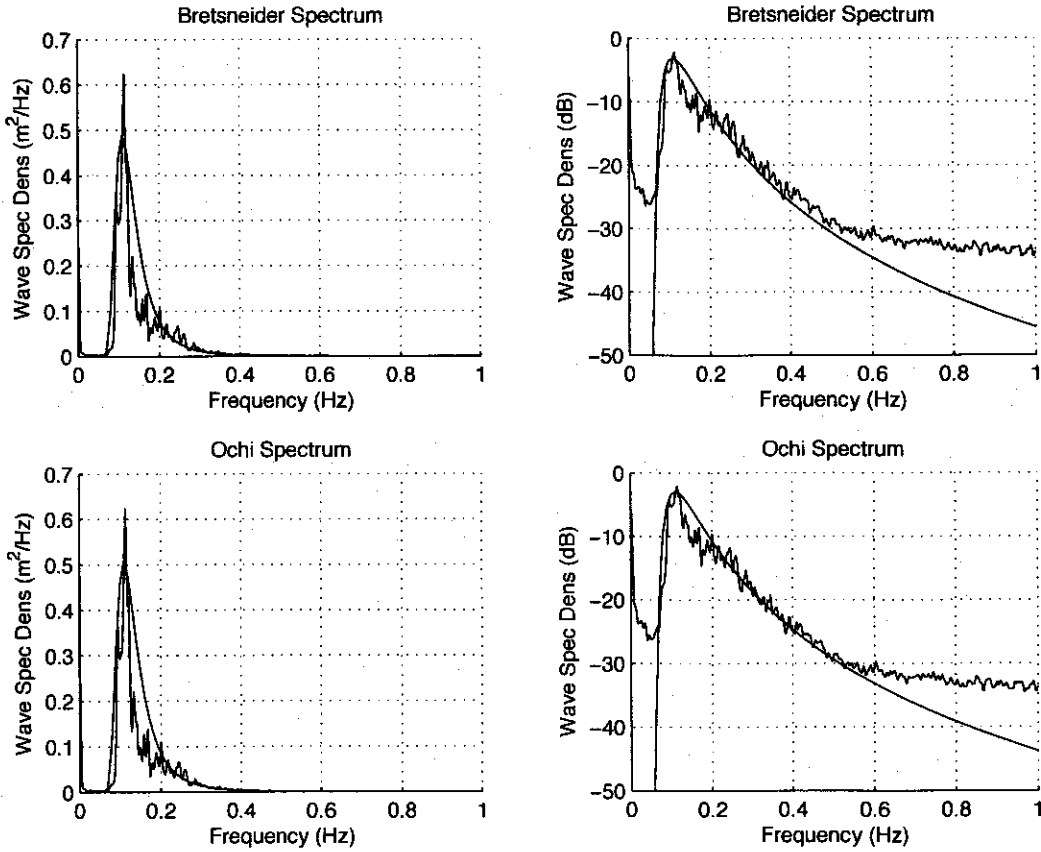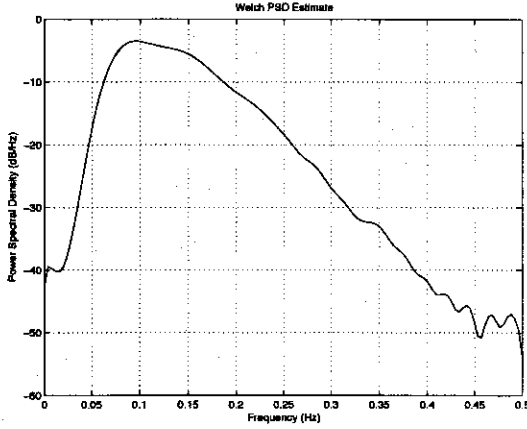
148

Figure 8-2: The Bretsneider and Ochi spectrums are shown to be comparable to the Pierson-Moskowitz spectrums.

two sets of waves at different frequencies and different phases are uncorrelated. The result is that the correlation structure is now the sum of many small correlated sets of waves.

Looking along beam 1,

$$
\begin{aligned}
\widetilde{R}_{11}(\vec{x}_a, t_a, \vec{x}_b, t_b) \quad &= E[\tilde{u}_1(\vec{x}_a, t_a)\tilde{u}_1(\vec{x}_b, t_b)] \\
&= E\left[\left(\sum_m A_m \omega_m (\cos\theta)\frac{\cosh(k_m z_a)}{\sinh(k_m h)}\cos(k_m \cos\theta x_a + k_m \sin\theta y_a - \omega_m t + \Theta_m)\right)\right. \\
&\qquad \left.\cdot \left(\sum_n A_n \omega_n (\cos\theta)\frac{\cosh(k_n z_b)}{\sinh(k_n h)}\cos(k_n \cos\theta x_a + k_n \sin\theta y_a - \omega_n t + \Theta_n)\right)\right] \\
&= \sum_{m=n} A_m^2 \omega_m^2 (\cos^2\theta)\frac{\cosh(k_m z_a)\cosh(k_m z_b)}{\sinh^2(k_m h)}\left(\frac{1}{2}\cos(\vec{k}_m \cdot \Delta\vec{x} + \omega\tau\right).
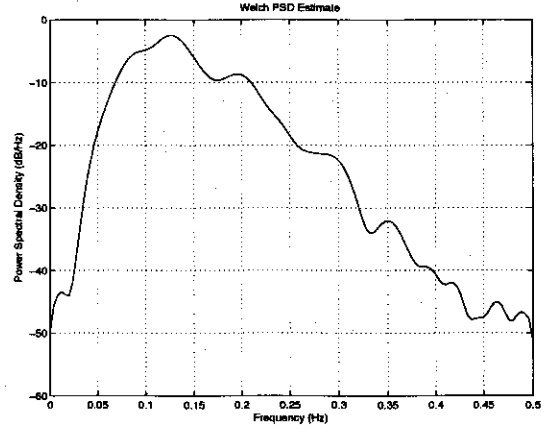\end{aligned}
$$
$$(8.14)$$

149

Figure 8-3: Power spectral densities of the simulated random sea and multidirectional sea. The data was generated by using random phases and setting the amplitude equal to the square root of the prescribed spectrums.

Generalizing then,

$$\widetilde{R}_{ij}(\vec{x}_a, t_a, \vec{x}_b, t_a) = \sum_m \frac{A_m^2 \omega_m^2}{\sinh^2(k_m h)} D_i(\theta) D_j(\theta) F_i(k_m z_a) F_j(k_m z_b) G_{ij}(\vec{k}_m \cdot \Delta\vec{x} + \omega\tau)$$

(8.15)

8.3 Waves originating from many directions

A more realistic sea state will have waves originating from many directions. At each frequency, the random amplitude can be smeared over a wide range of angles by multiplying it by a Gaussian distribution which is peaked in one direction, and has a standard deviation of any chosen directional spread. Adding a second distribution peaked in a different direction will make it is possible to simulate waves coming from two different sources. The amplitude must be normalized over the spread so that the integrated amplitude will have the same characteristics as the original spectrum that represents the sea state.

Letting θ_1 be the first main direction of incoming waves, and θ_2 be the second

150

main direction of incoming waves, the directional spread will be

$$\frac{1}{\text{NormConst}} \left[\frac{1}{\sqrt{2\pi\sigma_1^2}} e^{\frac{-(\theta-\theta_1)^2}{2\sigma_1^2}} + \frac{1}{\sqrt{2\pi\sigma_2^2}} e^{\frac{-(\theta-\theta_2)^2}{2\sigma_2^2}} \right], \qquad (8.16)$$

where NormConst is the constant that causes the distribution to integrate to 1. The variances, σ_1^2 and σ_2^2, control the influence of waves near the main directions.

Re-examining the correlation equations, all that changes is that the amplitude and phase are both a function of frequency and direction, $A(\omega, \theta)$, and $\Theta(\omega, \theta)$. Waves at different frequencies and different phases are uncorrelated, so the result is that the correlation structure is now the sum of many small correlated sets of waves. Given the horizontal and vertical velocities,

$$
\begin{aligned}
\tilde{u}_1(\vec{x}) &= \sum \theta \sum_m A_{m,\theta}\omega_m(\cos\theta)\frac{\cosh(k_m z)}{\sinh(k_m h)}\cos(k_m\cos\theta x + k_m\sin\theta y - \omega_m t + \Theta_{m,\theta}) \\
\tilde{u}_2(\vec{x}) &= \sum \theta \sum_m A_{m,\theta}\omega_m(\sin\theta)\frac{\cosh(k_m z)}{\sinh(k_m h)}\cos(k_m\cos\theta x + k_m\sin\theta y - \omega_m t + \Theta_{m,\theta}) \\
\tilde{u}_3(\vec{x}) &= \sum \theta \sum_m A_{m,\theta}\omega_n\frac{\sinh(k_m z)}{\sinh(k_m h)}\cos(k_m\cos\theta x + k_m\sin\theta y - \omega_m t + \Theta_{m,\theta})
\end{aligned}
\tag{8.17}
$$

Looking along beam 1,

$$
\begin{aligned}
\tilde{R}_{11}(\vec{x}_a, t_a, \vec{x}_b, t_b) &= E[\tilde{u}_1(\vec{x}_a, t_a)\tilde{u}_1(\vec{x}_b, t_b)] \\
&= E\left[\left(\sum_{\theta'} \sum_m A_{m,\theta'}\omega_m(\cos\theta')\frac{\cosh(k_m z_a)}{\sinh(k_m h)}\cos(k_m\cos\theta' x_a + k_m\sin\theta' y_a - \omega_m t + \Theta_{m,\theta'}) \right) \right. \\
&\qquad \left. \cdot \left(\sum_{\theta''} \sum_n A_{n,\theta''}\omega_n(\cos\theta'')\frac{\cosh(k_n z_b)}{\sinh(k_n h)}\cos(k_n\cos\theta'' x_a + k_n\sin\theta'' y_a - \omega_n t + \Theta_{n,\theta''}) \right) \right] \\
&= \sum_{\theta=\theta'=\theta''} \sum_{m=n} A_{m,\theta}^2\omega_m^2(\cos^2\theta)\frac{\cosh(k_m z_a)\cosh(k_m z_b)}{\sinh^2(k_m h)}\left(\frac{1}{2}\cos(\vec{k}_m \cdot \Delta\vec{x} + \omega\tau) \right)
\end{aligned}
\tag{8.18}
$$

Generalizing then,

$$\tilde{R}_{ij}(\vec{x}_a, t_a, \vec{x}_b, t_a) = \sum_\theta \sum_m \frac{A_{m,\theta}^2\omega_m^2}{\sinh^2(k_m h)} D_i(\theta)D_j(\theta)F_i(k_m z_a)F_j(k_m z_b)G_{ij}(\vec{k}_m \cdot \Delta\vec{x} + \omega\tau) \tag{8.19}$$

8.4 Multiple Events

Sometimes there are multiple sources of waves. For example, a storm in a far away location can send in waves, which then combine with the waves generated by the local conditions. When this occurs, each source is given its own spectrum, and the overall effect is the linear combination of them both. In the equations already presented, the amplitude can be modified as follows:

$$A_{m,\theta}^2 = A_{m1,\theta}^2 + A_{m2,\theta}^2. \tag{8.20}$$

This then gives a lot of flexibility in designing the ocean state.
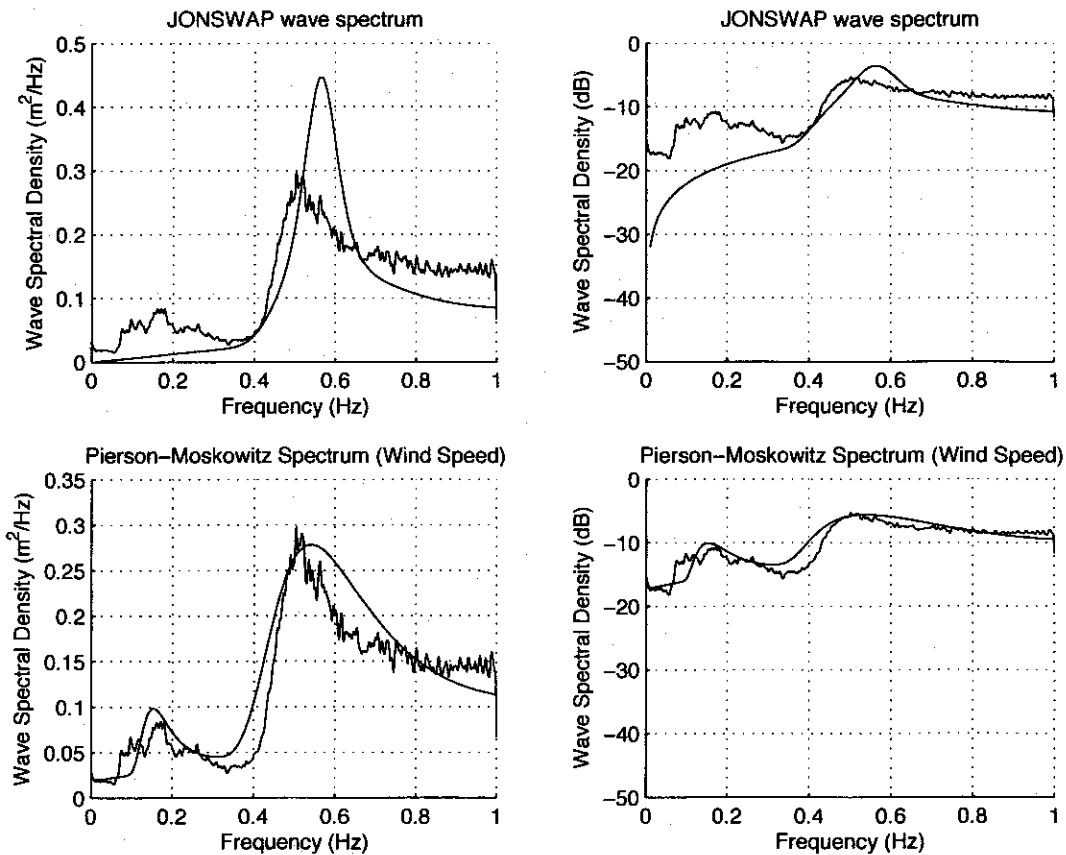

Figure 8-4: Independent events can be represented by individual spectrums. In general, the Pierson-Moskowitz spectrums can be determined by wind speed or by significant wave height.

Chapter 9

Wavenumber-Frequency Spectrum Analysis of Radial Velocities

It is difficult to separate the wave induced velocities from the turbulent fluctuations, since they share common frequencies and wavenumbers. However, as the two processes are different, it might be possible to exploit a differences in their joint wavenumber-frequency spaces. The basic idea is that the wave induced velocities are subject to the dispersion relationship, given by

$$\omega^2 = gk \tanh(kh), \tag{9.1}$$

while the turbuelent fluctuations are advected by the current and should follow a linear dispersion relationship (which is Taylor's Frozen Turbulence theorem).

$$\Delta x = v \Delta t \qquad \longrightarrow \qquad w = vk \tag{9.2}$$

However, it's their radial wavenumber-frequency spectrums which are of concern, since the ADCP only detects radial motions. In addition to the effects of combining horizontal and vertical velocities to form the radial velocities, natural filtering of wave induced velocities occurs with increasing depth in the water column, and ADCP signal transmission and subsequent processing introduce filtering effects.
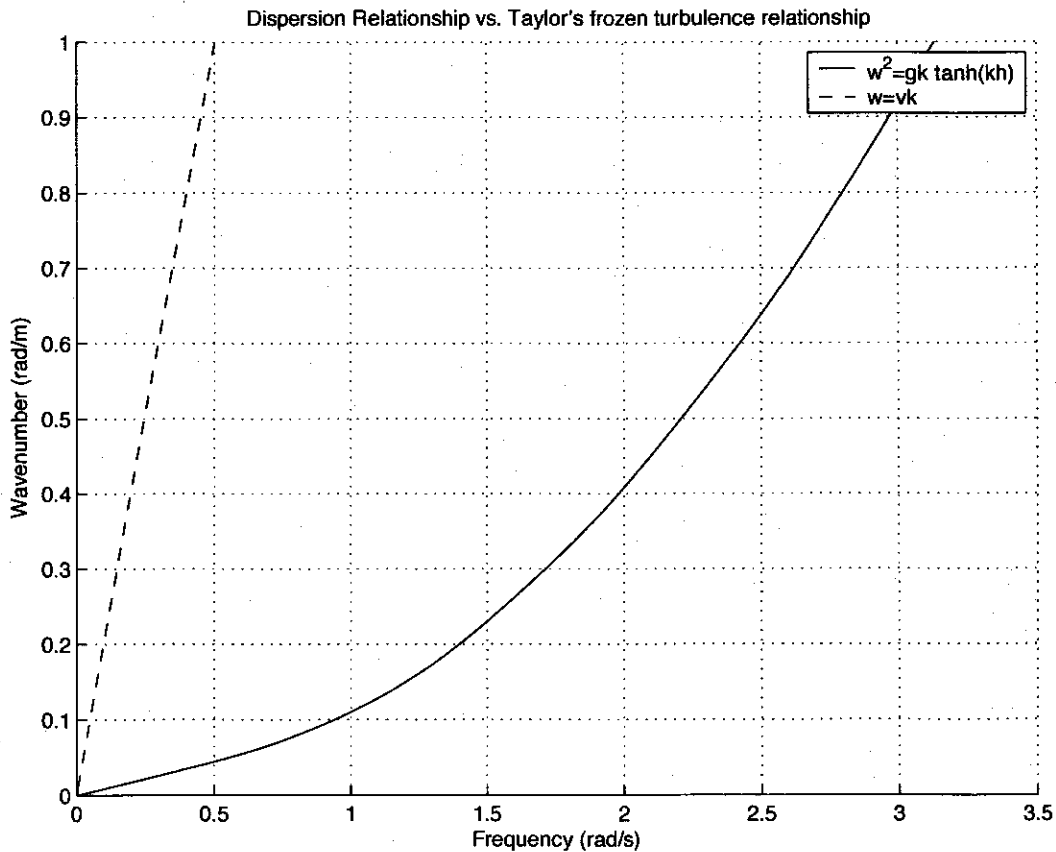
Figure 9-1: The expected separation of wave induced velocities from turbulent fluctuations in the wavenumber-frequency domain, using $\omega^2 = gk \tanh(kh)$ and w=vk respectively.

9.1 Natural filtering of wave-induced velocities

When solving the linearized wave equations, one of the general assumptions is that very far from the disturbance of the surface waves the water is still. In physical terms, that means there is a natural damping effect which attenuates both horizontal and vertical velocities.

In addition, the boundaries of the air-sea interface and the ocean bottom impose restrictions on the motions of the water. At the air-sea interface water motions follow the surface waves, but the ocean bottom suppresses vertical motion entirely. This is because it is a solid interface, and water does not penetrate through. Therefore, there is attenuation with increasing depth. Horizontal velocities do not attenuate as quickly
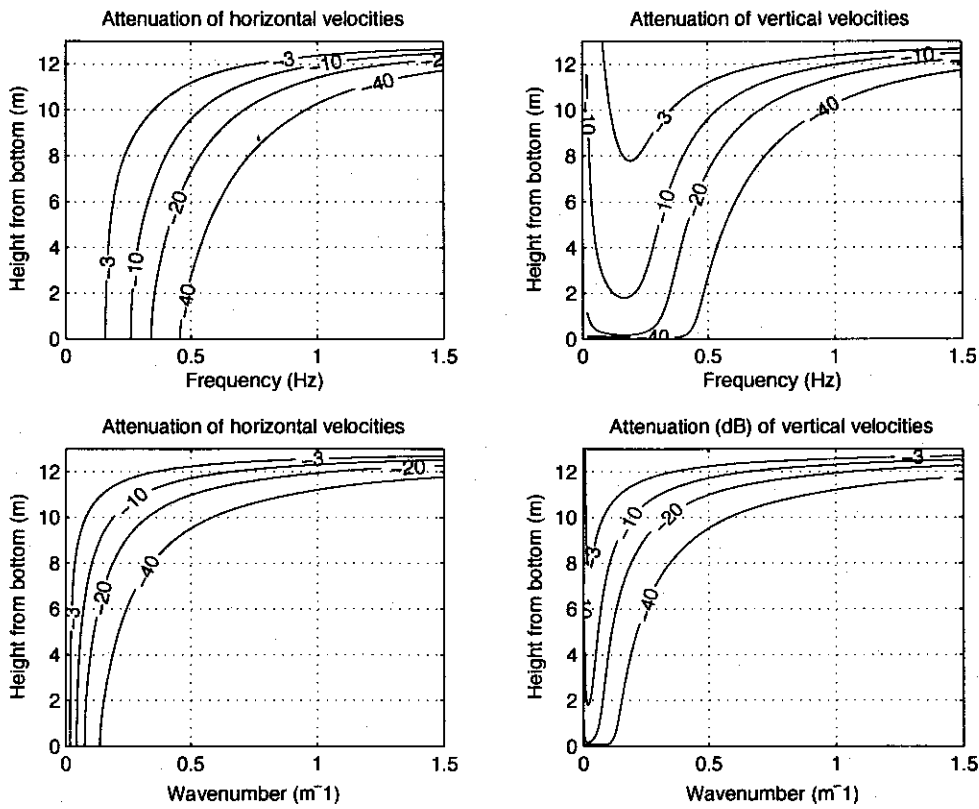
Figure 9-2: The water column acts like a low pass filter in both frequency and wavenumber. The attenuation in velocities is given in dB relative to waves having an amplitude of 1m on a surface that is 13 meters above the ocean bottom.

as vertical velocities, for there are no horizontal boundaries to impose constraints.

$$\text{horizontal velocity attenuation:} \quad \frac{\cosh(kz)}{\sinh(kh)}$$
$$\text{vertical velocity attenuation:} \quad \frac{\sinh(kz)}{\sinh(kh)} \tag{9.3}$$

What makes water depth act like a natural low pass filter is that higher frequencies and wavenumbers attenuate much more quickly than lower ones. In addition, for very low wavenumbers and frequencies, where $kh \ll 1$, the water is considered shallow and interaction with the bottom causes attenuation. The various types of attenuation can be seen in the above figure.

155

9.2 Transforming the radial wave-induced velocities

The radial velocity can be written in polar coordinates,

$$v(\vec{x}, t) \quad \longrightarrow \quad v(r, \phi, \gamma, t), \tag{9.4}$$

using the following transformation of coordinates:

$$
\begin{aligned}
x &= r\cos(\gamma)\sin(\phi) \\
y &= r\sin(\gamma)\sin(\phi) \\
z &= r\cos(\phi) + z_s
\end{aligned}
\tag{9.5}
$$

where ϕ is the tilt of the ADCP beam from the vertical, γ is the counter clockwise angle of rotation about the z-axis, r is the radial distance, and z_s is the height of the ADCP above the ocean bottom. The wavenumber-frequency spectrum is found by taking the multi-dimensional Fourier Transform.

$$v(k, w, \phi, \gamma) = \int_{-\infty}^{\infty} \int_{-\infty}^{\infty} v(r, t, \phi, \gamma) e^{-j(kr - \omega t)} dr dt \tag{9.6}$$

Since the radial velocity is a linear combination of horizontal and vertical velocities, the Fourier transforms may be handled componentwise.

$$
\begin{aligned}
u_1(r, t, \phi, \gamma, \theta, z_s) \quad &= \int_{-\infty}^{\infty} A_1(\omega_o, \phi, \theta)\cosh(k_o z)\cos(k_o\cos(\theta)x + k_o\sin(\theta)y - \omega_o t + \Theta_o)d\omega_o \\
&= \int_{-\infty}^{\infty} A_1(\omega_o, \phi, \theta)\cosh(k_o r\cos(\phi) + k_o z_s) \\
&\quad \cdot \quad \cos(k_o\cos(\theta)r\cos(\gamma)\sin(\phi) + k_o\sin(\theta)r\sin(\gamma)\sin(\phi) - \omega_o t + \Theta_o)d\omega_o \\
&= \int_{-\infty}^{\infty} A_{1,\omega_o}\cosh(B_{\omega_o}r + k_o z_s)\cos(C_{\omega_o}r - \omega_o t + \Theta_{\omega_o})d\omega_o \\
u_2(r, t, \phi, \gamma, \theta, z_s) \quad &= \int_{-\infty}^{\infty} A_{2,\omega_o}\cosh(B_{\omega_o}r + k_o z_s)\cos(C_{\omega_o}r - \omega_o t + \Theta_{\omega_o})d\omega_o \\
u_3(r, t, \phi, \gamma, \theta, z_s) \quad &= \int_{-\infty}^{\infty} A_{3,\omega_o}\sinh(B_{\omega_o}r + k_o z_s)\sin(C_{\omega_o}r - \omega_o t + \Theta_{\omega_o})d\omega_o
\end{aligned}
\tag{9.7}
$$

where

$$A_{i,\omega_o} = A_i(\omega_o, \phi, \theta)$$
$$B_{\omega_o} = k_o \cos(\phi) \tag{9.8}$$
$$C_{\omega_o} = k_o \sin(\phi)(\cos(\theta)\cos(\gamma) + \sin(\theta)\sin(\gamma))$$

and k_o is related to ω_o by the dispersion relationship. The Fourier transforms are as follows:

$$
\begin{aligned}
\breve{u}_{1,2} &= \int_0^R \int_{-\infty}^{\infty} \left[\int_{-\infty}^{\infty} A_{1,2,\omega_o} \cosh(B_{\omega_o}r + k_o z_s) \cos(C_{\omega_o}r - \omega_o t + \Theta_{\omega_o}) d\omega_o \right] e^{-j(kr-\omega t)} dt dr \\
&= \int_0^R \int_{-\infty}^{\infty} A_{1,2,\omega_o} \cosh(B_{\omega_o}r + k_o z_s) \\
&\quad \cdot \left[\pi e^{j(C_{\omega_o}r + \Theta_{\omega_o})} \delta(\omega - \omega_o) + \pi e^{-j(C_{\omega_o}r + \Theta_{\omega_o})} \delta(\omega + \omega_o) \right] e^{-jkr} d\omega_o dr \\
&= \int_0^R A_{1,2,\omega} \cosh(B_\omega r + k_\omega z_s) \pi e^{jC_\omega r} [e^{j\Theta_\omega} + e^{-j\Theta_{-\omega}}] e^{-jkr} dr \\
&= \pi A_{1,2,\omega} [e^{j\Theta_\omega} + e^{-j\Theta_{-\omega}}] \left[\frac{e^{k_\omega z_s} e^{-j(k-C_\omega+jB_\omega)r}}{-2j(k-C_\omega+jB_\omega)} \Big|_0^R + \frac{e^{-k_\omega z_s} e^{-j(k-C_\omega-jB_\omega)r}}{-2j(k-C_\omega-jB_\omega)} \Big|_0^R \right] \\
&= -j\pi A_{1,2,\omega} [e^{j\Theta_\omega} + e^{-j\Theta_{-\omega}}] \frac{k' \cosh(k_\omega z_s) - jB_\omega \sinh(k_\omega z_s) - e^{-jk'R}[k' \cosh(k_\omega z_s + B_\omega R) - jB_\omega \sinh(k_\omega z_s + B_\omega R)]}{(k')^2 + B_\omega^2} \\
\breve{u}_3 &= \int_0^R \int_{-\infty}^{\infty} \left[\int_{-\infty}^{\infty} A_{3,\omega_o} \sinh(B_{\omega_o}r + k_o z_s) \sin(C_{\omega_o}r - \omega_o t + \Theta_{\omega_o}) d\omega_o \right] e^{-j(kr-\omega t)} dt dr \\
&= \int_0^R \int_{-\infty}^{\infty} A_{3,\omega_o} \sinh(B_{\omega_o}r + k_o z_s) \\
&\quad \cdot \left[-j\pi e^{j(C_{\omega_o}r + \Theta_{\omega_o})} \delta(\omega - \omega_o) + j\pi e^{-j(C_{\omega_o}r + \Theta_{\omega_o})} \delta(\omega + \omega_o) \right] e^{-jkr} d\omega_o dr \\
&= \int_0^R A_{3,\omega} \sinh(B_\omega r + k_\omega z_s) j\pi e^{jC_\omega r} [-e^{j\Theta_\omega} + e^{-j\Theta_{-\omega}}] e^{-jkr} dr \\
&= j\pi A_{3,\omega} [-e^{j\Theta_\omega} + e^{-j\Theta_{-\omega}}] \left[\frac{e^{k_\omega z_s} e^{-j(k-C_\omega+jB_\omega)r}}{-2j(k-C_\omega+jB_\omega)} \Big|_0^R - \frac{e^{-k_\omega z_s} e^{-j(k-C_\omega-jB_\omega)r}}{-2j(k-C_\omega-jB_\omega)} \Big|_0^R \right] \\
&= \pi A_{3,\omega} [-e^{j\Theta_\omega} + e^{-j\Theta_{-\omega}}] \left[\frac{k' \sinh(k_\omega z_s) - jB_\omega \cosh(k_\omega z_s) - e^{-jk'R}[k' \sinh(k_\omega z_s + B_\omega R) - jB_\omega \cosh(k_\omega z_s + B_\omega R)]}{(k')^2 + B_\omega^2} \right]
\end{aligned}
\tag{9.9}
$$

where $k' = k - C_\omega$ and the transformed component $\breve{u}_i = \breve{u}_i(k, \omega, \phi, \gamma, \theta, z_s)$. It is worthwhile to pick a specific case, such as when beam 1 of the ADCP points along the the x-axis ($\gamma = 0$). This lessons the need for using all nine components of the transformation tensor. In this case, only four components are needed, and the radial wavenumber-frequency spectrum for beam 1 is calculated as follows:

$$
\begin{aligned}
E[|\breve{v}_{B1}(k, w, \phi, \gamma, \theta, z_s)|^2] &= E[|(\breve{u}_1(k, w, \phi, \gamma, \theta, z_s) \sin(\phi) + \breve{u}_3(k, w, \phi, \gamma, \theta, z_s) \cos(\phi)|^2] \\
&= E[\breve{u}_1 \breve{u}_1^*](\sin\phi)^2 + E[\breve{u}_1 \breve{u}_3^* + \breve{u}_3 \breve{u}_1^*](\sin\phi\cos\phi) + E[\breve{u}_3 \breve{u}_3^*](\cos\phi)^2
\end{aligned}
\tag{9.10}
$$

The expectation is over the random starting phase Θ, which is independent and identically distributed, with a uniform distribution from $-\pi$ to π. As a reminder,

$\Theta_\omega \neq \Theta_{-\omega}$. The various iterations of the expectation portion of the four transformation tensor components are as follows:

for $E[\breve{u}_1\breve{u}_1^*]$: $E[(e^{j\Theta_\omega} + e^{-j\Theta_{-w}})(e^{-j\Theta_\omega} + e^{j\Theta_{-w}})]$ $= E[2 + 2\cos(\Theta_\omega + \Theta_{-\omega})] = 2$

for $E[\breve{u}_1\breve{u}_3^*]$: $E[(e^{j\Theta_\omega} + e^{-j\Theta_{-w}})(-e^{-j\Theta_\omega} + e^{j\Theta_{-w}})]$ $= E[0 + 2j\sin(\Theta_\omega + \Theta_{-\omega})] = 0$

for $E[\breve{u}_3\breve{u}_1^*]$: $E[(-e^{j\Theta_\omega} + e^{-j\Theta_{-w}})(e^{-j\Theta_\omega} + e^{j\Theta_{-w}})]$ $= E[0 - 2j\sin(\Theta_\omega + \Theta_{-\omega})] = 0$

for $E[\breve{u}_3\breve{u}_3^*]$: $E[(-e^{j\Theta_\omega} + e^{-j\Theta_{-w}})(-e^{-j\Theta_\omega} + e^{j\Theta_{-w}})]$ $= E[2 - 2\cos(\Theta_\omega + \Theta_{-\omega})] = 2$

$$(9.11)$$

Finally, the transformed transformation tensor components are as follows:

$$
\begin{aligned}
E[\breve{u}_1\breve{u}_1^*] &= [2(\pi A_{1,\omega})^2/(k'^2 + B_\omega^2)^2] \\
&\quad \cdot (k'^2 [(\cosh(k_\omega z_s))^2 - 2\cos(k'R)\cosh(k_\omega z_s)\cosh(k_\omega z_s + B_\omega R) + (\cosh(k_\omega z_s + B_\omega R))^2] \\
&\quad + B_\omega^2 [(\sinh(k_\omega z_s))^2 - 2\cos(k'R)\sinh(k_\omega z_s)\sinh(k_\omega z_s + B_\omega R) + (\sinh(k_\omega z_s + B_\omega R))^2] \\
&\quad + 2k'B_\omega \sin(k'R) [\cosh(k_\omega z_s)\sinh(k_\omega z_s + B_\omega R) - \sinh(k_\omega z_s)\cosh(k_\omega z_s + B_\omega R)] \quad) \\
E[\breve{u}_3\breve{u}_3^*] &= [2(\pi A_{3,\omega})^2/(k'^2 + B_\omega^2)^2] \\
&\quad \cdot (k'^2 [(\sinh(k_\omega z_s))^2 - 2\cos(k'R)\sinh(k_\omega z_s)\sinh(k_\omega z_s + B_\omega R) + (\sinh(k_\omega z_s + B_\omega R))^2] \\
&\quad + B_\omega^2 [(\cosh(k_\omega z_s))^2 - 2\cos(k'R)\cosh(k_\omega z_s)\cosh(k_\omega z_s + B_\omega R) + (\cosh(k_\omega z_s + B_\omega R))^2] \\
&\quad + 2k'B_\omega \sin(k'R) [\sinh(k_\omega z_s)\cosh(k_\omega z_s + B_\omega R) - \cosh(k_\omega z_s)\sinh(k_\omega z_s + B_\omega R)] \quad)
\end{aligned}
$$

$$(9.12)$$

Holding frequency ω fixed and setting the derivative of $E[|\breve{v}_{B1}(k, w, \phi, \gamma, \theta, z_s)|^2]$ with respect to k' equal to zero, the maxima can be found. The derivative is zero when $k' = 0$, and this is certainly a maxima because the denominator is minimized. Then examining $k - C_\omega = 0$ provides insight into how the dispersion relationship is affected by looking radially through the water.

$$k_{pr} = k_\omega \sin(\phi)[\cos(\theta)\cos(\gamma) + \sin(\theta)\sin(\gamma)], \qquad (9.13)$$

where k_{pr} is the peak radial wavenumber and k_ω is the wavenumber given by the dispersion relationship. The term in braces is a unit vector dot product of the wave direction (θ) with the beam direction (γ), and determines whether wavenumbers can be seen by this component. For example, pointing the beam orthogonal to the
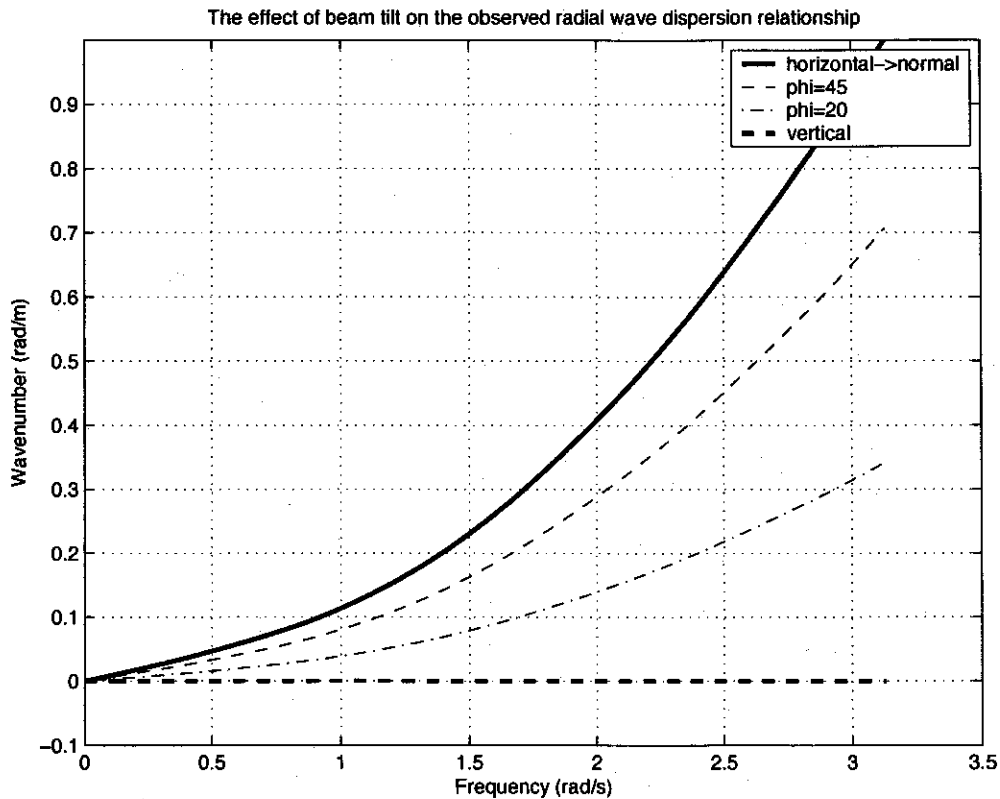
158

Figure 9-3: The wave dispersion relationship collapses to the frequency axis as the beam leaves the horizontal and approaches the vertical.

direction of the waves will cause $k_{pr} = 0$, meaning no wavenumbers will be seen (and only frequencies will be detected). Likewise, pointing the beam in the direction of the waves will potentially allow all frequencies and wavenumbers to be seen. Likewise, the full dispersion relationship is seen when the beam is horizontal ($\phi = 90$ degrees), and it collapses to $k_{pr} = 0$ when it is pointed directly overhead.

The other critical factor is that of radial range, R. Time is basically unlimited (or at least as long as stationarity of statistics holds), but the range is limited by the location of the ADCP, the tilt of the beams, and the frequency of transmission. Pointing the beams of the ADCP toward the ocean surface or bottom sets the geometrical limits R to (surface height)/$(\cos \phi)$, while amplitude attenuation sets the absolute limits of R should the sound beam not be limited geometrically. The main effect of limiting the range is to cause a window effect, which causes spectral averaging or smearing. This results because limiting range is equivalent to multiplication with a
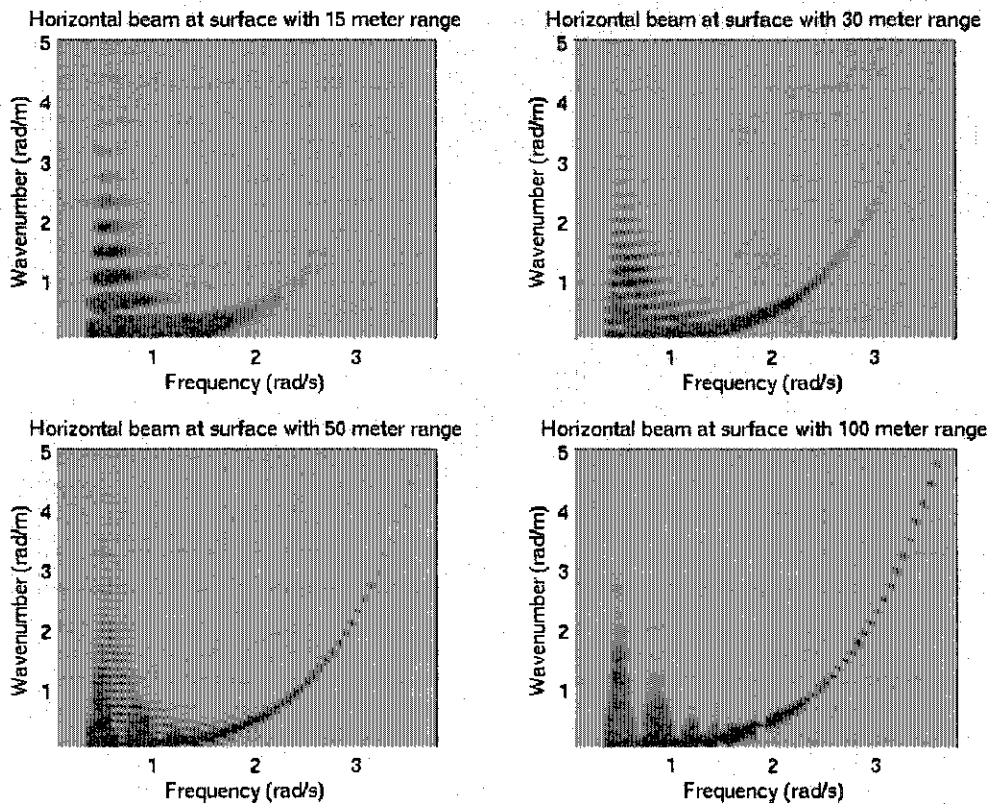
Figure 9-4: Shortening the length of the radial beam causes reduced resolution and smearing in the radial wavenumber domain.

square window function in the spatial domain, which translates to convolution with a sinc function in the wavenumber domain. However, the combination of components are not quite that simple, as figure 9-4 illustrates.

9.3   Averaging Effects of the ADCP

In addition to the natural filtering that occurs with depth, the ADCP adds it's own source of filtering due to signal transmission. When the ADCP sends out a pulse of sound, it ensonifies a volume of water at any given instant. As sound scatters back towards the ADCP, the front of the pulse has a chance to overlap with the tail end of the pulse. This causes the receieved signal to be a summation of all the echos in whatever volume of water is ensonified. This averaging has the effect of acting like a low pass filter, so that higher wavenumbers are removed. Now it is not a
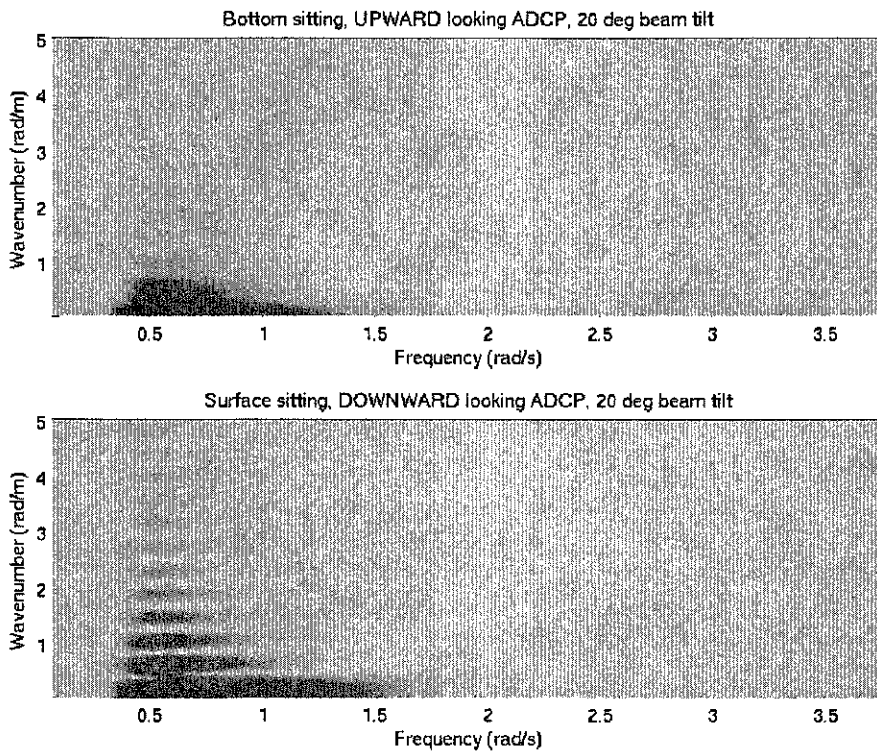
Figure 9-5: The positive quadrant of the predicted wavenumber-frequency spectrum for and ADCP with beam tilt of 20 degrees. Both upward (ADCP sitting on ocean floor) and downward (ADCP on ship at surface) perspectives are provided.

simple averaging, in that the volume has a conic shape, and the various wavenumber components are averaged differently.

Secondly, the ADCP performs range cell averaging (spatial) and ping averaging (temporal) in an attempt to reduce the velocity estimate error. This also has the exact effect of acting like a low pass filter in both wavenumber and frequency space. The end result is that higher wavenumbers and frequencies should not be aliased on the return signal.
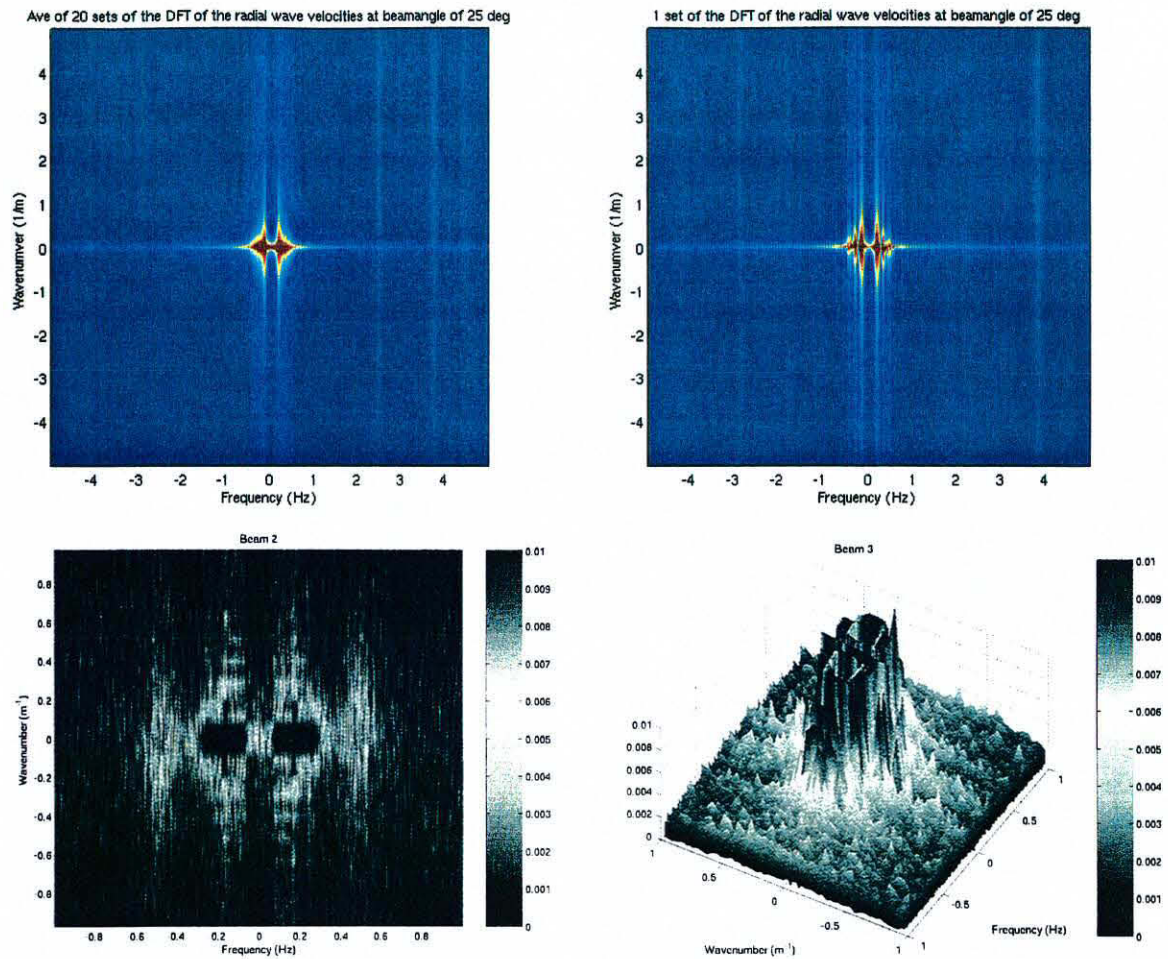
Figure 9-6: A simulated radial wavenumber-frequency spectrum (top) for 20 realizations of data (top left) and 1 realization (top right). Beneath are the true spectrums from data taken from the Martha's Vineyard Coastal Observatory. Intensities are in $(m/s)^2$.

9.4 Comparison of Real and Simulated Data

Figure 9-6 shows both simulated and real ocean radial wavenumber-frequency spectrums. All four quadrants are shown (whereas in previous figures only the positive quadrant was shown). It is clear that the waves dominate a localized region, whereas the turbulence is more evenly distributed. It is also satisfying that the simulated data has spectral characteristics similar to the real data.
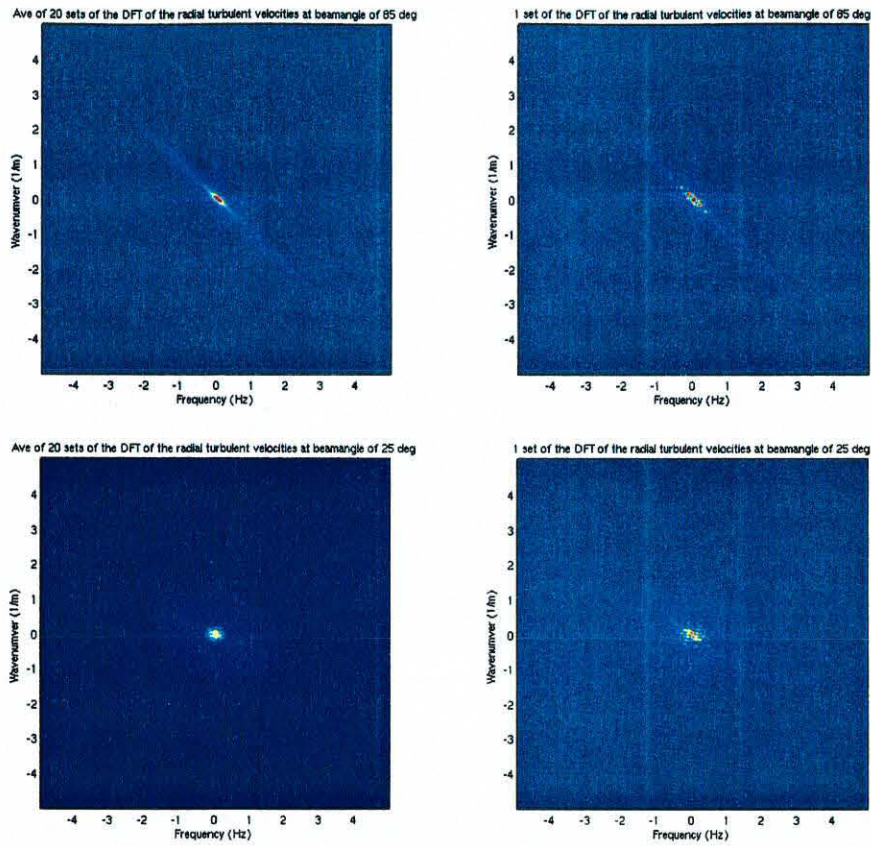
Figure 9-7: The radial wavenumber-frequency spectrum for a simulated turbulence. When the ADCP is pointed near horizontal (top), the wavenumber-frequency distribution of the turbulence falls on the predicted slope due to it's advection with the mean current. As the beam angle points more to the vertical (bottom), the wavenumber-frequency spectrum is diffused as the beam seems to see random eddies passing through.

9.5 Radial turbulent velocities

Figure 9-7 demonstrates the advection of turbulence with the mean current. The slope is predicted by $\omega = vk$, which is what Taylor's frozen turbulence approximation would predict. As the ADCP beam angle points more toward the vertical, it sees more random fluctuations passing through, and the wavenumber-frequency spectrum is diffused.

It is apparent that there is overlap with the wave spectrum in the central region of the spectrum. That is what makes this problem of separating the wave and turbulence processes so difficult. The theoretical space-time correlations should help in solving this problem.

Chapter 10

Estimate Error Prediction and Analysis

With statistical models now developed for the turbulence, wave, and error processes, it is now possible to see how model parameters effect the error in the estimates of Reynolds stress. Section 10.1 matches the turbulence models to the data obtained from an ADCP located at the Martha's Vineyard Coastal Observatory. Section 10.2 talks about the specific parameters that are used in the turbulence, wave, and error processes, and the sections that follow explore how specific parameters affect the error. Section 10.9 explores how using mean squared error estimates of the turbulent fluctuations can aid in analysis. In addition, specific equations for analyzing the effect of changing parameters on a tilted ADCP are presented for further investigation. The conclusion is that these statistical models work well in representing the features of the real profile estimates of Reynolds stress, and unfortunately reveal the profile to be dominated by error.
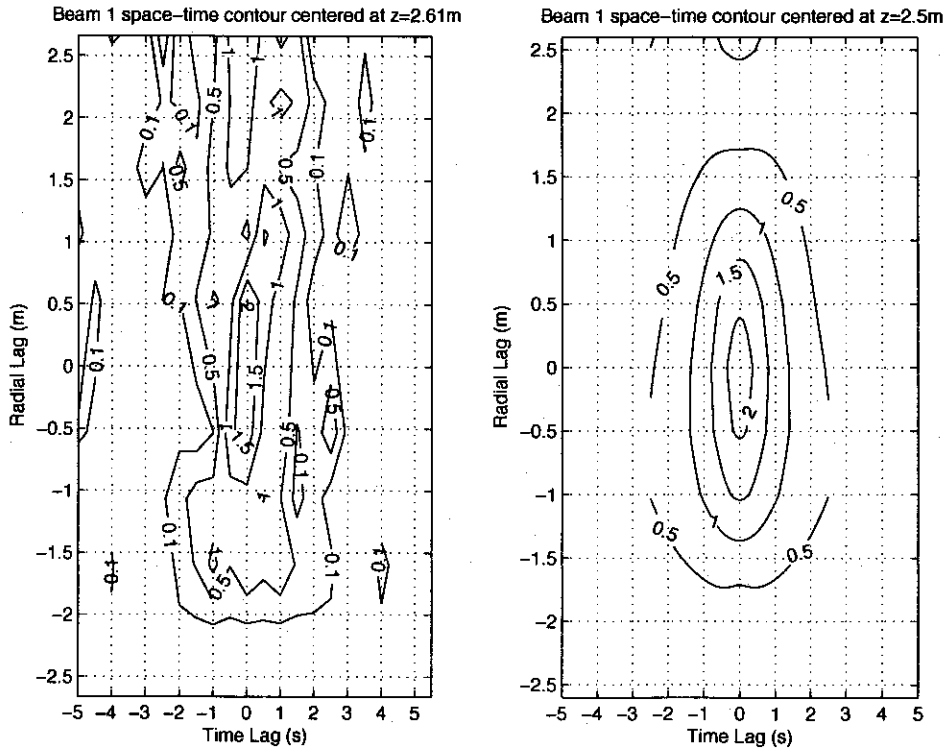
Figure 10-1: Radial space-time correlations for the data (first plot) and the turbulent shear model prediction (second plot) at locations along beam 1 of the ADCP.

10.1 Matching turbulence models to the data

Each of the different turbulence models works best to represent the space-time correlations of the data at different ranges. The turbulent shear model works best up to about 3 meters from the bottom, and can be seen in figure 10-1. The time-evoloving, homogeneous, isotropic turbulence model with the exponential approximation for f(r) (see section 6.4) works best in the range from 3-5 meters above the ocean floor, as seen in figure 10-2. Finally, the time-evoloving, homogeneous, isotropic turbulence model with the Gaussian approximation for f(r) (see section 6.4) works best above 5 meters from the ocean floor, as seen in figure 10-3.

Figure 10-2: Radial space-time correlations for the data (first plot) and the time-evolving, homogeneous, isotropic model prediction using the exponential approximation for f(r) (second plot) at locations along beam 1 of the ADCP.

10.2 Matching model parameters to the ADCP data

The parameters that determine the model characteristics for the turbulence, wave, error, and estimation processes are listed in this section, and have been set to match conditions of the ADCP that is stationed at the Martha's Vineyard Coastal Observatory. The sections that follow examine how changing these parameters will effect the error in the filtered Reynolds stress estimate.

Turbulence Parameters

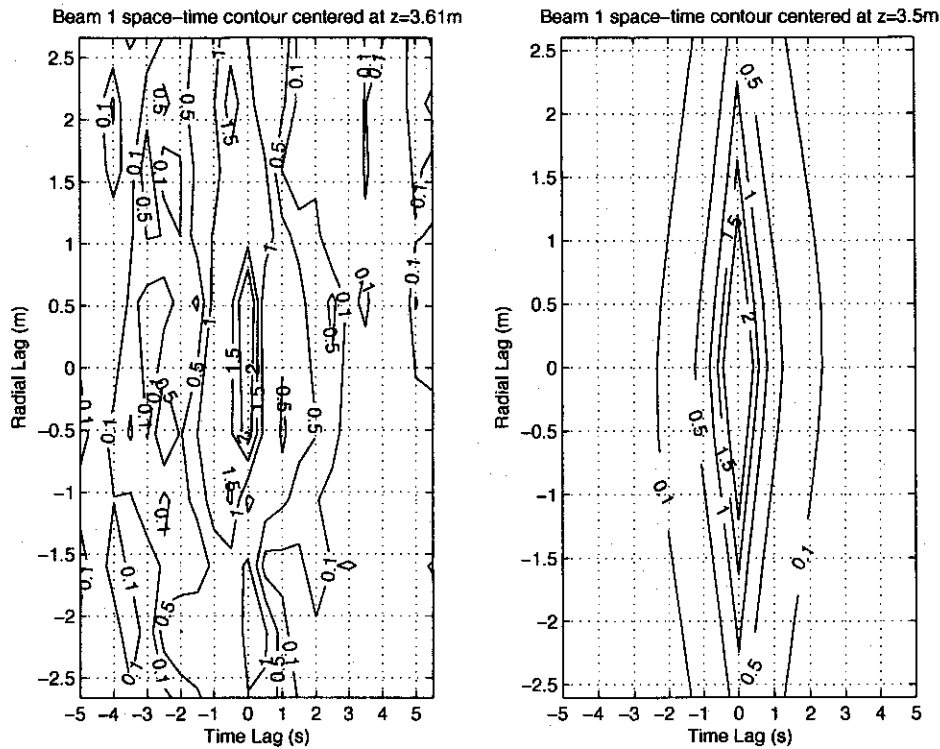|	
MVCO-profiles	current profile (shear)
v, varphi	current speed and direction
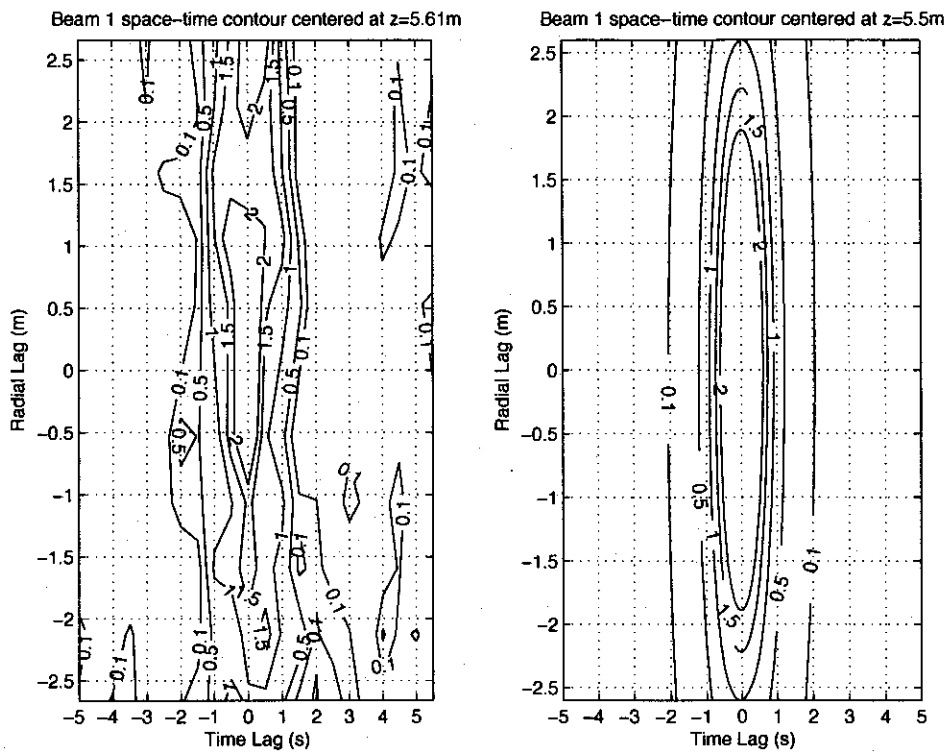
Figure 10-3: Radial space-time correlations for the data (first plot) and the time-evolving, homogeneous, isotropic model prediction using the Gaussian approximation for f(r) (second plot) at locations along beam 1 of the ADCP.

Wave Parameters

---

surfcloc=13;	water depth (m)
sig-amp=1.4;	Significant amplitude (m)
windspeed=[15 10];	Alternate to sig amp (m/s)
	Spectrum: Pierson-Moskcowitz
wave-directions=[170 230];	(geo) direction, waves coming FROM each event
multidirectional=true;	directional spread of waves

ADCP Error Parameters

WB=0.05;	Wavelength-Bandwidth product (m/s)
f=1200000;	Transmit frequency (Hz)
c=1500;	Speed of sound in water (m/s)
binsize=0.5;	Bin size (m)
rs=0.5;	Radial spacing (m)
fs=2;	Sampling rate (Hz)
t-ave=1200;	Averaging period (s)

ADCP general parameters

---

adcp-heading=289;	beam3 heading (geographical)
pitch=-6.3;	beam3 higher than beam4 (pos)
roll=0.5;	beam2 higher than beam1 (pos)
beamangle=20;	beamangle (degrees from vertical)
sensorloc=0;	height off bottom (m)
maxbeamlen=13;	distance where attenuation dominates (m)
	upward looking

Estimation Parameters

---

tau=10;	max time lag (s)
ts=1;	time lag spacing (s)
	selected beam locations

10.3 Fixed parameters

There are a number of parameters which are fixed by virtue of the fact that the ADCP at the Martha's Vineyard Coastal Observatory has a fixed set of parameters. It operates at 1200 kHz, pings at 2 Hz, has a bin size of about 0.5 m, and collects data for intervals of 20 minutes. In addition, its heading is 289 degrees (which is the direction beam 3 points in), and has a pitch of -6.3 degrees (beam 3 dips below beam 4), and a roll of 0.5 degrees (beam 1 dips below beam 2). The ADCP is seated on the ocean floor, under about 13 m of water, and its beam tilt has been factory set to 20 degrees from the vertical.

10.4 Typical parameters

There are a number of parameters which represent well the general conditions of the ocean environment where the ADCP is located. The ADCP is located on the south shore of Martha's Vineyard, and so the waves typically come from the south, south-east, and south-west. The Pierson-Moskocowitz spectrum represents the data well, with the addition that there can be multiple sources (multiple events), and that the waves can have a directional spread around the main incoming direction. The wavelength-bandwidth product for typical conditions in which the data is evaluated is about 5 cm/s, and the significant amplitude of the wave process is about 1.4 m. Current speeds vary from about 0.1 m/s near the bottom, to about 0.3-0.4 m/s in some upper regions of the water column.

As discussed previously (see section 4.10), the error variance given the fixed parameters of this ADCP (frequency, bin size, averaging time, and wavelenth-bandwidth product) is very small. In fact, only when decreasing the averaging time to under 2 minutes does the error variance have an overall effect on the estimate error.

When using locations on the same beam to make the estimate, the time lag does not need to be any longer than 2 seconds, but when using additional locations on other beams, the time lag needs to be longer for to account for the beam separation.
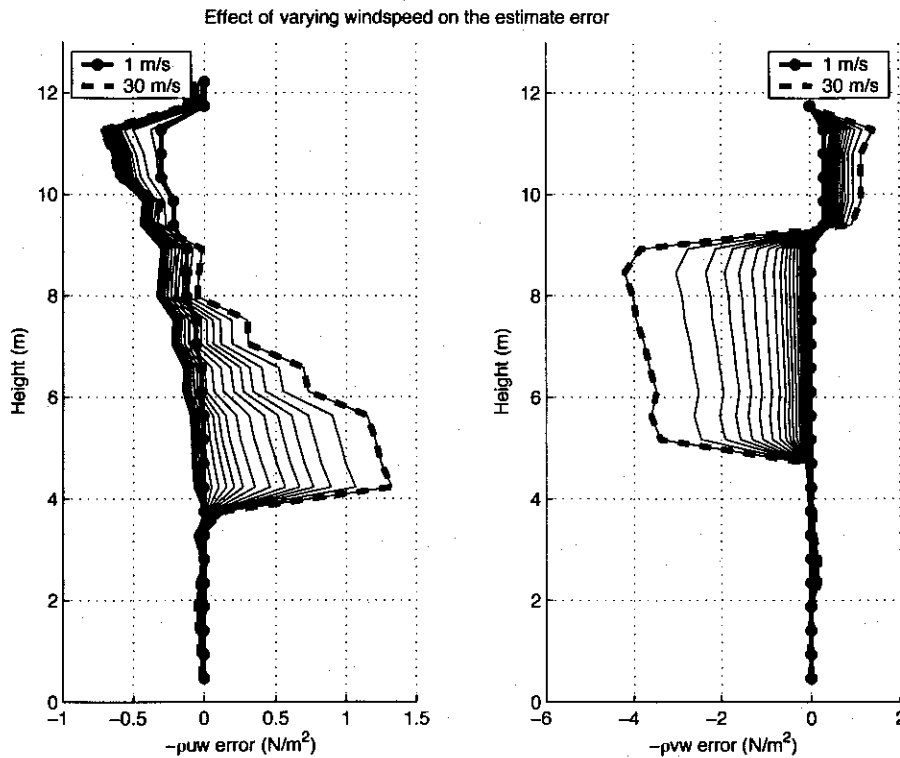
Figure 10-4: Surface wind speed variations from 1 to 30 m/s, and the resulting effect on the estimate error.

10.5 Effect of varying the wind speed on the estimate error

Parameter changes: wave-directions=[170], multidirectional=false
tau=15, windspeed=1:30

Figure 10-4 shows that increasing wind speed at the ocean surface has minimal effect below about 4 meters, but has significant effect in the midrange. When wind speeds are less than 13 m/s (just slightly less than the typical 15 m/s for this data set), the error in the Reynolds stress estimate is less than 0.05 N m^{-2}, indicating wind speed (or equivalently significant amplitude) will not be significant. However, above 13 m/s, the error increases rapidly, and the error in the estimates is of the same magnitude as the estimates.

171

Figure 10-5: Varying the direction of the incoming waves from 230 degrees to 140 degrees, and the resulting effect on the estimate error.

10.6 Effect of varying the incoming wave direction on the estimate error

Parameter changes: multidirectional=false, tau=15, wave-directions=240:-5:140

Figure 10-5 show that there is asymetry in results between the two ADCP axes. The change in wave direction has significant effect after 5 meters for the $\overline{uw}$ axis, and the error gradually increases with increasing height. The effects on the error are significant throughout the entire vertical profile for the $\overline{vw}$ axis. In addition, the mid-region is significantly affected. Therefore, only the roll axis will yield usable estimates (of course as wind speed decreases, both axes have some good estimates).
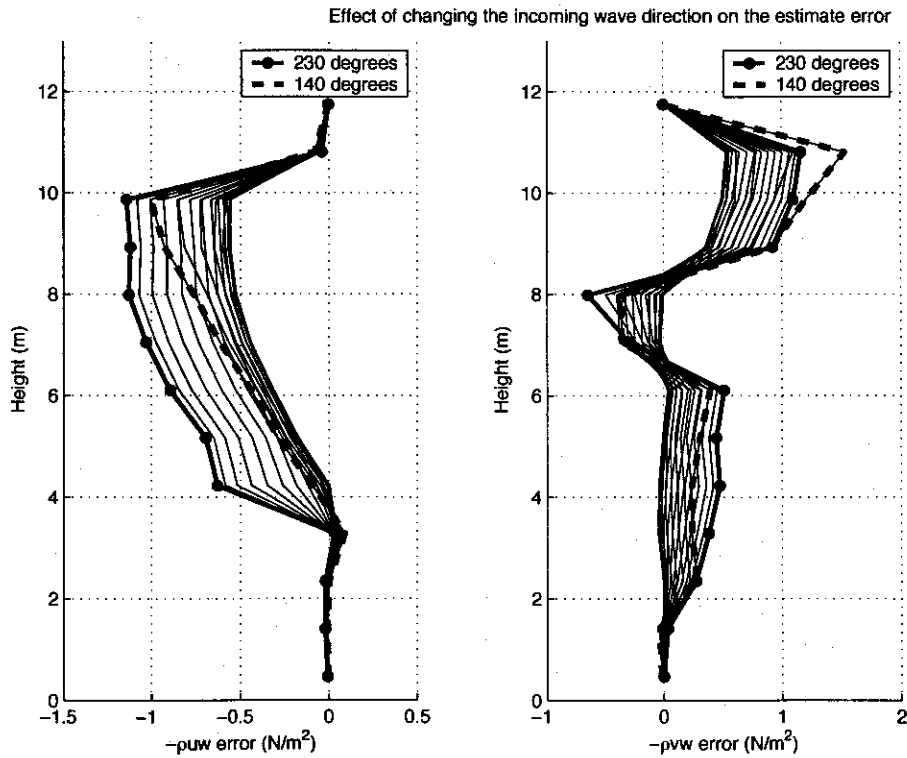
Figure 10-6: Varying the direction of the incoming waves from 230 degrees to 140 degrees, while increasing the number (to 3) of beam locations used to make the coherent estimate, and the resulting effect on the estimate error.

10.7 Effect of using three beam locations in the estimation process, on the estimate error

Parameter changes: multidirectional=false, tau=5, wave-directions=240:-5:140

Figure 10-6 shows that using multiple beam locations in the estimation process greatly minimizes the effects of other parameters. However, above 4 meters for estimates on the roll axis, and above 6 meters for estimates on the pitch axis, the error in the estimates is still too large. Near the surface the error appears to decrease. This is actually the result of the estimation process correctly removing wave induced velocities from each beam, but also (unwantingly) removing turbulent induced velocites from each beam (see section 10.9, 'Additional Analysis Tools', for further explanation).

Effect of changing the source direction of multidirectional waves on the estimate error
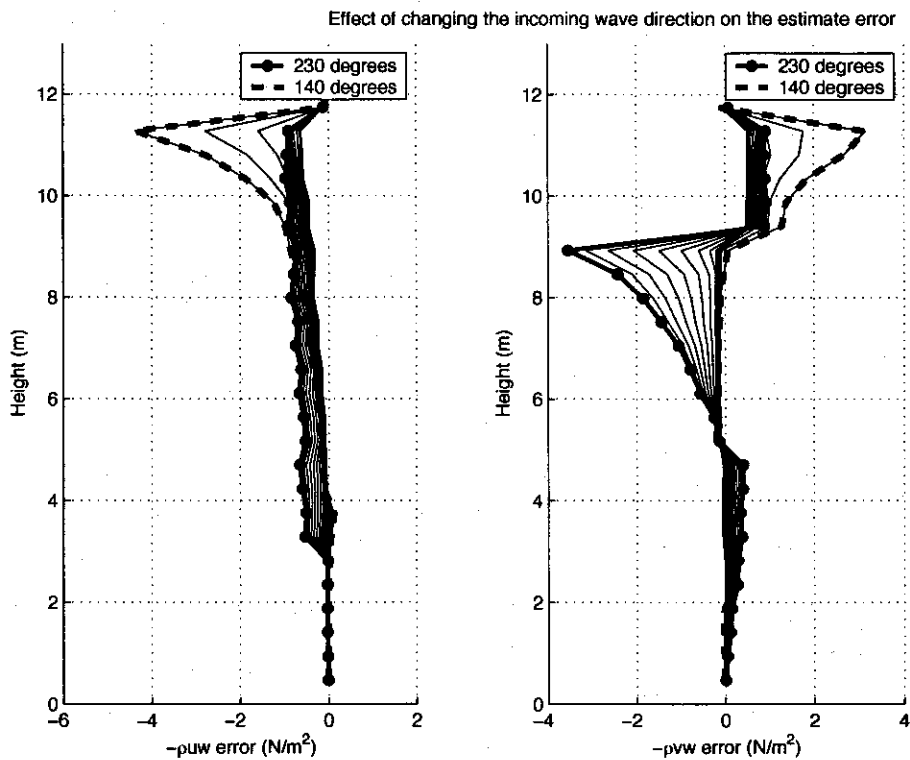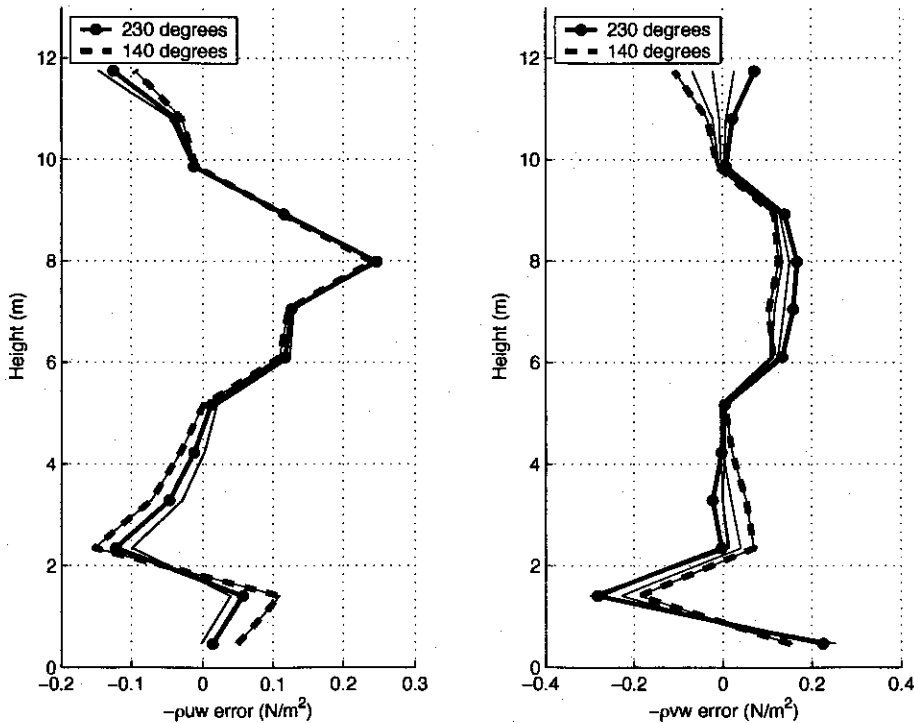

Figure 10-7: Varying the source direction of multidirectional waves, from 230 degrees to 140 degrees, and the resulting effect on the estimate error. These error profiles generated from the models have features similar to that of the Reynolds stress profiles generated using real ADCP data, as seen in figure 3-6.

10.8 Effect of varying the source direction of multidirectional waves on the estimate error

Parameter changes: tau=5, wave-directions=210:-20:140

Figure 10-7 shows that changing the source direction of incoming ways has little effect when the waves already have directional spread. Secondly, the profile has features similar to that of the actual estimated Reynold stresses using the filtered ADCP data (see figure 3-6), indicating that the multidirectional wave spread model is quite good at representing the real process. Since the error profile is similar to the profile of the estimates of Reynolds stress, that would mean the profile of Reynold stress estimates is equivalently an error profile, and there its estimates are suspect.

10.9 Additional Analysis Tools

As was seen in figures 10-4, 10-5, 10-6, and 10-7, the error of the estimate of the Reynolds stress is close to zero near the ocean surface. This results when both wave induced velocities and turbulence induced velocities are removed when forming the estimates of the variance of radial turbulent velocities in each beam individually. Wave induced velocities near the surface have additional (higher) frequencies than do wave induced velocities deeper in the water column (which have been filtered out - see chapter 9). To successfully remove these wave induced velocities, other locations with similar space-time content must be used, restricting spatial and temporal lags to be small. However, that violates the need for spatial and temporal lags to be large so that turbulence induced velocities are independent at separate beam locations. Near the surface, it is very difficult to strike the balance of removing as much as possible of the wave induced velocities, while removing as little as possible of the turbulence induced velocities. The fact that the plots show near zero error in the Reynolds stress estimates is a clue that this balance was not successfully met, and can further be verified by looking at the error in each beam individually.

For example, figure 10-8 shows the decomposition of the error in the estimate of the Reynolds stress, from the first plot of figure 10-6, into individual covariance estimates of the variance of radial turbulent velocities for opposing beams 1 and 2. The covariance estimates becomes negative when both wave induced velocities and turbulence induced velocites are being removed. The variance of the turbulent process is approximately $4.4 \cdot 10^{-4}$ $(m/s)^2$, so that when the negative of this value is reached, all of the turbulence induced velocities have been removed. Figure 10-8 reveals that this occurs in beam 1 after about 8 meters from the bottom, and in beam 2 closer to the surface.

Another issue is that covariances have the potential to be positive or negative, and when the final term in equation 3.33 is larger than the first two terms, the error is negative. That means that there is the possibility that the overall error of the estimate will be zero, even when the turbulent fluctuations are not perfectly predicted.
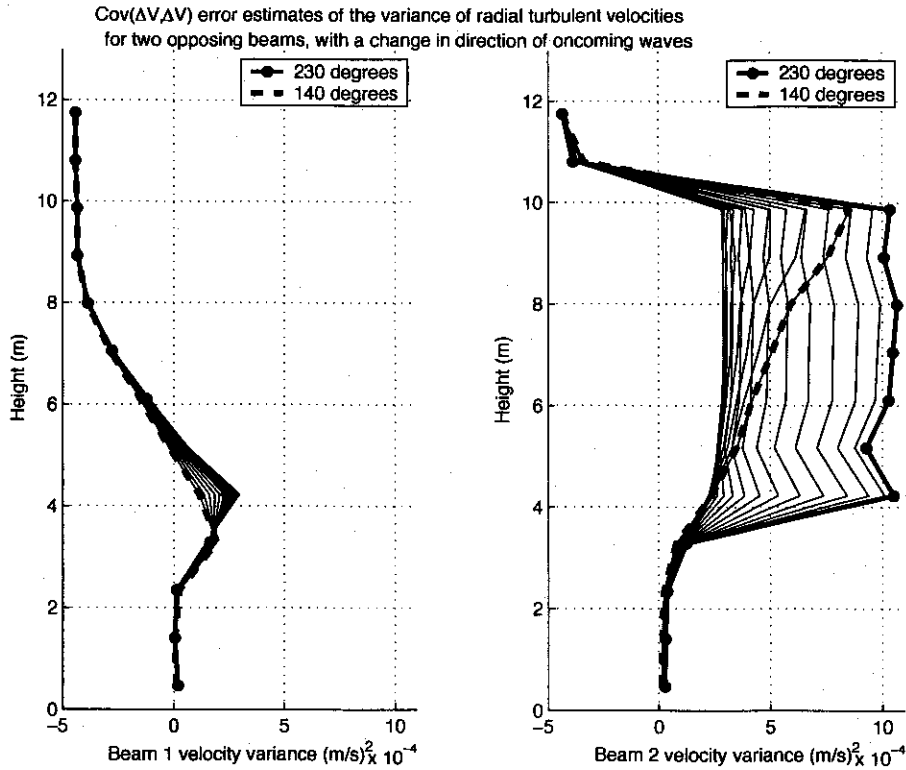
Figure 10-8: Covariance error estimates of the variance of radial turbulent velocities for two opposing beams, with a change in direction of oncoming waves. The variance of the turbulence process is approximately $4.4 \cdot 10^{-4}$ $(m/s)^2$, and its negative value gives the minimum value of the covariance estimates.

To know when the error is zero because the turbulent process is well predicted rather than when the different terms all sum to zero, the mean squared error of the turbulent fluctuations can be used as a point of comparison.

$$
\begin{aligned}
\overline{V_{B1}'^e(\vec{x}_a, t) V_{B1}'^e(\vec{x}_a, t)} &= \tfrac{1}{N}(\mathbf{v}_x' - \hat{\mathbf{v}_x'})^T(\mathbf{v}_x' - \hat{\mathbf{v}_x'}) \\
&= \tfrac{1}{N}(\mathbf{v}_x' - \Delta\mathbf{v}_x')^T(\mathbf{v}_x' - \Delta\mathbf{v}_x') \\
&= \tfrac{1}{N}[\mathbf{v}_x'^T\mathbf{v}_x' - 2\mathbf{v}_x'^T\Delta\mathbf{v}_x + \Delta\mathbf{v}_x^T\Delta\mathbf{v}_x] \\
&= \tfrac{1}{N}[\mathbf{v}_x'^T\mathbf{v}_x' - 2\mathbf{v}_x'^T(\mathbf{v}_x - \hat{\mathbf{v}_x}) + (\mathbf{v}_x - \hat{\mathbf{v}_x})^T(\mathbf{v}_x - \hat{\mathbf{v}_x})] \\
&= \tfrac{1}{N}[\mathbf{v}_x'^T\mathbf{v}_x' - 2\mathbf{v}_x'^T\mathbf{v}_x' + 2\mathbf{v}_x'^T\hat{\mathbf{v}_x} + \mathbf{v}_x^T\mathbf{v}_x - \mathbf{v}_x^T\hat{\mathbf{v}_x}] \\
&= \tfrac{1}{N}[\tilde{\mathbf{v}}_x^T\tilde{\mathbf{v}}_x + \mathbf{v}_x^{e^T}\mathbf{v}_x^e + (\mathbf{v}_x' + \mathbf{v}_x^e - \tilde{\mathbf{v}}_x)^T\mathbf{V}_y(\mathbf{V}_y^T\mathbf{V}_y)^{-1}\mathbf{V}_y^T\mathbf{v}_x]
\end{aligned}
$$
(10.1)

From the models, it is also possible to determine directly the effect that beam tilt has on the error of the estimate. In this case, the actual statistics of the tilted ADCP

will be denoted by $\mathring{\mathbf{R}}_{\mathbf{yy}}$ and $\mathring{\mathbf{R}}_{\mathbf{yx}}$, whereas the supposed statistics will be denoted by $\mathbf{R}_{\mathbf{yy}}$ and $\mathbf{R}_{\mathbf{yx}}$. Now, the two estimates of the Reynolds stress, $\mathrm{cov}(\mathbf{v}_{\mathbf{x}}, \Delta \mathbf{v}_{\mathbf{x}})$ and $\mathrm{cov}(\Delta \mathbf{v}_{\mathbf{x}}, \Delta \mathbf{v}_{\mathbf{x}})$, will be different. The optimal linear least squares estimate of the coherent components of of $\mathbf{v}_{\mathbf{x}}$ is (see equation 3.26)

$$
\begin{aligned}
\hat{\mathbf{v}}_x &= \mathbf{V}_{\mathbf{y}}(\mathbf{V}_{\mathbf{y}}^T \mathbf{V}_{\mathbf{y}})^{-1} \mathbf{V}_{\mathbf{y}}^T \mathbf{v}_x \\
&= \mathbf{V}_{\mathbf{y}}(\mathbf{R}_{\mathbf{yy}})^{-1} \mathbf{R}_{\mathbf{yx}},
\end{aligned}
\tag{10.2}
$$

and the incoherent estimate is given by equation 3.29, so that

$$
\begin{aligned}
\overline{V'_{B1}(\vec{x}_a, t)\widehat{V'_{B1}(\vec{x}_a, t)}} &= \mathrm{cov}(\mathbf{v}_{\mathbf{x}}, \Delta \mathbf{v}_{\mathbf{x}}) \\
&= \tfrac{1}{N}\mathbf{v}_{\mathbf{x}}^T \Delta \mathbf{v}_{\mathbf{x}} \\
&= \tfrac{1}{N}\mathbf{v}_{\mathbf{x}}^T (\mathbf{v}_{\mathbf{x}} - \hat{\mathbf{v}}_{\mathbf{x}}) \\
&= \tfrac{1}{N}[\mathbf{v}_{\mathbf{x}}^T \mathbf{v}_{\mathbf{x}} - \mathbf{v}_{\mathbf{x}}^T \hat{\mathbf{v}}_{\mathbf{x}}] \\
&= \tfrac{1}{N}[\mathbf{v}_{\mathbf{x}}^T \mathbf{v}_{\mathbf{x}} - \mathbf{v}_{\mathbf{x}}^T \mathbf{V}_{\mathbf{y}}(\mathbf{R}_{\mathbf{yy}})^{-1} \mathbf{R}_{\mathbf{yx}}] \\
&= Rxx(0) - \mathring{\mathbf{R}}_{\mathbf{xy}}(\mathbf{R}_{\mathbf{yy}})^{-1} \mathbf{R}_{\mathbf{yx}},
\end{aligned}
\tag{10.3}
$$

whereas

$$
\begin{aligned}
\overline{V'_{B1}(\vec{x}_a, t)\widehat{V'_{B1}(\vec{x}_a, t)}} &= \mathrm{cov}(\Delta \mathbf{v}_{\mathbf{x}}, \Delta \mathbf{v}_{\mathbf{x}}) \\
&= \tfrac{1}{N}\Delta \mathbf{v}_{\mathbf{x}}^T \Delta \mathbf{v}_{\mathbf{x}} \\
&= \tfrac{1}{N}(\mathbf{v}_{\mathbf{x}} - \hat{\mathbf{v}}_{\mathbf{x}})^T (\mathbf{v}_{\mathbf{x}} - \hat{\mathbf{v}}_{\mathbf{x}}) \\
&= \tfrac{1}{N}[\mathbf{v}_{\mathbf{x}}^T \mathbf{v}_{\mathbf{x}} - 2\mathbf{v}_{\mathbf{x}}^T \hat{\mathbf{v}}_{\mathbf{x}} + \hat{\mathbf{v}}_{\mathbf{x}}^T \hat{\mathbf{v}}_{\mathbf{x}}] \\
&= Rxx(0) - 2\mathring{\mathbf{R}}_{\mathbf{xy}}(\mathbf{R}_{\mathbf{yy}})^{-1} \mathbf{R}_{\mathbf{yx}} + \mathbf{R}_{\mathbf{xy}}(\mathbf{R}_{\mathbf{yy}})^{-1}\mathring{\mathbf{R}}_{\mathbf{yy}}(\mathbf{R}_{\mathbf{yy}})^{-1} \mathbf{R}_{\mathbf{yx}}.
\end{aligned}
\tag{10.4}
$$

When there is no beam tilt, $\mathbf{R}_{\mathbf{yy}} = \mathring{\mathbf{R}}_{\mathbf{yy}}$, $\mathbf{R}_{\mathbf{yx}} = \mathring{\mathbf{R}}_{\mathbf{yx}}$, and then once again $\mathrm{cov}(\mathbf{v}_{\mathbf{x}}, \Delta \mathbf{v}_{\mathbf{x}}) = \mathrm{cov}(\Delta \mathbf{v}_{\mathbf{x}}, \Delta \mathbf{v}_{\mathbf{x}})$. Finally, when considering the mean square error of the estimate of the turbulent fluctuations (expanding the 4th equality in equation 10.1),

$$
\begin{aligned}
\overline{V'^e_{B1}(\vec{x}_a, t)V'^e_{B1}(\vec{x}_a, t)} &= \tfrac{1}{N}[\mathbf{v}'^T_{\mathbf{x}} \mathbf{v}'_{\mathbf{x}} - 2\mathbf{v}'^T_{\mathbf{x}} \mathbf{v}'_{\mathbf{x}} + 2\mathbf{v}'^T_{\mathbf{x}} \hat{\mathbf{v}}_{\mathbf{x}} + \mathbf{v}_{\mathbf{x}}^T \mathbf{v}_{\mathbf{x}} - 2\mathbf{v}_{\mathbf{x}}^T \hat{\mathbf{v}}_{\mathbf{x}} + \hat{\mathbf{v}}_{\mathbf{x}}^T \hat{\mathbf{v}}_{\mathbf{x}}] \\
&= \tilde{R}_{xx}(0) + R^e_{xx}(0) - 2(\mathring{\mathbf{R}}_{\mathbf{xy}} + \mathring{\mathbf{R}}^e_{\mathbf{xy}})(\mathbf{R}_{\mathbf{yy}})^{-1} \mathbf{R}_{\mathbf{yx}} \; + \\
&\qquad \mathbf{R}_{\mathbf{xy}}(\mathbf{R}_{\mathbf{yy}})^{-1}\mathring{\mathbf{R}}_{\mathbf{yy}}(\mathbf{R}_{\mathbf{yy}})^{-1} \mathbf{R}_{\mathbf{yx}}.
\end{aligned}
\tag{10.5}
$$

177

Whereas section 2.2 dealt with the error due to beam tilt in a general sense, equations 10.3, 10.4, and 10.5, allow for the effects that beam tilt has on the error to be determined as the model parameters are changed.

10.10   Conclusions

The three models of turbulence, shear, exponential, and Gaussian, together do a reasonable job of approximating what is likely the actual turbulent process. The wave process is best represented by a multidirectional wave spread, and when used with the turbulence models, the predicted profiles of the error of Reynolds stress estimates has similar features to the profiles estimated from real ADCP data. This also indicates that the profiles resulting from the use of real data are revealing inner error mechanisms. Wind speed (or equivalenty, significant amplitude) is a significant part of the error when a certain threshold is crossed. Using multiple beams locations in the estimation does reduce the overall error, but knowing which locations to choose is challenging. When improperly chosen, both the wave induced velocities and some of the turbulence induced velocities are removed, lessoning the overall magnitude of the estimates of Reynolds stress (as seen in the near surface estimates).

One of the issues of using covariance estimates is that they can be positive or negative, and the zero crossing point may not reflect perfect estimation. Looking at the mean squared error of the turbulence estimates helps to determine when the low error in the estimates of Reynolds stress is a result of good estimation.

Finally, it is possible to determine how changing the model parameters on a tilted ADCP effect the error of the estimates of Reynolds stress by taking into account the statistics that represent the tilted ADCP.

Chapter 11

Ocean Simulator and ADCP Signal Generator

As the previous chapters have given methods on how to simulate various turbulent flows and a variety of ocean states, this chapter will present signal transmission and reception of the ADCP. Then the full simulation process is complete. Flows can be generated, sonar signals received, and then algorithms for estimation applied for evaluation. The significance of having simulated the whole process is that there is full knowledge of each of the processes, whereas in the ocean all processes are combined. On the other hand, the models presented in this thesis do not represent the more complex nonlinear or coupled processes within the ocean. It is a start.

11.1   ADCP - Ocean Signal Generator

The velocity field for both the waves and turbulence can now be simulated, and what is needed is to simulate the ADCP signal transmission. The basic idea is to simulate transmission, interaction with scatterers, and reception.

A coded signal will be used for transmission, which can be equally well represented by it's spectrum.

The ocean will be randomly seeded with ocean scatterers, which will be given velocities based on their location and the current sea state.

ADCP - Ocean Signal Generator

1. Create transmit signal
   (600 kHz, Barker Codes, 40 ms)

2. Look at frequency spectrum that
   scatterer receives to weight frequencies

3. Determine angle between ACDP
   and each scatterer

4. Apply scatter field equation for each
   weighted frequency, for each instant,
   for each scatterer

5. Received signal for that time
   instant is superposition of all
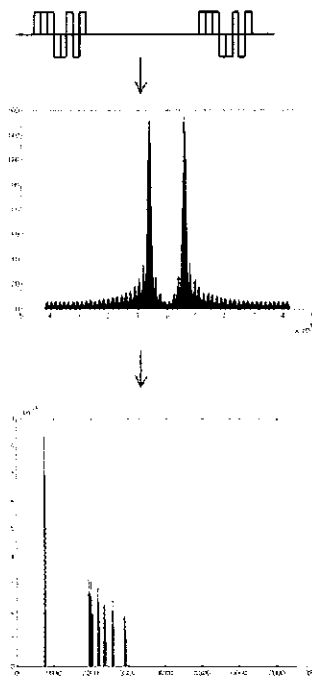   scatterer echo returns

6. Repeat for next time step

Figure 11-1: The received signal is a result of the scatterer location and velocity, random phase, and a range of frequencies due to the broadband nature of the transmitted pulse.

An analytic equation will be used to apply the appropriate Doppler shift for each frequency of the broadband signal that a scatterer encounters, and will account for signal attenuation based on travel distance.

The scatterers location will then be changed based on it's velocity and the timestep used, and the process repeated.

The final received signal will be a supposition of all received scatterer returns, with variable arrival times accounted for.

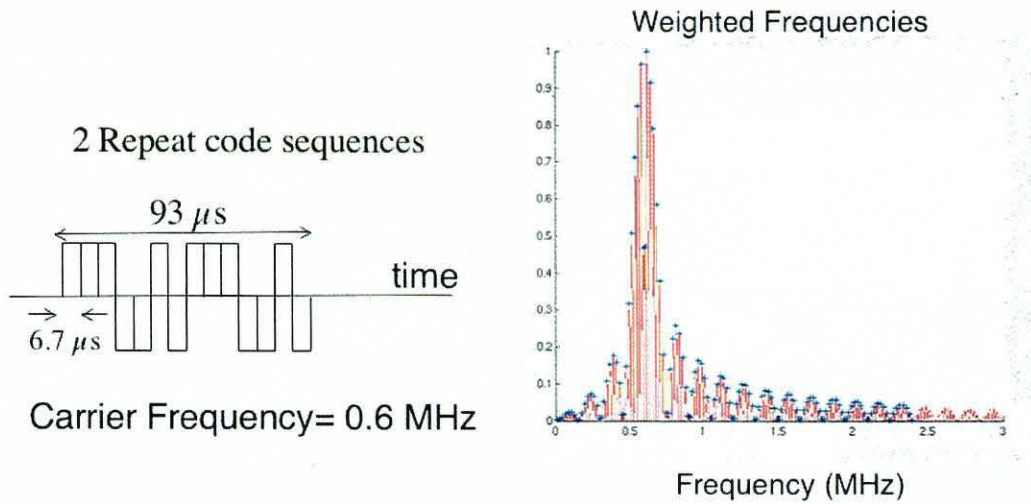## Transmitted Signal & Frequency Equivalence

Figure 11-2: The coded pulse and short duration lead to a range of frequencies being transmitted.

11.2   Frequency Generator

Figure 11-2 shows the effect of transmitting a limited duration pulse. For example, a standard Barker Code is repeated twice on a 600 kHz carrier signal, leading to a range of frequencies. To simulate this effect, the sound must be transmitted at each of the peak frequencies, so that the scatter response off the small ocean organisms will be accurate.

181

Scatterer Model

Copepod   1 mm

Euphasiid   1 cm

Pteropod   1 cm
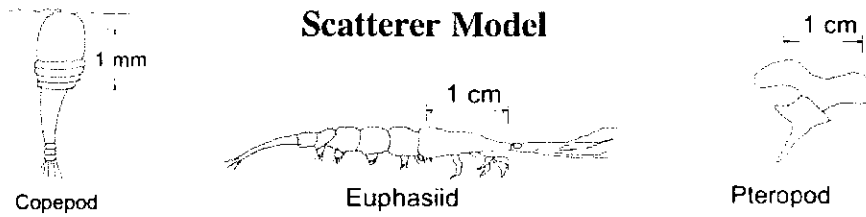
Distribution: Randomly scattered with set density

Orientation: Random

Scattering important:

Transmission wavelength on order of size of scatterer

Approximation:

Point scatterer with random complex amplitude

Location Updater: (using very small time steps)

$$\vec{l_2}(\vec{r_2}, t + \Delta t) = \vec{l_1}(\vec{r_1}, t) + \vec{v}(\vec{r_1}, t) \cdot \Delta t$$

Figure 11-3: The size of the ocean organisms can be on the same scale as the transmitted wavelenths, which means their scatter patterns are changing and complex. In the simulator, organisms will be assigned random locations, and then their locations tracked with the surrounding flow. The generated signals will interact with them at whatever is ther current location. The graphics are used with permission from RDI. [9]

11.3   Ocean Scatterers

The ADCP works on the assumption that small ocean organisms, in particular copepods, euphasiids, and pteropods, float passively with the currents. A 150 kHz ADCP sends pulses with wavelength of 1 cm, while a 1200 kHz ADCP sends pulses with wavelength 1.25 mm. These wavelengths are on the order of the size of the organisms, and therefore scattering is important. However, in this thesis the scatterers were approximated as point sources with random complex ampltitudes, and in general the superposition of the echo response of many scatterers can be characterized by a complex Gaussian random variable. [22]

Velocity Field Simulator for Scatterer Motions

Scatterer motions illuminated in one beam of ADCP

Surface Wave Field

$$u(\vec{r}, t) = A\omega \frac{\cosh(k(z+h))}{\sinh(kh)} \cos(kx - \omega t)$$

$$v(\vec{r}, t) = 0$$

$$w(\vec{r}, t) = A\omega \frac{\sinh(k(z+h))}{\sinh(kh)} \sin(kx - \omega t)$$

Turbulent field

$$u(\vec{r}, t) = U_{\text{mean}} + \text{fluctuations}$$

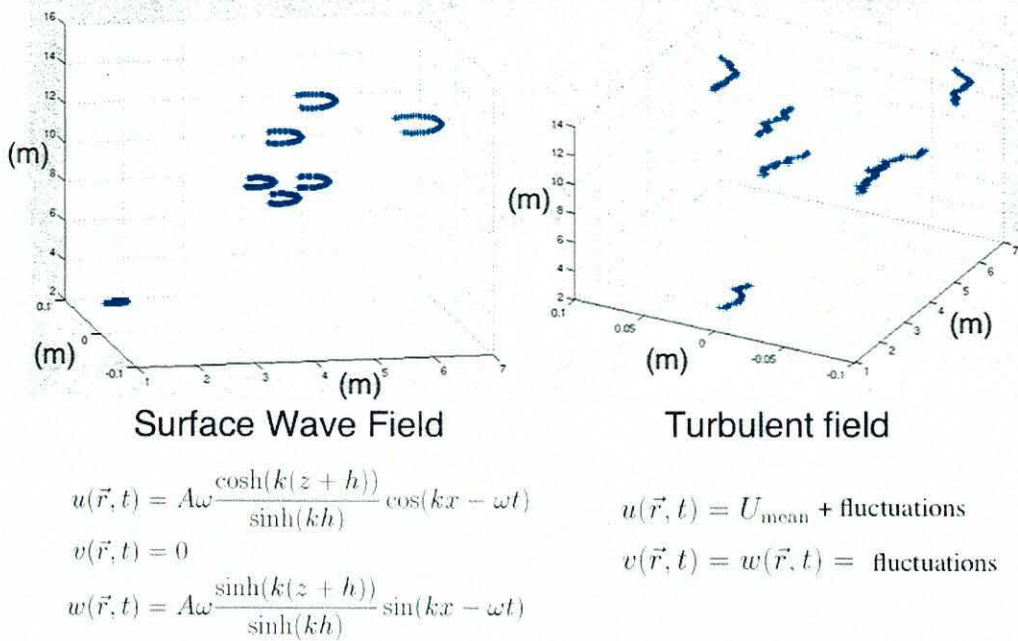$$v(\vec{r}, t) = w(\vec{r}, t) = \text{fluctuations}$$

Figure 11-4: Motions highlighted for a few selected scatterers within one beam path of the ADCP in monochromatic waves.

11.4   Scatterer Motions in the ADCP Beam Paths

The general area around the ADCP is seeded with scatterers, and their locations recorded. Those scatterers that fall within the beam path will then be selected to interact with the transmitted signal. Their velocities are the combination of both the wave field and the turbulent field.

At each time step the scatter locations are updated. Certain scatterers will leave the beam path while others enter in.

Scattering Model with Doppler Shift

Ocean organism (< 1cm)
moves with water motions

$\vec{v}_s$ Scatterer
velocity

$\vec{r}$ θ

ADCP
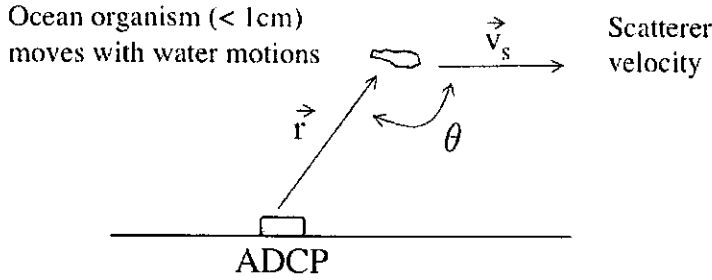
Doppler-shifted
scatter field:

$$\phi_s(r, t) = \frac{1}{1 - \frac{v_s}{c} \cos(\theta)} \frac{\exp^{i\omega((r/c) - t)}}{\frac{\omega}{c} r} \times S(\theta)$$

Doppler-shifted
frequency:

$$\omega = \omega_i \frac{1 + \frac{v_s}{c} \cos(\theta)}{1 - \frac{v_s}{c} \cos(\theta)}$$

Figure 11-5: The scatterer can be modeled as a point source with random phase.

11.5   Analytic Expression for Scattering Model

The Doppler-shifted scatter field can be represented by an expression which contains an ampltitude adjustment term, an attenuation term, a Doppler-shift frequency term, and a scatter function term.

The amplitude adustment term can be ommitted, as scatterer motion has little affect on it.

$$\frac{1}{1 - \frac{v_s}{c} \cos(\theta)} \approx 1 \tag{11.1}$$

The attenuation term, $\frac{\omega}{c} r$, is based on the distance and frequency of the signal. The phase term, $exp^{i\omega((r/c) - t)}$, is based on the distance the signal travels to interact with the scatterer, though it is essentially offset by the scatter function term, $S(\theta)$, which adds random phase.

The Doppler-shifted frequency, ω, is for a stationary source and a moving receiver. The equation must be applied a second time with the scatterer as a moving source.
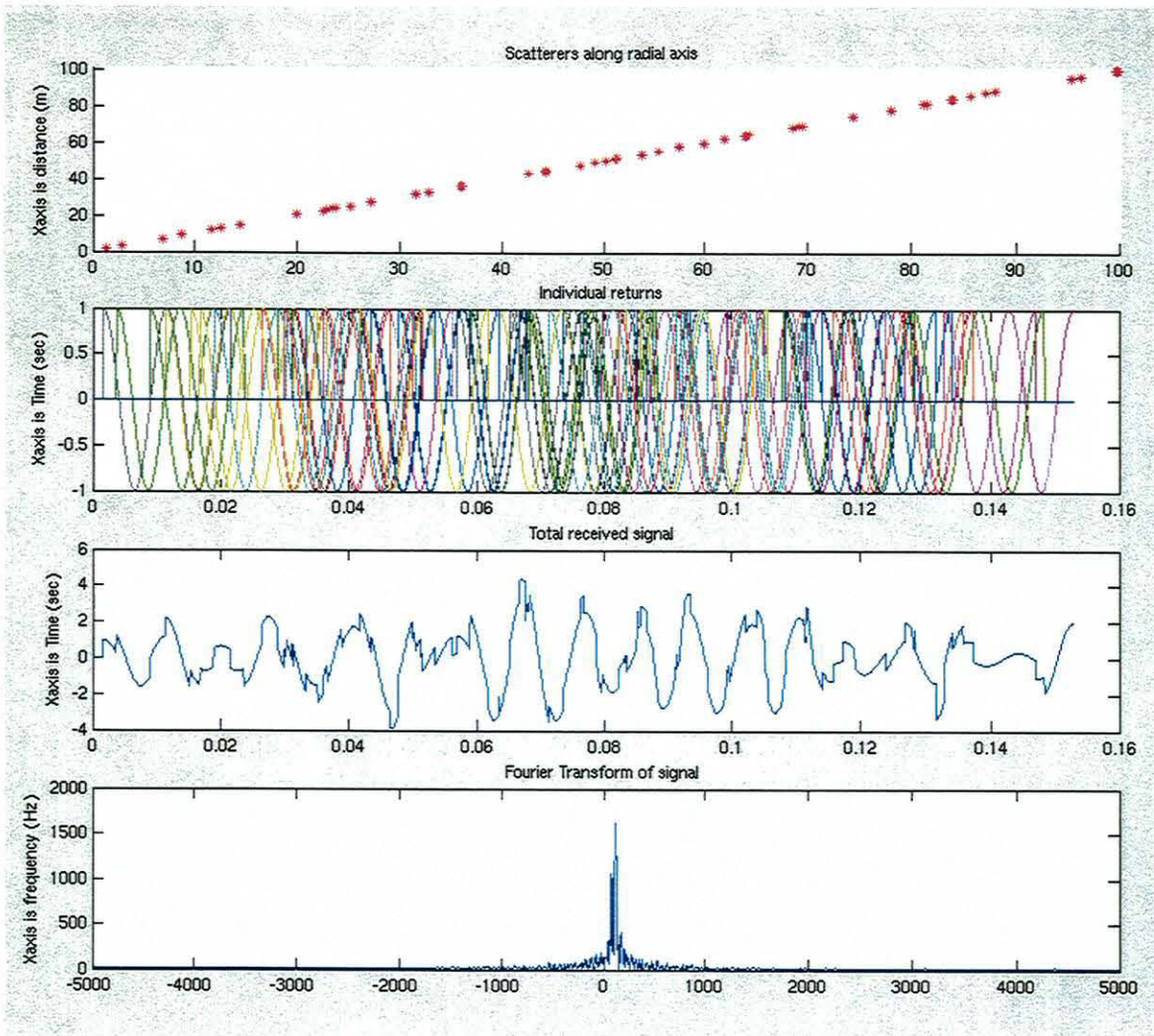
184

Figure 11-6: The received signal is a result of the scatterer location and velocity, random phase, and a range of frequencies due to the broadband nature of the transmitted pulse.

11.6 Results

The covariance technique can be applied to the return signal in order to estimate the Doppler shift and therefore the average scatterer velocities per range bin. These velocity estimates represent the ADCP measurements, and is what is assumed to be the true value of both wave and turbulent velocities combined. The signal processing algorithms will then work with this generated data to sort out the signals. When the ADCP simulator is unable to accurately represent the true velocities, the algorithms will be unable to recover the true velocities.

Chapter 12

Conclusion

The goal of this thesis was to determine if an ADCP could be used to obtain a vertical profile of Reynolds stress estimates in the presence of energetic surface waves. The main issue at hand is that any sort of beam tilt causes the wave-induced velocities to masquerade as Reynold stresses. Even without beam tilt, the variance of the estimates of Reynolds stress are greatly affected by the wave-induced velocities. Without filtering out wave-induced velocities, the best that the ADCP can do is give rough approximations of the Reynolds stress.

Linear least squares filtering was explored as a means of removing the wave-induced velocities. Applying this to real ocean data, the resulting estimates of Reynolds stress were still noisy. Even in the filtered estimate, an error term appeared. The vast bulk of this thesis was trying to determine the source of this error.

The sound transmission process by the ADCP and subsequent velocity estimation was examined as one source of error. Many different parameters effect the outcome of ADCP measurement error, but upon averaging over many samples, the variance the error becomes insignificant when compared with other competing sources of error.

The main source of error, even in the filtered estimates, is a result of wave-induced velocities. The estimates of the variance of the radial turbulent fluctuations are influenced by the strength and direction of the surface waves, and the error terms in each depend on which way the beams are pointing. Upon forming the estimates of Reynolds stress, the error in oposing beams does not cancel out, and therefore

introduces a bias which can be of the same order of magnitude as the Reynold stresses.

A great deal of work was done to characterize the turbulence, wave, and error processes, so that prediction and analysis of this error could take place. Each of these models provide a wealth of information about the space-time structure of these processes, and were found to represent the real ocean processes quite well. When used for diagnosis, these models produced an error profile that was found to have similar features to the profile of estimates of the Reynolds stress using filtered ADCP data. The conclusion is that the models worked all to well to reveal that the estimates of Reynolds stress from the filtered data are dominated by error.

With further effort, it may be possible to use the models to find ways of reducing or eliminating the error. However, the error profile reveals a complex relationship among the model parameters, that may be difficult to unravel. Should this process be attempted, the simulation techniques put forth in this thesis should allow for validation of any estimation algorithm tested.

Bibliography

[1] G. K. Batchelor. *The Theory of Homogeneous Turbulence.* Cambride University Press, 1960.

[2] Peter S. Bernard and James M. Wallace. *Turbulent Flow: Analysis, Measuremetn, and Prediction.* John Wiley & Sons, Inc., Hoboken, New Jersey, 2002.

[3] G. J. Bierman. *Factorization Methods for Discrete Sequential Estimation.* Academic Press, Inc., 1977.

[4] B.H. Brumley, R.C. Cabrera, K. L. Deines, and E.A. Terray. Performance of a broad-band acoustic doppler current profiler. *IEEE Journal of Oceanic Engineering,* 16,No.4:402–407, Oct 1991.

[5] D. E. Dudgeon and R. M. Mersereau. *Multidimensional Digital Signal Processing.* Prentice Hall, Inc., 1984.

[6] A. J. Favre. Review on space-time correlations in turbulent fluids. *Journal of Applied Mechanics,* 32 (2):241–257, 1965.

[7] D. S. Hansen. Asymptotic performance of a pulse-to-pulse incoherent doppler sonar in an oceanic environment. *IEEE Journal of Oceanic Engineering,* OE-10,No.2:144–157, April 1985.

[8] RD Instruments. Workhorse sentinel adcp. www.rdinstruments.com. 2 pages of specifications.

[9] RD Instruments. *Acoustic Doppler Currnet Profiler, Principles of Operation: A practical Primer*. RD Instruments, San Diego, CA, second edition for broadband adcps edition, January 1996.

[10] RD Instruments. Field service technical paper 001 (fst-001): Broadband adcp advanced principles of operation. San Diego, CA, October 1996.

[11] K.S. Miller and M. M. Rochwarger. On estimating spectral moments in the presence of colored noise. *IEEE Transactions on Information Theory*, IT-16,No.3:303–309, May 1970.

[12] K.S. Miller and M. M. Rochwarger. A covariance approach to spectral moment estimation. *IEEE Transactions on Information Theory*, IT-18,No.5:588–596, Sept 1972.

[13] K.S. Miller and M. M. Rochwarger. Some remarks on spectral moment estimation. *IEEE Transactions on Communications*, pages 260–262, April 1972.

[14] A. V. Oppenheim, R. W. Schafer, and J. R. Buck. *Discrete-Time Signal Processing, 2nd edition*. Pearson Education, Inc., 2002.

[15] W. R. C. Phillips. The wall region of a turbulent boundary layer. *Physics of fluids*, 30:2354–2361, 1987.

[16] W. R. C. Phillips. Eulerian space-time correlations in turbulent shear flows. *Physics of fluids*, 12:2056–2064, 2000.

[17] W. R. C. Phillips and J. T. Ratnanather. Eulerian space-time correlations in turbulent shear flows. *Physics of fluids A*, 2:427–434, 1990.

[18] R. Pinkel and J.A. Smith. Repeat-sequence coding for improved precision of doppler sonar and sodar. *Journal of Atmospheric and Oceanic Technology*, 9:149–163, April 1992.

[19] W. J. Shaw and J. H. Trowbridge. The direct estimation of near-bottom turbulent fluxes in the presence of energetic wave motions. *Journal of Atmospheric and Oceanic Technology*, 18:1540–1557, 2001.

[20] Gilbert Strang. *Introduction to Applied Mathematics*. Wellesley-Cambridge Press, Wellesley, Massachusetts, 1986.

[21] H. Tennekes and J. L. Lumley. *A First Course in Turbulence*. MIT Press, 1972.

[22] Kenneth B. Theriault. Incoherent multibeam doppler current profiler perfomance: Part i - estimate variance. *IEEE Journal of Oceanic Engineering*, OE-11:7–15, 1986.

[23] Harry L. Van Trees. *Detection, Estimation, and Modulation Theory*, volume 1, chapter 2.4, pages 52–85. John Wiley & Sons, Inc, New York, first edition, 1968.

[24] M.V. Trevorrow and D.M. Farmer. The use of barker codes in doppler sonar measurements. *Journal of Atmospheric and Oceanic Technology*, 9:699–704, Oct 1992.

[25] J. H. Trowbridge. Notes and correspondence: On a technique for measurement of turbulent shear stress in the presence of surface waves. *Journal of Atmospheric and Oceanic Technology*, 18:290–298, 1998.

[26] Eirwen Williams and John H. Simpson. Uncertainties in estimates of reynolds stress and tke production rate using the adcp variance method. *Journal of Atmospheric and Oceanic Technology*, 21:347–357, 2004.

[27] Alan S. Willsky, Gregory W. Wornell, and Jeffrey H. Shapiro. Stocahstic processes, detection, and estimation. 6.432 Course Notes, Cambridge, MA, 2004. 3.2.5.

[28] Dick Yu. 13.021 - marine hydrodynamics. MIT Open Course Ware, Cambridge, MA, 2001. Lecture 6.